

UNIVERSITE PARIS 13 – INSTITUT GALILEE

N° attribuée par la bibliothèque

THESE

Présentée pour obtenir le grade de

DOCTEUR DE L'UNIVERSITE PARIS 13

Discipline : Physique

Présentée et soutenue publiquement

Par

Quentin RIPAULT

Second-Harmonic Generation in Helium-implanted 2D-PPLN waveguides

Soutenue le: 16 Juillet 2013

M.	Vincent COUDERC	Rapporteur
M.	Philippe DELAYE	Rapporteur
Mme.	Sara DUCCI	Examinateur
M.	Frederick DU BURCK	Examinateur
M.	Esidor NSOENZOK	Examinateur
M.	Azzedine BOUDRIOUA	Directeur de Thèse
M.	Lung Hang PENG	Directeur de Thèse
M.	Min Won LEE	Membre encadrant

Acknowledgements

This thesis has been performed at the FEPED laboratory (Ferroelectric Photonics and Electronics Device lab.) of National Taiwan University and the LPL (Laboratoire de Physique des Lasers) of Paris XIII University.

First, I want to thank Prof. Vincent Couderc and Prof. Philippe Delaye for accepting to be a main examiner of this work. I also thank the other members of the jury, Prof. Sara Ducci, Prof. Frederic Du Burck, Prof. Esidor Ntsoenzok and Dr. Min Won Lee for the interest they have shown in my manuscript.

I express my deepest gratitude to Prof. Lung Peng Han and Prof. Azzedine Boudrioua who directed my thesis in Taiwan and France. I just thank both for their warm welcome. They have been present to advise and support me throughout my thesis. They are among those who have taught me what I know and forged me to this profession.

Many people think that the work of a thesis, particularly at the writing time, is a solitary adventure. This is partly true for having appreciated this great independence. However many people have contributed to the elaboration and the realisation of this work.

I warmly thank the CEMHTI team of the University of Orleans and particularly Esidor Ntsoenzok for having supported my work and having allowed me the realisation of optical waveguides by ion implantation.

Special thanks to Thierry Billeton for having shared his unique knowledge and expertise in precision optics and for his valuable help.

I extend my deepest acknowledgement to Fadwa, Faiza, Min, Hadi, François, Anthony, Mohamed, Getachew, Elias, Lei, all people of the lab and the lab next door, permanent and PhD students. To those who have fed me, supported and encouraged me during these years, to those who are part of my life in one way or another, to those who enlightened me of their precious advices, to those who helped me to mature as a researcher, who taught me to take care of the style and the efficiency of these pages, who also taught me like no one else independence and

love of learning, to those who would prevail their own intellectual path to share, confront, modify and constantly feed their paths with others.

For bringing all your heart. For making me see the world with your eyes. With the hope that you stay with me a long time.

I also want to thank those who read these pages. With the hope of sharing my path.

Table of Contents

General Introduction.....	9
Nonlinear Optics Theory.....	13
1.1. Introduction.....	13
1.2. Radiation-matter interaction	14
1.2.1. Second-Order Nonlinear Interactions.....	16
1.2.2. Second-Harmonic Generation	21
1.2.3. Achieving Phase-Matching.....	25
1.2.3.1. Birefringence Phase-Matching (BPM)	25
1.2.3.2. Quasi-Phase Matching (QPM).....	28
1.2.3.3. Second-harmonic conversion efficiency	33
1.2.3.4. Tuning and bandwidths in periodic structures	34
1.2.3.5. Spectral bandwidth.....	35
1.2.3.6. Temperature bandwidth.....	36
1.2.4. Materials for QPM.....	38
1.2.4.1. List of materials.....	39
1.2.4.2. Lithium Niobate	39
1.2.4.3. Poling methods	41
1.2.4.4. Poling Process according to Miller's model.....	43
1.3. General theory of integrated optics.....	47
1.3.1. Planar optical waveguides	48
1.3.2. Expression of the EM field profile.....	50
1.3.3. Equation of the guided modes.....	54
1.3.4. Reconstruction of the index profile by i-WKB method	56
1.4. SHG in waveguide configuration.....	60
1.4.1. Effect of optical confinement on SHG with Gaussian fundamental beam.....	60
1.4.1.1. Improvement of interaction length.....	61
1.4.1.2. Parametric Interaction of focused Gaussian beam for SHG.....	61
1.4.2. SHG interaction in waveguide	66
1.4.3. Expression of the Effective Area Overlap in a waveguide	69

1.4.4. Phase matching by modal dispersion	70
Summary.....	71
References.....	73

Nonlinear photonic crystal and fabrication process..... 81

2.1. Introduction.....	81
2.2. Second-harmonic generation in 2D nonlinear photonic crystals.....	81
2.2.1. Real Lattice.....	82
2.2.2. Reciprocal lattice.....	85
2.2.3. Angular tuning	89
2.2.4. Angular acceptance.....	93
2.3. PPLN Fabrication process.....	97
2.4. Fabrication of waveguides.....	103
2.4.1. Ionic diffusion technique	103
2.4.2. Ion exchange technique	105
2.4.3. Physical and chemical deposition	106
2.4.4. Organic materials.....	106
2.4.5. Nanocomposite materials	107
2.4.6. Ion implantation technique	107
2.4.7. Implantation in Lithium Niobate.....	108
2.4.8. Realisation of planar waveguide on PPLN by He ⁺ implantation.....	109
2.4.8.1. He ⁺ implantation process.....	109
2.4.8.2. Implantation parameters.....	111
2.4.8.3. Implantation interactions.....	112
2.4.8.4. Ion implantation advantages.....	116
2.4.8.5. Annealing treatment	117
Summary.....	118
References.....	119

Second-harmonic generation in He⁺ implanted 2D-PPLN..... 127

3.1. Introduction.....	127
------------------------	-----

3.2. Characterisation of implanted waveguides in 2D-PPLN	129
3.2.1. Linear characterisation	129
3.2.1.1. Dark m-line spectroscopy.....	129
3.2.1.2. Effective index measurements.....	131
3.2.1.3. Attenuation measurement by optical surface analysis setup	136
3.2.1.4. Experimental results	138
3.2.2. Nonlinear characterisation	143
3.2.2.1. Optical setup.....	143
3.2.2.2. SHG temperature tuning.....	147
3.2.2.3. SHG angular dependence.....	150
3.2.2.4. Conversion efficiency measurement in cw- and pulsed regime	153
3.2.2.5. Photorefractive effects	157
3.2.2.6. Photorefractive effect in the waveguide	160
3.3. Characterisation of implanted waveguide in doped MgO:2D-PPLN	164
3.3.1. Linear characterisation	164
3.3.1.1. Refractive index profile	164
3.3.1.2. Attenuation loss.....	167
3.3.2. Nonlinear characterisation	168
3.3.2.1. SHG temperature tuning.....	168
3.3.2.2. SHG angular dependence.....	170
3.3.2.3. Conversion efficiency measurements	171
3.3.2.4. Photorefractive effect.....	173
Summary	174
Reference	175
Conclusions	176
Annexe: implantation in nonlinear crystals	179
Scientific articles	183

Introduction

Nonlinearities are widely present in the world around us and are subject of study more and more deeply. The discipline of nonlinear optical science emerged by Franken *et al.* in 1961 [1]. However, nonlinear phenomena had been studied in other fields of physics a long time before: in mechanics, acoustics, fluid dynamics, electronics or chemistry. In general, the optical nonlinearities are weak phenomena and require significant optical fields to be highlighted. It is the advent of laser which led to the discovery of optical nonlinearities in volume, with an increase of the available optical power. Promptly, nonlinear optics had attracted much attention and created new research areas and technologies. For instance, wave-mixing via a nonlinear second-order interaction and second harmonic generation in nonlinear crystals were the areas which had received particular attention. The 1980's had seen the emergence of new research topics, particularly nonlinear optical study of coherent sources such as widely-tunable parametric oscillators [2] and ultra-short pulse lasers [3]. Therefore, nonlinear crystals such as LiNbO₃ have widely been used for this purpose. However, nonlinear effects are not optimised unless phase matching conditions are satisfied. Periodically-poled structures in 1D were proposed to overcome phase-matching problem in nonlinear crystals. The crystal studied in this thesis is periodically-poled lithium niobate (PPLN) allowing quasi-phase matching.

It is also this period during which the interest in nonlinearities in optical waveguides or optical fibres had increased. In fact, guided optics had opened new horizons in nonlinear optics thank to the light propagation over long distance and the suppression of diffraction effects and the increase of nonlinear effects by optical confinement and accumulation. Another advantage of the waveguide structure is its small size, which allows for the fabrication of compact optical circuits or chips together with other photonic components for a rich variety of applications [4, 5]. Many technologies have been developed for the fabrication of integrated optical components and now a huge number of components of this kind is commercially available. Most of components are integrated in a planar substrate. This integration aims at miniaturising optical systems like integrated electronic circuits for electronic devices. However, nonlinear effects are not always straightforward to integrated optics [6 - 8]. The difficulty lies on how to adapt the existing and abundant techniques of waveguides fabrication for nonlinear materials without altering their nonlinear properties.

In recent years, nonlinear optics has seen the new arrivals of nonlinear crystals with a periodic modulation of the nonlinear coefficient. The development of techniques for periodically-poled ferroelectric crystals in one or two dimensions allows very efficient quasi-phase matching technique proposed by N. Blombergen in 1962 [9]. Integrated optics using 2D nonlinear photonic crystals (NLPC) has recently been the subject of several developments for applications to the field of light sources and optical signal processing. Such an NLPCs produces many reciprocal lattice vectors (RLV) in the 2D reciprocal lattice. It has been reported that these lattice vectors provide one or more quasi-phase matching solution [10] compared to 1D structure. Despite of low QPM orders, the high flexibility of 2D structure allows multi-wavelength light generation by temperature and angular tuning. For this reason we have chosen 2D-PPLN to study SHG in a waveguide.

The combination of nonlinear and integrated optics is an important issue to take full benefit of the advantage of a large energy confinement, a longer interaction length and the ability to adjust the phase-matching by designing suitable periodically-poled structures. The spin-offs of this research area have boosted new technologies for further development of optical components, solid tuneable coherent and miniature light sources, etc. Many of these techniques will be reported.

Therefore, our study is based on the fusion of these principles and techniques: SHG by quasi-phase matching in helium-implanted NLPC optical waveguide, and constitutes the originality of our works.

In chapter 1, our aim is to bring to the reader an overview of the actual results and trends in integrated nonlinear optics. The choice is made to address most aspect favouring a theoretical and qualitative description of the phenomena and an intuitive analysis of concepts. Second-order nonlinear interactions, Quasi-phase Matching principle, effect of optical confinement on Second-harmonic generation and fabrication of optical waveguides in nonlinear materials are among the discussed topics.

Chapter 2 will be divided in two parts. The first part will focus on the special case of the second-harmonic generation in NLPC, especially 2D-PPLN with a square lattice. In a second part, we

will focus on the conception and the fabrication of our NLPC by electrical poling method and the fabrication of planar optical waveguide on the surface by helium implantation.

Finally, chapter 3 presents our experimental results on our samples. The chapter includes a study of linear properties of our waveguides. It mainly consists guiding properties of the sample after the implantation process. It also concerns an estimation of the attenuation in that structure. Then, a study of the nonlinear properties of the waveguide is presented. From the obtained experimental results, it will be demonstrated that this technique does not affect the non-linear properties of our 2D-PPLN. Furthermore, the waveguide influence on SHG according to QPM conditions is studied and compared with SHG in bulk crystal. Thus, through our observations and according to the theory, we will provide the information necessary for general understanding of a nonlinear interaction in that waveguide. This will allow us to conclude the high performance of our samples.

References:

- [1] P. Franken, A. E. Ill, C. Peter, G. Weinreich, *Generation of optical harmonics*, Phys. Rev. Lett. **7**, 118 - 121(1961).
- [2] F. J. Duarte, *Tunable Lasers handbook*, Optics and Photonics, Academic Press (San Diego, 1995).
- [3] C. Rulliere, *Femtosecond Laser Pulses: principles and experiments*, Springer 2nd Edition (New-York, 2004).
- [4] S. D. Smith, I. Janossy, H. A. MacKenzie, J. G. H. Mathew, J. J. E. Reid, Nonlinear optical circuit elements as logic gates for optical computers – the first digital optical circuit, Opt. Eng. **24**, 569 – 574 (1985).
- [5] J. Oksanen, *Modeling transmitters, amplifiers and nonlinear circuits for the next generation optical networks*, Helsinki University of Technology Laboratory and Computational Engineering Publication (2006).
- [6] I. Kaminov, J. Carruthers, *Optical waveguiding layer in LiNbO₃ and LiTaO₃*, Appl. Phys. Lett. **22**, 326 - 328 (1973).

[7] R. G. Hunsperger, *Integrated optics, theory and technology*, Springer (2002).

Chapter 1

Nonlinear Optics Theory

1.1. Introduction

The growing effort to miniaturisation, high performance low cost of optical devices have given rise to new research in materials and engineering fields for optical systems. Particularly, many integrated systems rely on second or third order nonlinear process.

The purpose of this thesis work is to combine the nonlinear properties of Nonlinear Photonic Crystals (NLPC) with waveguides fabricated by helium implantation. The theoretical development is similar to the bulk case with added considerations of propagation wave vectors.

This chapter is dedicated to the basic concepts of nonlinear optics and particularly the study of second-harmonic generation. We will provide the useful tools for understanding and exploiting the results presented in chapter 3. More specifically, we develop differential equations for modelling nonlinear interaction involving wave propagating in either bulk media and in optical waveguide.

Firstly, we will seek to understand how an electromagnetic (EM) wave interacts with a dense medium and can create a new wavelength according to the nonlinear optics theory. We will also describe the main techniques used to improve nonlinear effects in materials, especially in ferroelectric crystals. These techniques are called Birefringence Phase matching (BPM) and Quasi-Phase Matching (QPM) and meet the conditions of nonlinear new frequency generation. We linger longer on the Second-harmonic Generation (SHG) that occurs between the fundamental and harmonic waves with the conversion efficiency.

In a second time, after a brief theoretical review about the propagation of light in planar optical waveguides, we will discuss the SHG mechanism in nonlinear optical waveguides as well as the modifications brought by this kind of structures, particularly SHG tuning and tolerance changes through the general theory. We will see particularly the modal dispersion influence on the QPM when the waveguide is multimodal. Then, after seeing the waveguide influence on the phase matching conditions and with the help of integrated optics theory, we will seek how to enhance the performance of a material by the use of a guiding structure.

1.2. Radiation-matter interaction

Since the first experimental demonstration of laser effect, optics has undergone many upheavals due to the characteristics of laser sources such as the directivity, the degree of monochromaticity and the coherency. These characteristics gave rise to a number of new applications. Moreover their high optical power density has boosted nonlinear optics, many industrial applications and even Inertial Confinement Fusion projects for a new energy source [1]. In order to achieve frequency conversion, we usually need a laser with a reasonably high optical power, especially a pulsed laser. In fact, the electrical field of laser radiation can reach 10^8 V/cm. This order of magnitude corresponds to atomic and molecular electrical fields linking valence electrons in matter. The orbital modification of electrons under laser radiation creates a polarisation of the material which is no longer linear to the EM field applied. The linear refractive laws considering a constant refractive index is no longer valid. In fact, in the beginning of the 20th century, when Lorentz studied the first order dielectric susceptibility of materials, he considered electrons as harmonic oscillators in matter. In that case, the optical response of the material which processes such as reflection, transmission or absorption scale linearly with the intensity of the applied optical source. Then, Lorentz missed the anharmonic term which is not negligible when the applied electric field is close to the valence electron's one. It was with the development of the ruby laser by Maiman in 1960 [2] that the first nonlinear optical effect was observed by Franken *et al.* [3]. In fact, Franken noticed a weak optical signal at 347.1 nm which was generated in a quartz crystal when the material was illuminated with a high power ruby laser at 694.2 nm. It was surmised that the new light source was due to the coherent mixing of two electrical fields in the quartz as a second-harmonic response was produced in the material. Franken measured an optical conversion efficiency at 10^{-10} % and the SHG response was characterised by a quadratic

dependence on the strength of the applied optical field. From those observations, Bloembergen *et al.* [4] formulated many of the classical and quantum mechanical theory of nonlinear optics showing that the nonlinear responses of matter are extensions of the linear optical interaction, depending on more than one optical field strength. The fast growth in the nonlinear optical community has been driven, in part by the technological need for new coherent light sources and optoelectronic devices in the telecommunications industry.

The general description of nonlinear optical properties in this thesis is referred to R. L. Sutherland “Handbook of Nonlinear Optics” [5], Y. R. Shen “The principles of nonlinear optics [6], and R. W. Boyd “Nonlinear Optics”[7].

In order to understand this phenomenon, we consider the macroscopic electromagnetism. More specifically, the propagation of light is governed by the four Maxwell’s equations in the time domain:

$$\nabla \cdot \vec{D} = \rho_f \tag{1.1.a}$$

$$\nabla \times \vec{E} = -\partial_t \vec{B} \tag{1.1.b}$$

$$\nabla \cdot \vec{B} = 0 \tag{1.1.c}$$

$$\nabla \times \vec{H} = \vec{j} - \partial_t \vec{D} \tag{1.1.d}$$

In this set of equations, \vec{E} and \vec{H} are the macroscopic electric and the magnetic field vectors, respectively, \vec{D} and \vec{B} are the electric displacement field and the magnetic induction, respectively, and the quantities ρ_f and \vec{j} are the free electric charge and the current density, respectively, which are often considered as the sources of the fields \vec{E} and \vec{H} . Most dielectric materials have no free electric charge, and hence we can set $\rho_f = 0$. We shall further assume that there is no external current such that $\vec{j} = \vec{0}$. For a particular set of boundary conditions, Maxwell’s equation (Eq. (1.1)) cannot be solved uniquely unless the relationship between \vec{B} and \vec{H} and that between \vec{E} and \vec{D} are known. To obtain a unique determination of the field vectors, Maxwell’s equations must be supplemented by the constitutive equations,

$$\vec{D} = \epsilon_0 \vec{E} + \vec{P} \tag{1.2.a}$$

$$\vec{B} = \mu_0 \vec{H} + \vec{M} \tag{1.2.b}$$

where \vec{P} and \vec{M} are the electric and the magnetic polarisations, respectively. We can set $\vec{M} = 0$ since the material we use is non magnetic. The origin of electric polarisation \vec{P} lies at the microscopic level. When an electromagnetic field is present in matter, the electric field perturbs the motion of electrons and produces a polarisation \vec{P} per unit volume. The components of the instantaneous polarisation field P_α can be related to the component of the instantaneous electric field E_α of the optical beams with $\alpha, \beta, \gamma, \delta = x, y, z$ via the Taylor series expansion [5, 6]. If we consider only a single polarisation component of the electric field, P_α can be written as:

$$P_\alpha(\vec{r}, t) = \varepsilon_0 \chi_{\alpha\beta}^{(1)}(\vec{r}, t) E_\beta(\vec{r}, t) + \varepsilon_0 \chi_{\alpha\beta\gamma}^{(2)}(\vec{r}, t) E_\beta(\vec{r}, t) E_\gamma(\vec{r}, t) + \varepsilon_0 \chi_{\alpha\beta\gamma\delta}^{(3)}(\vec{r}, t) E_\beta(\vec{r}, t) E_\gamma(\vec{r}, t) E_\delta(\vec{r}, t) + \dots \quad (1.3)$$

where the quantities $\chi^{(n)}$, known as susceptibilities, arise from the material's atomic structure. In this series expansion, the susceptibility $\chi^{(n)}$ decreases with successive terms, so we generally need to consider the highest order terms only. The first term depends linearly on the electric field and defines the refractive index of the material, i. e. $n_{\alpha\beta} = \sqrt{1 + \chi_{\alpha\beta}^{(1)}}$. The rest of the terms can then be identified as the nonlinear polarisation field. It explains a nonlinear relationship between the instantaneous polarisation of the material and an applied electrical field. Hence the polarisation field can be split into:

$$\vec{P} = \vec{P}_L + \vec{P}_{NL} \quad (1.4)$$

where \vec{P}_L is the linearly dependant polarisation field and \vec{P}_{NL} contains the nonlinear polarisation field. We will see more closely in section 1.2.1, the possible nonlinear interactions due to the nonlinear polarisation field \vec{P}_{NL} and the nonlinear susceptibility $\chi^{(n)}$.

1.2.1. Second-Order Nonlinear Interactions

The susceptibilities $\chi^{(n)}$ are the intrinsic properties of material. The nonlinear susceptibilities describe the coupling efficiency of n optical fields in the bulk region of the material. Their tensorial forms reflect the structural symmetry of the material. For instance, the nonlinear susceptibility $\chi^{(2)}$ is a tensor of rank 3 ($\chi_{\alpha\beta\gamma}$) with 27 components according to the Cartesian

axes (x,y,z). With the product commutativity of the electrical fields $E_\beta(\vec{r}, t)E_\gamma(\vec{r}, t) = E_\gamma(\vec{r}, t)E_\beta(\vec{r}, t)$, the tensor can be reduced at 18 components.

The nonlinear polarisation can be written under the Voigt form:

$$\begin{bmatrix} P_{NL,x} \\ P_{NL,y} \\ P_{NL,z} \end{bmatrix} = \varepsilon_0 \begin{bmatrix} \chi_{111} & \chi_{122} & \chi_{133} & \chi_{123} & \chi_{113} & \chi_{112} \\ \chi_{211} & \chi_{222} & \chi_{233} & \chi_{223} & \chi_{213} & \chi_{212} \\ \chi_{311} & \chi_{322} & \chi_{333} & \chi_{323} & \chi_{313} & \chi_{312} \end{bmatrix} \begin{bmatrix} E_x^2 \\ E_y^2 \\ E_z^2 \\ 2E_yE_z \\ 2E_xE_z \\ 2E_xE_y \end{bmatrix} \quad (1.5)$$

Kleinman also demonstrate that $\chi^{(2)}$ is symmetric relatively to the axes [8] so that $\chi_{\alpha\beta\gamma} = \chi_{\alpha\gamma\beta} = \chi_{\beta\alpha\gamma} = \chi_{\gamma\alpha\beta} = \chi_{\gamma\beta\alpha}$. It reduces the tensor to 10 components. Finally, using the contracted notation $\chi_{\alpha\beta\gamma} = 2d_{\alpha\delta}$ where:

$\beta\gamma$	11	22	33	23 = 32	13 = 31	12 = 21
δ	1	2	3	4	5	6

We can write the new expression of the polarisation by using that notation:

$$\begin{bmatrix} P_{NL,x} \\ P_{NL,y} \\ P_{NL,z} \end{bmatrix} = \varepsilon_0 \begin{bmatrix} d_{11} & d_{12} & d_{13} & d_{14} & d_{15} & d_{16} \\ d_{16} & d_{22} & d_{23} & d_{24} & d_{14} & d_{12} \\ d_{15} & d_{24} & d_{33} & d_{23} & d_{13} & d_{14} \end{bmatrix} \begin{bmatrix} E_x^2 \\ E_y^2 \\ E_z^2 \\ 2E_yE_z \\ 2E_xE_z \\ 2E_xE_y \end{bmatrix} \quad (1.6)$$

In all materials with inversion symmetry, such as liquids, gases, amorphous solids, many crystals and optical fibres, i. e. the so-called centrosymmetric materials, the $\chi^{(2n)}$ tensor components vanish and third-order nonlinear effects take place due to $\chi^{(3)}$ instead. These vanishing $\chi^{(2n)}$ tensor components result from the odd inversion symmetry of the electric field vector \vec{E} and the electric polarisation vector \vec{P} .

There exists an important class of materials known as ferroelectric, of which Lithium Niobate (LiNbO₃) is a member. These materials possess a spontaneous electric dipole moment \vec{P}_S in zero external fields [7], which originates from the shift of an ion from a symmetrical site [9]. Note that in this case, the instantaneous polarisation is written as:

$$\vec{P} = \vec{P}_S + \vec{P}_L + \vec{P}_{NL}$$

This symmetry breaking results in nonzero $\chi^{(2)}$ tensor components [7], which are responsible for the nonlinear interactions we are interested in. Several second-order nonlinear interactions attributed to $\chi^{(2)}$ are qualitatively described in this section. From Eq. (1.3), for linearly-polarised light, the second-order polarisation in a nonlinear material is given by:

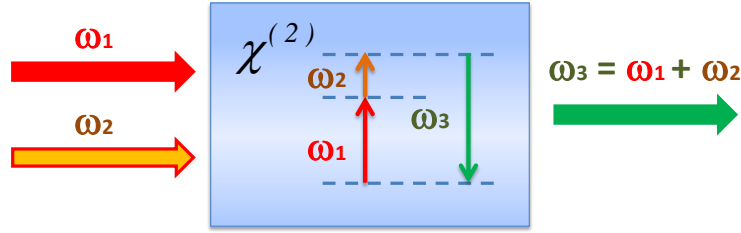
$$P_{NL}(\vec{r}, t) = \varepsilon_0 \chi^{(2)}(\vec{r}, t) E^2(\vec{r}, t) \quad (1.7)$$

Let us consider an electric field with two frequency components, ω_1 and ω_2 in a nonlinear crystal such as lithium niobate. The field can be represented in scalar form by:

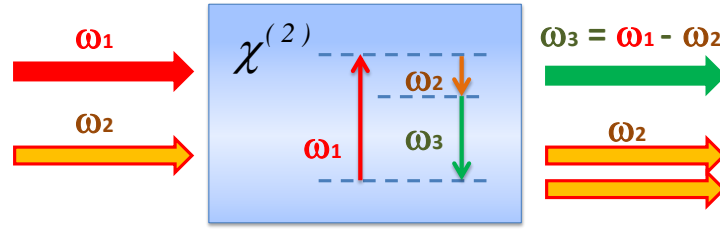
$$E(\vec{r}, t) = E_1 \exp[i(\vec{k}_1 \cdot \vec{r} - \omega_1 t)] + E_2 \exp[i(\vec{k}_2 \cdot \vec{r} - \omega_2 t)] + c. c. \quad (1.8)$$

where $|\vec{k}_j| = \frac{\omega_j}{c} \varepsilon(\omega_j) = \frac{\omega_j}{c} n^2(\omega_j)$ with the above electric field, the second-order nonlinear polarisation [Eq. (1.5)] can be rewritten as follows:

$$P_{NL}(\vec{r}, t) = \varepsilon_0 \chi^{(2)}(\vec{r}, t) \left\{ \begin{aligned} &E_1^2(\vec{r}, t) \exp[2i(\vec{k}_1 \cdot \vec{r} - \omega_1 t)] + E_2^2(\vec{r}, t) \exp[2i(\vec{k}_2 \cdot \vec{r} - \omega_2 t)] \\ &+ 2E_1 E_2 \exp[i(\vec{k}_1 + \vec{k}_2) \cdot \vec{r} - i(\omega_1 + \omega_2)t] \\ &+ 2E_1 E_2^* \exp[i(\vec{k}_1 - \vec{k}_2) \cdot \vec{r} - i(\omega_1 - \omega_2)t] + c. c. \end{aligned} \right\} + 2\varepsilon_0 \chi^{(2)}(\vec{r}, t) [|E_1|^2 + |E_2|^2] \quad (1.9)$$



(a) Sum frequency generation



(b) Difference frequency generation

Figure 1.1: Illustration of geometries and energy-level description for two different second-order nonlinear interactions in a nonlinear crystal.

One readily identifies the different frequency components of the nonlinear polarisation from the following interactions:

$$E_1^2(\vec{r}, t) \exp[-2i\omega_1 t], E_2^2(\vec{r}, t) \exp[-2i\omega_2 t] \quad \text{second-harmonic generation} \quad (1.10.a)$$

$$2E_1 E_2 \exp[-i(\omega_1 + \omega_2)t] \quad \text{sum-frequency generation} \quad (1.10.b)$$

$$2E_1 E_2^* \exp[-i(\omega_1 - \omega_2)t] \quad \text{difference-frequency generation} \quad (1.10.c)$$

$$|E_1|^2 + |E_2|^2 \quad \text{optical rectification} \quad (1.10.d)$$

The three first interactions are illustrated in Fig. 1.1. They are known as parametric interactions producing new frequencies. Although the three nonlinear effects may occur simultaneously, generally only one is favoured by the phase matching condition in the nonlinear crystal to generate an output signal efficiently. Hence, we can consider them separately.

Let us consider the sum-frequency generation (SFG). The input electric field has two distinct frequencies ω_1 and ω_2 which interact with each other along the nonlinear material to produce an

output wave at a frequency $\omega_3 = \omega_1 + \omega_2$. This phenomenon can be visualised in terms of photon virtual energy levels, as depicted in Fig.1.1(a). In this process, the photons with energy $\hbar\omega_1$ and $\hbar\omega_2$ are destroyed in the material to generate a new one. The energy conservation dictates that the produced photon has an energy $\hbar\omega_3 = \hbar\omega_1 + \hbar\omega_2$. In addition, the total momentum in the interaction must be conserved, i. e. $\vec{k}_3 = \vec{k}_1 + \vec{k}_2$. This requirement for the conservation of momentum is best-known as the phase-matching condition. For a collinear interaction, the conservation of momentum translates into $\omega_3 n(\omega_3) = \omega_1 n(\omega_1) + \omega_2 n(\omega_2)$. However, this condition cannot generally be satisfied due to the chromatic dispersion of materials, thus resulting in the phase mismatch $\Delta k = \vec{k}_3 - \vec{k}_1 - \vec{k}_2$. The phase mismatch deteriorates the power transfer between the three waves, reducing the conversion efficiency. Several methods have been proposed to achieve phase-matching which will be discussed in the next section. When the input waves are at a degenerated frequencies $\omega_1 = \omega_2$ this interaction contributes to second-harmonic generation (SHG) only. Both the phenomena are commonly used to generate electromagnetic waves at higher frequencies such as frequencies for ultraviolet that are inaccessible by standard quantum transitions of atoms and/or molecules.

The principle of difference frequency generation (DFG) is schematically depicted in Fig.1.1(b). The two input electromagnetic waves have distinct frequencies ω_1 and ω_2 which interact to produce an output wave at a frequency $\omega_3 = \omega_1 - \omega_2$. Both the energy and momentum must be conserved in this process, i. e. $\hbar\omega_3 = \hbar\omega_1 - \hbar\omega_2$ and $\vec{k}_3 = \vec{k}_1 - \vec{k}_2$. Superficially, DFG looks similar to SFG. However, upon close inspection of the energy level diagrams in Fig. 1.1(b), only higher-frequency photon is annihilated and another photon at lower frequency (ω_2) is created together with a new photon ω_3 in the nonlinear crystal. Therefore, the input wave at the lower frequency can be amplified. For this reason, this process is also known as optical parametric amplification (OPA) [10]. In this case, the $\hbar\omega_2$ photon at the input of the crystal stimulates the process. However, it can also occur with the $\hbar\omega_1$ photon at the input only, which is known as optical parametric fluorescence [11]. If the nonlinear crystal is put inside a resonator, the electromagnetic waves at ω_2 and/or ω_3 can build up a very high power. This configuration is known as an optical parametric oscillator (OPO) [12] with wide wavelength tuneability. Recently, an OPO using two nonlinear crystals was developed, giving a very wide range of tuneability [13].

Second-order phenomena	Third order phenomena
Sum-frequency generation [4 - 8]	Stimulated Raman scattering [4 - 8, 19]
Difference frequency generation [4 - 8]	Two-photon absorption [4 - 8, 20]
Second-harmonic generation [4 - 8]	Optical field induced birefringence [4 - 8]
Parametric amplification [4 - 14]	Self-focusing [4 - 8, 21]
Optical rectification [15]	Phase conjugation [4 - 8]
Optical field induced magnetisation [5, 16]	Third harmonic generation [4 - 8]
Electro-optic effects [17]	Electric-field induced SHG (Poling) [4 - 8, 22]
Magneto-optic effects [18]	Degenerate four-wave mixing [4 - 8, 23]

Table 1.1: list of second- and third-order nonlinear interactions

Most of second- and third-order nonlinear interactions are listed in Table 1.1. Generally, optical damages in materials limit most nonlinear effects at these orders.

1.2.2. Second-Harmonic Generation

In this section, we provide detailed SHG process as well as rigorous mathematical description. The description is done through the formulation of coupled mode equations for SHG and is easily applied to SFG. The coupled-mode equations can be formulated with Maxwell's equations. From Maxwell's equations (Eq. (1.1)) and the constitutive relation (Eq. (1.2)) wave equation taking into account the nonlinear polarisation field can be obtained as:

$$\nabla \times \nabla \times \vec{E}(\vec{r}, t) + \frac{n^2}{c^2} \partial_t^2 \vec{E}(\vec{r}, t) = -\mu_0 \partial_t^2 \vec{P}_{NL}(\vec{r}, t) \quad (1.11)$$

Note that a similar wave equation can be derived for the magnetic field vector \vec{H} . The nonlinear driving term on the right-hand side of the equation can be considered as a small perturbation to the linear differential equation on the left-hand-side, involving in light interaction between frequencies. This interaction leads to an energy transfer between the different frequencies during

the wave propagation. The solution of the above nonlinear wave equation can be written as a sum of their various frequency components:

$$\vec{E}(\vec{r}, t) = \sum_j \vec{F}_j(x, y) \vec{A}_j(z) \exp[i(\vec{k}_j \cdot \vec{r} - \omega_j t)] + c. c. \quad (1.12)$$

where $\vec{F}_j(x, y)$ is the transverse field profile, and $\vec{A}_j(z)$ is the slowly-varying amplitude of the electromagnetic wave at a frequency ω_j .

With the plane wave approximation we have $\vec{F}_j(x, y) = \vec{F}_j$. Moreover, if we assume that the transverse mode profile does not significantly change during the propagation, \vec{F}_j is independent on z . The angular frequency ω_j and the propagation vector \vec{k}_j determine the phase velocity of the wave $v_p = \frac{\omega_j}{|\vec{k}_j|}$.

We need to find equations for the amplitude $A_j(z)$ which describe the evolution of each frequency component ω_j due to the nonlinear effects. Let us consider the monochromatic case with an electromagnetic wave at the fundamental frequency (FF) ω_{FF} . The single frequency wave interacts with itself and $\chi^{(2)}$ medium, thus producing the following nonlinear polarisation wave at its second-harmonic frequency ($2\omega_{FF} = \omega_{SH} = \omega$):

$$\vec{E}(\vec{r}, t; \omega_i) = \vec{F}(x, y) \vec{A}(z) \exp[i(\vec{k}_i \cdot \vec{r} - \omega_i t)] + c. c. \quad (1.13)$$

with $|\vec{k}_{FF}| = 2\pi n_{FF} / \lambda_{FF}$, and $|\vec{k}_{SH}| = 4\pi n_{SH} / \lambda_{FF}$

$$\text{And } P_{NL,\alpha}(\vec{r}, t; \omega_{SH}) = \varepsilon_0 \chi_{\alpha\beta\gamma}^{(2)} E_\beta(\vec{r}, t; \omega_{FF}) E_\gamma(\vec{r}, t; \omega_{FF}) \quad (1.14)$$

For the sake of simplicity, we consider a FF wave with the polarisations parallel or perpendicular to the optic axis of the crystal, using only a single component of $\chi_{\alpha\beta\gamma}^{(2)}$ with $\alpha, \beta, \gamma = x, y, z$.

The substitution of Eq. (1.13) and Eq. (1.14) into Eq. (1.11), and the use of the slowly-varying envelope approximation (SVEA):

$$\left| \frac{d^2 A(z)}{dz^2} \right| \ll k \left| \frac{dA(z)}{dz} \right|$$

yields the following coupled-mode equations that govern the evolution of the FF and the SH amplitudes in the $\chi^{(2)}$ medium [7].

$$\frac{dA_{FF}(z)}{dz} = 2i\omega_{FF}\kappa dA_{FF}^*(z)A_{SH}(z)\exp(i\Delta kz) \quad (1.15.a)$$

$$\frac{dA_{SH}(z)}{dz} = i\omega_{SH}\kappa dA_{FF}^2(z)\exp(-i\Delta kz) \quad (1.15.b)$$

where $\Delta k = k(\omega_{SH}) - 2k(\omega_{FF}) = \pi/l_c$ is the phase mismatch caused by dispersion in the material, $l_c = \lambda_{FF}/4(n_{SH} - n_{FF})$ is called coherent length, and $d = \frac{1}{2}\chi_{\alpha\beta\gamma}^{(2)}$ the reduced second order nonlinear susceptibility.

The coupling coefficient κ is given by:

$$\kappa = \sqrt{\frac{2}{n_{FF}^2 n_{SH} \epsilon_0 c}} \sqrt{\frac{1}{S_{ovl}}} \quad (1.16)$$

where $n_j = n(\omega_j)$ is the refractive index of the material, and

$$S_{ovl} = \frac{\int |F_{SH}|^2 dx dy (\int |F_{FF}|^2 dx dy)^2}{(\int |F_{FF}|^2 |F_{SH}| dx dy)^2} \quad (1.17)$$

is called the effective overlap area between the transverse field profiles of the fundamental (F_{FF}) and harmonic waves (F_{SH}). We will see how the effective overlap area is included in the so called Boyd and Kleinman coefficient when the fundamental wave is considered with a Gaussian profile. One other global consideration is to lay that F_{FF} and F_{SH} are planar waves and x-, y-axis independent. In that case, we have S_{ovl} which corresponds to the FF beam surface in the crystal bulk (at the beam waist position). Although Equation (1.15) can be solved analytically [24], their solution is far from simple.

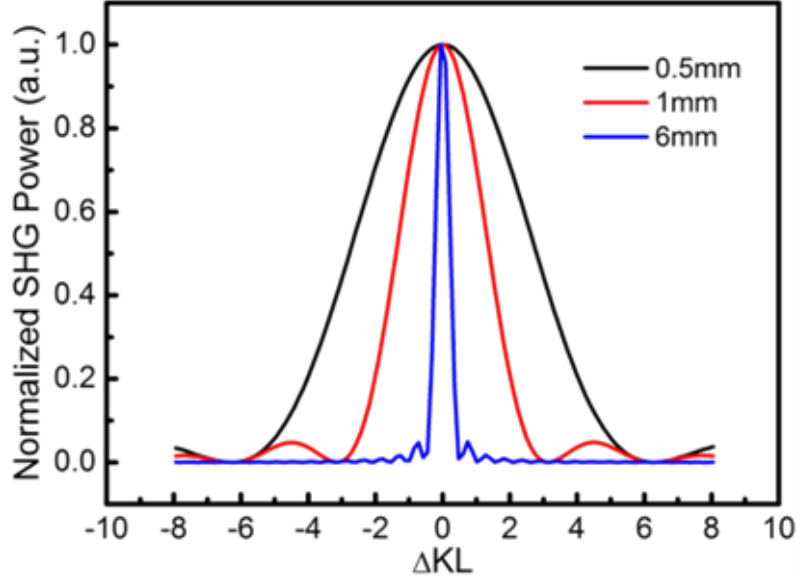


Figure 1.2: Second-Harmonic Generation tuning curve. We note that the maximum generated SHG power occurs when phase-matching ($\Delta k = 0$) is achieved.

A simple solution would be beneficial as it would provide physical understanding of the process. If the fundamental wave has sufficiently low input power in a way that the initial power is reduced less than 20 % throughout the interaction length, it can be considered undepleted, i. e. $A_{FF}(z) \approx A_{FF}$. Hence, the generated SH power in a material of length L can be obtained by integrating directly Eq. (1.15.b) with the boundary condition $A_{SH}(0) = 0$:

$$P_{SH}(L) = \left| \int_0^L \frac{dA_{SH}(z)}{dz} dz \right|^2 = (\omega_{SH} \kappa_{SH} d)^2 P_{FF}^2 L^2 \text{sinc}^2 \left[\Delta k \frac{L}{2} \right] \quad (1.18)$$

where $P_{FF}^2 = |A_{FF}(0)|^2$. Therefore, a $\chi^{(2)}$ material can usually be characterised by SHG tuning curve, which shows SHG power as a function of the phase-mismatch, as plotted in Fig. 1.2. Normally, the phase mismatch can be varied by tuning the temperature of material or the input wavelength.

A part from phase matching, in order to increase the SHG power, it is seen from Eq. (1.18) that we should also have:

- A high coupling coefficient κ , which particularly means a low effective overlap area in order to increase optical power density. More specifically in bulk case, it requires to seek the smallest beam size when injecting light into crystal. In single mode waveguide case,

the effective area is defined by the thickness of the guide. An additional problem is that we will have to take into account the transverse modal dispersion. In the case of multimode waveguide the effective overlap area can be decreased due to the nonlinear interaction between modes.

- A high interaction length L . In bulk configuration, the interaction length and interaction surface (connected to the beam waist size) are correlated, so it is necessary to optimise the rate between the two variables.
- A high nonlinear coefficient d . It depends on the choice of materials and the light polarisation used.
- Phase matching condition must be improved. It is therefore necessary to overcome the chromatic dispersion of materials. For that, we will show, in the following chapter, two well-known techniques that can be used in bulk crystals.

1.2.3. Achieving Phase-Matching

In order to satisfy phase matching condition, there exist two methods: birefringence phase matching and quasi-phase matching. The two methods will be described in this section.

1.2.3.1. Birefringence Phase-Matching (BPM)

A simple and common way to achieve phase-matching ($\Delta k = 0$) is the use of material birefringence. The ordinary and extraordinary indices in birefringent materials can give rise to phase-matching between polarised input waves, $\Delta k = 0$. However this method restricts the choice of the $\chi^{(2)}$ tensor component that can be used. In addition it is usually achieved by tilting birefringent crystal with respect to the optic axis maintaining perpendicular to the ordinary axis. Tilting crystal normally results in spatial and Poynting-vector walk-offs and these walk-offs shorten the effective interaction length, thus reduce nonlinear effects. In this case, the extraordinary refractive index is modified by the tilting angle θ between the fundamental propagation direction and the crystal optic axis (z):

$$\frac{1}{n_e^2(\theta)} = \frac{\cos^2(\theta)}{n_o^2} + \frac{\sin^2(\theta)}{n_e^2} \quad (1.19)$$

According to Eq. (1.19), the index of refraction associated with the propagation of the extraordinary wave can vary from n_o at $\theta = 0^\circ$ to n_e at $\theta = 90^\circ$. In a negative uniaxial crystal like Lithium Niobate, the ordinary index is greater than the extraordinary one ($n_o > n_e$). The ordinary and extraordinary refractive indices of Lithium Niobate are illustrated in Fig. 1.3(a). At a given temperature for certain wavelengths, we observe that phase-matching for SHG is possible when $n_e^{\omega_{SH}} = n_o^{\omega_{FF}}$. The fundamental wave is polarised perpendicular to the plane containing the z-axis of the crystal and the wave propagation axis, whereas the polarisation of SH wave is parallel to this plane (Fig. 1.3(b)). Furthermore, the effective nonlinear coefficient corresponding to the described SH and FF polarisation is given by: $d_B = \frac{1}{2}\chi_{311}^{(2)}$.

More generally, if the relation $n_e^{\omega_{SH}} < n_o^{\omega_{FF}}$ is satisfied, we can adjust the refractive indices by changing the FF propagation direction and/or the crystal temperature. There exists an angle θ at which $n_e^{\omega_{SH}}(\theta) = n_o^{\omega_{FF}}$. In order to achieve phase-matching in Lithium Niobate, the FF beam is launched along θ as an ordinary ray, the SH beam will be generated along the same direction as an extraordinary ray.

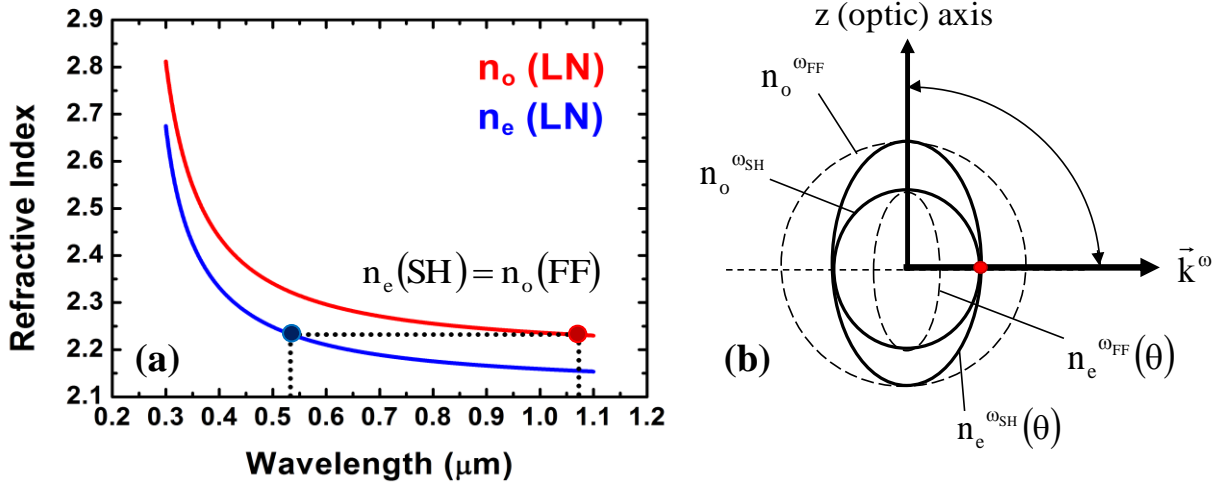


Figure 1.3: (a) The ordinary (red) and extraordinary (blue) refractive indices of raw lithium niobate at a temperature $T = 24.5^\circ\text{C}$, calculated from the Sellmeier equation [25, 26]. In this figure, n_o influences the fundamental wave at 1064 nm whilst n_e influences the SHG wave at 532 nm. (b) Normal index surface for the ordinary and extraordinary rays in that case. The condition $n_e^{\omega_{SH}} = n_o^{\omega_{FF}}$ is represented by the red point.

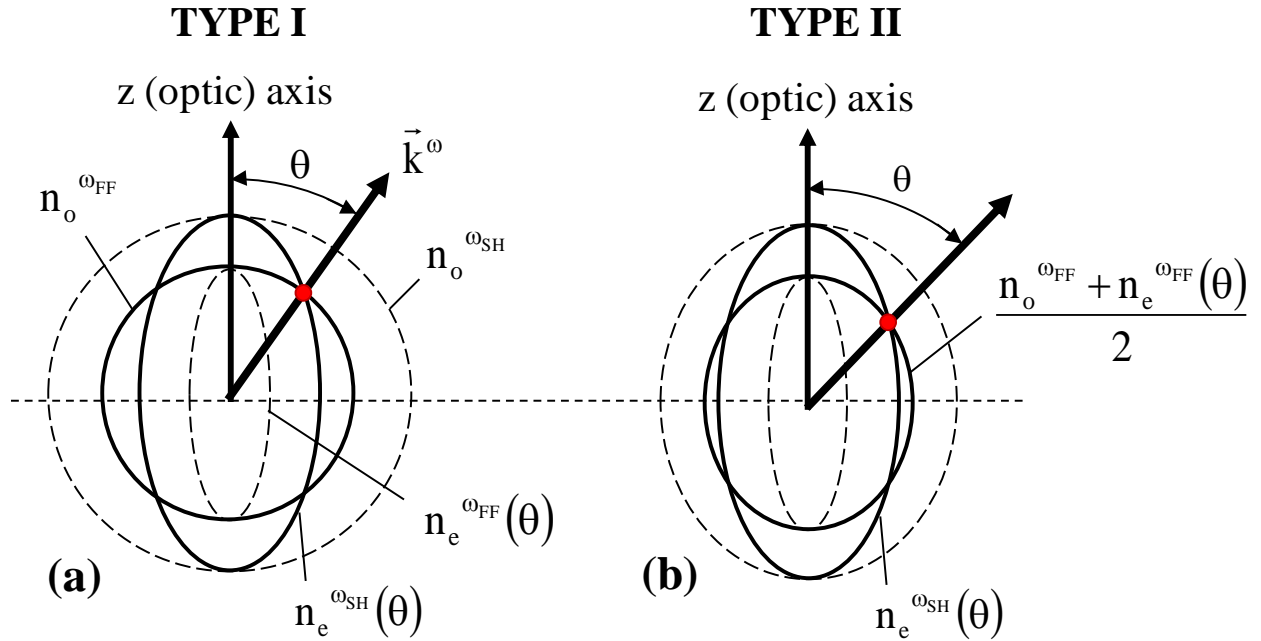


Figure 1.4: (a) type I phase matching (b) and type II phase matching for a negative uniaxial crystal.

The situation is described in Fig. 1.4(a), where the angle is determined by the intersection between sphere corresponding to the index surface of the ordinary beam at ω and the index surface of the extraordinary ray. The method of phase matching depicted in Fig. 1.4(a) is known as type I phase matching. It indicates that the polarisation states of the FF and the SH are mutually orthogonal. Another mode of phase matching is possible in which the FF wave is a mixture of ordinary and extraordinary wave. For negative birefringent crystal, the SH wave is an extraordinary wave. The latter is known as type II phase matching (Fig. 1.4(b)) and is generally possible when the birefringence ($\Delta n = n_o - n_e$) is twice larger than the index change due to chromatic dispersion ($n^{2\omega} - n^\omega$).

BPM has several limitations to satisfy the phase-matching conditions:

- The nonlinear crystal must be birefringent.
- The limited tuneability of nonlinear interactions.
- The limited nonlinear coefficient used, particularly BPM method cannot exploit the diagonal components of the susceptibility $\chi^{(2)}$ which are the highest in nonlinear crystals.

- The nonlinear interaction is usually non-collinear, with a short interaction length and high angular sensitivity.
- The generated beams have different polarisations.

1.2.3.2. Quasi-Phase Matching (QPM)

An alternative scheme, called quasi-phase matching (QPM), to compensate continuous phase drift was proposed by Armstrong et al. in 1962 [24]. The scheme involves a periodically-repeated inversion of the relative phase between the fundamental and the second-harmonic waves. The inversion period corresponds to an odd number of coherence lengths, in order to gain the SH wave along the interaction length. It consists of a $\chi^{(2)}$ micro-structured and geometrical shape in which the nonlinear coefficient sign is different from the background sign. In ferroelectrics, we use a repeated sign inversion of $\chi^{(2)}$. This can be done by reversing the spontaneous polarisation \vec{P}_S every coherent length l_c . For example, this can be achieved by applying a spatially periodic external electric field onto a ferroelectric material, i. e. electric field poling, in order to reverse \vec{P}_S with a period of twice coherence length l_c . The evolution of the second-harmonic wave along the interaction length is illustrated in Fig. 1. 6.

In this section, the basic theory of quasi-phase matching SHG is presented in the wave vector mismatch domain also called Fourier transform approach [27]. It can also be presented in the space domain as discussed by several authors [27]. The phase-matching condition can be satisfied by spatially varying the nonlinear coefficient $d(z)$ for SHG. From Eq. (1.15.b) with no pump depletion, we get:

$$\frac{dA_{SH}(z)}{dz} = i\omega_{SH}\kappa A_{FF}^2 d(z) \exp(-i\Delta kz) \quad (1.20)$$

And assuming that $d(z)$ consists of domains of nonlinear coefficient $\pm d$ with sign changes periodically at every half period $\Lambda/2$.

Let us write the normalised form of $d(z)$ as $g(z) = \frac{d(z)}{d}$, taking any value between +1 and -1 for $0 < z < L$. This function represents the space dependence of the nonlinear coefficients function. Equation (1.20) then takes the form:

$$A_{SH}(L) = i\omega_{SH}\kappa dA_{FF}^2 LG(\Delta k) \quad (1.21)$$

where $G(\Delta k)$ is the Fourier transform of $g(z)$ and called the mismatch function. It can be described by:

$$G(\Delta k) = \frac{1}{L} \int_0^L g(z) \exp(-i\Delta kz) dz \quad (1.22)$$

In the case of a rectangular wave of period Λ , having the values ± 1 , $g(z)$ can be written with the positive sections of length l , by:

$$g(z) = \sum_{m=-\infty}^{+\infty} G_m \exp(i\Delta kz) \quad (1.23)$$

By the m th-harmonic grating wave vector $K_m = \frac{2\pi m}{\Lambda}$ which is considered as closed to Δk , we have the total wave vector mismatch:

$$\Delta k'_m = \Delta k - K_m \quad (1.24)$$

Assuming an achieved phase matching $K_m = \Delta k$,

$$g(z) = \sum_{m=-\infty}^{+\infty} G_m \exp(iK_m z) \quad (1.25)$$

and noting the duty cycle as $D = l_c/\Lambda$, the corresponding Fourier coefficient is found using a standard transform pair to be:

$$G_m = \frac{2}{\pi m} \sin(\pi m D) \quad (1.26)$$

Equation (1.26) shows that the optimum duty cycle for odd number m is 50 %. In that case, as shown in Fig.1.5, we will only consider the 1st order QPM, in order to simplify the calculation. Likewise, the optimum duty cycle for $m = 2$ is 25% - 75 %. The second order QPM corresponds to the alternating domains of l_c and $3l_c$.

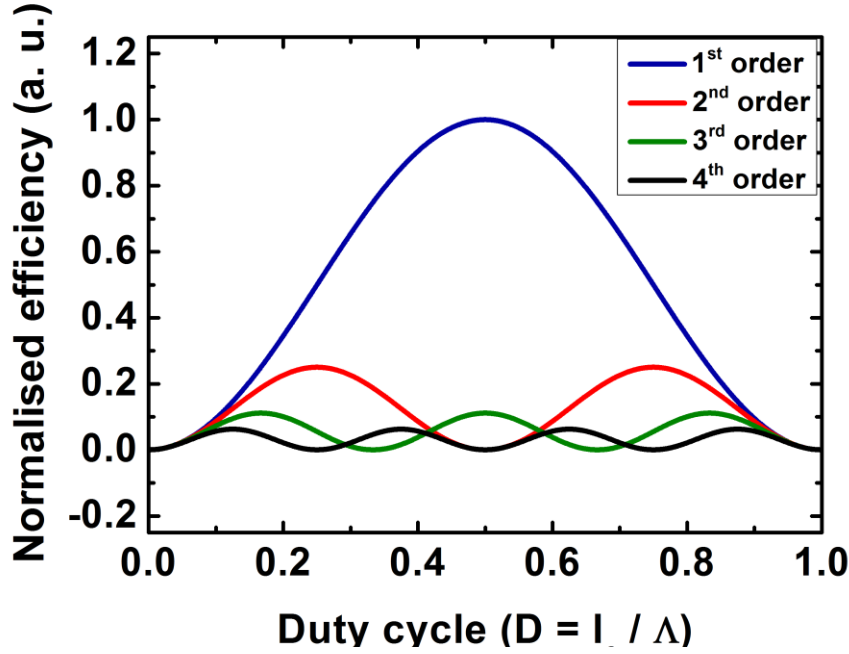


Figure 1.5: Dependence of the nonlinear coefficient $|G_m|^2$ and thus the normalised efficiency with respect to the duty cycle of the 1st, 2nd, 3rd, and 4th QPM order.

In a Fourier space picture, also called reciprocal lattice space, the compensation can be achieved by a periodic structure of which the reciprocal lattice vector may create new phase matching between the fundamental and the harmonic waves. The periodic inversion of the nonlinear coefficient along the interaction length can be represented by the following Fourier series from Eq. (1.20):

$$A_{SH}(L) = i\omega_{SH}\kappa A_{FF}^2 d \left[\sum_{m=-\infty}^{+\infty} \frac{2}{\pi m} \sin(\pi m D) \int_0^L \exp(-i\Delta k'_m z) \cdot dz \right] \quad (1.27)$$

$$A_{SH}(L) = -\omega_{SH}\kappa A_{FF}^2 L d \left[\sum_{m=-\infty}^{+\infty} G_m \exp\left(-\frac{i\Delta k'_m z}{2}\right) \text{sinc}\left(\frac{\Delta k'_m L}{2}\right) \right] \quad (1.28)$$

Thus, we can notice two differences between QPM and perfect phase matching. First, the phase mismatch includes an additional term K_m , introduced by a periodical modulation of the nonlinear coefficient, secondly, the effective nonlinear coefficient is reduced by a factor G_m .

Hence, we find that the intensity of the second harmonic $I_{SH}(L)$ for the case of perfect QPM ($\Delta k' = 0$) after an interaction length L and pumped with an intensity I_{FF} :

$$I_{SH}(L) = \omega_{SH}^2 \kappa^2 I_{FF}^2 L^2 d^2 |\sum_m G_m|^2 = \omega_{SH}^2 \kappa^2 I_{FF}^2 L^2 |\sum_m d_m|^2 \quad (1.29)$$

So, the interaction efficiency is proportional to the absolute square of the relevant Fourier coefficient G_m . We show now the relation to $|\sum_m G_m|^2$ as the normalised efficiency as illustrated in Fig. 1.5.

We find that at an optimum duty cycle D , for which the *sin* factor is unity, the effective nonlinear coefficient is written: $d_{eff,m} = d \cdot \frac{2d}{\pi m}$.

QPM order (m)	Duty cycle (D) %	$\eta_{\text{QPM}} / \eta_{\text{BPM}}$
1	50	$(2/\pi)^2$
2	25/75	$1/4(2/\pi)^2$
3	17/50/83	$1/9(2/\pi)^2$
4	12/38/62/88	$1/16(2/\pi)^2$

Table 1.2: Conversion efficiency rate between BPM and QPM considering the nonlinear coefficient constant.

Note that the duty cycle of crystal must be known in order to look on the contribution of each QPM order (Fig. 1.5) in the conversion efficiency. It is also noted that the duty cycle is chosen with respect to the coherence length and the QPM conditions which can be varied by temperature or pump wavelength. Thus, in order to modify the coherence length without lattice change, we have the possibility of varying wavelengths or temperature for SHG associated with a QPM order. Thereafter, for a given duty cycle ($D = 50\%$ in our case), we will define the global nonlinear coefficient $d_{eff}(D) = |\sum_m d_m(D)|$, with an odd number m . As expected, the maximum nonlinear interaction efficiency is achieved from the first order Fourier components ($m = 1$).

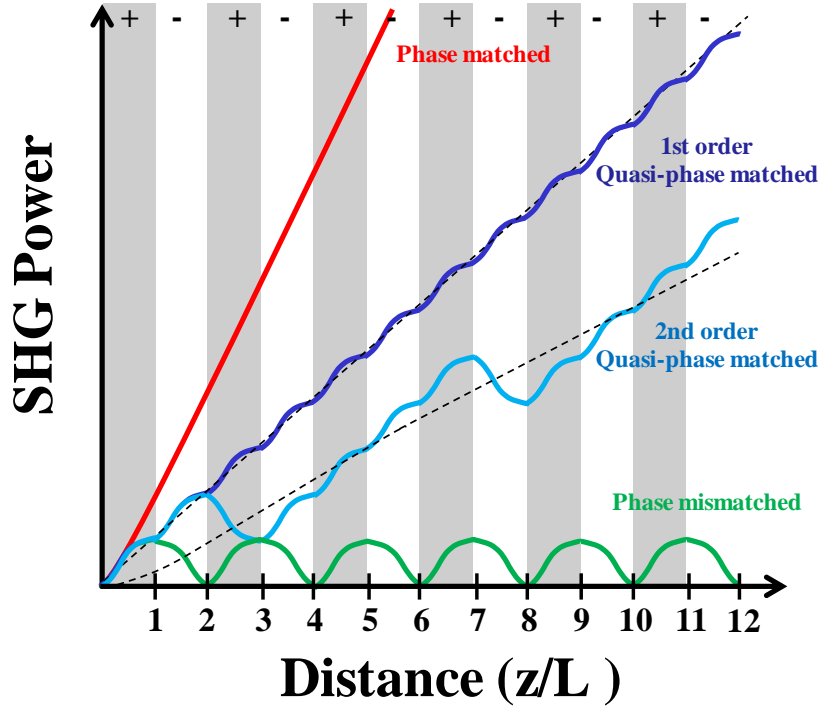


Figure 1.6: SHG power as a function of the propagation length in the units of coherence length for non-phase matching (green line), phase matching (red line), first-order quasi-phase matching (dark blue line) and second order (blue line) conditions.

For Lithium niobate, the QPM scheme is normally implemented with $\chi_{333}^{(2)}$ which is the highest $\chi^{(2)}$ tensor component of the crystal. Although the QPM scheme only allows 64% $\left(\frac{2}{\pi}\right)$ of $\chi_{333}^{(2)}$, it still provides a significant improvement of about 16 times over the birefringent phase-matching, considering $d_B = \frac{1}{2}\chi_{311}^{(2)} = 2.1 \text{ pm/V}$ and $d_{QPM} = \frac{1}{\pi}\chi_{333}^{(2)} = 8.6 \text{ pm/V}$. Besides, the low birefringence of Lithium Niobate renders impossible to SHG in blue using BPM, whilst QPM can be achieved at any frequencies by an appropriate choice of the grating period.

To resume, some benefits are found for QPM:

- An access in all nonlinear materials, particularly having low-birefringence properties.
- The ability to realise phase-matching at any frequencies in the crystal transparency range.
- The phase matching is realised in collinear direction and by keeping the same polarisation between pump and generated beam.
- An access to largest nonlinear coefficients, as illustrated with LiNbO_3 .

1.2.3.3. Second-harmonic conversion efficiency

We can notice that the maximum SHG power occurs when the phase-matching ($\Delta k = 0$) is achieved. As is apparent from Eq. (1.18), for $\Delta k = 0$, the resulting power scales quadratically with the interaction length. When the conversion efficiency is very low ($A_{FF}(z) \gg A_{SH}(z)$), it can be considered from Eq. (1.18) that the fundamental wave amplitude is not depleted and remains almost constant over the interaction length L . Thus, the expression of the SHG power with the interaction length L in a nonlinear medium is written as:

$$P_{SH}(L) = \left| \int_0^L \frac{dA_{SH}(z)}{dz} dz \right|^2 = (\omega_{SH} \kappa_{SH} d_{eff})^2 L^2 P_{FF}^2 = \eta_{nor} L^2 P_{FF}^2 \quad (1.30)$$

where the normalised conversion efficiency η_{nor} is the intrinsic nonlinear property of $\chi^{(2)}$ material at a frequency ω_{FF} . That value is independent on the input fundamental power and the interaction length:

$$\eta_{nor} = \frac{8\pi^2 d_{eff}^2}{\lambda_{FF}^2 n_{FF}^2 n_{SH} \epsilon_0 c} \cdot \frac{1}{S_{ovl}} \quad (1.31)$$

There are several ways to represent the conversion efficiency. The intrinsic conversion efficiency η_{nor} is usually expressed in $\%.W^{-1}.cm^{-2}$. Generally, for common nonlinear crystal like LBO, BBO, BiBO, KTP, LiNbO₃, LiTaO₃ and their periodically-poled derivatives, their intrinsic conversion efficiencies vary between 0.01 and 2%. $W^{-1}.cm^{-2}$. Another representation of conversion efficiency is the simple ratio between the SHG and FF powers. We see from Eq. (1.29) that the SHG power varies quadratically with the pump power. We define the nonlinear conversion efficiency as a drive parameter η_o :

$$\eta_o = \frac{P_{SH}(L)}{P_{FF}} = \eta_{nor} P_{FF} L^2 \quad (1.32)$$

Its unit is usually expressed in percentage (%). We will use both of these notations η_{nor} and η_o to compare our final results considering the constant pump power. However, in the case of pump depletion (SHG power is very high), it is necessary to include a z dependence on $A_{FF}(z)$. When we integrate Eq. (1.15) including the pump depletion, we will get:

$$\eta_o = \frac{P_{SH}(L)}{P_{FF}} = \tanh^2 \sqrt{\eta_{nor} P_{FF} L^2} \quad (1.33)$$

As things stand, we will see that pump depletion consideration is not relevant, especially for a continuous wave source with low power density.

1.2.3.4. Tuning and bandwidths in periodic structures

For practical applications of QPM devices, it is important to establish the tolerances for variations in temperature, wavelength or angle, by estimating their effects on the conversion efficiency [27]. The angular dependence concerns particularly 2D nonlinear photonic crystals and will be discussed later. The conversion efficiency is investigated by taking into account the phase mismatch induced by these different parameters. For a device of total length L containing a uniform period, the phase matching factor for the power conversion efficiency in Eq. (1.27) relies on, $\text{sinc}^2 \left[\Delta k'_m \frac{L}{2} \right]$, so that QPM condition is similar to that of BPM. It only has been shifted by the wave vector K_m of the periodic structure away from the bulk value of Δk . We may use the fact that $\text{sinc}^2 \left[\Delta k \frac{L}{2} \right] \approx 0.5$ when $\Delta k \frac{L}{2} = 0.4429\pi$, to find the full width at half maximum (FWHM) acceptance bandwidth for quantities as temperature, wavelength and angle tuning which affect the total wave mismatch.

The FWHM bandwidth of the SHG tuning curve in Eq. (1.18) is given by:

$$\Delta[\Delta k] \approx \frac{5.5656}{L} \quad (1.34)$$

Considering $\Delta k'_m = \Delta k - K_m$ is a function of a parameter ζ (with ζ the FF wavelength or the crystal temperature), Fejer et al. developed the total phase mismatch in a Taylor series with respect to the value ζ_0 such as phase matching is achieved ($\Delta k'_m(\zeta_0) = 0$):

$$\Delta k'_m(\zeta) = (\zeta - \zeta_0) \partial_\zeta \Delta k'_m \Big|_{\zeta=\zeta_0} + \frac{1}{2} (\zeta - \zeta_0)^2 \partial_\zeta^2 \Delta k'_m \Big|_{\zeta=\zeta_0} + \dots \quad (1.35)$$

In this case, $\Delta k'_m$ is widely accepted as a first order dependence on ζ and the higher order terms can be neglected. The FWHM bandwidth of length $\Delta\zeta$ is found by solving Eq. (1.35). The solution gives:

$$\Delta\zeta_{FWHM} \approx \Delta[\Delta k'_m(\zeta)] \Big| \partial_\zeta \Delta k'_m \Big|^{-1} = \frac{5.5656}{L} \Big| \partial_\zeta \Delta k'_m \Big|^{-1} \quad (1.36)$$

We will use this result throughout this section to calculate bandwidths for fundamental wavelength, temperature and angle of incidence. Note that it is inversely proportional to the interaction length. We will see that a large deviation from phase mismatching reduces significantly the conversion efficiency because a high power and/or a strong thermal effect can alter the acceptance bandwidth [27].

1.2.3.5. Spectral bandwidth

It is obvious that the fundamental wavelength tuning has no effect on periodicity of the structure (K_m). Thus, the unique contribution to the derivation of $\Delta k'_m$ comes from the phase mismatch due to the material:

$$\Delta k = \frac{4\pi(n_{SH} - n_{FF})}{\lambda}. \quad (1.37)$$

Taking Eq. (1.36) the wavelength bandwidth is given by:

$$\Delta\lambda_{FWHM} = \frac{5.57}{L} \left| \frac{\partial \Delta k}{\partial \lambda} \right|_{\lambda=\lambda_{1/2}}^{-1} = \frac{5.57}{L} \left| -\frac{n_{SH} - n_{FF}}{\lambda^2} + \frac{1}{2\lambda} \frac{\partial n_{SH}}{\partial \lambda} - \frac{1}{\lambda} \frac{\partial n_{FF}}{\partial \lambda} \right|_{\lambda=\lambda_{1/2}}^{-1} \quad (1.38)$$

where $\lambda_{1/2}$ is the value of the wavelength when $\text{sinc}^2 \left[\Delta k \frac{L}{2} \right] = 0.5$. The index variation with respect to the wavelength can be obtained numerically by using the Sellmeier equation fits for the material being used. At longer wavelengths the bandwidth tends to increase because of the decrease in index variation. Equation (1.38) is widely used to determine the interaction length experimentally by tuning the fundamental wavelength. But in our work, we will study rather the temperature bandwidth to calculate the interaction length and compare for the cases of bulk and waveguide.

Figure 1.7 shows the theoretical single-pass nonlinear conversion efficiency for a nonlinear photonic crystal η_λ studied in this thesis versus SHG wavelength at low-conversion efficiency (see Eq. (1.18) for the *sinc* dependence).

$$\eta_\lambda = \text{sinc}^2 \left[\left[\frac{4\pi}{\lambda} (n(\lambda/2) - n(\lambda)) - \frac{2\pi m}{\Lambda} \right] \cdot \frac{L}{2} \right] \quad (1.39)$$

In this case, we assume that the total periodically-polarised length (6 mm) is equal to the interaction length in the optimum configuration.

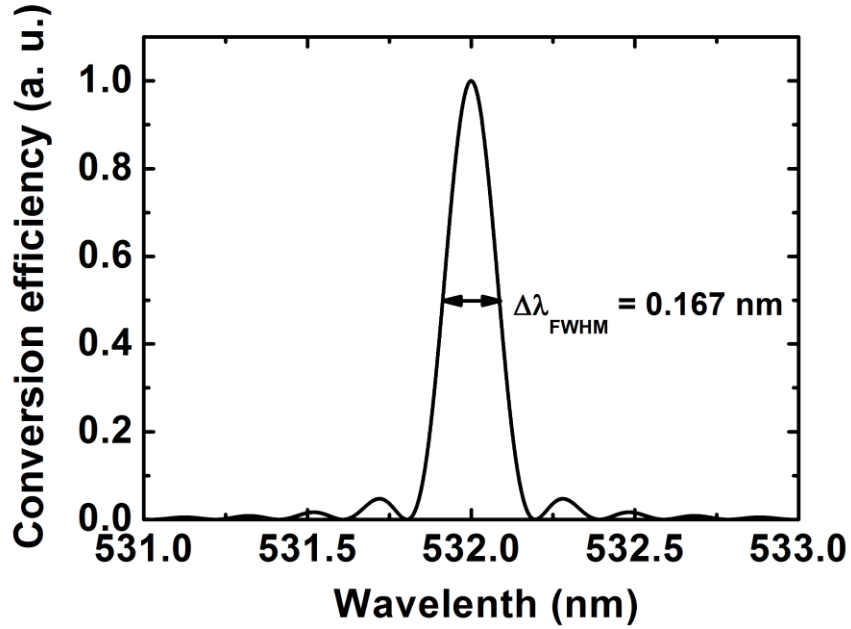


Figure 1.7: Theoretical nonlinear conversion efficiency (from Eq. (1.28)) as a function of the generated harmonic wavelength for collinear QPM SHG with $T = 56.12\text{ }^{\circ}\text{C}$, $\Lambda(25^{\circ}\text{C}) = 6.92\text{ }\mu\text{m}$, and $L = 6\text{ mm}$, the total periodically-polarised length of our samples.

1.2.3.6. Temperature bandwidth

When the temperature is tuned, not only Δk changes due to the temperature dependence of refractive indices, but also the crystal undergoes a thermal expansion which alters both the period Λ , therefore K_m , and the total length L of the device.

In this case, we must take the derivative expression with respect to the product $\Delta k'_m L$ instead of Δk . At a temperature T , considering $\Delta k'_m(T_0) = 0$ we have the following Taylor series:

$$\Delta k'_m(T) \cdot L(T) = (T - T_0)[L(T)\partial_T \Delta k'_m(T) + \Delta k'_m(T)\partial_T L(T)] + \dots \quad (1.40)$$

Firstly, with $\partial_T \Delta k'_m(T) = \partial_T \Delta k - \partial_T K_m$ and if we define α as the coefficient of the thermal expansion by:

$$\alpha = \frac{1}{x} \partial_T x \quad (1.41)$$

It means that $\partial_T L(T) = \alpha L(T)$ and $\partial_T K_m = \partial_T \left(\frac{2\pi}{\Lambda(T)} \right) = -\alpha K_m$.

In literature, the first order thermal expansion for congruent lithium niobate (48.6 mol.% LiO₂, poled along Z-axis) is 15.10⁻⁶ /°K along the z-axis direction correspond to the axis of wave vector propagation in the crystal. That value is 8 times higher than the coefficient of silicon. Now, taking $\Delta n(T) = (n_{SH}(T) - n_{FF}(T))$, we get the expression:

$$L \cdot \partial_T \Delta k'_m(T) = L[\partial_T \Delta k - \partial_T K_m] = L \left[\frac{4\pi}{\lambda} \partial_T \Delta n + \alpha K_m \right] \quad (1.42.a)$$

$$\Delta k'_m(T) \partial_T L(T) = \left[\frac{4\pi}{\lambda} \Delta n - K_m \right] \alpha L(T) \quad (1.42.b)$$

with λ the fundamental wavelength. Otherwise, we find that in Eq. (1.42), the terms involving K_m are cancelled.

Finally, we get:

$$\Delta k'_m(T) \cdot L(T) = (T - T_0) \cdot L(T) \frac{4\pi}{\lambda} [\partial_T \Delta n + \alpha \Delta n] \quad (1.43)$$

If now, taking Eq. (1.36) we can have the temperature bandwidth:

$$\Delta T_{FWHM} = \frac{5.5657}{L} \frac{\lambda}{4\pi} |\partial_T \Delta n + \alpha \Delta n|_{T=T_{1/2}}^{-1} \quad (1.44)$$

By determining ΔT_{FWHM} experimentally and calculating the Δn term with the Sellemier fits of the material, it is possible to estimate the interaction length L in a bulk or a waveguide. The semi-empirical determination of L by this method will be presented in chapter 3.

Figure 1.8 presents the theoretical temperature dependence of the conversion efficiency for the same nonlinear photonic crystal studied in Fig. 1.7. Using Eq. (1.27), the theoretical curve shown in Fig. 1.8 is obtained from:

$$\eta_T = \text{sinc}^2 \left[\left[\frac{4\pi}{\lambda_{FF}} (n_{SH}(T) - n_{FF}(T)) - \frac{2\pi m}{\Lambda(T)} \right] \cdot \frac{L}{2} \right] \quad (1.45)$$

We assume that the periodically-polarised length is equal to the interaction length in the optimum configuration. In this thesis, only the temperature bandwidth will be investigated in order to determine the interaction length.

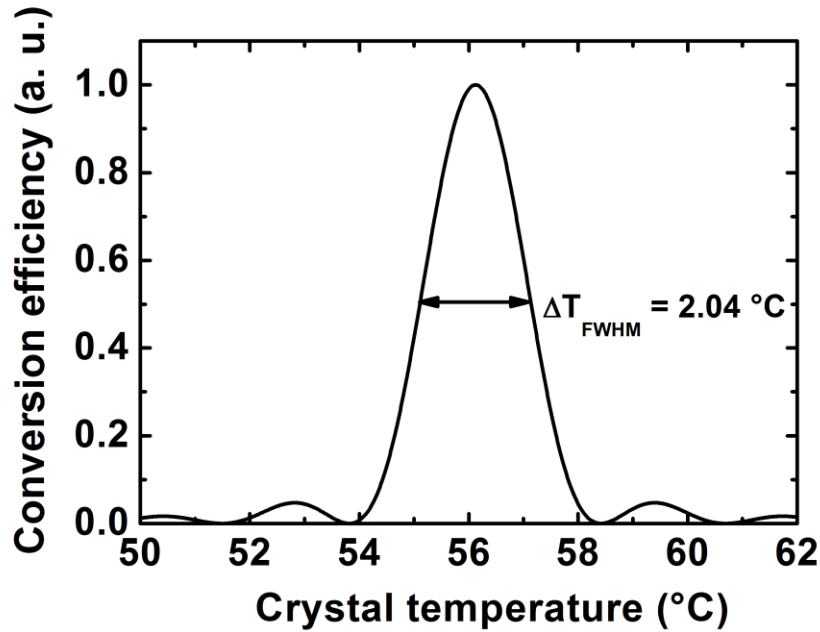


Figure 1.8: Theoretical conversion efficiency (from Eq. (2.28)) as a function of the crystal temperature for collinear QPM SHG with $\lambda_{FF} = 1064$ nm, $\Lambda(25^\circ\text{C}) = 6.92$ μm , and $L = 6$ mm, the total length of one of our periodically-polarised samples.

As the grating period Λ depends on the crystal temperature T , it can be read as:

$$\Lambda(T) \approx \Lambda(25^\circ\text{C})[1 + \alpha(T - 25^\circ\text{C})] \quad (1.46)$$

where the grating period is designed at a room temperature of 25°C . In fact, the thermal expansion coefficient α is very small. This can modify up to $\approx 0.03\%$ of the grating period at 200°C (the maximum temperature used in this thesis). So unlike the thermal variation of index, we neglect the thermal expansion dependence on the grating period later in our calculation.

1.2.4. Materials for QPM

As we have seen in section 1.2.3.2, the frequency conversion by QPM needs a periodical modulation of the nonlinear coefficient in the crystal. In this section, we make a brief list of the principal materials used for QPM, mainly focused on LiNbO_3 . Thus we will show why lithium niobate is an ideal material for the realisation of periodically poled structures. More details will be given in chapter 2 for the realisation of PPLN by applying high electrical field. This will be

the opportunity to present the developed method at the Graduate Institute of Photonics and Optoelectronics (GIPO) at NTU.

1.2.4.1. List of materials

Different materials are used for QPM applications. Few works use semiconductors as CdTe or AlGaAs [28], but most of the research were conducted on dielectric and ferroelectric components. Lithium tantalate (LiTaO_3) can be especially cited, as its transparency domain reach short wavelength, with high nonlinear coefficient and high optical damages threshold. [29 - 31]. Further works were done with KTP (KTiOPO_4) [32]. This material is even used on marketed chipsets. However, KTP has a high ionic conductivity so the electrical poling method which will be introduced in the next sections is not available with this material. Besides, a physical-chemical treatment has to be done before using. It consists on exchange potassium ions with rubidium ions on the surface of the crystal (RbTiOPO_4) [33]. It induces lower ion mobility as rubidium has a bigger size than potassium. Risk *et al.* [34] realised QPM experimentations with RTA (RbTTiOAsO_4). They used poling process proposed by Myers *et al.* [35]. This short list of materials show the furnished effort in research in order to develop PP structure for different applications: tuneable OPO laser sources, UV laser sources, integrated laser systems etc.

We have oriented our choice on congruent LiNbO_3 . This material has one of the higher nonlinear coefficients for SHG applications. Furthermore, this material has interesting properties for fabrication of optical integrated components.

1.2.4.2. Lithium Niobate

In this section, the crystal nature of lithium niobate (LiNbO_3) is described. This will allow us to introduce the reversal polarisation phenomena in such crystal.

Lithium niobate is a dielectric which does not exist in the natural state. The crystal was synthesised and described for the first time in 1928 by Zachariasen, but it is in 1948 that the ferroelectric character is described by Matthias and Remeika in Bell laboratories. The interest on this material increases in 1965 when Ballman and Fedulov announced independently the synthesis of monocrystals by Czochralsky method.

The crystal has further electrical properties in addition to the presence of a spontaneous polarisation. It has high piezoelectric coefficients ($d_{33} = 0.6 \cdot 10^{-11} \text{ C/N}$, $d_{15} = 6.92 \cdot 10^{-11} \text{ C/N}$) which is used for the fabrication of BAW (Bulk Acoustic wave) and SAW (Surface Acoustic Wave) sensors or resonators. The crystal has also a pyroelectric property meaning that the spontaneous polarisation decreases with temperature. An electric field appears when the material is subjected to a temperature gradient. The pyroelectric coefficient of lithium niobate is $85 \mu\text{C}/(\text{m}^2 \cdot \text{K})$ making it a good material for application in IR detection.

Its structure is generally represented by a stack of plans in a direction noted $c+$ and composed by three atoms of oxygen. Each successive triangle is shifted with an angle of 60° . It means that two successive plans form an octahedron. Considering that there is no stoichiometric defaults in crystal, ions of lithium (Li^+) fill the centre of the triangles for one third and ions of Niobium (Nb^{5+}) fill the centre of adjacent octahedrons as shown in Fig.1.9. Under the Curie temperature (1120°C), lithium niobate is in ferroelectric phase. The high Curie temperature indicates that the ferroelectric phase has good thermal stability. In this case, the positions of Li^+ range from 0.037 nm perpendicularly to the oxygen plans, taking away the Nb^{5+} from their initial position. The shifted position of ions is causing the spontaneous polarisation. The passage from one polarisation state to another is structurally realised by the passage of the lithium ion from one side the other of its nearest oxygen plane.

The crystal has an asymmetric configuration along the c axe. Figure 1.9. shows a perspective of (b) ferroelectric and (a) paraelectric phase where the spontaneous polarisation disappears. The paraelectric phase is observed at a temperature above the Curie temperature. There is different method to increase the Curie temperature in this material: when the ratio $\text{Li} : \text{Nb}$ is close to the stoichiometric ratio or when the crystal is doped with MgO .

LiNbO_3 crystallises in a rhombohedral lattice $R3c$, but is often describe as a hexagonal lattice considering three rhombohedral cells. The structure has three mirror planes forming an angle of 60° between them. The crystal is included in the symmetry group $3m$ with three symmetry axes around the c -axis as shown in Fig. 1. 9.(c). The convention sets the z -axis parallel to the c -axis, the y -direction is in one mirror plan, and the x -axis is normal to the y direction such as the triedron $Oxyz$ is direct.

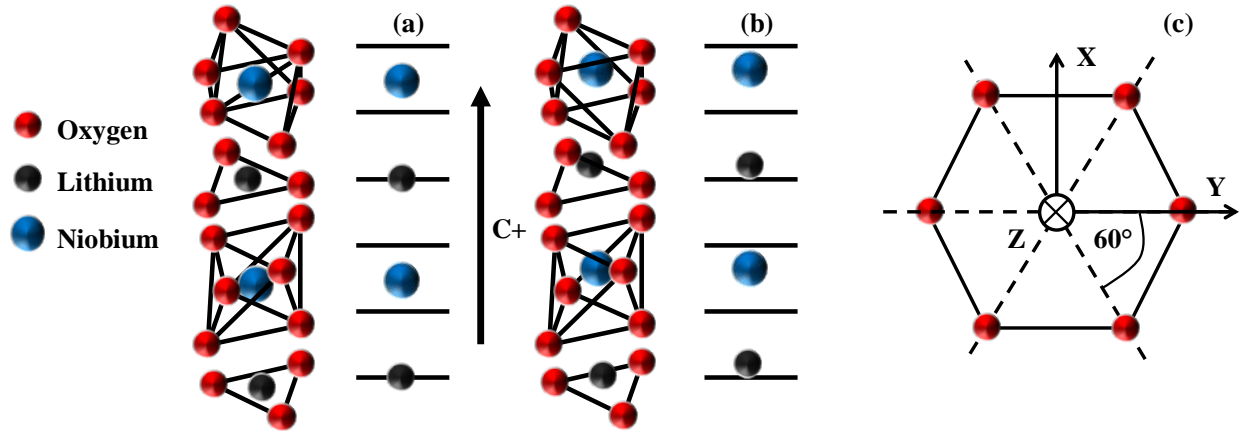


Figure 1.9: Position of Lithium and Niobium atoms compared to Oxygen plans in (a) paraelectric and (b) ferroelectric phases in LiNbO₃ [36]. (c) The oxygen atoms form the hexagonal lattice, the mirror plans are represented in broken lines.

The $z+$ face is defined as the side of ions Li^+ and Nb^{5+} . The poling process requires the $z+$ face identification, generally by using the pyroelectric effect: two electrodes are set on the $z+$ and $z-$ faces of the sample and are connected to an ammeter. When the crystal is heated, the sign of the output current identifies faces.

1.2.4.3. Poling methods

Further methods have been developed for the periodically poling of the spontaneous polarisation in ferroelectrics. It mainly concerns ionic diffusion or exchange, or by applying a periodical electrical field. In all configurations, a mask is used for photolithography, allowing the repetition of the pattern in micro-scale on bulk. The first results have been performed in integrated optics by using the ionic exchange or ionic diffusion on localised surface of the sample. The first PPLN have been realised by Ti in-diffusion process [37 - 39], by diffusing titanium strips at 1000°C on $z+$ face. The poling process is realised in the diffused volume and creates no index modulation. In 1987, Nakamura *et al.* reported another heat treatment with LiO_2 out-diffusion, which induces domain inversion in lithium niobate. The presence of titanium or the Li deficiency in the crystal is thought to lower the Curie temperature [40] and enables the pyroelectrically induced field to reverse the spontaneous polarisation [41]. Miyazama *et al.* [42] explain the partial domain switch of the spontaneous polarisation with the Titanium gradient concentration creating a field of charges.

PPLN were also produced using a modified-growth process which involved the application of a periodically alternating electric field during growth. Two growth techniques are currently used. The first one is the laser heated pedestal growth (LHPG) based on the fusion of a compressed mono or polycrystalline powder rod by a CO₂ laser at 10.6 μm. The orientation of the crystal is controlled by modifying the atmosphere or the pulling speed [43]. The second method comes from the Czochralsky (CZ) method and is called off-centred growth. It allows the fabrication of large size monocrystal with high optical quality. The reagents are lithium carbonate (Li₂CO₃) and niobium pentoxide (Nb₂O₅) and are annealed at 1000°C – 1200°C for 8h - 10 hours to ensure completion of the solid state reaction between the components of the compound and release of CO₂. Then, the melts are fused just over the melting-point of the material (1250°C for LiNbO₃) with a rotation of the system according to the temperature gradient. Bermudez *et al.* [44] have observed that the local variation of the components induced the formation of domains which have opposite spontaneous polarisations and the crystal has an eccentric growth comparing with the temperature gradient. The phenomenon is similar if the crystal is doped with ion of Yb²⁺ where its concentration gradient forces the direction of the polarisation at the Curie temperature.

The next technique developed for domain inversion involved proton exchange in benzoic or pyrophosphoric acid followed by a heat treatment at a temperature just below the Curie temperature [44]. Mizuuchi *et al.* [45, 46] explain that the diffusion of protons creates a substitution of ions Li⁺ by H⁺ in the crystal. Diffusion creates a sufficient electrical field to switch the polarisation. Fabrication process had developed sufficiently to allow a device of inversion period less than 4 μm to be fabricated for first-order SHG of blue light in lithium niobate [47].

All the processes mentioned required high temperature treatments which could degrade the sample for optical application. The first demonstration of room temperature domain inversion was reported in 1991 by Yamada and Kishima [48] in lithium niobate by using Electron Beam Scanning. They discovered that direct electron bombardment at 25 eV on the negative side of crystal caused domain inversion on a distance 100 times greater than that of electron penetration in bulk. This technique was immediately applied to LiTaO₃ [49], KTP [50], MgO:LiNbO₃ [51] and Ti:LiNbO₃ [52] and developed for harmonic generation with domain inverted grating periods of 3 μm. Recently, nano-domain (100 nm) structures are produced by Pulse Laser Heating [53] and

new techniques are developed by Vapour Transport Equilibration (VTE) treatment during the CZ growth in Nd doped near-stoichiometric LiTaO₃ having a low coercive field [54] or by plasma-source ion irradiation (Ar⁺), increasing the conductivity by oxygen out-diffusion [55].

The use of electrical field at room temperature had also been developed in 1993 [56]. The fabrication process was sufficient to produce fine period devices. The technique was developed in other materials, including LiTaO₃ [57], MgO:LiNbO₃ [58], Ti:LiNbO₃ [59], RbTiOAsO₄ [60] KTiOAsO₄ (KTA) [61] and KTP [62] for use in frequency generation. In the next section, we develop in details this fabrication, especially the one developed by Miller [37].

1.2.4.4. Poling Process according to Miller's model

Presently, the most widely used method for the realisation of QPM structure is the electrical field application made through related micro-electrodes and deposited on crystal surface. Different factor influence the fabrication and the QPM lattice quality: how electrodes are deposited, nature of liquid or gel involved in electrical contact, nature of applied electrical pulses on the sample (current, voltage, duration). G. D. Miller [37] conducted a complete study on these poling parameters and particularly, their influence on nucleation site density and reversed domain sizes (depth and diameter). Miller developed a model in order to predict the electrical field distribution in the crystal according to the geometry of electrodes. Four interesting observations have been expressed from the model:

- The electrical poling method proceeds step by step.

From Miller's calculation, the optimal applied electrical field has been determined as well as its spatial distribution. Following his observation, the model takes into account different assumptions in domain kinetics (domain creation and propagation) during electric field periodic poling:

-The poling domains are flat and normal to the crystal-x axis. The domains define regions in the crystal where the spontaneous polarisation is reversed comparing to the original crystal polarisation (Fig. 1.10).

The created domain walls grow transversally according to the z-component of the poling field.

- The domain walls have a transversal velocity related with the z-component of the poling field which is the same everywhere in the crystal.
- The nucleation occurs exclusively at the electrodes (domain nucleation).
- The ionic conductivity is neglected in all crystal volume. It indicates that dielectric relaxation times of the ferroelectric are assumed to be much longer than the poling time.

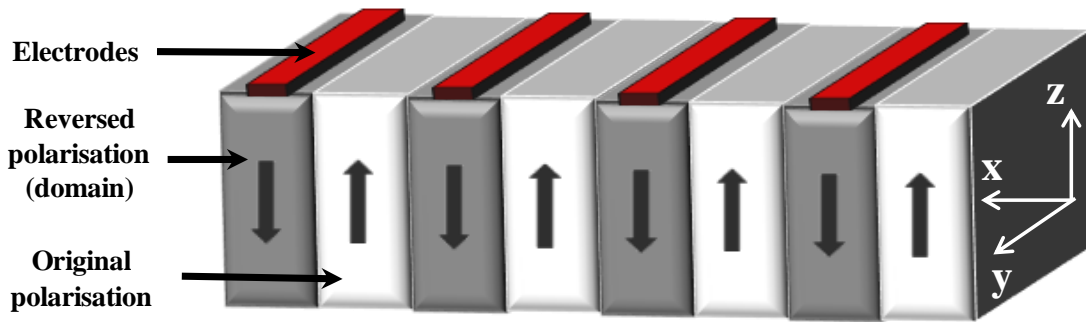


Figure 1.10: Illustration of typical domain configuration of electric field periodically poled LiNbO_3 . The directions of spontaneous polarisations are in the crystal-z axis and periodically inverted (black arrows).

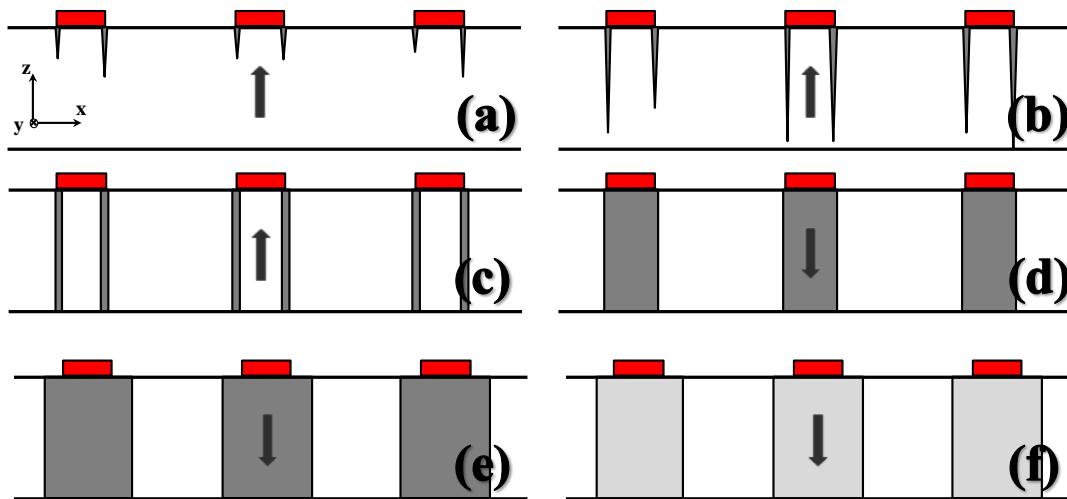


Figure 1.11: The six stages of domain kinetics during electric field periodic poling [37]. (a) Domain nucleation at the electrode edge. (b) Domain tip propagation toward the opposite face of the crystal. (c) Termination of the tip at the opposite side of the crystal. (d) Rapid coalescence under the electrodes. (e) Propagation of the domain walls out from under the electrodes. (f) Stabilisation of the new domains.

Furthermore, from these assumptions, the growth of domains is given in six steps shown in Fig. 1.11. First, domain nucleation starts at the edge of the electrodes. The created domains have a conical shape with a hexagonal base. Then, the domains propagate toward the opposite face of the crystal wherein the apex widens and take a hexagonal shape. Thus, the created domains have a tubular shape with a hexagonal cross section. At least, the domain wall spreads out in the perpendicular direction to that of the applied field, firstly under the electrodes and then at both sides of the electrodes.

- The electrical poling field has been determined depending on the crystal type.

R. C. Miller *et al.* established a method to measure [63] the domain walls velocity according to the field magnitude. In 1994, G. D. Miller used that method for LiNbO_3 by varying the electrical field from 19 kV/mm to 28 kV/mm [37]. He observed that domain wall velocity varies over 10 orders of magnitude in this interval with an inflection point measured at 20.75 kV/mm. At this value called coercive field of the material, the domain wall velocity is most sensitive to electrical field modifications and has a value of 10^{-5} mm/s. It is important to consider this value when reversed domains grow beyond electrodes, electrical charges are deposited on surface, decreasing the field value in material. Thus, it has been observed that with an electric field density of 20.75 kV/mm, poling stops before the complete reversal of polarisation within crystal (the coalescence).

The poling field density is generally determined by the study of the spontaneous polarisation hysteresis loop. It consists on applying a long ramp voltage (few seconds) from 0 to several kV/mm depending of the material and measuring the matched poling current delivered by the crystal. When we proceed in this way, a poling current is recorded when the applied voltage is sufficient to reach the coercive field. G. D. Miller determined that the coercive field for reversing and maintain the polarisation is 22.9 kV/mm and the coercive field to restore the original polarisation is -17.6 kV/mm [64]. The obtained hysteresis loop (Fig. 1.12) is used as an indicator of a built-in field.

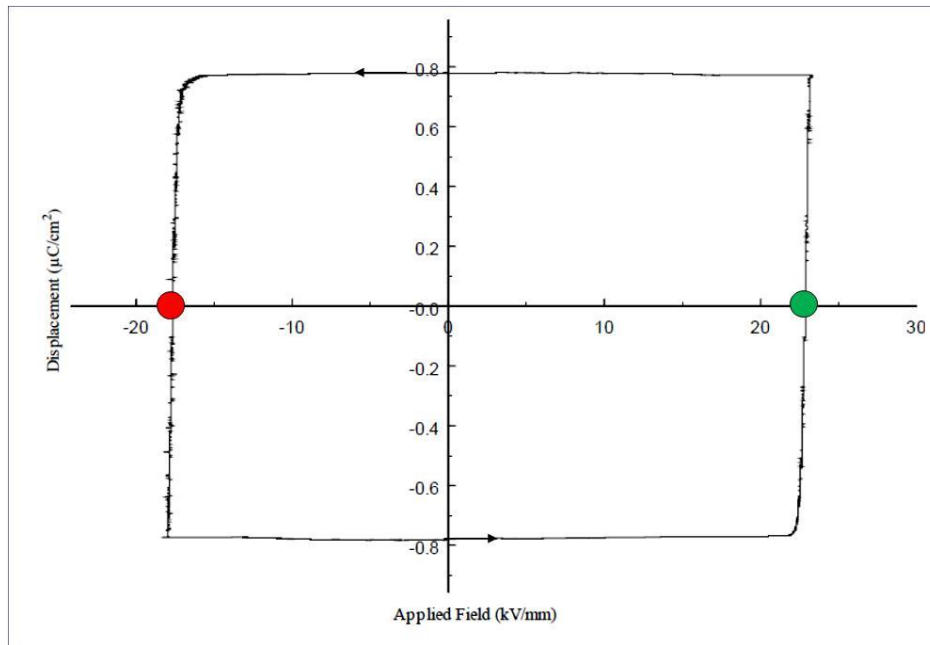


Figure 1.12: Hysteresis loop for LiNbO_3 [64], showing the needed coercive field in order to reverse the spontaneous polarisation (22.9 kV/mm) and restore it (17.6 kV/mm)

However, there are still some fundamental problems in such materials for fabricating precise domain structures. The high electric field density required a large internal field for domain switching. It poses limitations on the sample thickness and the ability to control domain periodicity. In our case, we have studied congruent lithium niobates undoped and doped at 5% mol with magnesium oxide (MgO). One of the advantages in MgO doping is that it increases the intrinsic conductivity of the material, reducing the applied electrical field density to 4.5 kV/mm while maintaining an accurate control of the domain propagation during poling process.

- The period and the geometry of electrodes have been studied, particularly for determining the fill factor at 50 % in PPLN.

In this work, our goal is to realise a PPLN structure for SHG at a wavelength of 1064 nm. Thus, according to the QPM conditions, the period Λ is determined at $\sim 6.9 \mu\text{m}$ and the fill factor is fixed at 50 %. According to Miller's results [37], we use a lattice of electrodes with a period $6.9 \mu\text{m}$ and the electrodes width (or diameter) is chosen at $\sim 2.5 \mu\text{m}$. The periodic electrodes are prepared by a lift-off process on the $z+$ face of the mono-domain crystal. The total process is explained in chapter 2.

Furthermore, it is interesting to note, that for 1D PPLN, Miller have determined that the angle between the electrodes and the crystal directions OX and OY has influence on the domain wall propagation. The best results have been obtained when electrodes are parallel with the OY direction. In our case, this consideration is not necessary, knowing that the inversed domains are symmetrical according to these axes.

- The metal of electrodes is selected according to their relative influence on nucleation site density (NSD) after poling process.

Miller tested different metal for electrodes such as aluminium, molybdenum, titanium, tantalum, chrome, nickel or nichrome. It has been determined that sputtered chrome, nichrome and nickel on z+ face greatly increase the NSD. We settled on titanium electrodes which has a lower cost for similar properties.

In the classic poling method, the electrodes lattice in direct contact with the crystal surface is subject to as slightly higher electrical field than the coercive field of the material. This electrical field is applied until the total formation of domains under the electrodes and toward the opposite face of the crystal. Then, it is usual to slowly decrease the electrical field magnitude to zero, in order to avoid backswitching phenomena within domains. It corresponds to a return of the polarisation in its initial direction. Shur *et al.* [39] used this phenomenon in order to produce submicron domain patterns through multiplication of the domain spatial frequency compared with the electrode one. In fact, when the electrical field is sharply reduced to zero, the backswitching happens only at the electrode edge.

1.3. General theory of integrated optics

Generally, dielectric media of high refractive index can be employed to confine the propagation of the beam. In this section we develop the general theory about the propagation of light in planar guiding structures. These structures can support confined and guided electromagnetic propagation. As we know, any light beam with a finite transverse dimension diverges as it propagates in a homogeneous medium. This divergence disappears in a guiding dielectric structure under certain conditions. We shall derive first the properties of guided modes in an asymmetric planar waveguide. The guided optical waves are presented as the solution of the

eigenvalue equations derived from Maxwell's equations, which are subject to the boundary conditions imposed by the waveguide geometry. Both the transverse electric (TE) and magnetic (TM) modes of the guided waves are presented in this section [65].

1.3.1. Planar optical waveguides

A planar optical waveguide can be built up into the superposition of three homogeneous and transparent dielectric layers. As shown in Fig.1.13, we call n_a , n_{wg} and n_s the refractive index of the air (zone I when $x > 0$), the guiding zone (zone II when $-l < x < 0$), and the substrate / optical barrier (zone III when $x < -l$), respectively. In the guiding zone, the optical wave can be confined by total internal reflection (TIR) between the two interfaces when $n_{wg} > n_s > n_a$. In this case the TIR is achieved at an angle Θ , but limited by a critical angle Θ_c with $\Theta < \Theta_c = \text{asin}\left(\frac{n_s}{n_{wg}}\right)$.

We will have to solve the equations of the propagation of an electromagnetic (EM) wave along the z-axis in the waveguide. The EM field at the pulsation ω is progressive along the axis and it can be decomposed as:

$$\vec{E}(\vec{r}, t) = \text{Re} \left[\vec{E}(y, x) e^{-i\beta z} e^{i\omega t} \right] \quad (1.47)$$

We set β the component of the wave vector in the z-direction, so the propagation constant is written by $\beta = k_0 n_{wg} \cdot \sin \Theta$ and $k_0 = \omega/c = \omega \sqrt{\epsilon_0 \mu_0}$. The norm of the propagation vector relies on ω inducing dispersion in material.

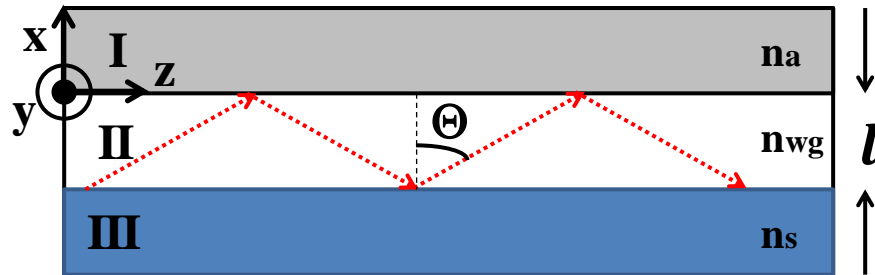


Figure 1.13: Schematic diagram of a planar optical waveguide with step index. The guiding layer must have a higher refractive index than those of the other layers in order to confine the electromagnetic wave.

In order to get the EM field profile and the dispersion equation of the guided waves the ray theory can be used, but in our case, Maxwell's equations will be solved.

We consider that in the structure, each zone is set to be dielectric medium ($\rho_f = 0, \vec{J} = \vec{0}$), with their own permittivity ϵ_{r_i} ($i = a, wg, s$), knowing that $\epsilon_{r_i} = n_i^2$. The permeability remains constant and equals to μ_0 . Thus, Maxwell's equations of the electric field \vec{E} and the magnetic field \vec{H} are written as:

$$\Delta \times \vec{E} = -i\omega\mu_0\vec{H} \rightarrow \begin{cases} \partial_y E_z - \partial_z E_y = -i\omega\mu_0 H_x \\ \partial_z E_x - \partial_x E_z = -i\omega\mu_0 H_y \\ \partial_x E_y - \partial_y E_x = -i\omega\mu_0 H_z \end{cases} \quad (1.48)$$

$$\Delta \times \vec{H} = i\omega\epsilon_0\epsilon_r\vec{E} \rightarrow \begin{cases} \partial_y H_z - \partial_z H_y = i\omega\epsilon_0\epsilon_{r_i} E_x \\ \partial_z H_x - \partial_x H_z = i\omega\epsilon_0\epsilon_{r_i} E_y \\ \partial_x H_y - \partial_y H_x = i\omega\epsilon_0\epsilon_{r_i} E_z \end{cases} \quad (1.49)$$

We will be interested in the electrical transversal modes (TE) and magnetic transversal modes (TM), knowing that all EM waves can be expressed as the linear combination of these polarisations. The TE and TM calculations will be detailed.

In the case of TE polarisation:

The electrical field is in the y -direction so that $E_x = 0$ and $E_y \neq 0$. The medium is considered as uniform in this direction, so $\partial_y = 0$. From Eq. (1.48) and Eq. (1.49) we can deduce that $H_y = E_z = 0$. Likewise, noting the operator $\partial_z = -i\beta$ we have from Eq. (1.49):

$$H_z = \frac{i}{\omega\mu_0} \partial_x E_y \text{ and } H_x = -\frac{\beta}{\omega\mu_0} E_y \quad (1.50)$$

Finally, we get Helmholtz's equation of the electrical field in the three zones:

$$\partial_z^2 E_y + (k_0^2 \epsilon_{r_i} - \beta^2) E_y = 0 \quad (1.51)$$

In the case of TM polarisation:

In this case, the magnetic field is in the x -direction, thus $H_z = E_y = 0$, the Maxwell equations are written as:

$$E_z = \frac{i}{\omega \varepsilon_0 \varepsilon_{r_i}} \partial_x H_y \text{ and } E_x = -\frac{\beta}{\omega \varepsilon_0 \varepsilon_{r_i}} H_z \quad (1.52)$$

Therefore, we obtain Helmholtz's equation of the magnetic field in the three directions:

$$\partial_z^2 H_y + (k_0^2 \varepsilon_{r_i} - \beta^2) H_y = 0 \quad (1.53)$$

The global nature of the solutions EM field in Eq. (1.51) and Eq. (1.53) depends on the sign of each term $(k_0^2 \varepsilon_{r_i} - \beta^2)$:

- If $(k_0^2 \varepsilon_{r_{wg}} - \beta^2) < 0$, the solutions are divergent in the three zones, so there is no physical solution.
- If $(k_0^2 \varepsilon_{r_{wg}} - \beta^2) > 0$, and $(k_0^2 \varepsilon_{r_s} - \beta^2) < 0$, we get a real sinusoidal solution in the waveguide (zone II) and its amplitude decreases exponentially beyond the waveguide (zone I and III). These conditions are necessary to observe the guiding properties of the waveguide. In this case the propagating EM field will be introduced by using the boundary conditions.
- If $(k_0^2 \varepsilon_{r_s} - \beta^2) > 0$, the solutions are sinusoidal in the waveguide and in the substrate: the EM field leaks out of the waveguide. This corresponds to radiating EM field.

1.3.2. Expression of the EM field profile

In the case of TE polarisation:

In the guiding configuration, we have expressed in each zone the electrical field $E_y(x)$, such that:

$$E_y(x) = \begin{cases} C_0 \exp(-\beta_a x) & \text{with } \beta_a = k_0 \sqrt{N_{eff}^2 - n_a^2} \text{ in zone I} \\ C_1 \cos(\beta_{wg} x) + C_2 \sin(\beta_{wg} x) & \text{with } \beta_{wg} = k_0 \sqrt{n_{wg}^2 - N_{eff}^2} \text{ in zone II} \\ C_3 \exp(\beta_s(x+t)) & \text{with } \beta_s = k_0 \sqrt{N_{eff}^2 - n_s^2} \text{ in zone III} \end{cases} \quad (1.54.a)$$

We call $N_{eff} = \beta/k_0$ the effective refractive index of the propagated EM field in the central layer. Taking into account this solution in Eq. (1.49), we find the expression of the magnetic field in the z direction:

$$H_z(x) = \begin{cases} -\frac{\beta_a}{i\omega\mu_0} C_0 \exp(-\beta_a x) & \text{in zone I} \\ \frac{\beta_{wg}}{i\omega\mu_0} [-C_1 \sin(\beta_{wg} x) + C_2 \cos(\beta_{wg} x)] & \text{in zone II} \\ \frac{\beta_s}{i\omega\mu_0} C_3 \exp(\beta_s(x+l)) & \text{in zone III} \end{cases} \quad (1.54.b)$$

Finally, by applying the boundary conditions to each component of the EM field:

$$\begin{aligned} E_{y,a}(0) &= E_{y,wg}(0) & E_{z,wg}(-l) &= E_{y,s}(-l) \\ H_{z,a}(0) &= H_{z,wg}(0) & H_{z,wg}(-l) &= H_{z,s}(-l) \end{aligned} \quad (1.55)$$

It is possible to calculate the constants C_1 , C_2 and C_3 :

$$\begin{cases} C_1 = C_0 \\ C_2 = -\frac{\beta_a}{\beta_{wg}} C_0 \\ C_3 = \left[\cos(\beta_{wg} l) - \frac{\beta_a}{\beta_{wg}} \sin(\beta_{wg} l) \right] C_0 \end{cases} \quad (1.56)$$

The normalisation constant C_0 is chosen so that the field E_y corresponds to a power flow of 1 Watt (per unit width in the y-direction) along the z-axis. The normalisation condition is given by [65]:

$$S_z = \frac{1}{2} \int Re[\vec{E} \times \vec{H}^*]_z dx = 1 \quad (1.57.a)$$

Or equivalently, from Eq. (1.52):

$$-\frac{1}{2} \int_{-\infty}^{+\infty} E_y \cdot H_x^* dx = \frac{\beta}{2\omega\mu_0} \int_{-\infty}^{+\infty} |E_y(x)|^2 dx = 1 \quad (1.57.b)$$

The substitution of Eq. (1.54.a) for the wave function in Eq. (1.57.b), carrying out the integration, leads to:

$$C_0 = 2\beta_{wg} \left[\frac{\omega\mu_0}{|\beta| \left(l + \frac{1}{\beta_a} + \frac{1}{\beta_s} \right) (\beta_{wg}^2 + \beta_a^2)} \right]^{1/2} \quad (1.58)$$

Thus, for this structure, we have presented the behaviour of the EM field in the guiding configuration which imposes the existence of a sinusoidal solution within the middle layer ($\beta_{wg}^2 \geq 0$), with evanescent waves in the outer media (β_s^2 and $\beta_a^2 \geq 0$).

In the case of TM polarisation:

The solutions of the magnetic field $H_y(x)$ keep the same behaviour as Eq. (1.54.a). From the new boundary conditions:

$$\begin{aligned} H_{y,sup}(0) &= H_{y,wg}(0) & H_{y,wg}(-l) &= H_{y,s}(-l) \\ E_{z,sup}(0) &= E_{x,wg}(0) & E_{z,wg}(-l) &= E_{x,s}(-l) \end{aligned} \quad (1.59)$$

By a calculation similar to Eq. (1.56), with $\tilde{\beta}_a = \frac{n_{wg}^2}{n_a^2} \beta_a$, we get the constants C_1 , C_2 , and C_3 :

$$\begin{cases} C_1 = C_0 \\ C_2 = -\frac{\tilde{\beta}_a}{\beta_{wg}} C_0 \\ C_3 = \left[\cos(\beta_{wg}l) + \frac{\tilde{\beta}_a}{\beta_{wg}} \sin(\beta_{wg}l) \right] C_0 \end{cases} \quad (1.60)$$

The normalisation constant is again chosen so that:

$$-\frac{1}{2} \int_{-\infty}^{+\infty} H_y \cdot E_x^* dx = \frac{\beta}{2\omega} \int_{-\infty}^{+\infty} \frac{|H_y(x)|^2}{n(x)^2} dx = 1 \quad (1.61)$$

And finally, with $\tilde{\beta}_s = \frac{n_{wg}^2}{n_s^2} \beta_s$ and by integrating $H_y(x)$ we obtain:

$$C_0 = -2 \frac{\beta_{wg}}{\sqrt{\beta_{wg}^2 + \tilde{\beta}_a^2}} \left[\frac{\omega \epsilon_0}{|\beta| \left(\frac{l}{n_{wg}^2} + \frac{1}{n_a^2 \beta_a} \frac{\beta_{wg}^2 + \beta_a}{\beta_{wg}^2 + \tilde{\beta}_a} + \frac{1}{n_s^2 \beta_s} \frac{\beta_{wg}^2 + \beta_s}{\beta_{wg}^2 + \tilde{\beta}_s} \right)} \right]^{1/2} \quad (1.62)$$

In this way, Figure 1.14 represents the EM field in TE and TM polarisations within the three layer structure of a He^+ implanted waveguide in LiNbO_3 (z-cut) at wavelengths of 1064 nm for FF and 532 nm for SHG. It can be observed that in a step index waveguide, the distribution of the transverse EM field is independent on the wavelength.

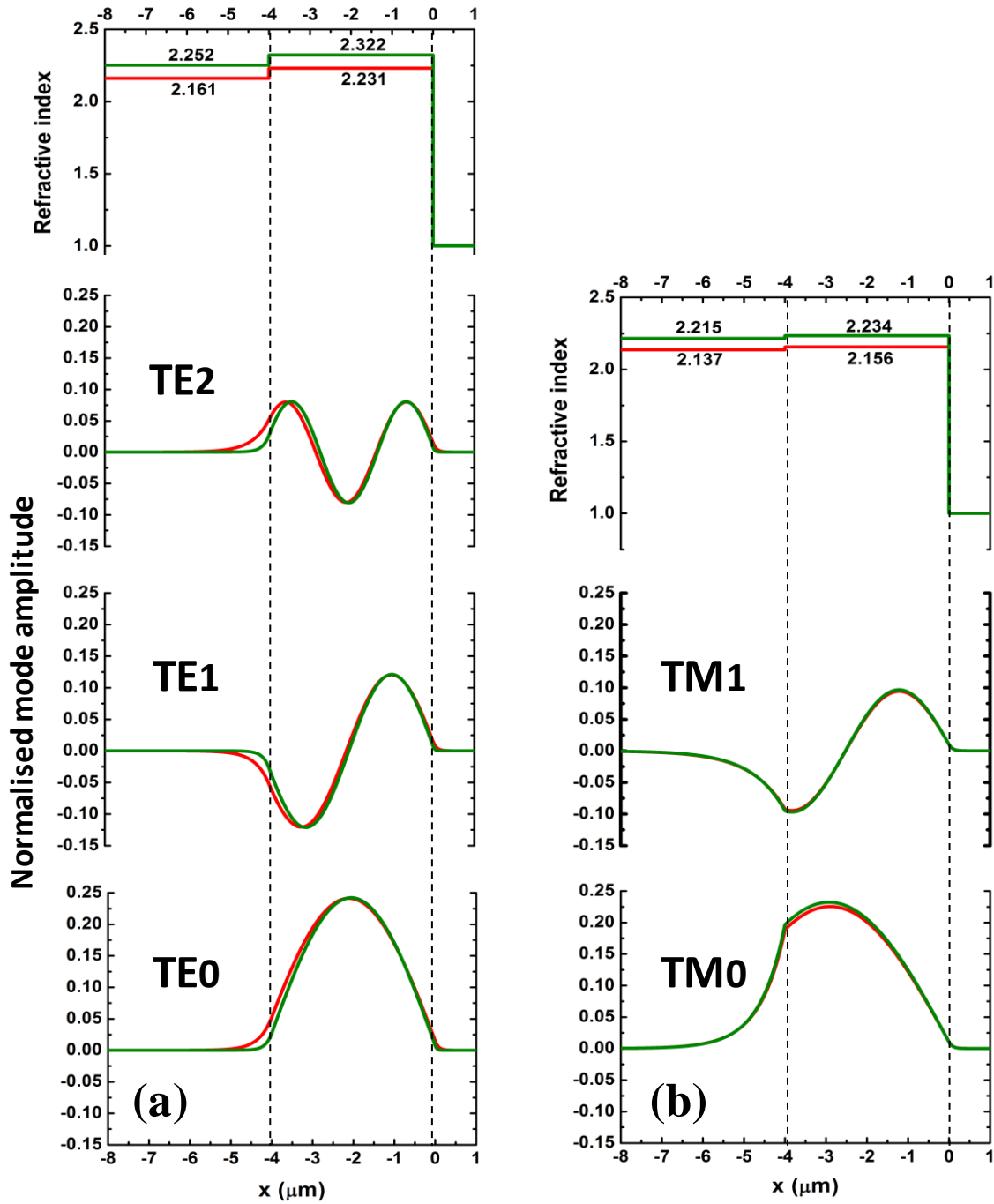


Figure 1.14. (a) Field distribution of the three TE modes (b) and the two TM modes at 1064 nm (red curve) and 532 nm (green curve) in a He^+ implanted LiNbO_3 asymmetric waveguide with $n_{wg,TE}(532 \text{ nm}) = 2.3221$, $n_{wg,TE}(1064 \text{ nm}) = 2.2312$, $n_{wg,TM}(532 \text{ nm}) = 2.2342$, $n_{wg,TM}(\lambda = 1064 \text{ nm}) = 2.1555$, $\Delta n_{TE} = 0.07$, $\Delta n_{TM} = 0.019$ [26].

In the case of SHG, this is of great interest for the optimisation of the effective overlap area S_{ovl} in Eq. (1.17), as the transverse field profiles match between FF and SHG ($F_{FF} = F_{SH}$). Thus, a monomode step index waveguide is beneficial to optimise nonlinear interactions. Otherwise, we can observe that the optical barrier on the substrate confines one TE mode more than the TM ones.

1.3.3. Equation of the guided modes

In the case of TE polarisation:

Up to now, we have not presented the concept of guided modes in the waveguide. Still using the Maxwell equations, Eq. (1.54.a) for the middle layer (zone II) can be rewritten as:

$$E_y(x) = C_1' \cos(\beta_{wg}x + \alpha) \quad (1.63)$$

By substituting: $C_1 = C_1' \cos \alpha$ and $C_2 = -C_1' \sin \alpha$

We call α the coefficient corresponding to the phase term induced at the waveguide-air interface. Thus, by applying the boundary conditions at $x = 0$ to $E_y(x)$ and $H_z(x)$ (Eq. (1.55)), one can obtain:

$$\alpha = -\arctan\left(\frac{\beta_a}{\beta_{wg}}\right) + m\pi \text{ with } m = 1, 2, 3, \dots \quad (1.64)$$

Likewise, at the interface waveguide-substrate (at $x = -l$) the guided mode dispersion relation for the TE modes is given by:

$$\beta_{wg}l - \arctan\left(\frac{\beta_s}{\beta_{wg}}\right) - \arctan\left(\frac{\beta_a}{\beta_{wg}}\right) + m\pi = 0 \quad (1.65)$$

It represents the condition to confine the TE-polarised light within the guiding layer. The parameters in arctan correspond to the phase shift due to the TIR occurred at the interfaces. According to Eq. (1.65), the integer m corresponds to a TE_m mode of the waveguide. In other words, not all ray trapped in the waveguide constitute a mode. By definition, a mode must have a unique propagation constant β_m (linked to the effective index $N_{eff,m}$) and a well-defined field amplitude at each point in space and time. So, we add into the propagation constant the transverse phase shift condition at the interfaces, which is an integer multiple of π .

In the case of TM polarisation:

In the same way, we develop $H_y(x)$ and $E_z(x)$ at the boundary conditions in Eq. (1.59), and we obtain:

$$\alpha = -\arctan\left(\frac{\tilde{\beta}_a}{\beta_{wg}}\right) + m\pi \text{ with } m = 1, 2, 3, \dots \quad (1.66)$$

And the dispersion relation:

$$\beta_{wg}t - \arctan\left(\frac{\tilde{\beta}_s}{\beta_{wg}}\right) - \arctan\left(\frac{\tilde{\beta}_a}{\beta_{wg}}\right) + m\pi = 0 \quad (1.67)$$

Thus for TM polarisations, the equation contains an additional factor related to the ration of permittivity for adjacent layers in each interface.

The dispersion equation for TE and TM modes allows a simulation of the effective index evolution as a function of the waveguide thickness for different modes. The method used to solve this transcendental equation is the dichotomy method [66]. It consists of finding the couple of values $(t, N_{eff,m})_m$ by solving Eqs. (1.65) and (1.67). Figure 1.15 shows the dependence of the effective index dispersion on the waveguide thickness for a He^+ -implanted LiNbO_3 waveguide (z-cut) at wavelengths of 1064 nm and 532 nm. As we consider a birefringent medium, the ordinary refractive index will be observed in TE polarisation and the extraordinary one in TM polarisation. The anisotropy of the crystal also induces a difference on the refractive index variation between the guiding layer and the optical barrier (considered as the substrate). Thus in such an implanted waveguide, we have found experimentally a maximum variation of 0.075 for the ordinary index and 0.034 for the extraordinary one (see section 3.3.2). On the one hand, the guided modes increase with the waveguide thickness. On the other hand, the effective index approaches its maximum value corresponding to a free propagation in the bulk whereas the minimum value corresponds to the substrate/optical-barrier refractive index below which the guided modes does not exist. From Eqs. (1.65) and (1.67), and suggesting $N_{eff} = n_s$, we can calculate the maximum number of modes existing in the waveguide:

$$M = 1 + IP \left\{ \frac{1}{\pi} \left[k_0 l \sqrt{n_{wg}^2 - n_s^2} - \arctan\left(\left(\frac{n_{wg}}{n_a}\right)^{2\rho} \sqrt{\frac{n_s^2 - n_a^2}{n_{wg}^2 - n_s^2}}\right) \right] \right\} \quad (1.68)$$

with $\rho = 0$ in TE polarisation and $\rho = 1$ in TM polarisation and IP means the integer part. We find that M increases with the waveguide thickness l and the variation of the refractive indices between the guiding layer and the substrate/optical-barrier ($\Delta n = n_{wg} - n_s$). It is also possible to define a cut-off thickness associated with each mode:

$$l_{c,m} = \frac{m\pi + \arctan\left(\left(\frac{n_{wg}}{n_a}\right)^{2\rho} \sqrt{\frac{n_s^2 - n_a^2}{n_{wg}^2 - n_s^2}}\right)}{k_0 \sqrt{n_{wg}^2 - n_s^2}} \quad (1.69)$$

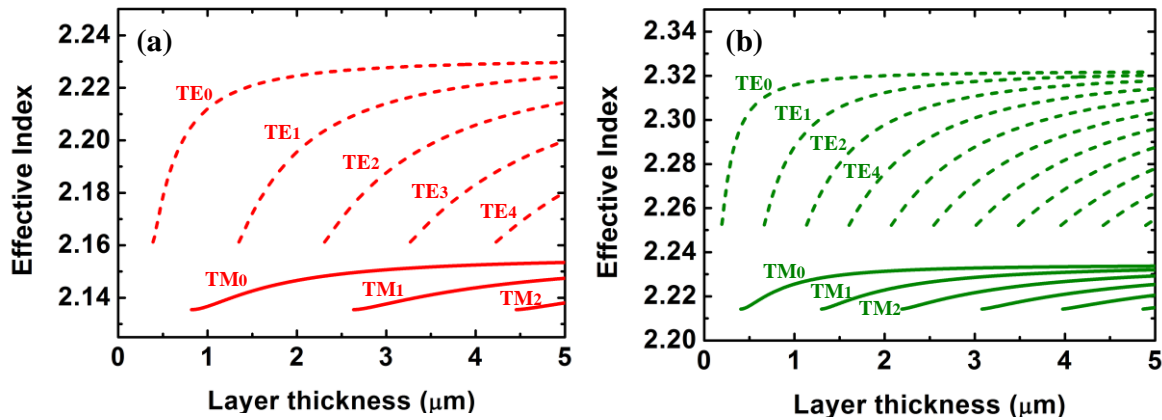


Figure 1.15: Effective index $N_{eff,m}$ vs. thickness of a He^+ - implanted LiNbO_3 planar waveguide for TE and TM modes at (a) 1064 nm and (b) 532 nm with $n_{wg,TE}(532 \text{ nm}) = 2.3221$, $n_{s,TE}(1064 \text{ nm}) = 2.2312$, $n_{s,TM}(532 \text{ nm}) = 2.2342$, $n_{s,TM}(\lambda = 1064 \text{ nm}) = 2.1555$, $\Delta n_{TE} = 0.075$, $\Delta n_{TM} = 0.034$ [26].

With a thickness of 4 μm , we can observe in Fig. 1.15, 2 TM modes at 1064 nm and 4 TM modes at 532 nm. This will be compared to the experimental ones in chapter 3.

1.3.4. Reconstruction of the index profile by i-WKB method

Up until now, we have considered that the implantation of Helium ions in LiNbO_3 creates asymmetric step index waveguides. In fact, during implantation, a low refractive index optical barrier is built up at the end of the ion track. The nuclear collisions produce lattice disorder in the crystal lattice and the creation of impurities (see section 2.7) [67]. The ionic implantation and the related damages distribution can induce material density and polarisation changes, modifying the

refractive index value. In general, the refractive index variation induced by ionic implantation can be represented with a gradual variation of the refractive index in the guiding layer (see Fig. 1.16). The obtained structure is a graded index planar waveguide. In this condition, the guided modes dispersion equations (1.65 – 1.67) become:

$$k_0 \int_0^t \sqrt{n^2(z) - N_{eff,m}^2} dz = m\pi + \phi_{wg/s} + \phi_{wg/a} \quad (1.70)$$

with $\phi_{wg/j} = \arctan \left[\left(\frac{n_{wg}}{n_j} \right)^{2\rho} \left(\frac{(N_{eff,m}^2 - n_j^2)}{(n_{wg}^2 - N_{eff,m}^2)} \right)^{1/2} \right]$, $j = a, s$ and $\rho = 0$ in TE polarisation and 1 in TM polarisation and $k_0 = 2\pi/\lambda$.

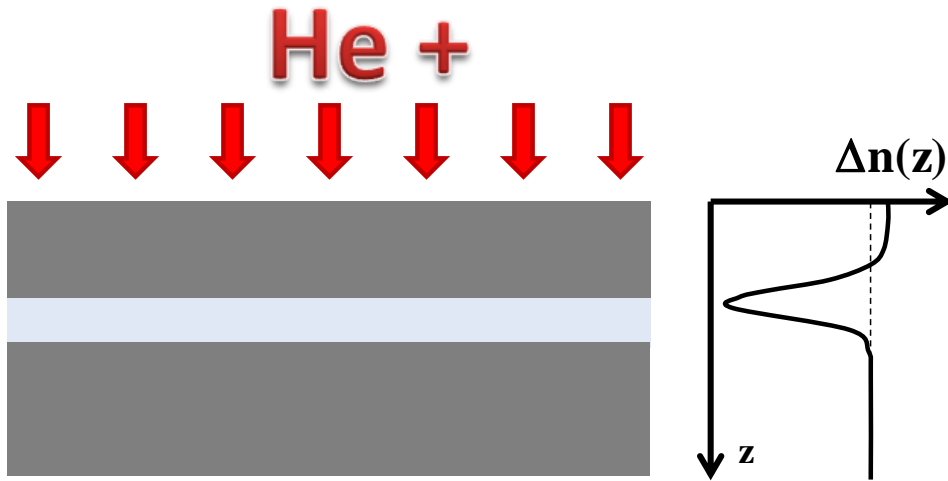


Figure 1.16: Effect of He^+ implantation on the refractive index of material.

The WKB method had been developed by Wentzel, Kramers and Brillouin concerning potentials which are continuously variable in quantum mechanics. There is great similarity between the Schrödinger equation of a particle in a potential well and the wave propagation equation in a planar waveguide. In that case, the waveguide is considered as a potential well: $V(z) = n^2(z)$. The i-WKB is a reconstruction method of refractive index profile $n(z)$ based on effective index.

J. W. White *et al.* [68] reported for the first time a reconstructive approach of refractive index by finding the turning points considering the following boundary conditions:

- $N_{eff,m} = n(z_m)$, with $n(z_0) = n_{wg}$ at $z_0 = 0$,
- the phase shift at the interfaces $\Phi_{w/a} = \frac{\pi}{2}$ and $\Phi_{w/z_m} = \frac{\pi}{4}$
- $n(z)$ decreases monotonically.

Equation (1.70) is written as a sum of integrals from Ref. [69], with $M = m + 1 = 1, 2, 3, \dots$:

$$\sum_{k=1}^m \int_{z_{k-1}}^{z_k} [n^2(z) - N_{eff,M}^2]^{1/2} dz = \frac{4M-1}{8} \lambda \quad (1.71)$$

Therefore:

$$\sum_{k=1}^m \int_{z_{k-1}}^{z_k} [n(z) - N_{eff,M}]^{1/2} \cdot [n(z) + N_{eff,M}]^{1/2} dz = \frac{4M-1}{8} \lambda \quad (1.72)$$

When $z_{k-1} \leq z \leq z_k$, $n(z)$ is developed in Taylor series at the first order:

$$n(z) \approx N_{eff,k} + \left(\frac{N_{eff,k-1} - N_{eff,k}}{z_k - z_{k-1}} \right) (z_k - z) \quad (1.73)$$

Then, in Eq. (1.73) if the second term of the Taylor series is replaced by a midpoint value of

$\frac{N_{eff,k+1} + N_{eff,k}}{2}$, we can develop and simplify the equation as:

$$\sum_{k=1}^M \int_{z_{k-1}}^{z_k} \sqrt{\frac{N_{eff,k+1} + N_{eff,k}}{2} + N_{eff,M}} \left(N_{eff,k} + \left(\frac{N_{eff,k-1} - N_{eff,k}}{z_k - z_{k-1}} \right) (z_k - z) - N_{eff,M} \right)^{1/2} dz = \frac{4M-1}{8} \lambda \quad (1.74)$$

The recursive formula for z_M is:

$$\begin{cases} z_0 = 0 \\ z_1 = \frac{9}{16} \left(\frac{N_{eff,0} + 3N_{eff,1}}{2} \right)^{-\frac{1}{2}} (N_{eff,0} - N_{eff,1})^{-\frac{1}{2}} \lambda \\ z_M = z_{M-1} + \left[\left(\frac{3}{2} \right) \left(\frac{N_{eff,M-1} + 3N_{eff,M}}{2} \right)^{-\frac{1}{2}} (N_{eff,M-1} - N_{eff,M})^{-\frac{1}{2}} \right] S \lambda \end{cases} \quad (1.75)$$

With:

$$S = \left(\frac{4M-1}{8} \right) - \frac{2}{3} \sum_{k=1}^M \sqrt{\frac{N_{eff,k+1} + N_{eff,k}}{2} + N_{eff,M}} \left(\frac{z_k - z_{k-1}}{N_{eff,k-1} - N_{eff,k}} \right) \left[(N_{eff,k-1} - N_{eff,M})^{3/2} - (N_{eff,k-1} - N_{eff,M})^{3/2} \right] \quad (1.76)$$

The refractive index profile can be reconstructed with a good approximation by adjusting the turning points set $(z_M, n(z_M) = N_{eff,M})$ by a polynomial function. We observe that z_1 depends on $N_{eff,0}$ ($m = -1$) which is unknown. An arbitrary method of selecting $N_{eff,0}$ is to choose a value of $N_{eff,0}$ that gives the smoothest profile. The method that leads to most realistic is to minimise the total area of the triangles built on the sets of points $(z_k, N_{eff,k}), (z_{k+1}, N_{eff,k+1}), (z_{k+2}, N_{eff,k+2})$. The transcendental equation is solved by Newton's iterative method. So the index profile is assumed to decrease monotonically for a mode number of $m > 3$.

Various methods of solution for z_M have also been proposed. Particularly we are interested in the one proposed by Chiang *et al.* [70] using a new recursive formula:

$$z_M = z_{M-1} + \left\{ \frac{2(N_{M-1} - N_M)/N_M^2}{\ln \frac{1}{\frac{N_{M-1} + \left[\left(\frac{N_{M-1}}{N_M} \right)^2 - 1 \right]^{1/2}}{N_M} + \frac{N_{M-1} \left[\left(\frac{N_{M-1}}{N_M} \right)^2 - 1 \right]^{1/2}}{N_M}}} \right\} S\lambda \quad (1.77)$$

with:

$$S = \left[\frac{4M-1}{8} - \frac{N_M}{2} \sum_{k=1}^M (z_k - z_{k-1}) \left(\ln \left\{ \frac{\frac{N_k + \left[\left(\frac{N_k}{N_M} \right)^2 - 1 \right]^{1/2}}{N_M}}{\frac{N_{k-1} + \left[\left(\frac{N_{k-1}}{N_M} \right)^2 - 1 \right]^{1/2}}{N_M}} \right\} + \frac{N_{k-1} \left[\left(\frac{N_{k-1}}{N_M} \right)^2 - 1 \right]^{1/2}}{N_M} - \frac{N_k \left[\left(\frac{N_k}{N_M} \right)^2 - 1 \right]^{1/2}}{N_M} \right) \right] \quad (1.78)$$

We have performed these methods in order to get the extrapolated refractive index profile of our He^+ implanted LiNbO_3 planar waveguides, all developed from the methods explained above. The missing parameters are the effective refractive indices of the waveguide $N_{eff,m}$. We have measured experimentally $N_{eff,m}$ by dark m-line spectroscopy [71] presented in section 3.3.1. The effective index values are listed in Fig. 1.17.

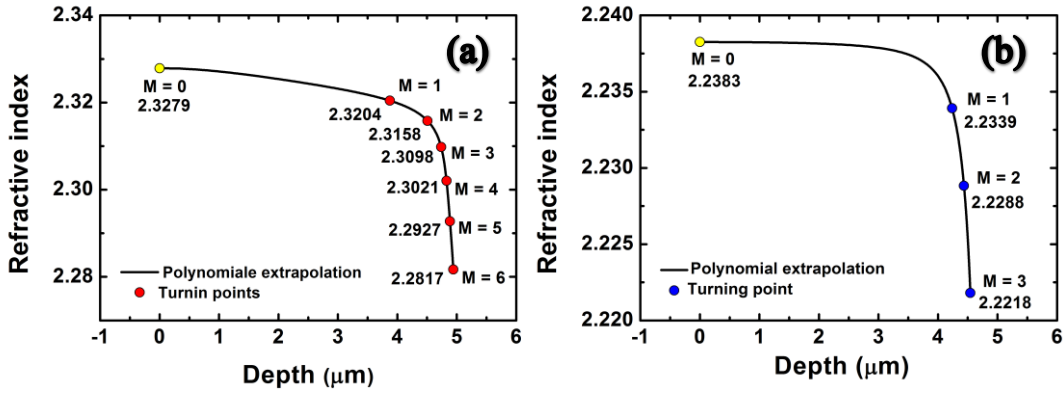


Figure 1.17: (a) Ordinary and (b) extraordinary refractive index profiles of a He^+ - implanted LiNbO_3 planar waveguide obtained by the i-WKB method from the measured effective index at 532 nm (red points for TE modes and blue points for TM modes).

From the measured effective indices, Figure 1.17 shows the turning points $(z_M, n(z_M) = N_{eff,M})$ calculated from Eq. 1.75. The missing point $(0, N_{eff,0})$ is obtained from the expression of z_1 and by minimizing the triangle surface defined by $[(z_1, N_{eff,1}), (z_2, N_{eff,2}), (z_3, N_{eff,3})]$. Finally, the reconstructed refractive index profile is fitted with a polynomial function in both polarisations. The full experimental results are presented and analysed in chapter 3.

1.4. SHG in waveguide configuration

We have detailed the basis of integrated optics in a planar waveguide. We will now study the influence of the waveguide on SHG QPM conditions and conversion efficiency.

1.4.1. Effect of optical confinement on SHG with Gaussian fundamental beam

One of the most interesting things about SHG in waveguide configuration is that the Gaussian beam diffraction problem can be overcome by guided-wave configuration. In such a configuration, the high optical density power is confined, thus increasing the interaction between waves along the waveguide. We will see in the next section that only the surface interaction term is modified in the expression of the efficiency.

1.4.1.1. Improvement of interaction length

Considering the optimum focusing conditions in bulk with Gaussian fundamental beam, the length L of confocal region (determined by the focal length of objectives and the minimum radius w_0 of the laser beam) is defined by:

$$L = k_{FF} w_0^2 \quad (1.79)$$

The efficiency improvement gained by this configuration can be estimated at:

$$\frac{\eta_{waveguide}}{\eta_{bulk}} = \frac{S_{bulk}}{S_{waveguide}} = \frac{\pi w_0^2}{S_{waveguide}} = \frac{\lambda L}{2n S_{waveguide}} \quad (1.80)$$

For instance, using a typical LiNbO₃ waveguide mode size $\sim 80 \mu\text{m}^2$ at 1064 nm, an improvement ratio is estimated at $\sim 30 L$ where L is in cm. Therefore, it is very attractive to study waveguide configuration in order to improve nonlinear interaction efficiency.

1.4.1.2. Parametric Interaction of focused Gaussian beam for SHG

With the effect of optical confinement, it is expected that SHG is more efficient in waveguide configuration than in the bulk. By confining the high power density, the waveguide allows a longer interaction length than that in PPLN bulk. However the measurement depends on the coupling system. In our case, we have used the optical coupling system with the same microscope objective for bulk and waveguide. The problem is that in the bulk configuration the pump beam divergence is very high and our configuration clearly does not meet the requirements to obtain optimum conditions. If we used an optical coupling system allowing the same interaction length as the one in waveguide, and if we used a more powerful laser in order to work with equivalent power density, it can be expected that the efficiencies of the bulk and the waveguide may be almost identical. However, this improvement is limited in bulk whilst the interaction length can be much longer in waveguide as in nonlinear optical fibre.

It is interesting to investigate the coupling injection of a collimated laser beam to a periodically poled crystal for an optimum SHG power. The key problem considered in this chapter is that the nonlinear interaction maximisation depends on the focusing optical components used to inject the FF beam in the crystal. Considering the optimum focusing conditions, it is important to examine the coupling injection to a crystal with Gaussian fundamental electric field. In practice,

we use a microscope objective with a short confocal parameter L which the length of confocal region given by Eq. 1.79 (determined by the focal length of objectives and the minimum radius w_0 of the laser beam in Fig. 1.18.).

In 1966, the theory of SHG using BPM and focused Gaussian beams was described by Kleinman *et al* for negative and positive uniaxial crystal [72]. This theory can be applied to the case of QPM with some simplifications. Thus, the FF Gaussian beam is characterised by the direction of beam axis, the location of the focus f in the crystal (given by the parameter $\mu = l - 2f/l$), the confocal parameter L , the frequency and the power. The crystal length l is fixed at 6 mm considering the length of the periodically poled zone of our samples (the details are given in section 3.1). The intrinsic linear and nonlinear optical properties of crystal are considered as the fixed parameters. In single-pass configuration (without resonator) the absorption of crystal is not considered for describing the interacting light field.

Boyd and Kleinman investigated the SHG power optimisation as a function of the focusing parameter $\xi = l/L$, a strong focusing limit ($\xi \gg 1$) and an optimum phase matching (given by the parameter $\sigma = L \cdot \Delta k/2$) for a variety of double refraction angles ρ (specific for anisotropic mediums). In our case, the QPM is implemented with a TM polarised FF beam, thus we assume a double refraction angle $\rho = 0$.

From these parameters we can deduce the optimised SHG power following the function $h(\sigma, \rho, \xi, \mu)$ also called Boyd and Kleiman function:

$$P_{SH} = \frac{16\pi^2 d_{eff}^2}{\lambda_{FF}^3 n_{FF} n_{SH} \epsilon_0 c} L \cdot P_{SH}^2 \cdot h(\sigma, \rho, \xi, \mu) \quad (1.81)$$

We observe that the SHG power P_{SH} is proportional to $L \cdot h(\sigma, \rho, \xi, \mu)$ considering a Gaussian pump and not to L^2 as shown before with a plane wave pump consideration.

The beam is linearly polarised so that there is no birefringence effect on the beam refraction ($\rho = 0$), and the focus position is set to the centre of crystal ($\mu = 0$). Therefore, we can define the simplified function h :

$$h(\sigma, 0, \xi, 0) = h(\sigma, \xi) = \left(\frac{\pi^2}{\xi}\right) |H(\sigma, \xi)|^2 \quad (1.82.a)$$

$$\text{And } H(\sigma, \xi) = \frac{1}{2\pi} \int_{-\xi}^{\xi} \frac{e^{i\sigma\tau}}{(1+i\tau)} d\tau \text{ with } \tau = \frac{2(z-f)}{b} \quad (1.82.b)$$

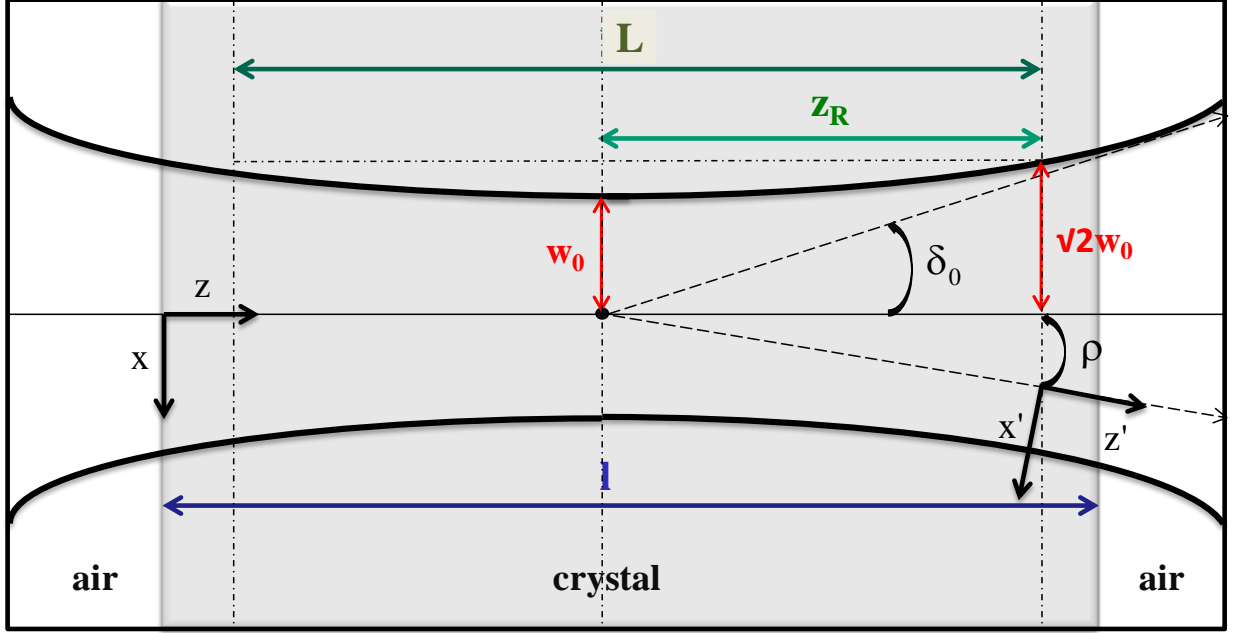


Figure 1.18: The crystal is shown as a rectangular solid with a length l . We consider the reference (x', y', z') to be a source point emitting to the observer in the reference (x, y, z) . The medium being embedded as an isotropic medium, we set $(x'=x, y'=y, z'=z)$. The laser beam is a Gaussian beam with a beam waist w_0 at $z=f$. b is the confocal parameter and δ_0 is the diffraction half-angle.

From Eq. (1.82), we use the optimum phase-matching parameter σ_m with respect to each ξ . According to Boyd and Kleinman, the general form of phase matching parameter is given by:

$$\sigma_m(\xi) = \frac{\text{atan}(\xi)}{\xi} \quad (1.83)$$

Figure 1.19(a) shows the phase matching parameter as a function of focusing parameter. As ξ increases, σ_m decreases. In Fig.1.19(b), we represent the Boyd and Kleinman focusing parameter $h(\sigma_m, \xi)$ according to ξ . Interestingly, the optimum phase-matching is observed for $\Delta k \neq 0$.

Thus at a confocal focusing ($\xi = 1$), we get $\sigma_m \approx 0.79$ and $h(\sigma_m, \xi) \approx 0.8$. An optimum focusing of $h(\sigma_m, \xi) \approx 1.068$ is obtained when $\xi = 2.84$.

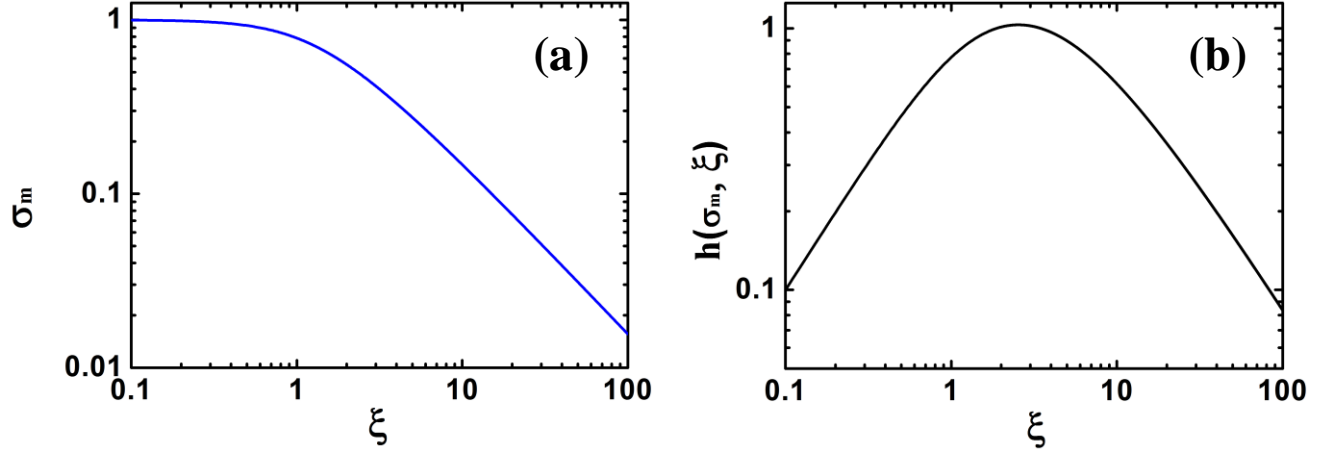


Fig 1.19(a): The optimum phase-matching parameter $\sigma_m(\xi)$, with $\sigma = L\Delta k/2$ in one of its approximation in log-log scale. (b): The SHG power is represented with the function $h(\sigma_m, \xi)$ for optimum phase matching in log-log scale.

In this thesis, we characterise SHG in PPLN bulk and guided-wave configurations and taking care of the Gaussian beam focus consideration. Once the periodically poled region length l determined and the optimum focusing parameter ξ fixed, it is possible to study SHG in the optimised focusing condition in the waveguide. Then, we will see how the beam focus affects the conversion efficiency by comparing our results in both the configurations. Furthermore from Eq. 1.81, and knowing the Boyd and Kleiman function, it is possible to compare our results according to the beam shape in bulk and waveguide configurations. In order to facilitate the comparison we supposed that the waveguide effective index is identical with the bulk refractive index.

In bulk configuration, as we supposed before, there is no birefringence effects ($\rho = 0$), the focus position is set to the centre of crystal ($\mu = 0$) in order to get the maximum efficiency. The other considered parameters are the general form of the phase matching parameter $\sigma = L\Delta k/2$ depending on the interaction length L .

We consider that the interaction length correspond to twice the Rayleigh length (the length between which the beam goes from a radius of w_0 to a radius of $\sqrt{2}w_0$). For instance, by taking a beam radius of $9 \mu m$ theory gives that the interaction length in the bulk is:

$$L = \frac{2\pi n_{FF} w_0^2}{\lambda_{FF}} = 1 \text{ mm} \quad (1.84)$$

Thus it is possible to obtain the optimum phase-matching parameter $\sigma_m(\xi = l/L = 6, \mu = 0)$ and the calculated function $h(\sigma_m, \xi = 6, \mu = 0)$ in the bulk case. In Fig. 1.20, the results of $h_{wg}(\sigma_m, \xi, \mu = 0)$ are exhibited in black curve with $h(\sigma_m, 6, 0) \approx 0.827$ (blue spot).

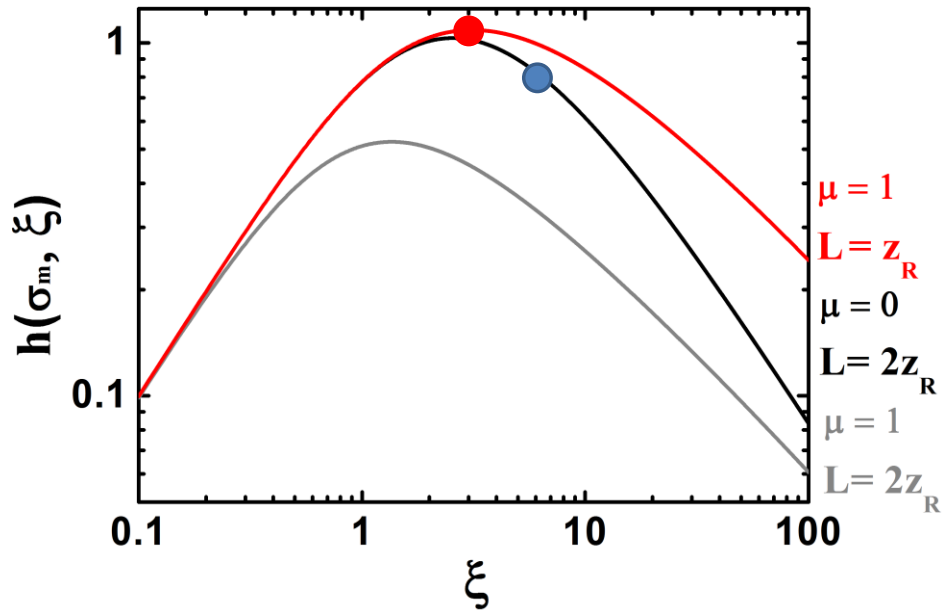


Figure 1.20: Boyd and Kleiman focusing parameter $h_{wg}(\sigma_m, \xi, 1)$ (red curve), $h(\sigma_m, \xi, 0)$ (black curve) and $h(\sigma_m, \xi, 1)$ (grey curve). We estimate $h_{wg}(\sigma_m, 3, 1) \approx 1.093$ (red spot) in the waveguide and $h(\sigma_m, 6, 0) \approx 0.8274$ in the bulk case (blue spot).

Concerning the waveguide configuration, the light is coupled to the waveguide by focusing on the front facet of the sample (with $\mu = 1$). This time, the interaction length is fixed equal to once the Rayleigh length. Considering $\mu = 1$, the Boyd and Kleiman focusing parameter can be written as:

$$h_{wg}(\sigma_m, \xi, \mu = 1) = \left(\frac{\pi^2}{\xi}\right) |H_{wg}(\sigma, \xi, \mu = 1)|^2 \quad (1.85)$$

with $H_{wg}(\sigma, \xi, \mu = 1) = \frac{1}{2\pi} \int_0^{2\xi} \frac{e^{i\sigma\tau_{wg}}}{(1+i\tau_{wg})} d\tau_{wg}$ and this time $\tau_{wg} = \frac{(z-f)}{b} = \frac{\tau}{2}$

In Fig. 1.20, $h_{wg}(\sigma_m, \xi, \mu = 1)$ is plotted in red curve. The maximum focusing parameter corresponding to the optimal focusing condition in this configuration is found $h_{wg}(\sigma_m, \xi = 3.02, \mu = 1) = 1.093$ (red spot).

By this way, from Eq. 1.81, we can approximate a SHG power rate between bulk and waveguide. From Fig. 1.20, it is expected that by keeping the same optical coupling system, and considering only the focusing dependence, the SHG in the bulk is 24 % lower than that in the waveguide.

1.4.2. SHG interaction in waveguide

From the previous section, we have seen that waveguides are obtained by increasing locally the refractive index compared to surrounding ones. Such structures do not allow EM radiation to propagate freely. Instead, the EM radiation propagates as discrete modes inside the waveguide. The solution to the wave equation for the electric field $\vec{E}(\vec{r}, t)$ in such a structure is given by:

$$\vec{E}(\vec{r}, t) = \sum_q \sum_j \overrightarrow{F_j^{(m)}}(x, y) \vec{A}_j^{(m)}(z) \exp \left[i(\omega_j t - \beta_j^{(m)} z) \right] + c. c. \quad (1.86)$$

where m denotes the mode index, $\beta_j^{(m)} = \frac{\omega_j}{c} N_{eff,m}$ is the propagation wave vector of mode m with frequency ω_j inside the waveguide, with $N_{eff,m}$ being the effective refractive index of the propagating mode.

The coupled-mode equations describing the evolution of the fundamental and the second harmonic waves inside a waveguide are formally identical to Eq. (1.15), and are given by:

$$\frac{dA_{FF}(z)}{dz} = 2i\omega_{FF}\kappa dA_{FF}^*(z)A_{SH}(z)\exp(i\Delta\beta z) \quad (1.87.a)$$

$$\frac{dA_{SH}(z)}{dz} = i\omega_{SH}\kappa dA_{FF}^2(z)\exp(-i\Delta\beta z) \quad (1.87.b)$$

The coupling coefficient κ , similar to Eq. (1.16), is given by:

$$\kappa = \sqrt{\frac{2\mu_0}{N_{eff,FF}^2 N_{eff,SH} c}} \sqrt{\frac{1}{S_{ovl}}} \quad (1.88)$$

There are two main differences in the above equations compared to Eq. (1.15):

- The bulk material wave vector mismatch Δk is replaced by the waveguide wave vector mismatch:

$$\Delta\beta = \beta_{SH}^{(m)} - 2\beta_{FF}^{(n)} \quad (1.89)$$

where m, n represent the mode indices of the fundamental and generated waves.

- The new effective overlap area S_{ovl} is developed in the next section. Note also that the effective overlap area in waveguide can be optimised by a proper design of the waveguide structure to improve the conversion efficiency.

As described before, the interaction between the FF wave and the material in the waveguide produces a polarisation wave P_α^{NL} with SHG [See (Eq. 1.14)]. The polarisation wave travels at the same phase velocity as the fundamental wave, which is determined by $N_{eff,FF}^{(n)}$, the effective index at ω_{FF} . The polarisation wave then radiates the SHG wave which travels at the phase velocity determined by $N_{eff,SH}^{(m)}$, the effective index at ω_{SH} . When both the fundamental and the second harmonic waves propagate at the same phase velocity, then the energy transfers from the FF to the SHG waves. As previously mentioned, from Eq. (1.89) this condition is called phase-matching and corresponds to $\Delta\beta = \frac{4\omega_{FF}}{c} (N_{eff,SH}^{(m)} - N_{eff,FF}^{(n)})$. However, it is known that $N_{eff,SH}^{(m)} \neq N_{eff,FF}^{(n)}$ due to the variation of index with respect to the wavelength in most materials, including Lithium Niobate. In Fig. 1.20 the variation of effective index $N_{eff}^{(m)}$ calculated for $m = 0, 1, 2$ is shown for TM polarisation in the helium-implanted waveguide studied in this work. In this case, we have experimentally measured a refractive index difference of $\Delta n \approx 0.03$ between the waveguide and the bulk, and a waveguide thickness of $4 \mu\text{m}$. For TM polarisation, the extraordinary refractive index is considered. Hence the fundamental and the second harmonic waves travel at different phase velocities, leading to a continuous phase shift between the waves. This phase shift alters the energy transfer between the FF and the SHG waves, as illustrated by

the green curve in Fig. 1.6. The alternation of the power flow yields a growth and decay cycle of the SHG wave along the interaction length. The length over which the fundamental and the second harmonic waves produce a π -phase shift is called the coherence length:

$$l_c = \frac{\pi}{\Delta\beta} = \frac{\lambda}{4[N_{eff,SH} - N_{eff,FF}]} \quad (1.90)$$

which is a half period of the growth and decay cycle of the SHG wave.

In the QPM case, the wave vector mismatch $\Delta\beta$ in Eq. (1.89) must then be replaced with:

$$\Delta\beta'_m = \Delta\beta - K_p \quad (1.91)$$

with the p th-harmonic grating wave vector. We have so far assumed a perfectly-periodic QPM structure which remains unchanged between bulk and waveguide configuration. The waveguide is considered as homogeneous in the propagation direction. By comparing Eq. (1.24) with Eq. (1.91), we expect to observe a slight shift in the phase matching conditions by QPM between bulk and waveguide induced by index changes.

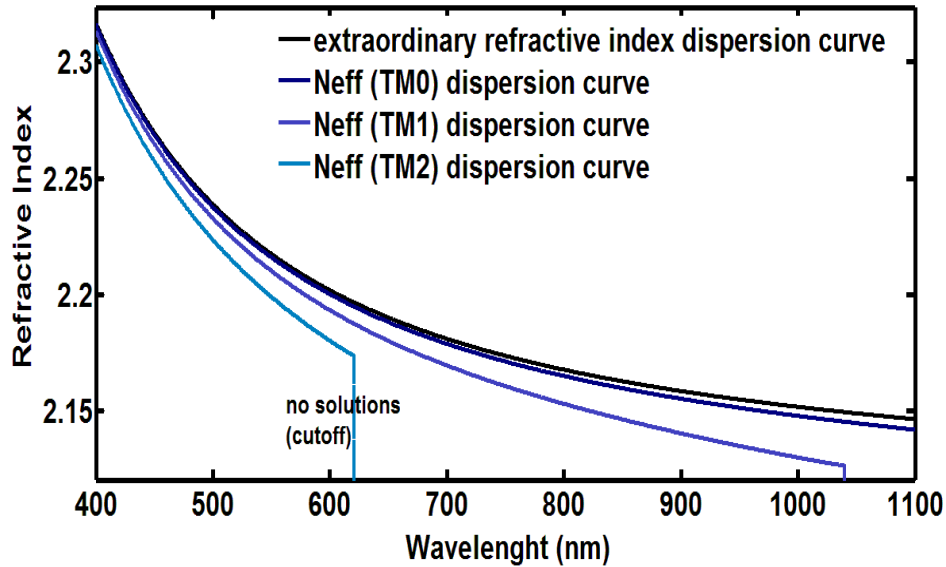


Figure 1.20: Variation of effective index $N_{eff}^{(m)}$ for $m=0, 1, 2$ for TM polarisation in a typical helium implanted waveguide with $\Delta n \approx 0.02$, and a thickness of $4 \mu\text{m}$.

1.4.3. Expression of the Effective Area Overlap in a waveguide

The calculation of the effective area overlap in a waveguide takes into account the EM field distribution between the possible FF and SHG transversal modes. For the expression of S_{ovl} , we start from the expression of the normalised EM field with a spatial interaction between TM modes ($TM_{FF}^{(m)} \rightarrow TM_{SH}^{(n)}$). The calculation can be generalised with other polarisations.

$$S_{ovl} = \frac{\int |H_{y,SH}^{(m)}|^2 dx.dy \left(\int |H_{y,FF}^{(n)}|^2 dx.dy \right)^2}{\left(\int |H_{y,SH}^{(m)}| |H_{y,FF}^{(n)}|^2 dx.dy \right)^2} \quad (1.92)$$

From expression (1.90) and the normalisation condition given by Eq. (1.61), we define the overlap efficiency (expressed in m^{-1}) such as:

$$\eta_{ovl} = \sqrt{\frac{1}{S_{ovl}}} = \frac{\int |H_{y,SH}^{(m)}| |H_{y,FF}^{(n)}|^2 dx.dy}{\sqrt{\int |H_{y,SH}^{(m)}|^2 dx.dy \int |H_{y,FF}^{(n)}|^2 dx.dy}} \quad (1.93)$$

The overlap efficiency must be optimised, taking a value as close as possible of 1. The ideal case would be to have an interaction when $m = n$. In order to limit the energy dispersion in different propagation modes, it is important to work with single-mode waveguides, at least for the FF wavelength. As the dispersion probability is maximum between two modes with the same parity, we set a limit condition at 2 TM modes at 1064 nm. Considering the He^+ implanted $LiNbO_3$ planar waveguide in Fig. 1.17, a thickness of $l = 4\mu m$ has been determined. The waveguide supports 1, almost 2 TM modes at the FF wavelength, and 4 TM modes at the SHG wavelength. If now we consider the obtained refractive index turning point from i-WKB, and we consider the refractive index profile as a multi-layer structure as shown in Fig. 1.21 (a), it is possible to plot the field distribution of the TM modes at 1064 nm (red curve) and 532 nm (green curve) in the waveguide. $H_{y,FF}^{(0)}$ and $H_{y,SH}^{(0)}$ are represented in Fig. 1.21 (b).

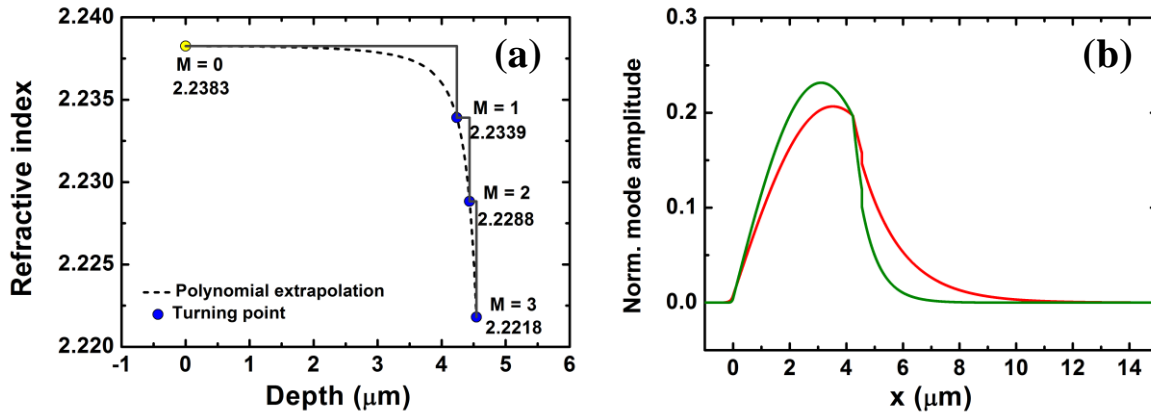


Figure 1.21: (a) The refractive index profile is approximated as a multi-layer structure with the considered turning point obtained from i-WKB. (b) TM₀ field distribution at 1064 nm (red curve) and at 532 nm (green curve).

With this coarse approximation on the refractive index profile, it is already possible to observe a large dependence of the field distribution with the wavelength. By applying Eq. 1.93, the overlap efficiency η_{ovl} between $H_{y,SH}^{(0)}$ and $H_{y,FF}^{(0)}$ has been determined at 68.3%. Furthermore, we have calculated that SHG interactions are preferably carried out for low-order modes. For instance, the effective area overlap between $H_{y,SH}^{(1)}$ and $H_{y,FF}^{(1)}$ is calculated at 54.9%.

1.4.4. Phase matching by modal dispersion

An effective SHG must satisfy the condition $\Delta\beta'_p = 0$. We have seen that in a multimodal waveguide, the effective index takes a value between the refractive index of the waveguide, and the highest refractive index of the surrounding layers. Figure 1.22. shows that phase matching possibilities are numerous. However, it should be noted that the conversion efficiency is very different according to the considered interaction due to the integration overlap in Eq.1.93. It is known that interactions between odd and even modes are highly disadvantaged. In addition, the losses (tunnelling losses) increase significantly with the propagation mode number. It can be assumed that the privileged modes interaction is between the modes of order 0.

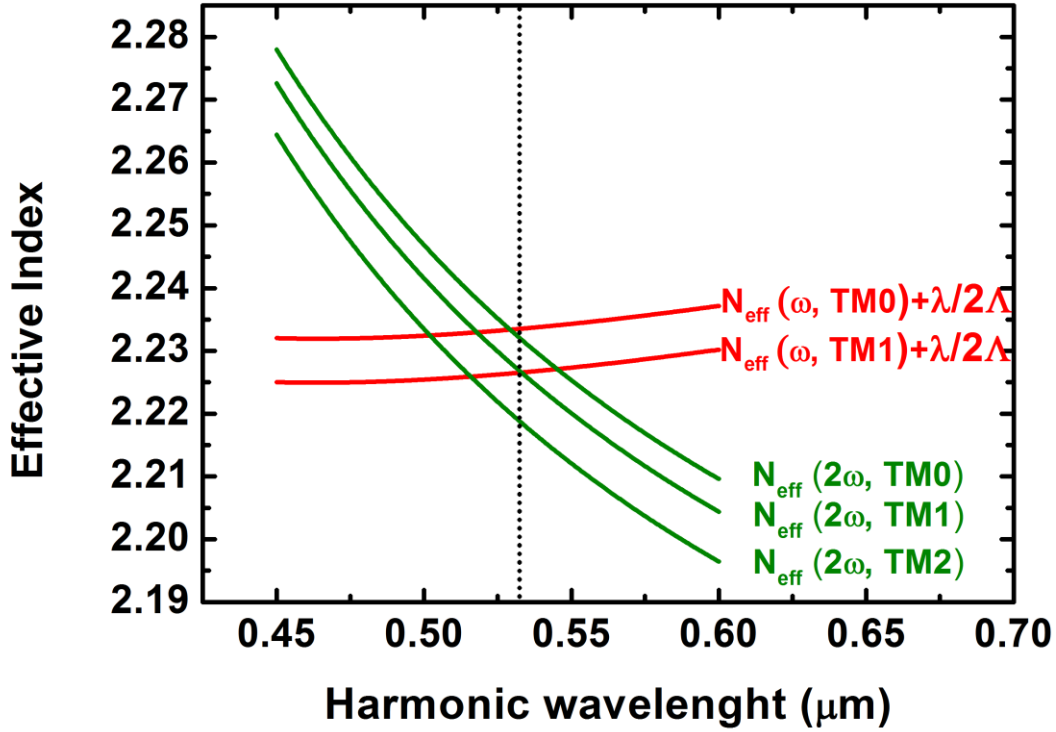


Figure 1.22: Modal dispersion of effective indices in a planar waveguide.

However, the modal dispersion can cause multiple phase matching conditions. From $\Delta\beta'_p = 0$, we get:

$$N_{eff,SH}^{(n)} = N_{eff,FF}^{(m)} + \frac{\lambda}{2\Lambda}p \quad (1.94)$$

As illustrated in Fig. 1.22, by plotting the equation left side with the right side for different TM modes, we can observe the different effective SHG conditions at the crossing points. In this Figure, we have plotted the chromatic dispersion of different effective indices of a He^+ implanted PPLN ($\Lambda = 6.92 \mu\text{m}$) waveguide ($t = 4\mu\text{m}$, $\Delta n_{TM} = 0.019$) at given temperature of 53°C . The utilisation of waveguide has an additional interest, it allows phase matching at different wavelength, even if the conversion efficiencies are far to be equal.

Summary

General qualitative descriptions of nonlinear interactions are presented in this chapter. Among nonlinear interactions, the Second-Harmonic generation (SHG) theoretical framework was

developed in this chapter. The principles that underlie the nonlinear optic effect in materials, particularly for achieved SHG by Quasi-phase Matching (QPM) have been theoretically described. The analysis revealed that the efficiency of the nonlinear interaction reaches maximum when the phase matching condition is achieved. Quasi-Phase Matching technique is an elegant scheme to achieve this condition by introducing an artificial periodic structure. The phase-matching wavelength can be chosen by changing the structure period. The whole theories provide the basis for the experimental analysis developed in chapter 3.

Finally, we introduce integrated optics theory in order to understand the modifications bring by the waveguide in SHG interaction. Interactions between propagating modes and nonlinear improvements in a periodically poled lithium niobate guiding layer are particularly developed. It is provided by tight optical confinements and long interaction lengths. A helium implanted planar waveguide in PPLN is investigated for the purpose of enhancing the conversion efficiency.

References:

- [1] D. Besnard, *The megajoule laser program - ignition at hand*, Eur. Phys. J. D **44**(2), 207–213, (2007).
- [2] T. Maiman, *Stimulated optical radiation in ruby*, Nature, vol. **187**, 493 - 496 (1960).
- [3] P. Franken, A. E. Ill, C. Peter, G. Weinreich, *Generation of optical harmonics*, Phys. Rev. Lett. **7**, 118 - 122 (1961).
- [4] J. A. Armstrong, N. Bloembergen, J. Ducuig and P. S. Pershan, *Interactions between light waves in a nonlinear dielectrics*, Phys. Rev. **127**(6), 1918 - 1921 (1962).
- [5] R. Sutherland, *Handbook of Nonlinear Optics*, 2nd Edition, Marcel Dekker (2003).
- [6] Y. Shen, *The Principles of Nonlinear Optics*, Wiley-Interscience (1984).
- [7] R. Boyd, *Nonlinear optics*, Academic Press, INC. (1992).
- [8] D. Kleinman, *Nonlinear dielectric polarization in optical media*, Phys. Rev. **126** (6), 1977 – 1979 (1962).
- [9] D. Mills, *Nonlinear Optics: Basic Concepts*, Springer-Verlag, New York, 1965.
- [10] R. Baumgartner and R. L. Byer, *Optical Parametric Amplification*, IEEE J. of Quant. Elect. **15**(6), 432 – 444 (1979).
- [11] S. E. Harris, M. K. Osman and R. L. Byer, *Observation of tunable Optical Parametric Fluorescence*, Phys. Rev. Lett. **18**, 732 – 734 (1967).
- [12] M. H. Dunn and M. Ebrahimzadeh, *Parametric Generation of tunable light from continuous-wave to femtosecond pulses*, Science **286**, 1513 – 1517 (1999).
- [13] N. M. Kroll, *Parametric amplification in spacially extended media and application to the design of tuneable oscillators at optical frequencies*, Phys. Rev. **127**(4), 1207 – 1211 (1962).
- [14] R. A. Baumgartner, R. L. Byer, *Optical parametric amplification*, IEEE J. Quantum Electron. QE – **15**(6), 432 - 435(1979).

- [15] M. Bass, P. A. Franken, J. F. Ward, G. Weinreich, *Optical rectification*, Phys. Rev. Lett. **9**(11), 446 – 448 (1962).
- [16] J. P. Van der Ziel, P. S. Pershan, L. D. Malmstrom, *Optically-induced magnetisation resulting from the inverse Faraday effect*, Phys. Rev. Lett. **15**(5), 190 – 193 (1965).
- [17] M. Drdomenico, S. H. Wemple, *Oxygen-ocatedra Ferroelectrics. I. Theory of electro-optical and nonlinear optical effects*, J. Appl. Phys. **40**(2), 720 – 735 (1969).
- [18] P. S. Pershan, *Magneto-optical effects*, J. Appl. Phys. **38**(3), 1482 – 1491 (1967).
- [19] C. V. Raman, *A new radiation*, I. J. of Phys. **2**, 387 – 398 (1928).
- [20] A. Hayat, P. Ginzburg, M. Orenstein, *Observation of two-photon emission from semiconductors*, Nature Photon. **2**, 238 – 241 (2008).
- [21] R. Y. Chiao, T. K. Gustafson, P. L. Kelley, *Self-focusing of optical beam*, www.eecs.berkeley.edu/~tkg/Selffocus_8-16.pdf.
- [22] G. S. He, S. H. Liu, *Physics of nonlinear optics*, World Scientific Publishing Co. Pte. Ltd. (1999).
- [23] R. L. Carman, R. Y. Chiao, P. L. Kelley, *Observation of degenerate stimulated four-photon interaction and four-wave parametric amplification*, Phys. Rev. Lett. **17**(26), 1281 – 1283 (1966).
- [24] J. A. Armstrong, N. Bloemberger, J. Ducuig and P. S. Pershan, *Interactions between light waves in a nonlinear dielectrics*, Phys. Rev. **127**(6), 1918 - 1921 (1962).
- [25] M. Lawrence, *A temperature-dependance dispersion equation for congruently grown lithium niobate*, Opt. and Quant. Elect. **16**(37), 687 - 690(1984).
- [26] D. Jundt, *Temperature-dependent Sellmeier equation for the index of refraction, n_o , in congruent lithium niobate*, Opt. Lett. **22**(10), 1553 - 1556 (1997).
- [27] M.M. Fejer, G.A. Magel, D.H. Jundt, and R.L. Byer, *Quasi-phase matching Second Harmonic Generation: Tuning and Tolerance* IEEE J. Quant. Electr. QE-**28**, 2631-2654 (1992).

- [28] M. G. Angell, R. M. Emerson, J. L. Hoyt, J. F. Gibbons, L. A. Eyres, M. L. Bortz, M. M. Fejer, *Growth of alternating $\langle 100 \rangle / \langle 111 \rangle$ - oriented II – VI regions for quasi-phase matched nonlinear optical devices on GaAs substrates*, App. Phys. Lett. **64**(23), 3107 – 3110 (1994).
- [29] Y. Y. Zhu, S. N. Zhu, Z. Y. Zhang, N. B. Ming, *Studies on domain inversion in LiTaO₃ and LiNbO₃*, MRS Proceedings **417**, 387 - 396 (1995).
- [30] H. Ishizuki, T. Taira, *High energy quasi-phase matched optical parametric oscillation using Mg-doped congruent LiTaO₃ crystal*, Opt. Exp. **18**(1), 253 – 258 (2010).
- [31] K. Mizuuchi, K. Yamamoto, and M. Kato. *Generation of ultraviolet light by frequency doubling of a red laser diode in a first-order periodically poled bulk LiTaO₃*, Appl. Phys. Lett. **70**(10), 1201 - 1204 (1997).
- [32] G. Li, S. Zhao, K. Yang, D. Li, *Laser-diodepumped passively Q-switched Nd :YVO₄ green laser with periodically poled KTP and GaAs saturable absorber*, J. of Mod. Opt. **54**(1), 107 – 117 (2007).
- [33] H. Karlsson, F. Laurell, L. K. Cheng, *Periodic poling of RbTiOPO₄ for quasi-phase matched blue light generation*, App. Phys. Lett. **74**(11), 1519 – 1521 (1999).
- [34] W. P. Risk and G. M. Loiacono. *Periodic poling and waveguide frequency doubling in RbTiOAsO₄*, Appl. Phys. Lett. **69** (3), 311 - 314 (1996).
- [35] L. E. Myers, G. D. Miller, R. C. Eckardt, M. M. Fejer, R. L. Byer, W. R. Bosenberg, *Quasi-phase matched 1.064 μm pumped optical parametric oscillator in bulk periodically poled LiNbO₃*, Opt. Lett. **20**(1), 52 – 54 (1995).
- [36] S. C. Abrahams, H. J. Levinstein, J.M. Reddy, *Ferroelectric lithium niobate 5. Polycrystal X-ray diffraction study between 24° and 1200°C*, J. of Phys. and chemistry of Solids **27**(6 - 7), 1019 – 1026 (1966).
- [37] G. D. Miller, *Periodically poled lithium niobate: modeling, fabrication, and nonlinear-optical performance*, Thesis (1998).

- [38] R. C. Miller, *Further experiments on the sidewise motion of 180° domain walls in BaTiO₃*, Phys. Rev. **115**, 1176 – 1180 (1959).
- [39] V. Ya. Shur, E. L. Rumyantsev, E. V. Nikolaeva, E. I. Shishkin, D. V. Fursov, R. G. Batchko, L. A. Eyres, M. M. Fejer, R. L. Byer, *Nanoscale backswitched domain patterning in lithium niobate*, Appl. Phys. Lett. **76**(2), 143 – 145, (2000).
- [40] J. R. Carruthers, G. E. Peterson, M. Grasso, P. M. Bridenbaugh, *Nonstoichiometry and crystal growth of lithium niobate*, J. Appl. Phys. **42**(5), 1846 – 1852 (1971).
- [41] L. Huang, N. A. F. Jaeger, *Discussion of domain inversion in LiNbO₃*, Appl. Phys. Lett. **65**(14), 1763 – 1766 (1994).
- [42] M. Minakata, S. Saito, M. Shibata, S. Miyazawa, *Precise determination of refractive index changes in Ti:diffused LN optical waveguides*, J. Appl. Phys. **49**, 4677 – 4682 (1978).
- [43] V. Bermudez, D. Callejo, . Dieguez, *On the cooling effect in the formation of periodic poled lithium niobate crystals grown by Cz technique*, E. J. Of Crystal Growth **207**(4), 303 – 307 (1999).
- [44] H. Ahlfeldt, J. Webjorn, G. Arvidsson, *periodic domain inversion and generation of blue-light in lithium tantalite waveguide*, IEEE Photon. Tech. Lett. **3**(7), 638 – 639 (1991).
- [45] K. Mizuuchi, K. Yamamoto, K. Kato, *Harmonic blue light generation in bulk periodically poled MgO:LiNbO₃*, Electron. Lett. **32**, 2091 – 2092 (1996).
- [46] K. Mizuuchi, K. Yamamoto, *Domain inversion in LiTaO₃ using proton exchange followed by heat treatment*, J. Appl. Phys. **75**(3), 1311 – 1317 (1994).
- [47] X. Cao, R. Srivastava, R. V. Ramaswamy, *Simultaneous blue and green second harmonic generation in quasi-phase matched LiNbO₃*, Appl. Phys. Lett. **60**(26), 3280 – 3283 (1992).
- [48] M. Yamada, K. Kishima, *Fabrication of periodically reversed domain structure for SHG in LiNbO₃ by direct electron beam lithography at room temperature*, Electron. Lett. **26**, 188 – 191 (1991).

- [49] W. Y. Hsu, M. C. Gupta, *Domain inversion in LiTaO₃ by electron-beam*, Appl. Phys. Lett. **60**(1), 1 - 3 (1992).
- [50] M. C. Gupta, W. P. Risk, A. C. G. Nutt, S. D. Lau, *Domain inversion in KTiOPO₄ using electron beam scanning*, Appl. Phys. Lett. **63**(9), 1167 – 1170 (1993).
- [51] S. Kurimura, I. Shimoya, Y. Uesu, *Domain inversion by an electron-beam induced electric field in MgO:LiNbO₃*, Japanese, J. Appl. Phys. II **35**(1A), L31 – L33 (1996).
- [52] C. Restoin, C. Darraud Taupiac, J. L. Decossas, J. C. Vareille, J. Hauden, A. Martinez, *Ferroelectric domain inversion by electron beam on LiNbO₃ and Ti:LiNbO₃*, J. Appl. Phys. **88**(11), 6665 – 6669 (2000).
- [53] V. Y. Shur, E. A. Mingaliev, D. K. Kusnetsov, M. S. Kosobokov, *Micro- and nanodomain structures produced by pulse laser heating in congruent lithium tantalite*, Ferroelectrics **443**(1), 95 – 102 (2013).
- [54] C. C. Wu, R. K. Choubey, C. W. Lan, *Generation of annularly symmetric periodic ferroelectrics domains in Nd doped near stoichiometric LiTaO₃ crystals by the vapour transport equilibration processing*, Mat. Lett. **67**(1), 88 – 90 (2012).
- [55] V. I. Pryakhina, V. Ya. Shur, D. O. Alikin, S. A. Negashev, *Polarisation reversal in MgO:LiNbO₃ single crystals modified by plasma-source ion irradiation*, Ferroelectrics **439**(1), 20 – 32 (2012).
- [56] M. Yamada, N. Nada, M. Saitoh, K. Watanabe, *First-order quasi-phase matched LiNbO₃ waveguide periodically poled by applying an external field for efficient blue second-harmonic generation*, Appl. Phys. Lett. **62**(5), 435 – 438 (1993).
- [57] S. Zhu, Y. Zhu, Z. Zhang, H. Shu, H. Wang, J. Hong, C. Ge, *LiTaO₃ crystal periodically poled by applying an external pulse field*, J. Appl. Phys. **77**(10), 5481 – 5483 (1995).
- [58] A. Kuroda, S. Kurimura, Y. Uesu, *Domain inversion in ferroelectrics MgO:LiNbO₃ by applying electric fields*, Appl. Phys. Lett. **69**(11), 1565 – 1568 (1996).

- [59] J. Armin, V. Pruneri, J. Webjorn, P. St. Russel, D. C. Hanna, J. S. Wilkinson, *Blue light generation in a periodically poled Ti:LiNbO₃ channel waveguide*, *Op. Comm.* **135**(1 - 3), 41 – 44 (1996).
- [60] Z. W. Hu, P. A. Thomas, J. Webjorn, G. M. Liaocano, *Domain inversion in RbTiOAsO₄ using electric field poling*, *J. Phys. D: Appl. Phys.* **29**(6), 1681 – 1684 (1994).
- [61] G. Rosenman, A. Skliar, Y. Findling, P. Urenski, A. Englander, P. A. Thomas, Z. W. Hu, *Periodically poled KTiOAsO₄ crystal for optical parametric oscillation*, *J. Phys. D. Appl. Phys.* **32**(14), L49 – L52 (1999).
- [62] G. Rosenman, A. Skliar, D. Edger, M. Oron, M. Katz, *Low temperature periodic electrical poling of flux-grown KTiOPO₄ and isomorphic crystal*, *Appl. Phys. Lett.* **73**(25), 3650 – 3653 (1998).
- [63] R. C. Miller, *Further experiments on the sidewise motion of 180° domain walls in BaTiO₃*, *Phys. Rev.* **115**, 1176 – 1180 (1959).
- [64] G. D. Miller, Poster presentation at the Center for Nonlinear Optical Materials Annual Review (1994).
- [65] A. Yariv, P. Yeh, *Photonics, Optical electronics in modern communications*, Oxford University Press (2007).
- [66] R. L. Burden, J. D. Faires, *Numerical Analysis*, Brooks/Cole 9th Ed. (2000).
- [67] P. D. Townsend, *Optical effects of ion implantation*, *Rep. Prog. Phys.* **50**, 501 – 558 (1987).
- [68] J. M. White, P. F. Heidrich, *Optical waveguide refractive index profiles determined from measurement of mode indices: a simple analysis*, *Appl. Opt.* **15**(1), 151 – 155 (1976).
- [69] P. K. Tien, S. Riva-Sanseverino, R. J. Martin, A. A. Ballman, H. Brown, *Optical waveguide modes in single-crystalline LiNbO₃/LiTaO₃ solid-solution films*, *Appl. Phys. Lett.* **24**, 503 – 507 (1974).
- [70] K. S. Chiang, *Construction of refractive index profiles of planar dielectric waveguides from the distribution of effective indexes*, *J. Lightwave Techn.* **3**, 385 – 390 (1985).

[71] R. G. Hunsperger, *Integrated optics, theory and technology*, Springer (2002).

[72] G. D. Boyd and D. A. Kleinman, *Parametric interaction of focused Gaussians Light Beams*, J. of Appl. Opt. **39**(8), 3597 – 3639 (1968).

Chapter 2

Nonlinear photonic crystal and fabrication process

2.1. Introduction

In this second chapter, we will specifically develop SHG theory in two-dimensional nonlinear photonic crystal (2D NLPC) particularly 2D PPLN. This study derived from the non linear theory in 1D NLPC seen in chapter 1. We will particularly see, how the nonlinear susceptibility change in this structure and how new QPM orders appears in the poled structure. Then, we will explain the fabrication process of periodically poled lithium niobate (LiNbO_3) for QPM applications especially for 2D-PPLN with a square poled lattice.

A second part deals with the existing fabrication process of optical waveguide in nonlinear materials with their advantages and their disadvantages. This will allow us to introduce the contribution of our used method on the realisation of optical waveguide by ion implantation. Then, we will develop our waveguide fabrication conditions in PPLN.

2.2. Second-harmonic generation in 2D nonlinear photonic crystals

Nonlinear photonic crystals (NLPC) in two dimensions have a periodic or quasi-periodic two-dimensional (2D) spatial distribution of $\chi^{(2)}$ whilst their linear susceptibility $\chi^{(1)}$ is homogeneous. For ferroelectrics crystals like LiNbO_3 or LiTaO_3 , the sign of the nonlinear coefficient are regularly inverted in order to create a lattice in two dimensions. Since the introduction of two-dimensional NLPC by Berger in 1998 [1], there has been a growing interest

in these structure and in their potential applications. Two-dimensional NLPC provides greater flexibility in the nonlinear frequency conversion processes in a single crystal. Such structures have been studied for non-collinear SHG [2 - 4], simultaneous conversion of multiple wavelengths [5], third- to fifth-harmonic generations [6 - 8], multistep cascaded conversions [9], conversion of broadband sources [10] and conversion for ultrashort optical pulses [11]. Several structure designs of 2D NLPC were proposed to achieve simultaneous phase matching of arbitrary conversion processes. Most of the analyses on NLPCs have focused on the QPM aspect using the analysis of the 1D case seen in the last section and employing reciprocal lattices to picture the QPM process. Thus, in this 2D structure, the non-collinear QPM aspect can be reduced as a scalar problem, which simplifies the notations.

2.2.1. Real Lattice

In the case of nonlinear crystal in one dimension, we have investigated the spatial distribution of $\chi^{(2)}$ with a periodic rectangular function which is approximated by a Fourier series (sum of sinus functions). In the case of 2D configuration, the $\chi^{(2)}$ distribution is represented differently. Apart from aperiodic lattices, there are five types of periodic two-dimensional non linear structures as shown in Fig. 2.1. in the real space: hexagonal, square, rectangular, centred-rectangular and oblique. In these configurations, we can define two primitive, non collinear vectors $\vec{\Lambda}_1$ and $\vec{\Lambda}_2$ and \vec{r}_{mn} the linear sum of these vectors, such as: $\vec{r}_{mn} = m\vec{\Lambda}_1 + n\vec{\Lambda}_2$, where m and n are real integer. Thus, the lattice can be represented as a distributed Dirac delta functions:

$$u(\vec{r}) = \sum_{m,n} \delta(\vec{r} - \vec{r}_{mn}) \quad (2.1)$$

In order to complete the real distribution of $\chi^{(2)}$ we have to convolve the real lattice distribution $u(\vec{r})$ with a suitable nonlinear optical motif delimitating the zone where the nonlinear coefficient is different comparing to the background. In the case of domain inverted ferroelectrics crystal, we consider an opposite sign of the nonlinear coefficient between the background and the motifs inner part.

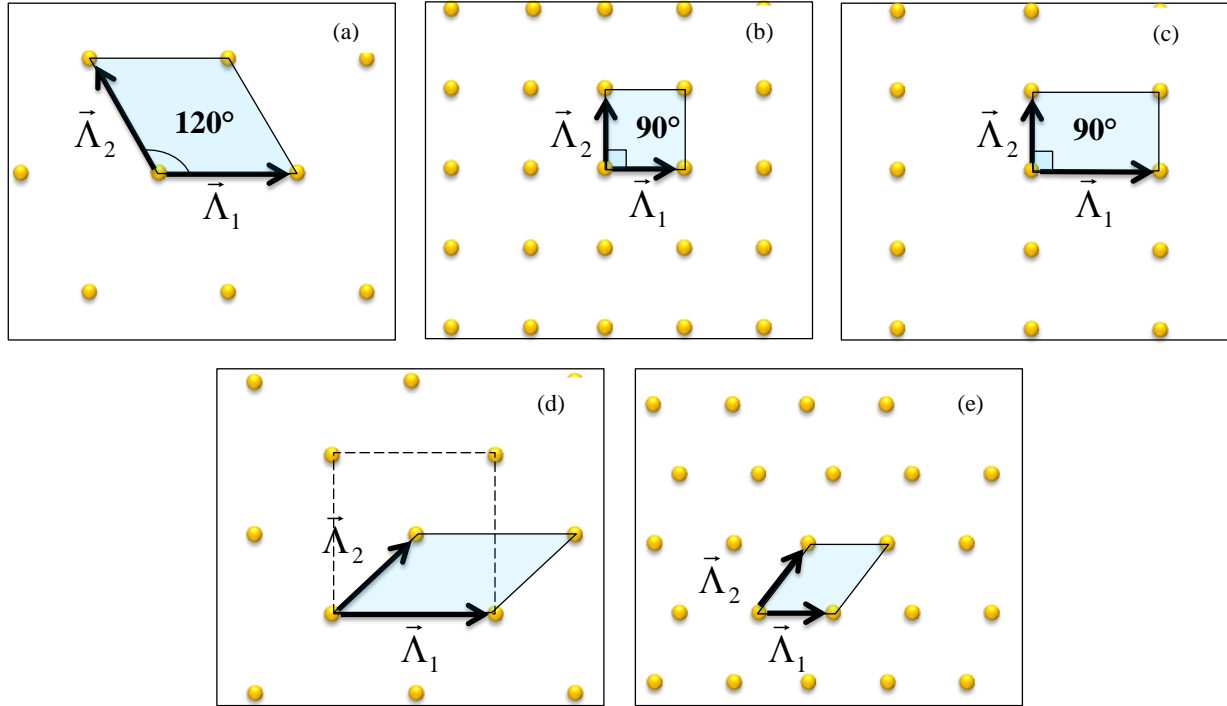


Figure 2.1: The different types of direct-space lattices are referenced (also called Bravais lattices): (a) Hexagonal, (b) Square, (c) Rectangular, (d) centred-rectangular, and (e) Oblique.

[12]

Different patterns can be used and were studied [12]. In our work we focus on the case of square motifs and circular motifs. The circular motifs are convenient approximation of hexagonal inversed domain which is widely adapted to NLPCs with ferroelectrics as lithium niobate and lithium tantalate as shown in Fig. 2.2. In the case of square motif, with a side length of R , the motif function is given by:

$$v_s(\vec{r}) = \text{rect}\left(\frac{x}{R}\right) \cdot \text{rect}\left(\frac{z}{R}\right) \equiv \begin{cases} 1 & |x|, |y| < R/2 \\ 0 & \text{elsewhere} \end{cases} \quad (2.2)$$

For a circular motif with a radius of R , the motif function is written:

$$v_c(\vec{r}) = \text{circ}\left(\frac{r}{R}\right) \equiv \begin{cases} 1 & r < R/2 \\ 0 & \text{elsewhere} \end{cases} \quad (2.3)$$

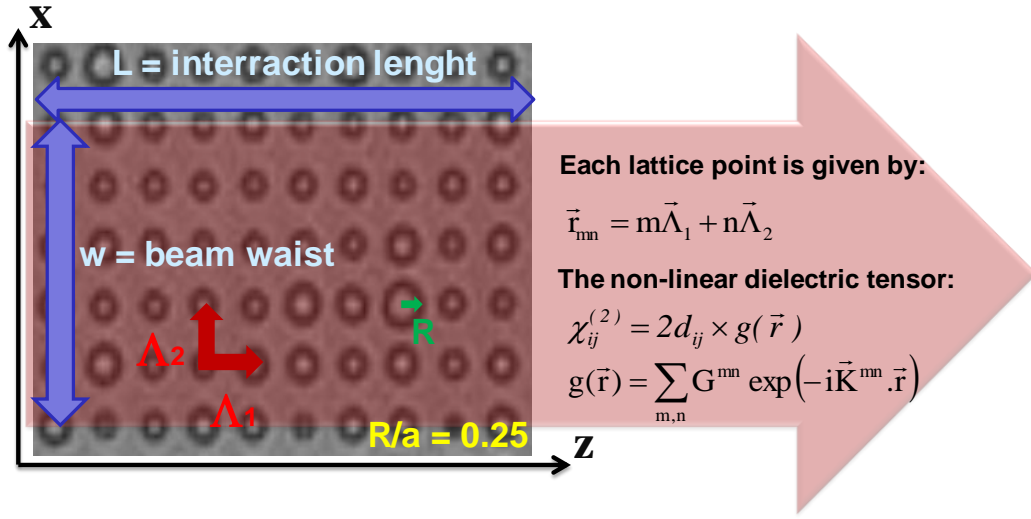


Fig 2.2: Representation of the $\chi^{(2)}$ lattice constants used in a set of distributed functions for a nonlinear photonic crystal in two dimensions.

Furthermore, the considered lattice area is restricted by the crystal physical size and by an effective interaction area where QPM is achieved. We assume that the “active” area function is rectangular (this is not valid for a nonlinear interaction with a Gaussian beam) with an interaction length L within the crystal and a width corresponding to the beam spot size. In that case, the area function is:

$$s(\vec{r}) = \text{rect}\left(\frac{z}{L}\right) \cdot \text{rect}\left(\frac{x}{w}\right) \quad (2.4)$$

The relevant Cartesian component of the nonlinear dielectric tensor as a function of position can be therefore expressed mathematically into a spatial nonlinear coefficient function:

$$\chi_{ij}^{(2)}(\vec{r}) = 2d_{ij} \cdot g(\vec{r}) = 2d_{ij} \cdot s(\vec{r}) \cdot [u(\vec{r}) \otimes v(\vec{r})] = 2d_{ij} \cdot \sum_{m,n} G_{mn} \cdot \exp(-i\vec{K}_{mn} \cdot \vec{r}) \quad (2.5)$$

where d_{ij} is the component of the nonlinear susceptibility tensor for the Cartesian indices i and j , \vec{K}_{mn} are the possible grating wave vectors (see the next section) and \otimes is the convolution operator. We have to express Eq. (2.5) in the Fourier space as it is developed for NLPC in one dimension.

2.2.2. Reciprocal lattice

From the reciprocal geometrical shape mentioned above, QPM can easily be observed according to multiple possible grating wave vectors. These so-called reciprocal lattice vectors (RLV) are linear solutions of the reciprocal primitive vectors $\vec{\kappa}_1$ and $\vec{\kappa}_2$ (defining the first Brillouin zone):

$$\vec{K}_{mn} = m\vec{\kappa}_1 + n\vec{\kappa}_2 \quad (2.6)$$

As such, real and reciprocal primitive vectors follow the orthogonality relation: $\vec{\Lambda}_i \cdot \vec{\kappa}_j = 2\pi\delta_{ij}$.

In that case, the phase mismatch function is now written by: $\Delta k'_{m,n} = \Delta \vec{k} - \vec{K}_{mn}$ (see Eq. (1.24)). In Figure (2.3), we see the potential reciprocal lattice vectors observed in a square lattice which can contribute to the SHG according to the phase mismatch function.

Thus, considering the presented lattice, we will develop the expression of the relevant (m, n) QPM order RLVs, and the corresponding Fourier coefficients which are important to estimate the interaction efficiency within the crystal.

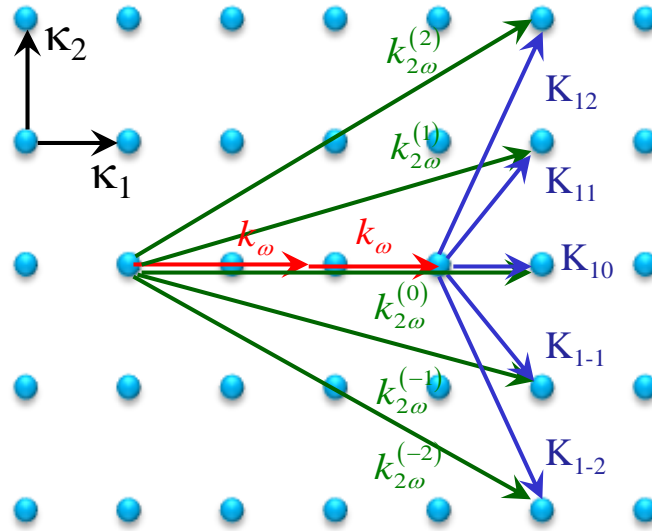


Figure 2.3: Representation of the phase mismatch function with different RLVs (blue arrows), in a square reciprocal lattice.

Denoting γ the angle between the two primitive vectors $\vec{\Lambda}_1$ and $\vec{\Lambda}_2$, we can define the general and the complete primitive system in the real and reciprocal lattice:

$$\vec{\Lambda}_1 = (\Lambda_1, 0), \quad \vec{\Lambda}_2 = (\Lambda_2 \cos \gamma, \Lambda_2 \sin \gamma)$$

$$\vec{\kappa}_1 = \frac{2\pi}{\Lambda_1} \left(1, -\frac{1}{\tan \gamma}\right), \quad \vec{\kappa}_2 = \frac{2\pi}{\Lambda_2} \left(0, \frac{1}{\sin \gamma}\right) \quad (2.7)$$

with $\Lambda_1 = \Lambda_2 = \Lambda$ and $\gamma = 90^\circ$ in a square lattice.

$$\vec{\kappa}_1 = \frac{2\pi}{\Lambda} (1, 0), \quad \vec{\kappa}_2 = \frac{2\pi}{\Lambda} (0, 1), \quad \text{and the norm of } \vec{K}_{mn}: \|\vec{K}_{mn}\| = \frac{2\pi}{\Lambda} \sqrt{m^2 + n^2}.$$

Furthermore, it is important to evaluate the conversion efficiency of the 2D lattice which depends on the calculated Fourier coefficients from Eq. (2.5). The general form is written by:

$$G_{mn} = \frac{1}{A_{UC}} \cdot G(\Delta\vec{k}) = \frac{1}{\Lambda^2} \cdot [U(\Delta\vec{k}) \otimes S(\Delta\vec{k}) \cdot V(\Delta\vec{k})] \quad (2.8)$$

with G , S , U , and V the two-dimensional Fourier transform of the direct lattice functions g , s , u and v respectively.

A_{UC} corresponds to the area unit cell with a relation $A_{UC} = |\Lambda_{1x}\Lambda_{2y} - \Lambda_{1y}\Lambda_{2x}|$. For a square lattice we get $A_{UC} = \Lambda^2$. By separating the ‘‘active’’ area contribution $G_s(\Delta\vec{k})$ and the lattice contribution $G_v(\Delta\vec{k})$ from the efficiency, we get:

$$G(\Delta\vec{k}) = G_s(\Delta\vec{k}) \cdot G_v(\Delta\vec{k}) \quad (2.9.a)$$

With:

$$G_s(\Delta\vec{k}) = \frac{(2\pi)^2}{\Lambda^2} \sum_{m,n} \delta(\Delta\vec{k} - \vec{K}_{mn}) \otimes Lw. \text{sinc}(\pi\Delta\vec{k}_z L) \cdot \text{sinc}(\pi\Delta\vec{k}_x w) \quad (2.9.b)$$

For the square motif:

$$G_{vs}(\Delta\vec{k}) = \frac{(2\pi)^2}{\Lambda^2} \sum_{m,n} \delta(\Delta\vec{k} - \vec{K}_{mn}) R^2 \text{sinc}(\pi\Delta\vec{k}_z R) \cdot \text{sinc}(\pi\Delta\vec{k}_x R) \quad (2.9.c)$$

For the circular motif:

$$G_{vc}(\Delta\vec{k}) = \frac{(2\pi)^2}{\Lambda^2} \sum_{m,n} \delta(\Delta\vec{k} - \vec{K}_{mn}) \frac{R}{\Lambda\sqrt{m^2+n^2}} J_1\left(\frac{\pi R}{\Lambda} \sqrt{m^2+n^2}\right) \quad (2.9.d)$$

With J_1 defined as the first order Bessel function.

Finally, Eq. (1.27) can be rewritten in two dimensions:

$$A_{SH}(L) = -\omega_{SH}\kappa A_{FF}^2 L d \left[\sum_{m,n} G_{mn} \exp\left(-i\left(\frac{\Delta k'_{z,mn}L}{2} + \frac{\Delta k'_{x,mn}W}{2}\right)\right) \text{sinc}\left(\frac{\Delta k'_{z,mn}L}{2}\right) \cdot \text{sinc}\left(\frac{\Delta k'_{x,mn}W}{2}\right) \right] \quad (2.10)$$

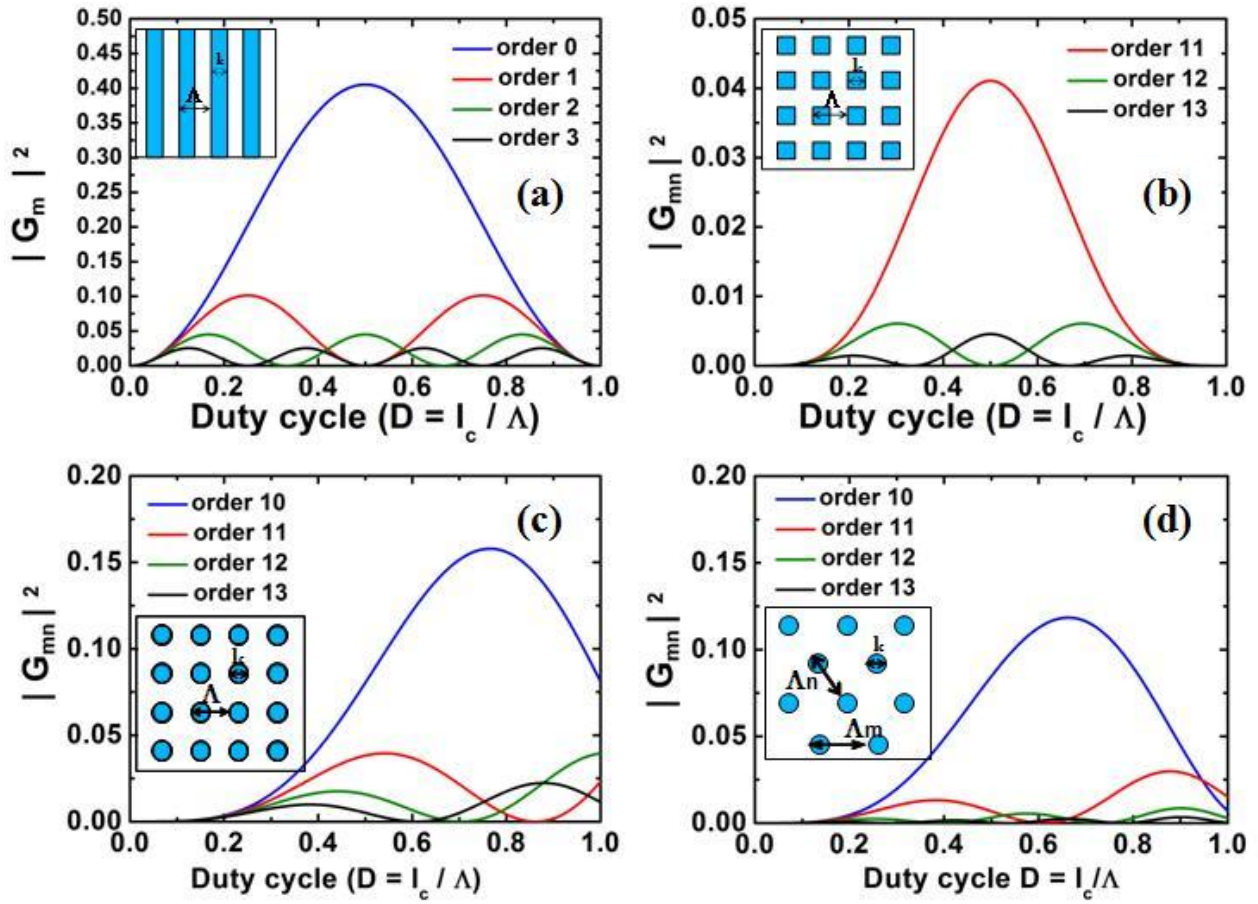


Figure 2.4: Dependence of the nonlinear coefficient $|G_{mn}|^2$ and thus the normalised efficiency with the duty cycle for the mn^{th} QPM order, (a) in NLPC 1D, (b) NLPC 2D with square motif and square lattice, (c) NLPC 2D with circular motif and square lattice, (d) NLPC 2D with circular motif and hexagonal lattice.

If we only consider the contribution of the Fourier coefficient G_v to the efficiency with a duty cycle $D = 2R/\Lambda$ and square motif, we have:

$$G_{mn} = 2 D^2 \text{sinc}(\pi m D) \cdot \text{sinc}(\pi n D) \quad (2.11)$$

In this configuration, it is observed that the QPM order (1, 0) is similar to the QPM order 0 in one dimension.

And for the circular motif, we find the expression:

$$G_{mn} = \frac{D}{\sqrt{m^2+n^2}} \cdot J_1(\pi D \sqrt{m^2 + n^2}) \quad (2.12)$$

With these motifs the efficiencies are simulated and presented in Fig.2.4. This simulation allows determining of dimensions and shape of the motif to optimise the efficiency.

	Square motif		Circular motif	
QPM order (m,n)	D	$\eta_{\text{QPM}}/\eta_{\text{BPM}}$	D	$\eta_{\text{QPM}}/\eta_{\text{BPM}}$
(1,0)	50	0.405	77	0.158
(1,1)	50	0.041	55	0.039
(1,2)	30/70	0.006	44/100	0.017/0.039
(1,3)	50	0.005	87	0.022

Table 2.1: Conversion efficiency rate between QPM and BPM considering the nonlinear coefficient constant for 2D – NLPC with square and circular motifs.

In Fig.2.4, we choose four specific QPM orders in each lattice: (m =1, n = 0, 1, 2, 3) , and we compare these results with those obtained in the 1D case. The first QPM order is generally the most efficient in a 2D structure. For instance, in the 1D case (m = 1) and the 2D case with square motif (m = 1, n = 0), which have the same expression of the efficiency; we find that the

maximum efficiency is 0.405 when $D = 0.5$ for perfect phase matching. Concerning the lattice with circular motifs, the results are very different: for $D = 0.766$ the maximum efficiency is reached at 0.158. We summarise results in the Table 2.1. It is also seen that the maximum efficiency tends to decrease more slowly when the QPM order n increase in the case of lattice with circular motif which is finally the closest model of our samples.

The efficiency is also calculated considering hexagonal lattice with circular motif. In this case, the angle between the two primitive vectors is $\gamma = 120^\circ$ and $\Lambda_1 = \Lambda_2 = \Lambda$. The expression of the Fourier coefficient is:

$$G_{mn} = \frac{D}{\sqrt{m^2+n^2+mn}} \cdot J_1\left(\frac{2\pi}{\sqrt{3}}D\sqrt{m^2+n^2+mn}\right) \quad (2.13)$$

As can be observed in Fig. 2.4(d), the maximum efficiency of 0.118 is achieved at the QPM order ($m = 1, n = 0$) when $D = 0.66$. In general, the calculated magnitude has lower value than one in square lattice. In this case, we conclude that the rectangular lattice is the most efficient structure, providing a higher efficiency than hexagonal lattice.

In this study, a square lattice samples with a circular motif and a duty-cycle close to 50% is chosen. This configuration is very interesting and can provide at least 2 or 3 QPM orders. This theoretical approach will help us to interpret our experimental results in chapter 3, particularly to compare the conversion efficiencies of the different QPM orders in our 2D NLPC.

2.2.3. Angular tuning

We now study the QPM condition depending on the angle between the grating vector \vec{K} and the fundamental wave vector \vec{k}_{FF} . We will compare the angular dependence to the extraordinary refractive index one in a BPM device. In this section we will also see how the different phase matching conditions are satisfied in 2D NLPCs according to the $\chi^{(2)}$ structure in crystals. Furthermore, this will allow us to calculate the angular bandwidth as studied in the previous sections for wavelength and temperature.

First, we consider the phase matching case, with the geometry indicated in the wave vector diagram of Figure 2.5(a). In the figure, θ is the angle between the fundamental wave vector \vec{k}_{FF} and the periodic wave vector \vec{K} . For the sake of ease, we use \vec{K} and rather than \vec{K}_{mn} to indicate

the spatial harmonic contributing to the QPM. Ψ is the angle between \vec{k}_{FF} and the wave vector of the second harmonic wave \vec{k}_{SH} . Following the law of sines we find the angle relation:

$$\sin \Psi = \frac{\|\vec{K}\|}{\|\vec{k}_{SH}\|} \sin \theta \quad (2.14)$$

When the fundamental wave vector is not parallel to the structure wave vector ($\theta \neq 0$), a “walkoff” of SHG ($\Psi \neq 0$) can be observed. Note that in the case of an isotropic medium n_{FF} and n_{SH} do not depend on the angle.

For a fundamental wavelength λ_{FF} , we can use the law of cosines in order to find the angular dependence of a NLPC (Eq. 2.14) and the period required for mn^{th} order QPM (Eq. 2.14):

$$\|\vec{K}_{mn}\|^2 = \|2\vec{k}_{FF}\|^2 + \|\vec{k}_{SH}\|^2 - 2\|2\vec{k}_{FF}\| \cdot \|\vec{k}_{SH}\| \cos \Psi \quad (2.15)$$

$$\|\vec{k}_{SH}\|^2 = \|2\vec{k}_{FF}\|^2 + \|\vec{K}_{mn}\|^2 + 2\|2\vec{k}_{FF}\| \cdot \|\vec{K}_{mn}\| \cos \theta \quad (2.16)$$

From Eq. (2.15) we can determine the “walkoff” angle Ψ between the fundamental and the harmonic wave vectors for the mn^{th} order QPM within the crystal:

$$\Psi_{mn} = \arccos \left[\frac{\left(\frac{\|\vec{K}_{mn}\| \lambda_{FF}}{4\pi} \right)^2 - (n_{SH}^2 + n_{FF}^2)}{2n_{SH}n_{FF}} \right] \quad (2.17)$$

Moreover, we can write Eq. (2.15) in the form of the nonlinear Bragg’s law which is generalised for nonlinear optics of Bragg’s law such as:

$$\lambda_{FF} = \frac{2\pi}{n_{SH} \|\vec{K}_{mn}\|} \sqrt{(n_{SH} - n_{FF})^2 + 4n_{SH}n_{FF} \sin^2 \frac{\Psi}{2}} \quad (2.18)$$

If the medium has no dispersion ($n_{SH} = n_{FF}$), Eq. (2.18) gives the resonant scattering direction by a periodic set of scatterers:

$$\lambda_{FF} = \frac{4\pi}{\|\vec{K}_{mn}\|} \sin \frac{\Psi}{2} = 2d \sin \frac{\Psi}{2} \quad (2.19)$$

where d is the period between two planes of scatterers. We presume that the direction of propagation is subject to the Huyghens-Fresnel principle, giving the phase relation between the scatterers.

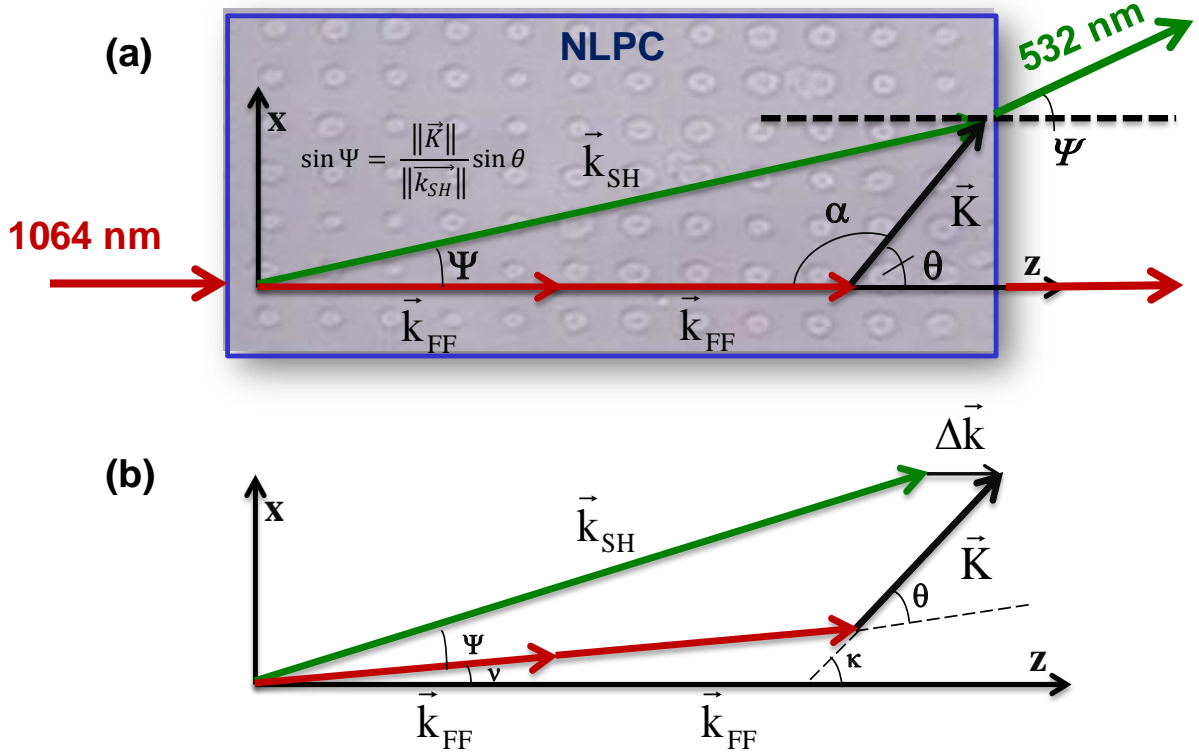


Figure 2.5: Wave vector diagram for QPM angle tuning analysis in the phase matched case (a) and the non phase matched case (b).

For 2D NLPC, using Snell's law (the refractive index of air is considered as 1) and Eq. (2.17) we can predict the numerous far-field SHG “walkoff” angles ψ from the interface crystal/air traversed by the SHG wave.

$$\psi_{mn} = \arcsin \left[n_{SH} \cdot \sqrt{\frac{(n_{SH} - n_{FF})^2 - \left(\frac{\|\vec{K}_{mn}\| \lambda_{FF}}{4\pi} \right)^2}{2n_{SH}n_{FF}}} \right] \quad (2.20)$$

In the last section, we have studied the case of a 2D NLPC with a square lattice and the periodic wave vectors norms $\|\vec{K}_{mn}\|$. Thus, we have calculated the angular distribution of the SHG signal obtained from a sample with a square lattice and a period of $\Lambda = 6.92 \mu\text{m}$ at different temperatures and with the temperature dispersion of n_{FF} and n_{SH} (Figure 1.3(a)).

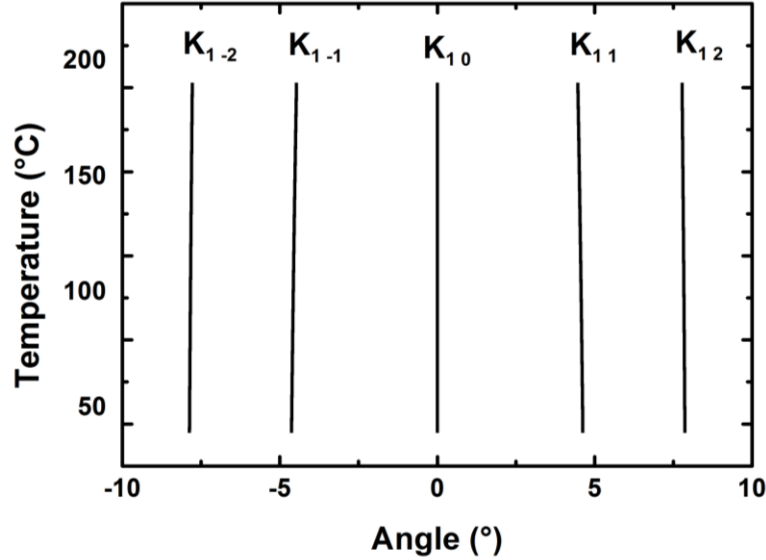


Figure 2.6: Calculated angles of the SHG signal for each RLV, obtained from a sample with a square lattice and a period of $\Lambda = 6.92 \mu\text{m}$.

From Eq. (2.20), the calculated angles at 60°C which is the optimal crystal temperature of RLV \mathbf{K}_{10} for QPM are 0° for \mathbf{K}_{10} , $\pm 4.58^\circ$ for $\mathbf{K}_{1\pm 1}$ and $\pm 7.86^\circ$ for $\mathbf{K}_{1\pm 2}$. At 120°C which is the optimal temperature of RLV $\mathbf{K}^{1\pm 1}$ for QPM we find $\pm 4.53^\circ$ for $\mathbf{K}_{1\pm 1}$ and $\pm 7.82^\circ$ for $\mathbf{K}_{1\pm 2}$. It is clearly seen from these angles that the temperature dispersion of the refractive index has quite no influence on the angle dispersion.

By the same way, Eq. (2.15) can be rewritten according to θ , resolving Eq. (2.16) and taking $\|\vec{K}_m\|$ as unknown:

$$\|\vec{K}_{mn}\|^2 + 2 \cdot \|2 \cdot \vec{k}_{FF}\| \cdot \|\vec{K}_{mn}\| \cos \theta + \|2 \cdot \vec{k}_{FF}\|^2 - \|\vec{k}_{SH}\|^2 = 0 \quad (2.21)$$

From the condition of the side – side angle congruence ambiguity in geometry we can deduce from Eq. (2.21) two solutions for $\|\vec{K}_{mn}\| \sin \theta < \overrightarrow{k}_{SH} < 2 \cdot \overrightarrow{k}_{FF}$ or just one solution for $2 \cdot \overrightarrow{k}_{FF} < \overrightarrow{k}_{SH}$ which correspond to our QPM situation.

$$\|\vec{K}_{mn}\| = \frac{4\pi}{n_{FF}\lambda_{FF}} [\sqrt{(n_{SH})^2 - (n_{FF} \sin \theta)^2} - n_{FF} \cos \theta] \quad (2.22)$$

Thus, Eq. (2.22) leads to the determination of the period for the m th order QPM away from normal incidence of the fundamental input beam with the periodic structure. This is equivalent to adapt $\|\vec{K}_{mn}\|$ for an optimal QPM by turning the NLPC, or even by achieving new QPM conditions by tuning fundamental wavelength or crystal temperature.

2.2.4. Angular acceptance

We now determine the angular acceptance bandwidths of the FF source in a square lattice NLPC represented in Fig 2.5.(b), assuming the refractive index as isotropic. The fundamental wave vector \overrightarrow{k}_{FF} lies in the $x - z$ plane at an angle ν . The grating wave vector is at angles θ and κ with respect to \overrightarrow{k}_{FF} and the z -axis, respectively. The SHG wave vector \overrightarrow{k}_{SH} propagates at an angle Ψ with respect to \overrightarrow{k}_{FF} . For $\theta \neq 0$ the situation is analogous to critical phase matching where the fundamental wave is not collinear to the grating wave vector. According to Eq. (1.35) we need to know $\Delta\nu_{FWHM}$ precisely to evaluate the angular acceptance bandwidth and its coherence length dependence. With the assumed geometry, we define $\Delta\vec{k} = \Delta k \cdot \vec{z}$ and the boundary conditions for the SHG require:

$$k_{SH,x} = 2k_{FF,x} + K_{mn,x} \quad (2.23.a)$$

$$\Delta k = k_{SH,z} - 2k_{FF,z} - K_{mn,z} \quad (2.23.b)$$

From the derivation of Eq. (2.23.b) with respect to ν , replacing $\partial_\nu k_{SH,x} = -k_{SH,x}$ from Eq. (2.23.a), considering Eq. (2.14), and the angle $\theta = \kappa - \nu$ with $\theta \neq 0$ we find:

$$\partial_\nu \Delta k = -\frac{2k_{FF} \sin \Psi}{\cos(\nu + \Psi)} \quad (2.24)$$

Finally, we get from Eq. (2.23):

$$\delta\nu = \frac{5.5657}{L} |\partial_\nu \Delta k|^{-1} = \frac{5.5657 \cdot \cos \nu}{2\pi\sqrt{m^2+n^2} \cdot \sin(\kappa-\nu)} \frac{\Lambda}{L} \left[1 + \frac{\cos(\kappa)}{\nu} \frac{m\lambda_{FF}}{2\Lambda n_{FF}} \right] \approx \frac{5.5657 \cdot \cos \nu}{2\pi\sqrt{m^2+n^2} \cdot \sin(\kappa-\nu)} \frac{\Lambda}{L} \quad (2.25)$$

If we approximate the following form by assuming $\Lambda \gg \lambda_{FF}$ and $\theta = \kappa - \nu \neq 0$

$$\Delta\nu_{FWHM} = \frac{5.5657}{2\pi\sqrt{m^2+n^2} \cdot \sin\theta} \frac{\Lambda}{L} |\cos \nu|_{\nu=\nu_{1/2}} \quad (2.26)$$

From Eq. (2.26) we see that for critical phase matching the pump angular bandwidth is inversely proportional to the number of domains $N = 2L/\Lambda$. In 2D NLPC, we can also see that when the n th QPM order increases (with $n \neq 0$), θ increases, so the angular acceptance bandwidth of the fundamental input source decreases with n .

In the case where $\theta \rightarrow 0$, we have $\nu \rightarrow \kappa$. We have to develop Eq. (1.35) to the second order term of the Taylor series as Δk has no first order dependence on ν . In the case that the fundamental beam is quite collinear to the RLV \mathbf{K}_{10} , we obtain the angular acceptance bandwidth for non-critical phase matched interaction, as:

$$\delta\nu = 2\sqrt{\frac{5.5657}{L} |\partial_\nu^2 \Delta k|^{-1}} \quad (2.28)$$

Finally, with the same approximation made in Eq. (2.27), we have:

$$\Delta\nu_{FWHM} \approx 2,66 \sqrt{\frac{n_{SH}}{n_{FF}} \frac{l_c}{L} |\cos \nu|_{\nu=\nu_{1/2}}} \quad (2.29)$$

It is seen that the pump angular bandwidth depends inversely on the square root of the device length, resulting in a great enhancement of the angular bandwidth when $\theta \rightarrow 0$. Fig 2.7 presents the theoretical angular dependence of conversion efficiency for the same NLPC studied in Fig. 1.7 and Fig. 1.8. The configuration corresponds to a fundamental wave vector which is collinear to the grating wave vector with the given mn^{th} QPM order. At a fixed fundamental wavelength, the theoretical angular dependence of conversion efficiency is given by:

$$\eta_\nu = \text{sinc}^2 \left[\left[\frac{4\pi}{\lambda_{FF}} (n_{SH} - n_{FF}) - \frac{2\pi\sqrt{m^2+n^2} \cdot \cos \nu}{\Lambda} \right] \cdot \frac{L}{2} \right] \quad \text{when } \theta \rightarrow 0, \quad (2.30)$$

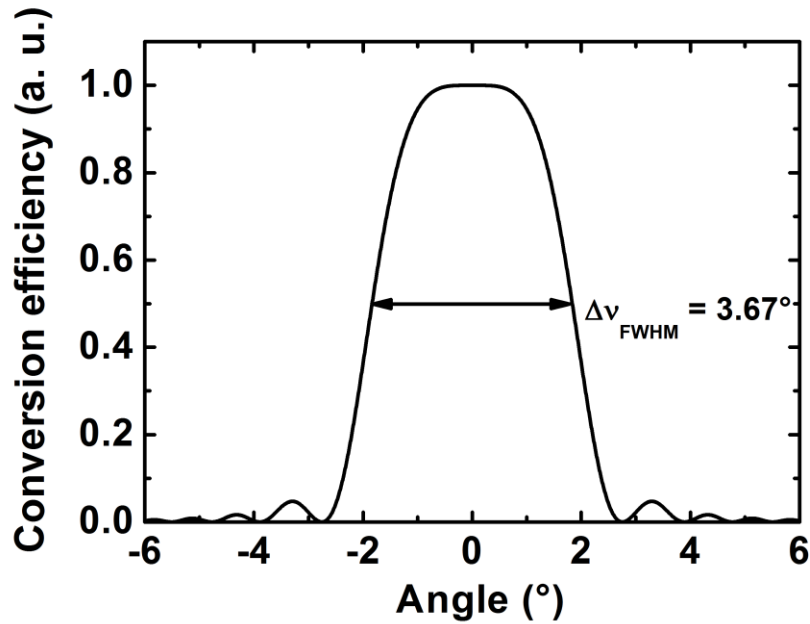


Figure 2.7: Theoretical angular acceptance (ν) for $(1, 0)$ QPM order and the angular acceptance bandwidth of 6 mm long 2D periodically-poled lithium niobate (PPLN) with $\lambda_{FF} = 1064$ nm, $T = 53$ °C and $\Lambda = 6.92$ μm .

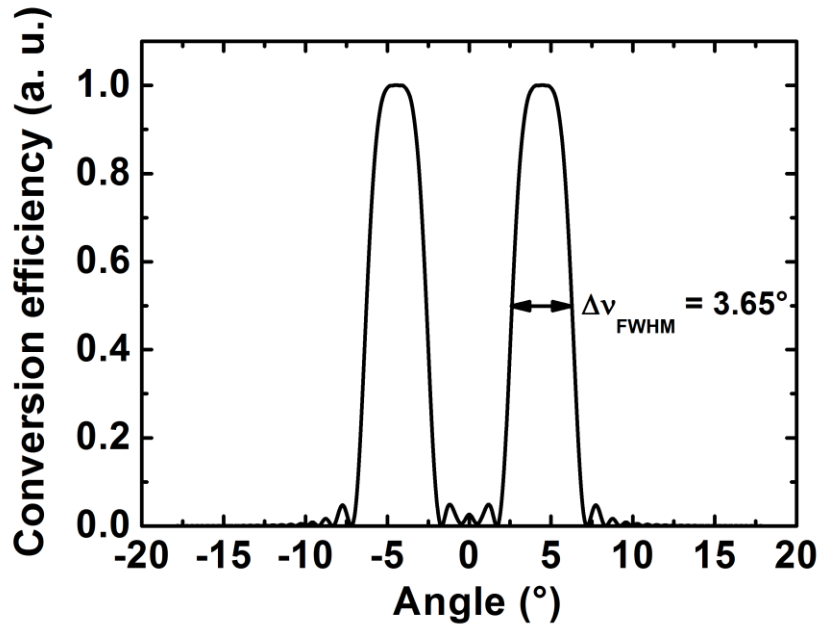


Figure 2.8: Theoretical representation of angular acceptance (ν) for $(1, \pm 1)$ QPM order and the Calculated angular acceptance bandwidth of 6 mm (see Eq. 2.30) long PPLN nonlinear photonic crystal with $\lambda_{FF} = 1064$ nm, $T = 195.1$ °C and $\Lambda = 6.92$ μm .

In Fig. 2.7, the fundamental wave vector \vec{k}_{FF} is collinear with $(\mathbf{1}, \mathbf{0})$ QPM order RLV \vec{K}_{10} . η_ν can reach its maximum value when ν is equal to zero. And the bandwidth $\Delta\nu_{FWHM}$ can be calculated from Eq. (2.30).

Figure 2.8 shows the theoretical angular dependence of the conversion efficiency when the fundamental wave vector is not collinear with the m th QPM order grating wave vector ($\theta \neq 0$). In this case, the theoretical angular dependence of conversion efficiency is given by:

$$\eta_\nu = \text{sinc}^2 \left[\left[\frac{4\pi}{n_{FF}\lambda_{FF}} \left[\sqrt{(n_{SH})^2 - (n_{FF} \sin \theta)^2} - n_{FF} \cos \theta \right] - \frac{2\pi\sqrt{m^2+n^2} \cdot \cos(\nu + \Psi_{mn})}{\Lambda} \right] \cdot \frac{L}{2} \right] \quad (2.31)$$

The parameters used in Fig. 2.8 are the same as those used in Fig. 2.7, with the same interaction length. The FWHM is almost the same as one in Fig. 2.7. We see that η_ν reaches its maximum value when $\nu + \Psi_{mn}$ is equal to zero with Ψ_{mn} given by Eq. (2.31).

In this section, it has been shown that the SHG in 2D-NLPC depends on new parameters according to the geometry of the lattice. The two-dimensional QPM orders create new conditions for non-collinear SHG. The conversion efficiency for optical intensity includes the effects of lattice, motif, and QPM order. From the theory, it has been shown that square lattice allows higher efficiency. Moreover, the non-collinear interaction set an angular dependence of the SHG which is important to estimate. A general analysis of conversion efficiency has been also presented according to the angular acceptance. This analysis is particularly important to establish the SHG tolerance of the crystal in a 2D lattice and understand the angular tuning in this kind of structure.

Once the structure defined, the next section is focused on the fabrication of our NLPC according to these parameters.

2.3. PPLN Fabrication process

The PPLN samples have been realised at the Graduate Institut of Photonics and Optoelectronics (GIPO) of National Taiwan University. We have realised a lattice of metallic electrodes by lift-off process. It is also possible to realise electrodes by wet etching with acid.

The following improved poling process has been realised:

- Samples preparation.

The sample surface is around 1 cm^2 with a thickness of 1 mm. We have performed a chemical cleaning: the sample is degreased with an ultrasonic bath of acetone during 3 min, then deionised water bath during 3 min, then ultrasonic bath of methanol. Finally, the sample is dried with nitrogen.

- Photolithography.

We use positive photo resist Shipley 18/13. The Shipley deposition is made on z+ face of the crystal by spin coating in two steps: 1000 rotations per second during 10 second then 4000 rotations per second during 40 seconds. At this rotation velocity, the Shipley is deposited to a thickness of around $1.2 \mu\text{m}$. After this stage, the sample is being heated at 115°C on a hot plate (soft back) during 2 minutes. Then, the sample is air-cooled during few minutes in order to avoid thermal shocks. The sample is UV insulated with a mercury lamp behind an optical mask in order to lithography the photo resists lattice. The exposure time depends on the pattern size. For the realisation of a lattice with a periodicity of $\sim 6.9 \mu\text{m}$ the exposure time is 5 seconds. This parameter is even shorter that reflections on the opposite face of the crystal can over-insulated the Shipley. The feel factor quality highly depends on that exposure time. We have put our sample in a solution of microposit MF-319 developer during 40 seconds. Then, the sample is directly cleaned with deionised water. The result is shown in Fig. 2.9. We observe that at low periodicity, the pattern resolution remains excellent and correspond to our mask.

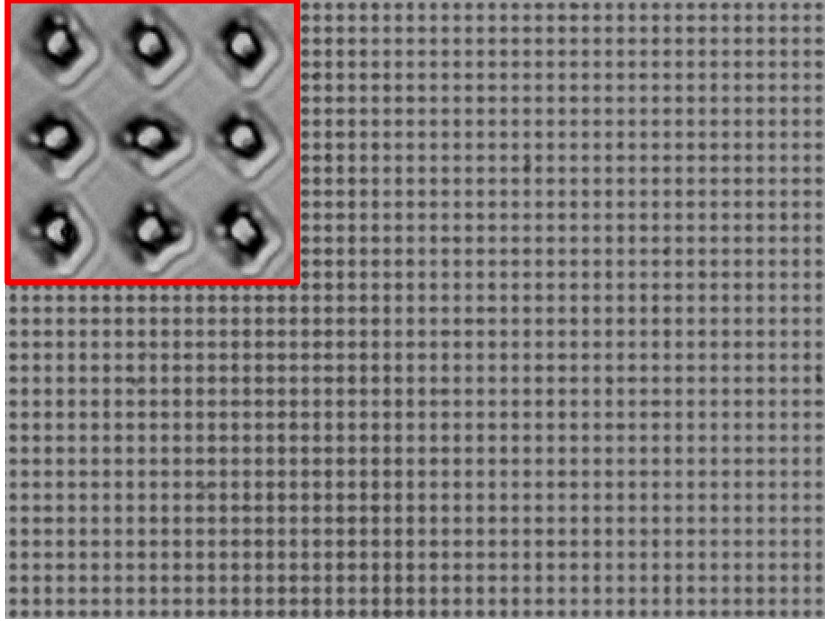


Figure 2.9: Example of photo resist lattice. The periodicity of holes is $6.92 \mu\text{m}$.

- Realisation of electrodes lattice.

Once the structure determined by photo-lithography, the metal is directly sputtered on the resin mask. The metal directly in contact with crystal forms the electrodes. We have sputtered 200 nm to 300 nm of titanium on the photo resist lattice. The metal part that is not covered by the photo resist (in direct contact with the substrate) will form the electrodes. We can complete the lift-off by dissolving the photo resist with acetone. However, this step is not necessary as the photo resist thickness is sufficient to block the poling current. An additional step is to over-coat the metallised z+ face with an insulator (generally with photo resist or spin-on glass). An opening of $1 \times 6 \text{ mm}$ in the insulator is created to allow the contact between electrodes and electrolytes.

- High voltage poling step.

The poling dispositive includes a poling cell holding the sample between two o-ring contacts. The whole is immersed in a liquid electrode (tap water) used as contact. Note that experimental outcomes are not dependant on the choice of electrolyte comparing to metallic contact [12]. It is just necessary to ensure the absence of air bubbles, which can cause point effect and break the sample. Moreover, a metallic contact would provide local heating with the increased resistance at high voltage.

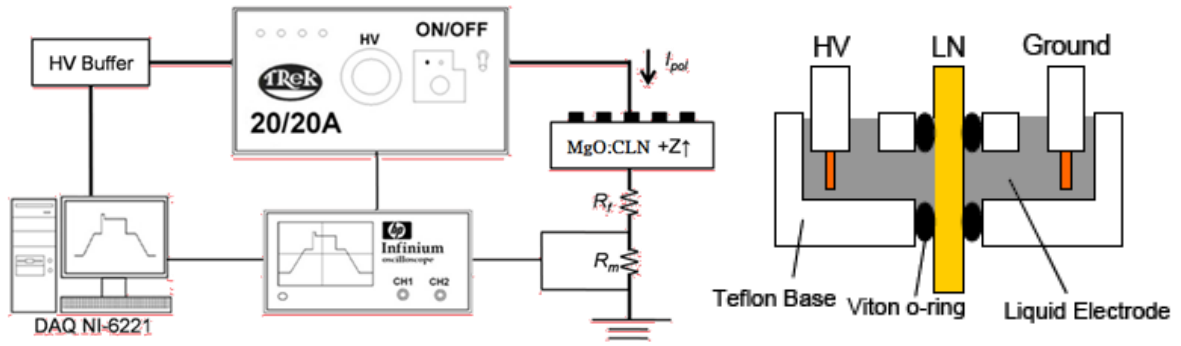


Figure 2.10: High voltage poling system with a detailed scheme of the sample holder.

The applied voltage is directly recorded by an oscilloscope and the poling current I_{pol} through the wafer is calculated from the measured voltage across the monitoring resistor $R_m = 4.7 \text{ k}\Omega$ as such as:

$$I_{pol} = \frac{V_{measure}}{R_m} \quad (2.32)$$

A current limiting resistor $R_f = 3 - 150 \text{ M}\Omega$ is used in order to protect the circuit transmitting the current.

During the poling process, the corresponding applied voltage (the blue line in Fig. 2.12) has gradual ramps at the beginning and the end of the process. This waveform has been chosen in order to maximise the duty cycle uniformity (maximise the number of nucleation sites for the poling initiation) and avoid domains to flip back in the back-switching process at the end. The poling duration is of around 50 ms with a sharp increase and decrease of the applied voltage to the corresponding coercive field (depending on the thickness of the sample). The poling current (the red line in Fig. 2.12) is recorded by oscilloscope at this duration. This measurement gives information on the domain wall velocity according to the method of Miller and Savage [13].

The same procedure may be repeated few times until a design is obtained that achieves the desired domain duty cycle. In fact, as the domain duty cycle is proportional to the delivered charge in the sample, the accumulated charge is calculated by integrating the poling current with time. This value has been experimentally determined at $20 \text{ }\mu\text{C}$.

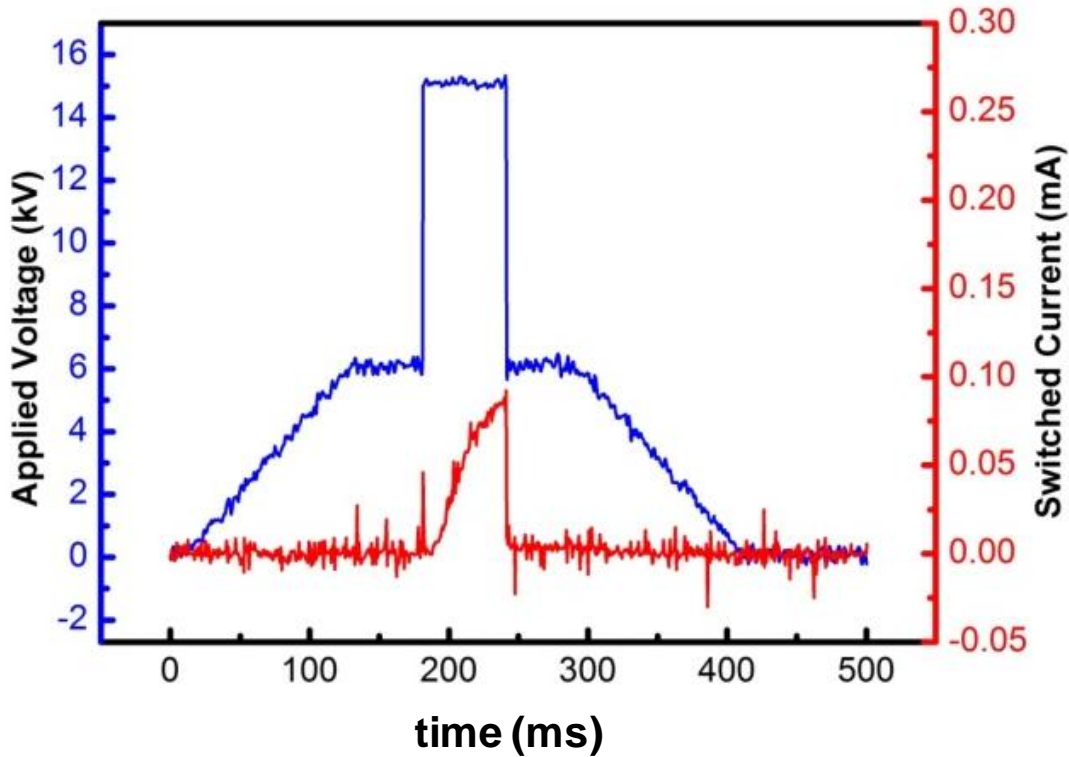


Figure 2.12: Poling current according to the applied voltage for LiNbO_3 during poling step. It is often necessary to repeat the operation several time in order to get a sufficient coalescence of the domain wall.

It is important to note that the thickness of the bulk is limited at $500 \mu\text{m}$ to 1 mm . In fact, at higher thicknesses, the electrical field periodicity created by electrodes disappears and become homogeneous. Furthermore, the poling thickness is even lower than the period is small.

- Revelation of PP structures.

After the poling step, the sample is cleaned with acetone, and deionised water. The domain pattern is revealed by hydrofluoric acid etching (HF) during 30 seconds and then abundantly rinsed with cold water. Chemical etching using HF acid is well known to selectively etch the z- crystalline face, with no effect on the z+ face. The chemical reaction goes fast and do not change after a while.

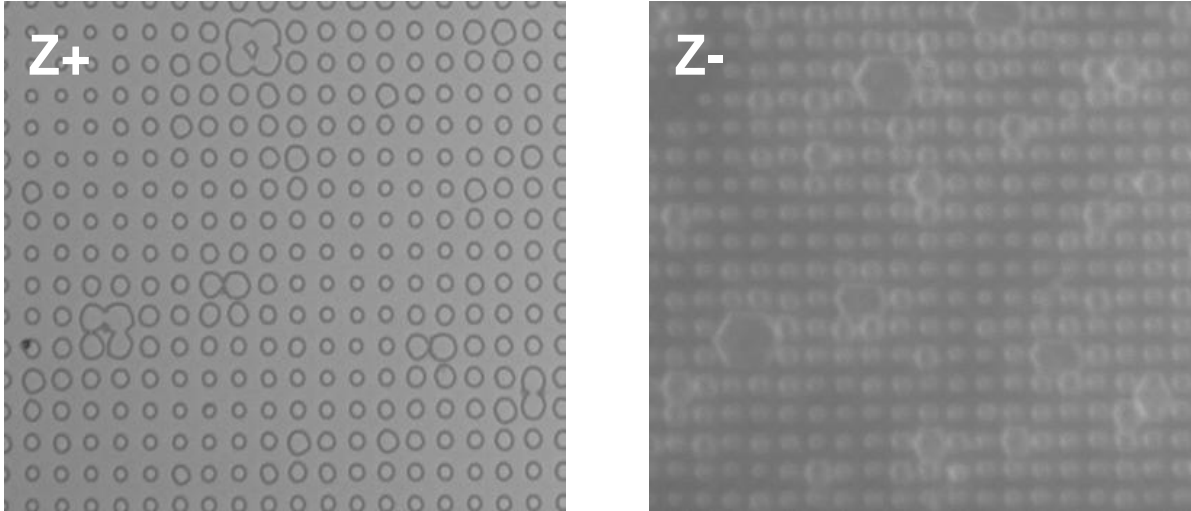


Figure 2.13(a): z+ and z- periodically-poled surfaces of congruent 2D-PPLN with a square lattice period of $6.92 \mu\text{m}$ revealed by chemical etching.

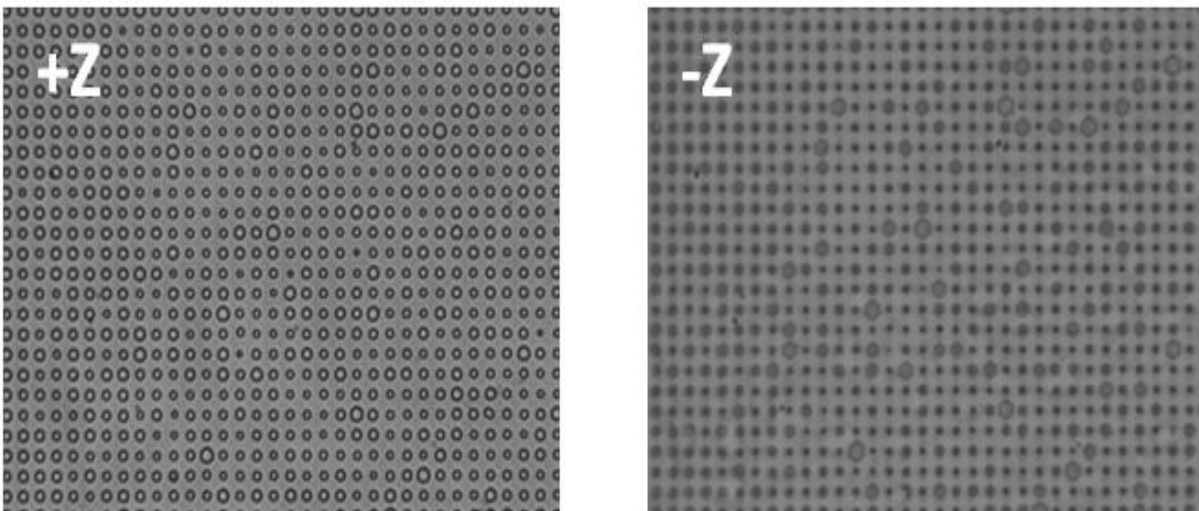


Figure 2.13: z+ and z- periodically-poled surfaces of doped MgO:PPLN with a square lattice period of $6.96 \mu\text{m}$ revealed by chemical etching.

The domain uniformity and the PP structuration are finally inspected with a microscope. For instance, an obtained poled area with congruent lithium niobate is shown in Fig. 2.13. The poled area is $6 \text{ mm} \times 6 \text{ mm}$ at the centre of the sample and the thickness of the ample is 1 mm . Figure 2.13 indicates both z+ and z- faces of the poled region with a 2D square lattice with a period of $\Lambda = 6.92 \mu\text{m}$ and a duty cycle of 50%. This square lattice period is particularly chosen to obtain QPM for SHG at 1064 nm .

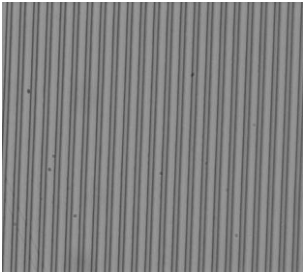
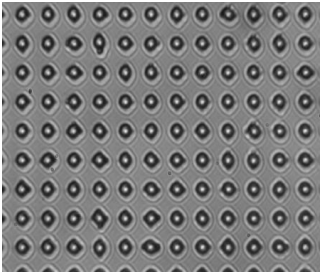
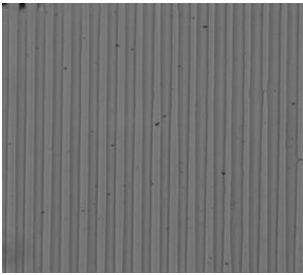
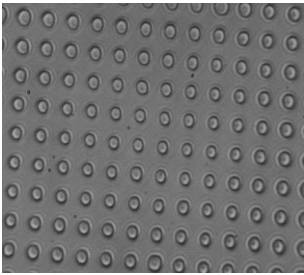
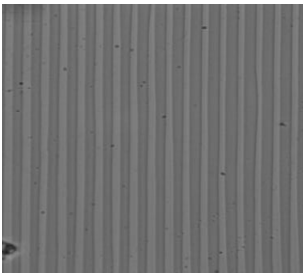
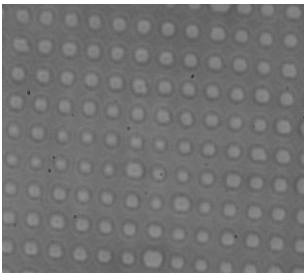
	PPLN 1D	PPLN 2D
After photolithography		
Photoresist	S1813	S1813
UV exposition	20 s	20 s
Developer	MF319	MF319
Period domain	6,79 μm (electrode width versus electrode period=1:3)	6,92 μm (electrode width versus electrode period=1:3)
After poling etching (z+ face)		
After poling etching (z- face)		
Poling condition	Applied voltage 16 kV	Applied voltage 16 kV
accumulation charge	38,9 μC	20,3 μC

Table 2.1: Summary of the poling conditions for congruent 1D-PPLN and 2D-PPLN.

2.4. Fabrication of waveguides

In this section, the most commonly used fabrication techniques of optical waveguides in LiNbO_3 are reviewed. Diffusion processes such as out-diffusion of lithium oxide from the crystal surface, in-diffusion of metals, ion exchange and proton exchange, and finally ion implantation are analysed. Planar and stripes dielectric waveguides can be fabricated on LN using these various technological processes. Waveguide fabrication techniques aim at creating a local variation of refractive index with a graded or a step profile.

There are two distinct methods to realise waveguides:

- By locally changing the structure of the material. Using this method the refractive index of the substrate surface can be modified. Thus. Ionic diffusion, ionic exchange and ionic implantation are different techniques illustrating this method.
- By depositing a thin layer with a higher refractive index than the substrate such as epitaxy methods, chemical vapour deposition (CVD) or sol-gel method.

Most of the reported works focus on LiNbO_3 , LiTaO_3 , KTP, which are widely used because of their good performance in nonlinear optics. These materials are available as transparent crystal with excellent electro-optical and acousto-optical properties. Therefore, they are commonly used for several active integrated optoelectronics devices such as modulators, switches, polarisation controllers and ring resonators.

2.4.1. Ionic diffusion technique

The first waveguides on LiNbO_3 and LiTaO_3 were developed by using out-diffusion which simply consists in heating the material at a temperature of about 1000 - 1100°C in vacuum or oxidizing ambient. At this temperature, lithium oxide is taken off (out-diffused) from the surface with a slight increase of the extraordinary index ($\Delta n_e = 0.005$) [14]. In fact, LiNbO_3 can crystallise in the slightly non-stoichiometric form $(\text{Li}_2\text{O})_y (\text{Nb}_2\text{O}_5)_{1-y}$. Although the ordinary index is not affected as Li_2O is removed from the crystal surface and the extraordinary index increases approximately linearly as y decreases. This process also depends strongly on crystal orientation and the parameters of diffusion and vaporisation processes at the out-diffusion temperature. However, this technique has not become popular in favour of the diffusion of

metals or exchange proton. The different reasons are: the Curie temperature lies between 1100 - 1180°C so the depolarisation of the crystal could occur except when y is in the $0.48 < y < 0.50$ range, the out-diffusion process can produce optical waveguides of thickness of the order of 10 μm , with a large effective width which may limit the operation of integrated optoelectronic devices based on LiNbO_3 .

The thermal diffusion of metal such as Mg, Ni, Zn, Fe, Co, Cr, Ti, V for the elaboration of waveguides on LiNbO_3 is more interesting because it allows a much higher index contrast ($\Delta n = 0.02$) for both polarisations. Thin films (10 - 100 nm) of metal are first deposited on the crystal surface by vacuum evaporation or sputtering. The diffusion process occurs at high temperature (850 to 1150 °C) in inert or reactive atmosphere, with activation energy typically in a range of 1.0 – 3.0 eV during few hours [15]. The diffusion of divalent metallic atoms such as Ni, Zn and Mg causes a reduction of the extraordinary index. The ordinary index also decreases when Ni or Zn diffuses. When trivalent or tetravalent atoms (Fe, Cr, and Ti) diffuse into LiNbO_3 , both n_o and n_e increase. While divalent atoms are substitution of lithium atoms tri- or tetravalent atoms are substitutional of Nb in the LiNbO_3 crystal lattice.

The study of titanium in-diffusion into lithium niobate has received much attention because Ti yields a good light confinement with a relatively large increase of n_o and n_e ($\Delta n_e < 0.04$, $\Delta n_o < 0.02$) [16], with a Gaussian profile. Consequently, this technique allows the fabrication of optical waveguides supporting both TE and TM modes. Sugii *et al.* [17] suggested that the refractive index change is due to the increase of polarisability, and the photoelastic effect caused by the different size of Ti and Nb ions. Naitoh *et al.* [18] demonstrated the relationships between the surface index change, the diffusion depth and fabrication conditions.

Titanium is more widely used because of the easy to deposit of a thin layer, its weak absorption in both visible and IR ranges and its high diffusion coefficient. The formation of low-loss ($< 1 \text{ dB/cm}$) slab and stripe waveguides by this technique has extensively been investigated since it was first used in 1974 [19]. Furthermore, the waveguide do not show significant photorefractive effect. At visible wavelengths, no optical damage has been observed using energy densities up to 10^5 J/cm^2 [20].

2.4.2. Ion exchange technique

This technique was developed using nonlinear materials by *Shah* in 1975 [21] and opened a wide range opportunities for optical components development [22]. The waveguides obtained by ion exchange on glass are already widely used in optical components such as multiplexers, demultiplexers, optical gyroscopes, couplers [23].

Shah developed the technique with x-cut LiNbO₃. The crystal was immersed in a bath of molten silver nitrate at 360 °C for several hours (>3h). The substitution of Li⁺ ions by Ag⁺ modifies the structure and produces an increase of n_o and n_e with maximum change of 0.13, and a step like index profile allowing a high index variation. Unfortunately poor quality waveguides were produced with optical attenuation of around 6 dB / cm. *Li et al.* [24] first presented the double proton exchange process with $\Delta n_e = 0.11$ and an optical loss of 0.4 dB/cm at 632.8 nm. They also demonstrated the possibility of combining this new fabrication process with Ti-indiffusion to produce good quality waveguides supporting both TE and TM modes (TIPE waveguides).

Among ion exchange techniques, proton exchange is mainly adapted to the development of low-loss waveguides. Proton exchange increases the extraordinary index ($\Delta n_e \approx 0.1$) and decreases the ordinary index ($\Delta n_o \approx -0.05$) in LiNbO₃. The extraordinary refractive index assumes a very nearly step distribution. Furthermore, there have been achieved for x- and z- cut samples a high stability in time, low optical losses (0.5 – 1dB/cm), low in-plane scattering levels and a good electro-optic property [25]. In many works on LiNbO₃, this technique has allowed the realisation of reliable waveguide for nonlinear optics [22]. More marginal tests were performed on the lithium niobate directly using water as source of protons [26].

These ion exchanges are usually done by immersing the crystal in an acid bath such as melted cinnamic acid ($\Delta n_e = 0.12$) [27], pyrophosphoric acid ($\Delta n_e = 0.131$) [27], benzoic acid ($\Delta n_e = 0.12$) [28], toluic acid ($\Delta n_e = 0.118$) [29], or stearic acid ($\Delta n_e = 0.12$) [30] at low temperature (150 – 300°C). A complete or partial exchange (under 75 %) can be made depending on the acidity of the medium. Complete exchange may cause structural modifications and cracks in the substrate. This can be avoided by adding lithium benzoate (1%) in acid bath.

Then, other ions like thallium, copper, manganese or chromium are also used for ionic exchanges.

In 1982, Jackel and Rice [31] showed that when lithium niobate is immersed in silver nitrate, ion exchange does not take place between Ag^+ and Li^+ , but between H^+ and Li^+ . The proton source is the water from the molten nitrate salts. In fact, the use of dehydrated salts prevents the proton exchange in the samples. A significant improvement was obtained by Jackel who produced waveguides with lower optical losses $<2\text{dB} / \text{cm}$ for $\Delta n_e \approx 0.05$.

Ionic exchange is also widely used on KTP and periodically-poled KTP for SHG [32 - 34] with Rb, Rb – Ba [35], Rb – Sr, Cs, Ba, Sr [36], Cu [37].

2.4.3. Physical and chemical deposition

The epitaxy is used to achieve deposition of $\text{LiNb}_{1-x}\text{Ta}_x\text{O}_3$ and LiNbO_3 in liquid phase [38] or by molecular spay [39]. Liquid Phase Epitaxy (LPE) consists of immersing the substrate in a bath containing oxides or dopants like rare-earth. The substrate is used as crystal seed and allows the growth of one or multiple thin layer in a similar lattice structure. By this way, Nd, Tm, Er, or Yb doped YAG thin layer have been obtained on nonlinear crystals as YAG substrate [40, 41]. Thin films of barium borates have been also obtained by this technique [42]. The epitaxy allows a good crystalline quality but often requires the use of monocrystalline substrate.

Pulsed laser deposition (PLD) [43] allows the epitaxial deposition of dense thin-films on various substrates at low temperature but on small surface, typically around 1 or 2 cm^2 [44].

Thin films of LiNbO_3 were also made by chemical vapour deposition (CVD) from metalorganic precursors (MOCVD) [45 -47] or by thermal plasma spray CVD [48, 49].

Finally, by sol-gel deposition [50], thin-films of LiNbO_3 with good optical quality have recently been obtained. However, the polycrystalline structure greatly increases the attenuation in the waveguide.

2.4.4. Organic materials

The recent interest in organic materials for nonlinear optics comes, at its origin, from the molecular engineering. Now, it is possible to give tailored nonlinear properties to these materials. Thus in the field of the second-order nonlinear optics, many organic materials have higher and faster nonlinear response than dielectrics crystals and are subject to a large number of studies.

The integration of organic materials in optical devices requires their implementation in a solid matrix ensuring their cohesion. The first studied nonlinear and doped polymer consists of a polymethylmethacrylate matrix (PMMA) doped with molecules of Disperse Red 1 (DR1) [51]. Many studies have shown the interest and performance of these molecules. The first work on matrices composed entirely of inorganic oxides (SiO_2 , TiO_2) consisted of layer of TiO_2 5% doped with DANS molecules [52]. The use of silicon matrices synthesised by sol-gel process has demonstrated the feasibility of such composites but also their weaknesses (bad aging, difficulty in maintaining the chromophores orientations which is necessary to maintain good nonlinear properties) [53]. Nucleation and growth of the organic phase in the pores of the silicon matrix occur when the temperature is lowered, decreasing the solubility caused by nucleation [54]. However, many research group working in this exciting field have shown the feasibility of waveguides for SHG from periodically-oriented polymer films, whose the conversion efficiency is very close to the conversion efficiency of periodic-poled structures on KTP and LiNbO_3 [55].

2.4.5. Nanocomposite materials

Most optical nonlinear materials currently used are normally not compatible with the standard silicon based technology. However, the technique described above using organic chromophores in glass can also be applied to the fabrication of a fully-inorganic composite material by nucleation and growth of nanocrystals in silicon. For example, it is possible to obtain nonlinear and luminescent materials used for self-doubling materials within a laser cavity.

2.4.6. Ion implantation technique

The key of this technique is to create a layer of defects at a well-defined depth from the substrate by bombarding the substrate with ions. The impinging ions penetrate the substrate, losing their energy through electronic excitation and nuclear collision. It results in a crystalline surface layer damaged slightly and decreasing refractive index locally, thus, creating an optical barrier. The ion implantation with different ions such as N^+ , B^+ , He^+ , or Ne^+ is possible with an index difference greater than 0.1, depending on the implantation dose [56]. The details of this technique will be developed in section 2.4.9. This technique has an advantage of waveguide fabrication on a wide variety of materials, but the damages created by radiations through the guiding layer reduce significantly its quality. Since the first proton-implanted waveguide in

fused-silica in 1968, implanted waveguides have been so far fabricated in more than 100 optical materials, in a wide range of ions at energies of several keV up to several MeV. Waveguides for SHG fabricated by ion implantation have been made on LiNbO_3 , LiTaO_3 , KTP, and more recently on borates (LTB, β -BBO, and LBO) [56].

2.4.7. Implantation in Lithium Niobate

Among all the electro-optical materials, LiNbO_3 has been studied most extensively because of its combination of various excellent properties. Lithium niobate waveguides formed by the implantation of various ions, including H, He, B, C, N, O, F, Si, P, Ti, Cu, Ni, and Ag, with different electrovalence, energies and doses have been studied. The majority of these studies were focused on the fabrication and refractive index characterisations of LN waveguides by implantation of ions at a low dose ($\approx 10^{14}$ ions/cm²) [57 - 61]. For the He^+ -implanted LN waveguides at high doses ($\approx 10^{16}$ ions/cm²), the ordinary refractive index had a typical barrier type profile, while the extraordinary refractive index had a more complex change: at the surface region n_e was increased, but the maximum increase was found to be peaked deep inside the guide. An index decreased barrier was located at the end of the ion track. Based on the experimental results, several hypotheses or models were suggested to explain the refractive index behaviour induced by the implantation. For high birefringent crystals ($\Delta n \approx 0.08$), low dose implantation may induce a positive change of the lower index (n_e for LiNbO_3) while decrease the higher one (n_o for LiNbO_3) [62]. Further investigations of the index behaviours focus on the electronic and nuclear damages created by the interactions between the implanted ions and the substrate lattice. The electronic energy deposition causes positive index changes in terms of Li diffusion or lattice relaxation. As we will see in the annealing treatment part, the ion implantation cause defects and lattice disorders in crystal. A high dose can even destroy the lattice which imposes a limitation in implantation doses provided to the crystal. These limited doses depend on the implanted ions. For instance, the case of O^{3+} implanted LN with a dose above $4 \cdot 10^{14}$ ions/cm², where it seems difficult to remove the lattice defects by annealing treatment in this case. For H^+ ion irradiation at even much higher doses (up to $2 \cdot 10^{17}$ ions/cm²), the structure recovers to approximate original lattice [59], while He^+ ion implantation generates large dimension clusters of different crystalline nature [60].

It has been shown that after H^+ - He^+ implantation the values of electro-optic coefficients r_{13} and r_{33} were well preserved in the waveguide at high dose ($5 \cdot 10^{16} - 10^{17}$ ions/ cm^2) [60]. The same thing has been observed for the non linear coefficient d_{33} in H^+ implanted waveguides while for the He^+ implanted one it is reduced by $\approx 48\%$ [63]. The non-linear properties of those waveguides were found to be well retained in the guiding region.

2.4.8. Realisation of planar waveguide on PPLN by He^+ implantation

This section describes the basic methods of ion-implanted waveguide fabrication and investigation. We have seen in section 1.2 that a planar waveguide can be made by increasing the refractive index of a blank LN substrate locally via ionic incorporation on the surface: exchange and diffusion techniques. On the other hand, the mechanism of implantation works differently. In fact, the refractive index decreases locally in a zone called nuclear damaged zone. The ions of the incident beam penetrate the substrate and lose their kinetic energy by multiple electronic and nuclear collisions within the crystal. So, the bombarded ions are stopped and accumulated in a zone which is used as an optical barrier. As such, the implantation parameters such as energy and dose affect the quality of waveguide. So the implantation energy and dose will be discussed for our waveguides.

2.4.8.1. He^+ implantation process

Ion implantation is a mature technology for semiconductor production, and has been widely used in the optical communication devices. In the research area of the ion-implanted waveguides, Van Der Graaf accelerators are often used because they offer high energies of specific implanted ion at acceptable dose [64]. We use an ECLAIR track 5 dispositive cooled by water at $18^\circ C$. The accelerator is composed of a generator where a high potential difference is built up and maintained on a smooth conducting surface by the continuous transfer of positive static charges from a moving isolated belt. The ions are created in a source chamber inside the high voltage terminal and are accelerated by the electric voltage between the high voltage terminal and ground. The implanted ions normally with positive charges are extracted out from the sources. A mass/energy – separating energy magnet is used to select the ion species (elements and isotopes) of interest. After this, the selected ions are focused and bombarded into the target materials ($LiNbO_3$) by beam sweeping technique. A uniform and isotopically pure irradiation is ensured

over the sample surface. The implantation system is shown in Fig. 2.13. The ion beam has a dimension of 1.2×1.2 cm before focusing and 5×6 mm. The vacuum condition in the implantation chamber is 9.1×10^{-5} mbar and the average fluence is 2.12×10^{12} ion/cm²/s.

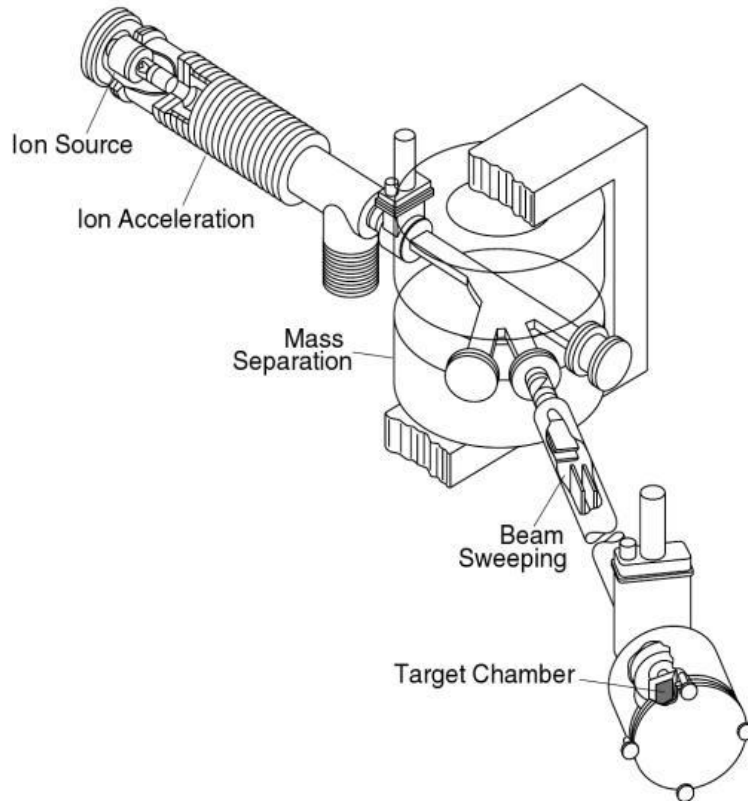


Figure 2.13: Schematic drawing of an ion implantation system [65].

That method has been adopted for waveguide fabrication in a large number of optical materials and the ion-implanted waveguide have refractive index profile of optical barrier. The planar waveguide (1D) may be fabricated by directly ion implantation into the sample, in which case no specific masks are required as we could need for 2D waveguide formation. In the earlier works, masks were made by first depositing a thin photoresist or metal (e. g. Au), and using standard photolithography technique, then the waveguides are formed in the mask-protected region. Finally forming negative or positive metal stripes as protective layer according to the waveguide type. Alternatively, a special setup was lately designed for channel waveguide formation by Moretti *et al.* In that technique, the sample was fixed on a rotatable target holder, and then irradiated through a movable metal slit. By varying the angle of incident beam with sample surface continuously, the implantations of ions could create a closed barrier wall inside the

substrate, hence forming channel waveguides [66]. In our works, we have consciously made planar waveguides on z+ face of the 2D nonlinear photonic crystals, in order to study SHG for multiple QPM orders in guiding conditions.

2.4.8.2. Implantation parameters

Different parameters influence implantation:

- The nature of ions.

For equivalent implantation energy (kinetic energy), the lightest ions undergo more deeply in the substrate. The damages due to the passage of ions and their influence on the refractive index modification depend on the nature of implanted ions. We have exclusively used Helium ions (He^+) during implantation, but one of the advantages of ion implantation is that the choice of implant ions is not limited by conventional rules or solubility and any ions may be used.

- The nature of substrate.

The materials do not react in the same way with implantation. Their refractive indices can be raised or reduced independently of the nature of implanted ions.

- The dose (quantity of ions per unit surface).

This parameter is important to control the refractive index variation. The refractive index behaviour is highly dependent on dose. It can even be contradictory in some cases. For instance, the extraordinary refractive index of LN increases at low dose whereas it decreases at high dose.

- The implantation energy.

This parameter affects the ions distribution in depth. Energy is associated with the ions penetration depth in material. This parameter is important to fix the waveguide thickness. An illustration is given in Fig. 2.14 [67], where the He^+ penetration depth in LiNbO_3 is estimated with TRIM (Transport of Ion in Matter) [68] according to the implantation energy.

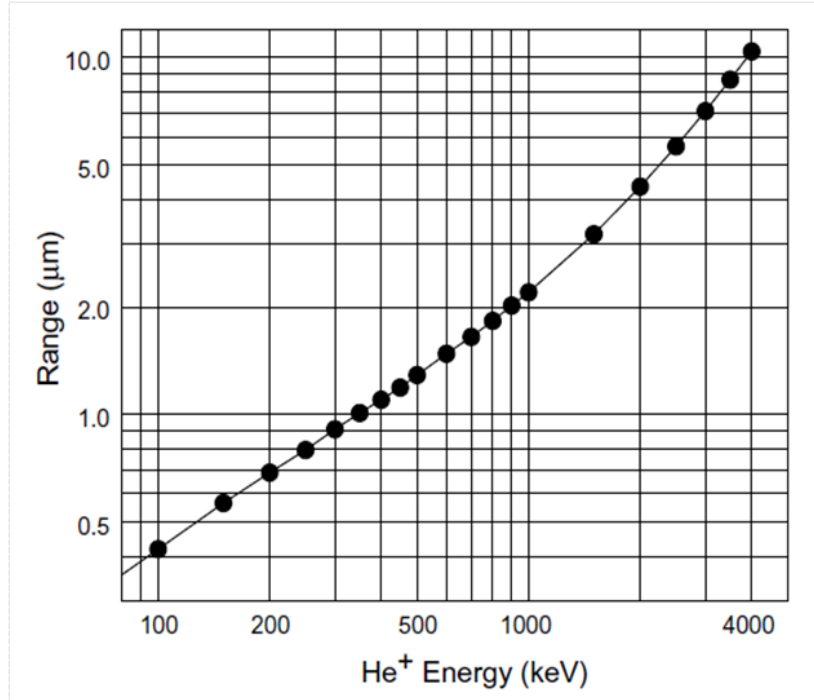


Figure 2.14: He⁺ penetration depth in LiNbO₃ is estimated with TRIM (Transport of Ion in Matter) [68] according to the implantation energy [67].

- The incident beam angle.

This parameter has also an influence on penetration depth. In order to avoid channelling effect in substrate, the incident beam angle is fixed at a minimum angle of 7°.

- The substrate temperature.

The temperature has to be maintained constant and close to the room temperature. In fact, uncontrolled annealing effect disturbs the ions distribution in crystal.

2.4.8.3. Implantation interactions

The interaction ion/matter has different origins enumerated below:

- Interaction with electrons at high energy:

When charged particles go through matter, they mainly lose their energy by interaction with linked electrons. For ions at high energy, most of the transferred energy goes in ionizing inelastic collisions with creation of free electrons from the target and a potential energy decreasing for the

residual created ions (lattice ions). It includes the formation of damages through the ejected electrons path and chemical reaction with lattice ions. The free electron can be trapped by lattice defects forming coloured centres and absorbing certain wavelength.

- Interaction with electrons at low energy:

When the ions kinetic energy decreases, electrons are captured or delivered from residual ions (charge transfer with matter) with creation of new residual ions in matter. In that case, there are no ejected free electrons. Rarely, free electrons are delivered from ions without creating residual ions in lattice.

- Interaction with the Coulomb field of atoms.

The charged particles slow down almost entirely by Coulomb interaction with atomic electrons. In one hand, this phenomenon prevails with rapid particles (with a kinetic energy of few MeV) or heavy particles (from a few hundred keV). In that case, the ions trajectory is not deflected during the transfer energy process. On the other hand the Coulomb interaction becomes negligible for particles at the end of their run.

- Collisions with nucleus in matter.

When the kinetic energy becomes sufficiently low, there is not enough energy transfer between projectiles and target particles to excite the atomic energy levels. The projectiles undergo nuclear elastic collision with atoms. Generally, it induces multiple cascade collisions within the crystal creating atomic displacement and gap in lattice. Both are known as Frenkel pair. Furthermore, the elastic collision creates vibrations of the crystal lattice dissipated as heat.

- Magnetic momentum interactions between particles.
- Radiation losses at very high energies (> 100 MeV) by the bremsstrahlung process, Cherenkov radiation and nuclear reactions.

Each of these interactions contributes on the ion kinetic energy loss by collisions with electrons and atoms of the crystal. In our work, the involved energies are in the MeV range. In that case, only the four first processes occur and contribute to the formation of the waveguide.

Generally, the sum of interactions is expressed as the sum of kinetic energy loss by implanted ions. It is divided in one hand with inelastic process as electronic excitation and ionisation (electronic losses) and on the other hand with elastic process as nuclear collisions and displacements (nuclear losses). These interactions are schematically presented in Fig. 2.15 (a). They play a crucial role in the creation of a refractive index profile and the waveguide formation as illustrated in Fig. 2.15 (b).

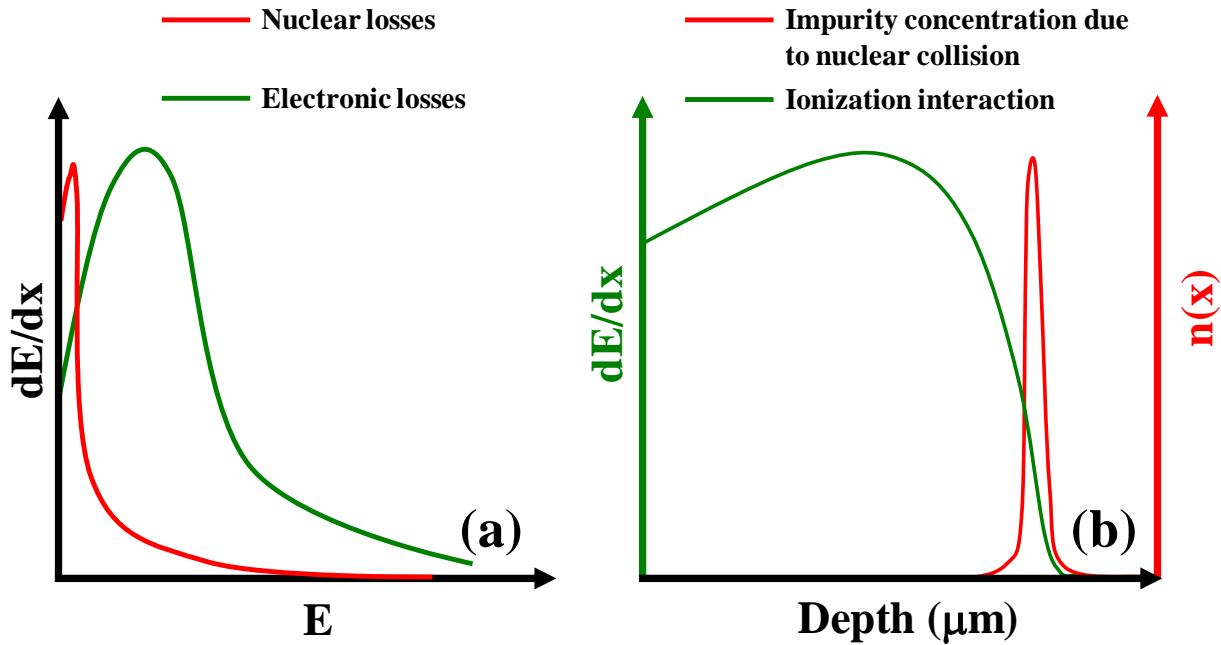


Figure 2.15: (a) Nuclear (red curve) and electronic (green curve) rates of the implanted ions energy deposition (or energy loss) according to their kinetic energy. Typically, nuclear loss are maximum for energies between 10 – 100keV, an electronic loss for energies of the order of MeV.

(b) Accordingly, the ionisation deposition (green curve) and the impurity concentration (red curve) due to nuclear collisions (also called Bragg's peak) are represented along the ionic path in the substrate.

Thus, the total energy loss is defined as the sum of electronic and nuclear interactions:

$$-(\partial_x E) = -(\partial_x E)_{elec.} - (\partial_x E)_{nucl.} \quad (2.33)$$

with x the direction of the ion beam and $E = \frac{1}{2}mv^2$ the kinetic energy of the incident ions.

Considering the electronic collisions, the electronic energy losses are calculated from the Bethe-Bloch formula [69], which is a good approximation in the energy domain from several hundred keV to several hundred GeV:

$$-(\partial_x E)_{elec.} = \frac{4\pi Z_i^2 Z_t e^4 N}{(4\pi\epsilon_0)^2 m_e c^2 \beta^2} \left[\ln \left(\frac{2m_e c^2 \beta^2}{I} \right) - \beta^2 - \frac{\delta}{2} \right] \quad (2.34)$$

Where Z_i is the atomic number of the implanted ion, Z_t the atomic number of the targeted atoms, e the elementary charge (1.6×10^{-19} C), N the atomic concentration of the target, ϵ_0 the permittivity, m_e is the mass of electron, $\beta = v/c$ the incident ion speed, I the average excitation potential of the targeted atoms and δ the correction from the charge density effect.

We can consider different regimes according to the incident ion speed:

- If $v > e^2/h = 2.2 \times 10^8 \text{ cm.s}^{-1}$ the orbital velocity of electrons, the electronic energy loss varies as $\ln(E)/E$. It corresponds to the electronic interaction at high energy [70].
- If $v < e^2/h$, we have to take into account the charge transfer with matter. The electronic energy loss varies linearly with v (or \sqrt{E}). It corresponds to the electronic interaction at low energy [71].

When the two velocities are equal, there is charge exchange with a capture of electrons by the ions.

Considering the elastic nuclear loss, a physical model has been proposed by Lindhart *et al.* [71]:

$$-(\partial_x E)_{nucl.} = \frac{E\rho}{x\varepsilon} \partial_\rho \varepsilon \quad (2.35)$$

with the reduced coordinates:

$$\rho = \frac{m_i m_t}{(m_i + m_t)^2} 4\pi N a^2 x \quad \text{and} \quad \varepsilon = \frac{m_i}{m_i + m_t} \frac{4\pi\epsilon_0 N a}{Z_i Z_t e^2} E \quad (2.36)$$

and $a = \frac{a_0}{\sqrt{Z_i^{2/3} + Z_t^{2/3}}}$ is defined as the screening length (a_0 is the Bohr radius 6×10^{-9} cm), m_i the ion mass and m_t the targeted atom mass.

The ions trajectory, the number of collisions and the fraction of energy lose at each collision are random values. The range distribution of the implanted ions is described according to the Maxwell-Boltzmann statistic. This results in the expression of the mean free path of the ions R in the incident direction [72]:

$$R = \int_{E_0}^0 \frac{dE}{(\partial_x E)} \quad (2.37)$$

The typical ion distribution is approximately a Gaussian in shape and may therefore be characterised by a projected range R_P and a straggling ΔR_P such as:

$$N(x) = \frac{D}{\sqrt{2\pi}\Delta R_P} e^{-\left(\frac{x-R_P}{\sqrt{2}\Delta R_P}\right)^2} \quad (2.38)$$

With D the total number of ions per cm^2 (the dose). This distribution is illustrated in Fig. 2.15. (b). Information about irradiation damage can be obtained from the Monte Carlo simulation in TRIM (Transport of Ion in Matter) [69] developed by Ziegler, Biersack and Littmark. In these simulations the ion track of the implanted ion and all resulting recoils and atomic displacement are displayed. It allow us to simulate the electronic and nuclear loss profile, the impurity density profile causing the optical barrier and the pulverisation rate (ejected atoms from the surface leading to its erosion).

2.4.8.4. Ion implantation advantages

The technique of ion implantation needs heavy equipment in comparison with other techniques like ion exchange or diffusion methods. However, implantation gives access to a large control of different parameters (dose, energy, number of implantations, nature of ions,...) allowing the fabrication of quasi-step index waveguides with desired thickness and index variation. For instance, a precise control of the number of implanted ions is simple, as the ion beam is monitored as a current, a judicious choice of energy and dose can develop any desired refractive index profile under the surface, both being controlled by the implantation dose and energy. Moreover, the choice of implant ions is not limited by conventional rules of solubility and any

ion may be used with a high isotopic purity from the ion beam. It is also possible to place different ions at different depths. It is generally used to form a larger optical barrier and thus reduce the loss by tunnelling effect. Another advantage is that the implantation is made at low-temperature which is essential to maintain the crystal phase, the nonlinearity and the poled lattice of the crystal, which is not often the case for other techniques. The temperature during implantation never exceeds 77°C.

Moreover, since 1998, Levy *et al.* [72] have used this technique in order to obtain optical thin films by crystal ion slicing (CIS), with thicknesses at the micron or even nanometre scale. The effect of the high dose implantation ($> 5 \times 10^{16} \text{ He}^+ / \text{cm}^2$) is to generate a buried amorphous layer and bubbles under the surface. A lift-off by wet-etching (5% HF solution) or a thermal treatment allows peel-off the thin layer from the substrate. With this processing, LiNbO₃ films can be bounded to silicon or other materials for further photonic applications. Further works have been previously made with obtained thin films of 4 μm. However, it remains several problems with the proceeding: high losses, technological difficulties in the integration of these thin films in optical devices, cracks formation, weakening or even amorphisation of the implanted surface occur during implantation. We have tried to use this technique in order to perform PPLN thin layers having sufficient optical quality for SHG. We will briefly develop our experimental results in the perspective section. In fact, our results remains partial and work remains to be done to achieve NLPC thin layer.

Our choice is naturally focused on this technique in order to perform and improve performance for NLPC.

2.4.8.5. Annealing treatment

Since the implantation creates optical absorption sites by electronic energy deposition, and destroys somehow the equilibrium of the original structures by nuclear collision (the implantation could destroy the lattice at high doses), an annealing treatment is commonly necessary for all ion-implanted waveguides [73]. The aim of anneals is to remove the unwanted defects within the guide region to maximally preserve the electro-optic or non-linear optic properties. The used method of annealing treatment includes a conventional oven. Thermal treatment at 220°C is performed for one hour (with a slow temperature ramp up and down:

3°/min). That method may reduce the propagation losses of the waveguides. Some other new techniques were performed using laser beam processing [73]. The laser energy may be confined to the surface layer to realise local heating which may remove intrinsic defects and induce crystal-line re-growth or solid phase epitaxy.

Summary

In this chapter, we develop the theory of the second-harmonic generated by quasi-phase matching in nonlinear photonic crystal. We observe that in 2D configuration, a periodically poled structure presents some differences comparing to 1D configuration. The modifications are mainly due to the occurrence of multiple-QPM orders in the crystal. These modifications concern the expression of the effective nonlinear coefficients and the angular dependence of the SHG associated with each QPM orders. Our choice fell on 2D-PPLN having a square reciprocal lattice for which we describe the fabrication process by electrical poling method.

A second section is dedicated to the fabrication of optical waveguides in nonlinear materials. This preliminary overview allows us to understand the advantages and the limits of ion implantation process comparing with the other methods. Ion implantation is one of the most commonly used techniques of optical waveguides in lithium niobate. It is mainly due to a large control of the waveguide optical properties and geometrical configuration, a high index modification and reasonably conservation of the nonlinear properties of the optical waveguide. From literature, we develop and describe our own implantation proceeding with 2D-PPLN.

References:

- [1] V. Berger, *Nonlinear photonic crystals*, Phys. Rev. Lett. **81**, 4136 – 4139 (1998).
- [2] K. Gallo, C. Codemard, C. B. E. Gawith, J. Nilsson, P. G. R. Smith, N. G. R. Broderick, D. J. Richardson, *Guided-wave second-harmonic generation in a LiNbO₃ nonlinear photonic crystal*, Opt. Lett. **31** (9), 1232 – 1234 (2006).
- [3] L. –H. Peng, C. C. Hsu, Y. C. Shih, *Second-harmonic green generation from two-dimensional $\chi^{(2)}$ nonlinear photonic crystal with orthorhombic lattice structure*, Appl. Phys. Lett. **83**(17), 3447 – 3449 (2003).
- [4] N. G. R. Broderick, G. W. Ross, H. L. Offerhaus, D. J. Richardson, D. C. Hanna, *Hexagonally poled lithium niobate: a two-dimension a nonlinear photonic crystal*, Phys. Rev. Lett. **84**, 4345 – 4348 (2000).
- [5] L. –H. Peng, C. C. Hsu, A. H. Kung, *Broad multiwavelength second-harmonic generation from two-dimensional $\chi^{(2)}$ nonlinear photonic crystal of tetragonal lattice structure*, IEEE J. of Sel. Top. in Quant. Elect. **10**(5), 1142 – 1148 (2008).
- [6] A. Solntsev, A. Sukhorukov, D. Neshev, R. Illiew, R. Geiss, T. Pertsch, Y. S. Kivshar, *Cascaded third-harmonic generation in lithium niobate nanowaveguides*, Appl. Phys. Lett. **98**(23), 231110 (2011).
- [7] L. Mateos, P. Molina, J. Galisteo, C. Lopez, L. E. Bausa, M. Ramirez, *Simultaneous generation of second to fifth harmonic conical beams in a two dimensional nonlinear photonic crystal*, Opt. Exp. **20**(28), 29940 (2012).
- [8] N. G. R. Broderick, R. T. Bratfalean, T. M. Monroe, D. J. Richardson, C. M. De Sterke, *Temperature and wavelength tuning of second-, third-, and fourth-harmonic generation in a two-dimensional hexagonally poled nonlinear crystal*, J. Opt. Soc. Am. B **19**, 2263 – 2272 (2002).
- [9] H. – C. Liu, A. H. Kung, *Substantial gain enhancement for optical parametric amplification and oscillation in two dimensional $\chi^{(2)}$ nonlinear photonic crystal*, Opt. Exp. **16**(13), 9714 – 9725 (2008).

- [10] D.- L. Ma, M. -L. Ren, Z. -Y. Li, *Broadband response of second-harmonic generation in a two dimensional quasi-random quasi-phase matching structure*, Chin. Phys. Lett. **28**(7), 074218, (2011).
- [11] N. Fujioka, S. Ashihara, H. Ono, T. Shimura, K. Kuroda, *Cascaded third-harmonic generation of ultrashort optical pulses in two-dimensional quasi-phase matching gratings*, J. Opt. Soc. Am. B **24**(9), 2394 – 2405 (2007).
- [12] A. Arie, N. Habshoosh, A. Bahabad, *Quasi-phase matching in two-dimensional nonlinear photonic crystals*, Opt. Quant. Electron **39**, 361 -375 (2007)
- [13] R. C. Miller, *Further experiments on the sidewise motion of 180° domain walls in BaTiO₃*, Phys. Rev. **115**, 1176 – 1180 (1959).
- [14] I. Kaminov, J. Carruthers, *Optical waveguiding layer in LiNbO₃ and LiTaO₃*, Appl. Phys. Lett. **22**, 326 - 328 (1973).
- [15] R. V. Schmidt, I. P. Kaminov, *Metal-diffused optical waveguides in LiNbO₃*, Appl. Phys. Lett. **25**(8), 458 – 461 (1974).
- [16] M. Minakata, s. Saito, M. Shibata, S. Miyazawa, *Precise determination of refractive index changes in Ti:diffused LN optical waveguides*, J. Appl. Phys. **49**, 4677 – 4682 (1978).
- [17] K. Sugii, M. Fukuma, H. Iwasaki, *A study on titanium diffusion into LN waveguides by electron probe analysis and X-ray diffraction methods*, J. Mat. Sci. **13**, 523 – 533 (1978).
- [18] H. Naitoh, M. Nunoshita, T. Nakayama, *Mode control of Ti-diffused LN slab optical waveguide*, Appl. Opt. **16**(9), 2546 – 2549 (1977).
- [19] R. V. Schmidt, I. P. Kaminow, *Metal diffused optical waveguides in LN*, Appl. Phys. Lett. **25**, 458 – 460 (1974).
- [20] M. N. Armenesis, *Dependence of in-plane scattering level in Ti:LN optical waveguide on diffusion time*, IEE Proc. H. **131**, 295 – 298 (1984).
- [21] M. L. Shah, *Optical waveguides in LN by ion exchange technique*, Appl. Phys. Lett. **26**, 652 – 653 (1975).

- [22] Y. Korkishko, V. Fedorov, *Ion exchange in single crystals for integrated optics and optoelectronics*, Cambridge International Science Publishing (1999).
- [23] A. Tervonen, *Critical issues in designing glass integrated optical circuits*, Proc. SPIE CR53 25-52.
- [24] S. L. Li, *Optical waveguides in LiNbO₃ crystals by proton exchange*, Sc. China G **51**(10), 1479 – 1488 (2008).
- [25] M. N. Armenise, S. M. Al-Shukri, A. L. Dawar, R. M. Delarue, *Characterization of proton exchanged slab waveguide on LN*, Proc. IEEE J. **133**, 113 – 117 (1986).
- [26] Y. S. Son, H. V. Lee, Y. K. Jhee, S. Y. Shin, B. G. Kim, *Fabrication of LiNbO₃ channel waveguides using water*, IEEE Phot. Tech. Lett. **4**(5), 457 – 458 (1992).
- [27] E. Y. B. Pun, P. S. Chung, K. K. Loi, *Index profile of proton exchanged waveguides in lithium niobate using cinnamic acid*, Elec. Lett. **27**(14), 1282 – 1283 (1991).
- [28] N. Goto, G. L. Yip, *Characterisation of proton-exchange and annealed LiNbO₃ waveguides with pyrophosphoric acid*, Appl. Opt. **28**(1), 60 – 65 (1989).
- [29] J. L. Jackel, C. E. Rice, J. J. Veselka, *Proton exchange for high-index waveguides in LiNbO₃*, Appl. Phys. Lett. **41**, 607 – 612 (1982).
- [30] K. K. Loi, E. Y. B. Pun, P. S. Chung, *Proton-exchanged optical waveguides in z-cut LiNbO₃ using toluic acid*, Elec. Lett. **28**(6), 546 – 548 (1992).
- [31] E. Y. B. Pun, P. S. Chung, K. K. Loi, A. Zhao, *Proton-exchanged LiNbO₃ using stearic acid*, IEEE Phot. Tech. Lett. **3**(11), 1006 – 1008 (1991).
- [32] J. L. Jackel, C. E. Rice, *Variation in waveguide fabricated by immersion of LiNbO₃ in AgNO₃ and TiNO₃: the role of hydrogen*, Appl. Phys. Lett. **26**(11), 652 – 653 (1975).
- [33] F. Laurell, M. Roelofs, W. Bindloss, H. Hsiung, A. Suna, J. Bierlein, *Detection of ferroelectrics domain reversal in KTiOPO₄*, J. Appl. Phys. **71**(10), 4664 – 4670 (1992).

- [34] X. Mu, I. Zotova, Y. Ding, W. Risk, *Backward second-harmonic generation in submicron-period ion exchanged KTP waveguide*, Opt. Comm. **181**, 153 – 159 (2000).
- [35] K. Daneshvar, E. Giess, A. Bacon, D. Dawes, L. Gea, L. Boatner, *Ion exchange in potassium titanyl phosphate*, Appl. Phys. Lett. **71**(6), 756 -758 (1997).
- [36] I. Savatinova, I. Savova, E. Liarokapis, C. C. Ziling, V. V. Atuchin, M. N. Armenise, V. M. N. Passaro, *A comparative analysis, of Rb :KTP, and Cs :KTP optical waveguides*, J. Phys. D: Appl. Phys. **31**, 1667 – 1672 (1998).
- [37] M. Roelofs, P. Morris, J. Bierlein, *Ion exchange of Rb, Ba, and Sr in KTiOPO₄*, J. Appl. Phys. **70**(2), 720 – 728 (1991).
- [38] L. Shi, T. Chong, Z. Zhuo, W. Hou, P. Hu, *Properties of ion exchange planar and channel optical waveguides fabricated in Cu-doped KTiOPO₄ substrate*, Appl. Phys. Lett. **71**(19), 2737 – 2739 (1997).
- [39] D. Callejo, S. Manotas, M. D. Serrano, V. Bermudez, F. Agullo-Rueda, E. Dieguez, *Compositional study of LiNbO₃ thin films grown by liquid phase epitaxy*, J. of Crystal Growth **226**(4), 488 – 492 (2001).
- [40] R. A. Betts, C. Pitt, *Growth of thin-film lithium niobate by molecular beam epitaxy*, Elec. Lett. **21** (21), 960 – 962 (1985).
- [41] A. Rameix, C. Borel, B. Chambaz, B. Ferrand, D. P. Sheperd, T. J. Warburton, D. C. Anna, A. C. Tropper, *An efficient diode pumped, 2 μm Tm:YAG waveguide laser*, Opt. Comm. **142**(4), 239 - 243 (1997).
- [42] D. Pelenc, B. Chambaz, I. Chartier, B. Ferrand, C. Wyon, D. P. Sheperd, D. C. Anna, A. C. Large, A. C. Tropper, *High slope efficiency and low threshold in a diode-pumped epitaxially grown Yb:YAG waveguide laser*, Opt. Comm. **115**(5), 491 – 497(1997).
- [43] J. Liu, C. Xia, X. He, G. Zhou, J. Xu, *Residual stress in beta barium borate (BaB₂O₄) thin films grown by liquid-phase epitaxy*, J. Cryst. Growth **267**, 161 – 165 (2004).

- [44] F. Sanchez, N. Domingo, M. V. Garcia-Cuenca, C. Guerrero, C. Ferrater, M. Varela, *Pulsed laser deposition of epitaxial buffer layers on LiNbO₃*, Appl. Surf. Science **186**(1-4), 397 – 402 (2002).
- [45] Z. Ye, J. He, L. Ye, B. Zhao, W. Weng, H. Lu, *Highly c-axis oriented LiNbO₃ thin film grown on SiO₂/Si substrate by pulsed laser deposition*, Mat. Lett. **55**(4), 265 – 268 (2002).
- [46] A. A. Wernberga, H. Gysling, A. Filo, T. Blanton, *Epitaxial growth of lithium niobate thin films from a single-source organometallic precursor using metalorganic chemical vapor deposition*, Appl. Phys. Lett. **62**, 946 – 948 (1993).
- [47] S. Y. Lee, R. S. Feigelson, *Reduced optical losses in MOCVD grown lithium niobate thin films on sapphire by controlling nucleation density*, J. Cryst. Growth **186**(4), 594 – 606 (1998).
- [48] S. Hirano, T. Yogo, W. Sakamoto, Y. Takeichi, S. Ono, *Processing of highly oriented LiNbO₃ thin films through a metal-organic precursor solution*, J. of the European Ceramic Society **24**(2), 435 – 440 (2004).
- [49] N. Yamaguchi, T. Hattori, K. Terashima, T. Yoshida, *High-rate deposition of LiNbO₃ films by thermal plasma spray CVD*, Thin Solid Films **316**(1-2), 185 – 188 (1998).
- [50] T. Majima, H. Yamamoto, S. A. Kulinich, K. Terashima, *High-rate deposition of LiNb_{1-x}Ta_xO₃ films by thermal plasma spray CVD*, J. Cryst. Growth **220**(3), 336 – 340 (2000).
- [51] M. Takahashi, K. Yamauchi, T. Yagi, A. Nashiwaki, K. Wakita, N. Ohnishi, K. Hotta, I. Sahashi, *Preparation and characterization of high-quality stoichiometric LiNbO₃ thick films prepared by the sol-gel method*, Thin Solid Films **458** (1-2), 108 – 113 (2004).
- [52] K. Singer, J. Sohn, S. Lalama, *Second harmonic generation in poled polymerfilms*, Appl. Phys. Lett. **49**, 248 – 250 (1986).
- [53] Y. Nosaka, N. Tohriwa, T. Kobayashi, N. Fujii, *Two-dimensionally poled sol-gel processing of TiO₂ film doped with organic compounds for nonlinear optical activity*, Chem. Mater. **5**, 930 – 932 (1993).

- [54] N. Sanz, Elaboration, *structural characterization and study of linear and nonlinear optical properties of organic nanocrystals in sol-gel matrix*, Ph. D. Thesis, University of Grenoble (2000).
- [55] J. Ju, J. Kim, J. Y. Do, M. Kim, S. Park, M. Lee, *Second harmonic generation in periodically poled nonlinear polymer waveguides*, Opt. Lett. **29**(1), 89 – 91 (2004).
- [56] P. Moretti, M. –F. Joubert, S. Tascu, B. Jacquier, M. Kaczkan, M. Malinowskii, J. Samecki, *Luminescence of Nd³⁺ in proton or helium-implanted channel waveguide in Nd:YAG crystals*, Opt. Mater. **24**, 315 – 319 (2003).
- [57] F. Chen, X. Wang, K. Wang, *Development of ion-implanted optical waveguides in optical materials: a review*, Opt. Mat. **29**, 1523 – 1542 (2007).
- [58] H. Hu, F. Lu, F. Chen, B. R. Shi, K. M. Wang, D. Y. Shen, *Monomode optical waveguide in lithium niobate formed by MeV Si⁺ ion implantation*, J. Appl. Phys. **89**(9), 5224 - 5227 (2001).
- [59] H. Hu, F. Lu, F. Chen, F.X. Wang, J.H. Zhang, X.D. Lu, K.M. Wang, B.R. Shi, *Optical waveguide formation by MeV H⁺ implanted into LiNbO₃ crystal*, Opt. Commun. **177**, 189 - 193 (2000).
- [60] F. Chen, *Photonic guiding structures in lithium niobate crystals produced by energetic ion beam*, J. Appl. Phys. **106**(8), 081101 (2009).
- [61] L. Zhang, P.J. Chandler, P.D. Townsend, *Extra strange modes in ion implanted lithium niobate waveguides*, J. Appl. Phys. **70**(3), 1185 - 1190 (1991).
- [62] J. Rams, J. Olivares, P.J. Chandler, P.D. Townsend, *Mode gaps in the refractive index properties of low-dose ion-implanted LiNbO₃ waveguides*, J. Appl. Phys. **87**(7), 3199 - 3203(2000).
- [63] R. Kremer, A. Boudrioua, P. Moretti, J.C. Loulergue, *Measurement of the nonlinear d₃₃ coefficients of light-ion implanted lithium niobate by second-harmonic generation in total reflexion geometry*, Opt. Commun. **219**, 389 - 393 (2003).

- [64] A. Dunlop, F. Rullier-Albenque, C. Jaouen, C. Templier, J. Davenas, *Materials under irradiation*, Trans Tech Publications LTD, Aedermannsdorf, 30 – 31 (1992).
- [65] M. Nastasi, J. W. Mayer, *Ion implantation and synthesis of materials*, Springer-Verlag Heidelberg Ed. (2006).
- [66] P. Moretti, M. –F. Joubert, S. Tascu, B. Jacquier, M. Kaczkan, M. Malinowskii, J. Samecki, *Luminescence of Nd³⁺ in proton or helium-implanted channel waveguide in Nd:YAG crystals*, *Opt. Mater.* **24**, 315 – 319 (2003).
- [67] G. Poberaj, M. Koechlin, F. Sulser, A. Guarino, J. Hajfler, P. Gunter, *Ion-sliced lithium niobate thin films for active photonic devices*, International workshop on photonic and electronic materials, 3, San Sebastian, Esp (2007).
- [68] J. P. Biersack, J. F. Ziegler, U. Littmarck, vol.1, Pergamon Press, New-York (1985).
- [69] H. A. Bethe, *Nuclear dynamics, theoretical*, *Rev. Mod. Phys.* **9**, 69 – 244 (1937).
- [70] J.E. Valdés, J.C. Eckardt, G.H. Lantschner, N.R. Arista, *Energy loss of slow photons in solids: deviation from the proportionality with projectile velocity*, *Physical Review A* **49**(2), 1083 - 1087 (1994).
- [71] J. Lindhart, M. Scharf, *Energy dissipation by ions in the keV region*, *Phys. Rev.* **124**, 128 – 135 (1961).
- [72] M. Levy, R. M. Osgood, R. Liu, L. E. Cross, G. S. Cargill, A. Kumar, H. Bakhru, *Fabrication of single-crystal lithium niobate films by crystal ion slicing*, *Appl. Phys. Lett.* **73**, 2293 – 2296 (1998).
- [73] H. Hu, F. Lu, F. Chen, F.X. Wang, J.H. Zhang, X.D. Lu, K.M. Wang, B.R. Shi, *Optical waveguide formation by MeV H⁺ implanted into LiNbO₃ crystal*, *Opt. Commun.* **177**, 189 - 193 (2000).

Chapter 3

Second-harmonic generation in He⁺ implanted 2D-PPLN

3.1. Introduction

In the previous chapters, we have developed a full theoretical study on the nonlinear behaviour of NLPC, especially SHG by QPM process. Moreover, we have carried out this study for planar waveguides and we have seen how SHG, particularly phase matching condition are affected by the waveguide structure. In this chapter, we will describe their behaviours observed experimentally. First, guiding properties due to ionic implantation will be show by identifying the transverse propagation modes of our structures. Following this, we will determine the optical losses and finally we will provide the experimental results on the nonlinear properties of NLPC in waveguide configuration.

We have seen in chapter 2 the effects of ion implantation on dielectric materials. Particularly, the choice of energy (E) and dose (D) can develop any desired impurity profile beneath the surface, allowing the fabrication of suitable optical waveguides. By this method, we look for the fabrication of waveguides in periodically-poled lithium niobate with the least amount of possible transversal modes in order to avoid excessive TM modal dispersion with SHG. On the other hand, the number of modes must be enough to be able to calculate the index profile. In fact, single-mode implanted waveguides present the disadvantage of high optical loss because of the optical tunnelling effect (the tunnelling loss mechanism trends to change in $1/l^4$ with l the waveguide thickness). The compromise is to obtain at least two TM modes in the waveguide

with different parity) at the fundamental wavelength 1064 nm. Thus, by using simulation TRIM [1], we have obtained implantation parameters to be set.

First, a poling process described in Chapter 2 is done on LiNbO_3 to realise PPLN samples. He+ implantation on the PPLN samples to fabricate waveguides should be performed after this process. In fact, the quality of PPLN structure depends on the purity of the substrate and the accommodated impurities at the optical barrier can disrupt the domain growth in the crystal. The procedure used in our work (poling, implantation, then annealing) allows the fabrication of optical waveguides preserving its nonlinear properties and the domain structure.

Two PPLNs are prepared for implantation. The first one (PPLN 1) is a 2D-PPLN (congruent) with a poled area of 6 mm x 6 mm in the middle of the substrate. The thickness is 1 mm and a 2D square lattice in the poled area has a period of $\Lambda = 6.92 \mu\text{m}$ and a duty cycle of 50%. The second one (PPLN 2) is the same as PPLN 1, but it is doped with magnesium oxide (MgO) at 5% mol. and it has a poled period of $\Lambda = 6.96 \mu\text{m}$.

The implantation dose is set to 1.5×10^{16} ions/cm² which may weaken the surface of the samples. However, this dose ensures a maximum refractive index variation at the optical barrier, leading to a good optical confinement. The implantation energy is fixed at 1.5 MeV. The implantation is performed on the whole surface of the samples for building a planar waveguide.

In general, it is recommended to perform a series of implantations with different energies in order to enlarge the optical barrier. However, the process takes very long the time during which the beam energy is changed (around 8 hours). For instance, Vincent *et al.* [2] made on the same sample a triple implantation with different energies of 1.5 MeV, 1.6 MeV and 1.7 MeV with the same dose 5×10^{15} ions/cm² (the total being 1.5×10^{16} ions/cm²). In this thesis, we have performed a single implantation in a few hours.

After the implantation, the sample is annealed at 200°C for one hour in an oven [2]. The annealing treatment allows the crystal to recover from the implantation-induced defects [3]. Even if an optical barrier is created, it is quite impossible to observe guided modes, especially for TM polarisation without this treatment [3].

3.2. Characterisation of implanted waveguides in 2D-PPLN

The purpose of this section is the linear and nonlinear study of the He⁺ - implanted 2D-PPLN waveguide (PPLN 1). It is proved that ion implantation creates a guiding layer in the crystal, and the global optical loss is measured. We seek a good optical confinement, a conservation of nonlinear properties of the implanted region, and a low attenuation along the waveguide. An experimental study of SHG is led in bulk and waveguide, and according to the different QPM orders.

3.2.1. Linear characterisation

The waveguide fabricated by the implantation is characterised by the refractive index profile and the optical attenuation. These characterisations are performed by indirect measurements. The *m*-line spectroscopy and i-WKB method are carried out to measure the index profile, and CCD camera is used to measure the optical loss.

3.2.1.1. Dark *m*-line spectroscopy

Dark *m*-line spectroscopy is an experimental non-destructive method of optical analysis in order to determine the effective index of a guided mode. The principle consists in exciting the waveguide modes via a coupling prism through the surface of the waveguide. In fact, this method is one of the easiest ways to inject the incident wave to the waveguide with phase matching between the horizontal components of the incident wave vector and the guided wave vector. By scanning the incident wave angle, it is possible to seek the propagation modes one by one. Angles related to coupling in the waveguide are called synchronous angles.

The *m*-line setup used in this thesis is illustrated in Fig. 3.1. The waveguide is pressed against the base of the prism at a gap distance of $g \approx \lambda/2$. The incident beam is focused on the prism base in a zone called coupling point and is totally reflected with an angle Γ_m according to the Snell law. This reflection is accompanied with an evanescent wave which is coupled into the waveguide. Thus, the prism must have a higher refractive index than the thin layer and the substrate. Then, using a goniometer on which the coupling system is mounted, the normal direction of the prism input face is referenced by auto-collimation (collimation between the incident beam and the

reflected beam normal to the prism input face). It determines the zero angle Γ_{\perp} . The determination of the synchronous angles $\Phi_m = \Gamma_m - \Gamma_{\perp}$ is performed by measuring the reflected intensity. A sharp decreasing of the reflected intensity indicates that the incident beam is well coupled into the waveguide at these angles. This causes the appearance of dark lines on the reflected image of the incident beam. From the angular position of a dark line, the effective index of the mode is determined by the relation:

$$N_{eff,m} = n_p \sin \left[A_p - \arcsin \left(\frac{\sin \Phi_m}{n_p} \right) \right] \quad (3.1.a)$$

with A_p the prism angle and n_p its refractive index. Equation (3.1.a) can be simplified:

$$N_{eff,m} = \sin A_p \sqrt{(n_p^2 - \sin^2 \Phi_m)} + \cos A_p \sin \Phi_m \quad (3.1.b)$$

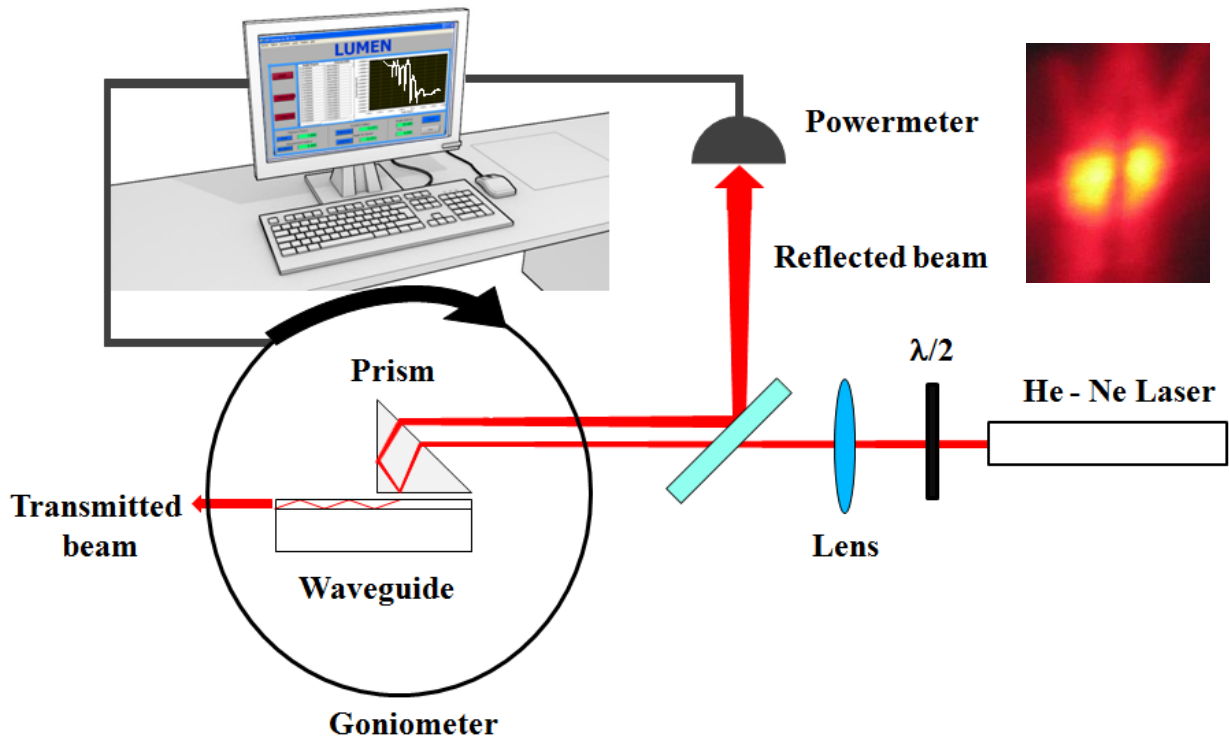


Figure 3.1: The “*m*-line” setup used in the thesis. The photography at the upright side shows reflected dark-lines indicating a light coupling in the waveguide.

Equations 3.1.b show that the measurable effective index range depends on the choice of the prism index n_p . Our choice fell on a right angle prism with angles of $30^\circ - 60^\circ - 90^\circ$ made with

the crystalline titanium oxide under the rutile form. Rutile is transparent at the used wavelength (532 nm and 632.8 nm) and the orientation of the prism optical axis (ordinary axis) is perpendicular to its lateral faces such as $n_o = 2.5911$ and $n_e = 2.8719$ at 632.8 nm. The prism dimension is 5 x 5 mm at its base.

It is possible to perform angular spectroscopy with the transmitted beam. In this case, the synchronous angles are determined by measuring the intensity at the edge of the waveguide or by using a decoupling prism. This configuration is particularly interesting to measure losses mode by mode. In that case, it is necessary to prepare a large sample so as to put two prisms.

3.2.1.2. Effective index measurements

First, we have measured the guiding properties of our He^+ NLPC sample at different wavelengths (532 nm and 632 nm). For this purpose, we have used the well-known dark m -lines method based on prism coupling in order to excite the structure guided modes (see section 2.4.1). Figure 3.2 presents the index profile obtained by m -line measurements in polarisation TE and TM for PPLN 1. Our LiNbO_3 sample is z -cut. Therefore, we can see from the figure that the waveguide supports both the ordinary and extraordinary guided modes for TE and TM modes, respectively. In fact, our samples are all cut according to the z -direction. The TE polarisation gives information on ordinary refractive index and TM polarisation on extraordinary index. To check our results, the measures must be invariant if the sample is turned around its z -axis.

The m -line measurements of angle Φ_m are converted into the effective indices $N_{eff,m}$ by Eq. (3.1.b). From this measurement in Fig. 3.2, the ordinary and extraordinary effective indices are calculated by i -WKB method. From the figures, 5 TE and 2 TM modes are almost well identified in the sample at both wavelengths. The higher order modes are considered as radiating modes and not taken into account for the i -WKB calculation. Tables 3.1 summarise the effective refractive indices of each sample measured in the PPLN zone. We have also measured m -lines in blank LiNbO_3 area (non-PPLN area), but no significant difference is observed compared to the one in the PPLN area. So it is evident that the poling process has no influence on the waveguide formation.

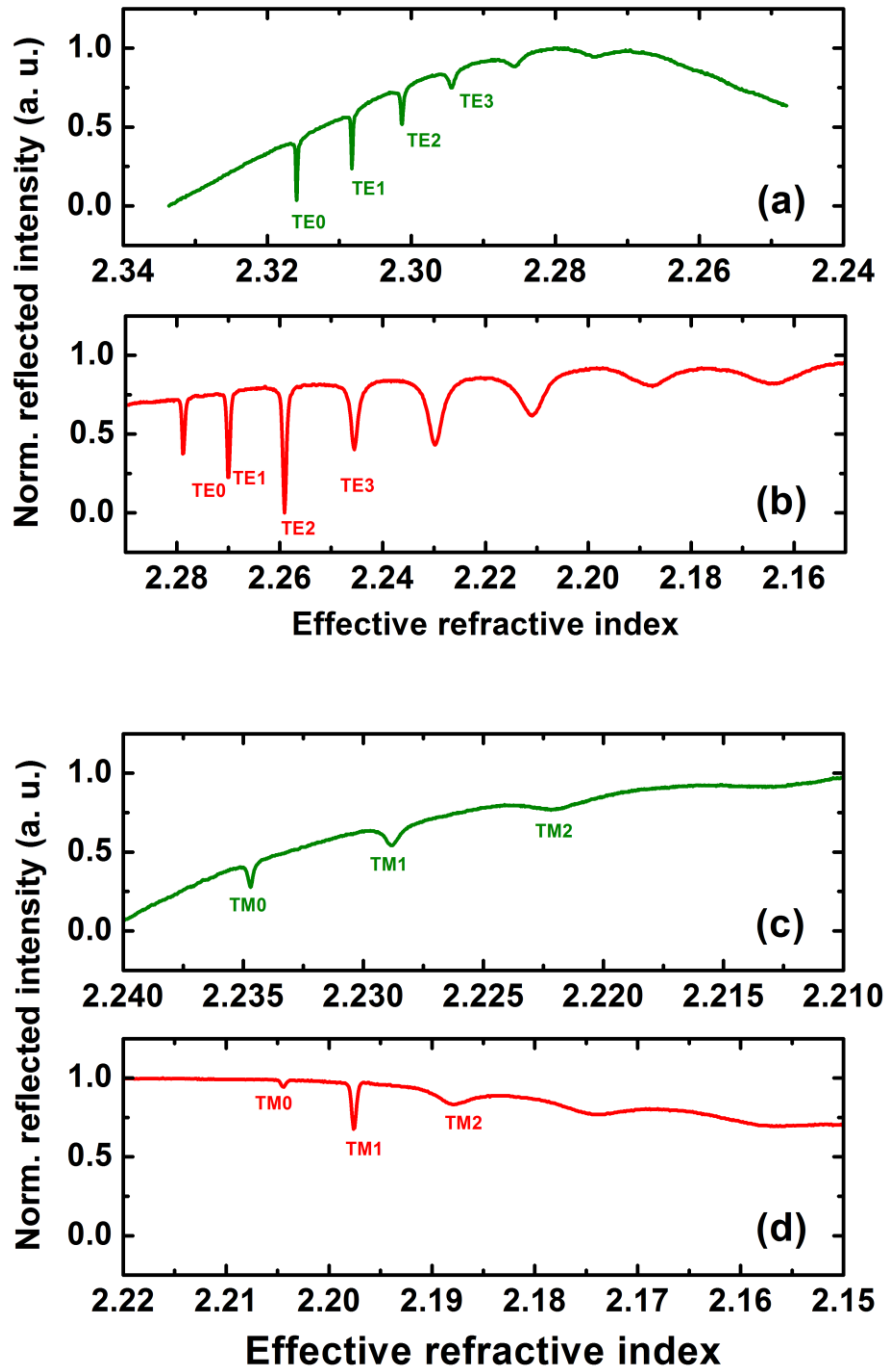


Figure 3.2: M-line measurements in PPLN 1 for TE modes (a) at 532 nm and (b) 633 nm (red line) TM-modes (c) at 532 nm and (d) 633 nm (red line).

At 532 nm	Pol.	n_{wg}	Depth (μm)	Mode order	Eff. index
PPLN 1	TE	2.3229	3.76	0	2.3159
				1	2.3082
				2	2.3014
				3	2.2945
				4	2.2856
	TM	2.2431	3.70	0	2.2347
				1	2.2288
2				2.2221	
At 632 nm	Pol.	n_{wg}	Depth (μm)	Mode order	Eff. index
PPLN 1	TE	2.2858	3.68	0	2.2787
				1	2.2701
				2	2.2589
				3	2.2454
				4	2.2297
	TM	2.2137	3.62	0	2.2045
				1	2.1979
				2	2.1868

Table 3.1: Effective index measured at 532 nm and 632 nm.

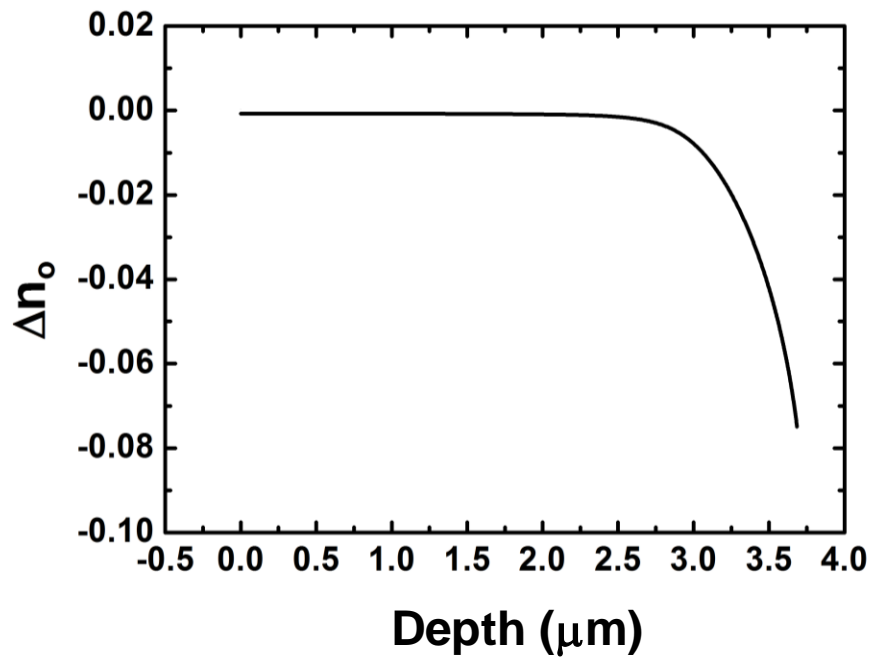


Figure 3.3(a): Ordinary refractive index profile of PPLN 1 obtained by i-WKB resolution.

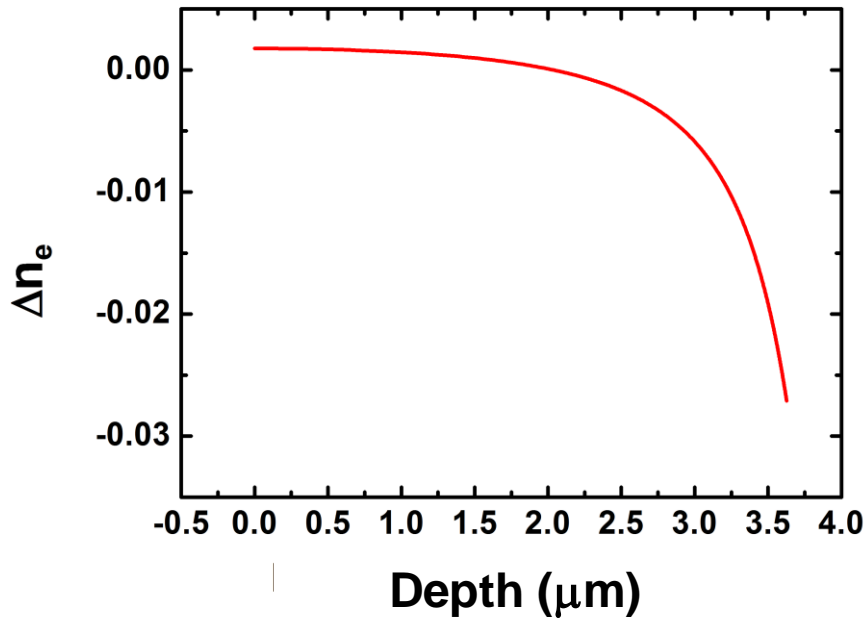


Figure 3.3(b): Extraordinary refractive index profile of PPLN 1 obtained by i-WKB resolution.

From the measured effective indices, we can determine the refractive index profile of our waveguides following the i-WKB method (see section 1.3.4). Figures 3.3(a) and 3.3(b) show the polynomial extrapolation from the calculated turning points ($z_M, n(z_M) = N_{eff,M}$) of PPLN 1 at 632 nm for both the polarisations. The index changes (Δn) are obtained by subtracting the effective indices from the refractive indices of LiNbO₃ at 632 nm ($n_o = 2.2866, n_e = 2.2023$). The i-WKB method shows the refractive index variations at the surface of the sample due to the ionisation interaction as well as in the waveguides.

We observe in Figs. 3.3 that ionic implantation has not the same influence on the ordinary and the extraordinary indices. Three points are to be noted:

- We have less extraordinary propagation modes than ordinary ones. It has a direct influence on the refractive index contrast of the waveguide. We observe refractive index variation $\Delta n_e = 0.034$ and $\Delta n_o = 0.075$. Since LiNbO₃ is a crystalline material This difference indicates that during ion implantation, channelling effect of incident ions in the crystal reveal that on-axis implantation (extraordinary direction) causes less damage and less stress in the lattice that in off-axis case (ordinary direction) [4].

- The extraordinary refractive index in the guiding region $(n_e)_{wg}$ increases slightly after the implantation, whereas the ordinary one $(n_o)_{wg}$ decreases. We find that $\delta n_e = (n_e)_s - n_e = +0.0007$ and $\delta n_o = (n_o)_s - n_o = -0.0002$. Hereafter, this will be considered in the QPM calculations. The positive change of n_e in the near surface region is well known. The profile has a typical enhanced well + barrier-type distribution as shown in Figs. 3.3. At higher dose extraordinary and ordinary refractive indices significantly change [3]. At a very high dose, the amorphisation of crystals can happen.
- The optical barrier depth is estimated to 3.7 μm in the ordinary direction and 3.6 μm in the extraordinary direction. The results are in correlation with TRIM (Transport Ion in Matter) simulation, as the ion range at 1.5 MeV has created a barrier at 3.6 μm as shown in Fig. 3.4. Therefore, the ion range results in the index barrier and this barrier depth is used as the thickness of our waveguides.

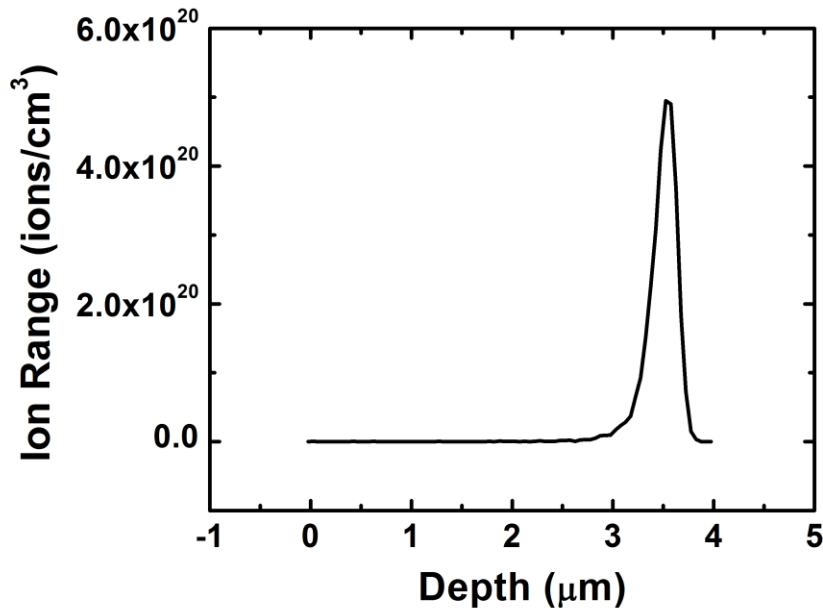


Figure 3.4: Simulated TRIM He^+ concentration in congruent LiNbO_3 after an implantation at 1.5MeV.

Finally, there has to be noted that Zhang *et al.* [5] observed that the extraordinary profile has its maximum index position buried at a certain distance beneath the surface, which can confine light propagation in several modes called missing modes. These first modes cannot be detected by

traditional m -line techniques, unless by polishing the sample surface to a suitable thickness and by measuring the difference value of the first modes. They also attributed the n_e increase in this region to the depletion of lithium due to radiation-enhanced diffusion. The lithium ions diffuse toward the nuclear damage region at the end of the ion track and from the near surface region. The same diffusion process is possible at the substrate side, creating a second positive well beyond the optical barrier.

3.2.1.3. Attenuation measurement by optical surface analysis setup

In order to complete the linear characterisation of our samples, the attenuation loss in the waveguide is measured in TE configurations. It gives information about how the light is carried along the waveguide with reliability. Thus, in this section, we briefly recall the various physical origins of losses in the waveguide. The technique used to characterise the light attenuation in our waveguides is a surface analysis of the scattered light along the waveguide as shown in Fig. 3.5. In fact, if we consider that the surface scattered intensity is proportional to the guided intensity, it is possible to estimate the attenuation coefficient α corresponding to overall losses. The light injection in the waveguide is performed by a microscope objective following the end-fire coupling technique. The attenuation has been measured with CCD camera at three different wavelengths: 532 nm, 632 nm and 1064 nm. From the top-view of the light track, we have plotted the recorded scattered intensity along the waveguide. In general, the observation condition depends on the surface quality and the number of scattering sites in the waveguide. We have limited our observation to the PP area (6×6 mm) where the scattered light is more intense and easier to measure. The main difficulty is that it should be ensured to have an identical coupling at each wavelength and in both waveguides in order to overcome the coupling loss. For instance, the scattered light from the surface of the waveguide PPLN 1 is shown in Fig. 3.6.

One other camera is placed at the output side in order to check the precise alignment of the experimental setup. It is also possible to measure the optical attenuation by collecting the transmitted intensity for waveguides with different length. The utilisation of this technique presents the disadvantage of non-selectivity of modes. It means that all guided modes are simultaneously excited and the individual mode cannot be collected. Furthermore, this technique needs a prior optical polishing of the waveguide edges.

The decay of light intensity as a function of travelled distance is written:

$$I(z) = I_0 \cdot e^{-\alpha_{cm^{-1}} z} \quad (3.2.a)$$

It can be expressed as $dB \cdot cm^{-1}$ rather than Np/cm as follows:

$$\alpha_{dB \cdot cm^{-1}} = 10 \cdot \log_{10}(e) \cdot \alpha_{cm^{-1}} \approx 4.343 \alpha_{cm^{-1}} \quad (3.2.b)$$

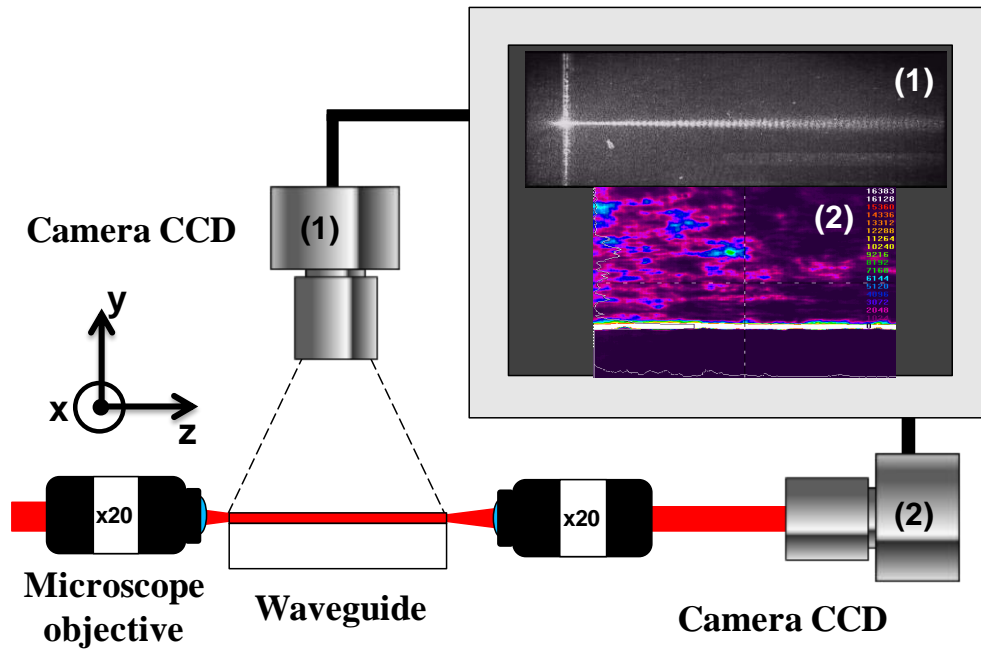


Figure 3.5: Loss Measurements by the end-coupling method. Camera 1 takes a picture of the surface scattered light in order to estimate the attenuation in the waveguide. Camera 2 takes an image of the transmitted intensity. Images (1) and (2) in the figure are from Camera (1) and (2), respectively.

Different mechanisms are at the origin of the optical losses in the waveguide:

- Absorption losses: generally, absorption occurs when the photons transfer their energy to other particles. According to the nature of particle, different reasons may lead to increasing the absorption of the material: interband transitions of electrons which generally occur in semiconductor materials, intraband absorption when photons transfer their energy to free carrier (electrons from the conduction band or holes from the valence band) or absorption due to the presence of impurities.

- Radiation losses: they are linked to the confinement quality of the waveguide. This corresponds to the dissipated energy of the propagated wave in the substrate or the superstrate by tunnelling effect. It is generally predominant for leaky modes where the value of the effective indices is close to the cut-off index of the substrate. Radiation losses must increase with the order modes, and is generally considered negligible compared with the other losses at low order modes.
- Conversion losses: they are associated to the energy transfer between different modes in a multimodal non-homogeneous waveguide structure. As the guided modes are orthogonal, the energy transfers between modes are generally omitted.
- Diffusion losses: This can take two different forms. The first one is caused by the crystalline imperfections and defects in the material and called volume diffusion losses. It depends on the concentration of diffusions centre within the crystal. The second one is due to the surface roughness of the waveguide and called surface diffusion losses. These losses are linked to the total reflections number at the waveguide interfaces. That is why surface diffusion losses increase with higher order modes.

However, the optical setup used in the work does not allow finding out the origin of losses, but give information on the overall losses by observing the light scattered at the surface of the waveguide.

3.2.1.4. Experimental results

For planar optical waveguides (with a confinement in one direction), the analysis of the intensity variation according to the propagation distance is possible by using two methods:

The simplest one is to analyse the intensity decay on few pixel range and all along the light track. The intensity is linearly fitted in log scale according to Eq. (3.2). In that case, the difficulty is an appropriate selection of the area. Statistically, the measurement of the attenuation coefficient on adjacent pixels lines can change of few percent. In Fig.3.8, the experimental variation of light intensity as a function of the propagation distance is fitted by a linear regression in a logarithmic scale (see Eq. 3.2) in order to determine the optical losses.

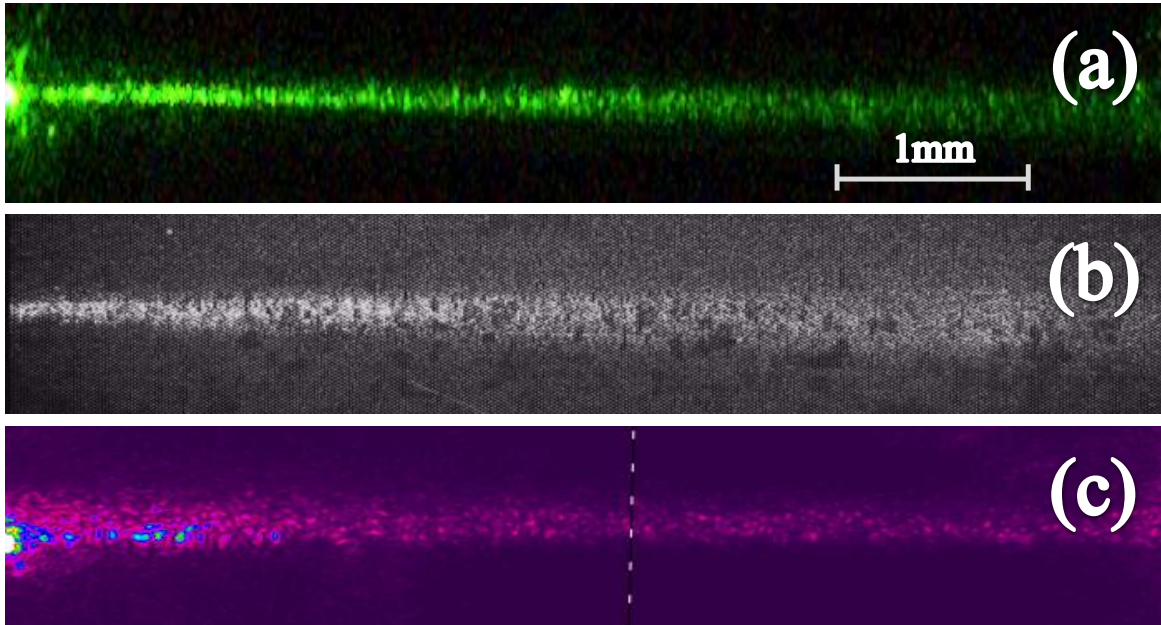


Figure 3.6: Overall optical losses recorded on the surface of PPLN 1 waveguide with a CCD camera (a) at 532 nm, (b) 632 nm (c) and a SPIRICON CCD camera at 1064 nm.

We have found from Fig.3.8 that PPLN 1 present a global optical loss of 3 dB/cm. The precision in our loss estimation is not very accurate since a tendency is taken on a line with few pixels wide (about 10). In fact, a maximum difference of 0.2dB/cm (fixed as absolute error) can be observed between two adjacent pixel lines. From Fig. 3.7, we remark that optical loss decreases as the wavelength increases.

As described in section 2.3.1, diffusion, absorption and tunnelling effects are at the origin of optical losses. We know that row PPLN is transparent at the considered wavelengths. By ion implantation nuclear defects and stress are created in the implanted region. They lead to increasing the absorption at short wavelength. Concerning diffusion loss, Rayleigh diffusion (for defects around 10 nm) can be at the origin of the attenuation behaviour ($1/\lambda^4$), whereas the Mie diffusion is maximal at wavelengths close to the defaults size.

Compared to scattering losses the loss due to tunnelling effect as an opposite effect on the optical loss behaviour with wavelength. In fact, as shown in Fig. 2.10, higher is the wavelength, higher is the electrical field penetration at the optical barrier. By this way, the optical losses should be higher at the pump wavelength (1064 nm) that at the SHG wavelength (532 nm). This behaviour

is assumed to be negligible comparing to scattering effect and considering the measurement precision.

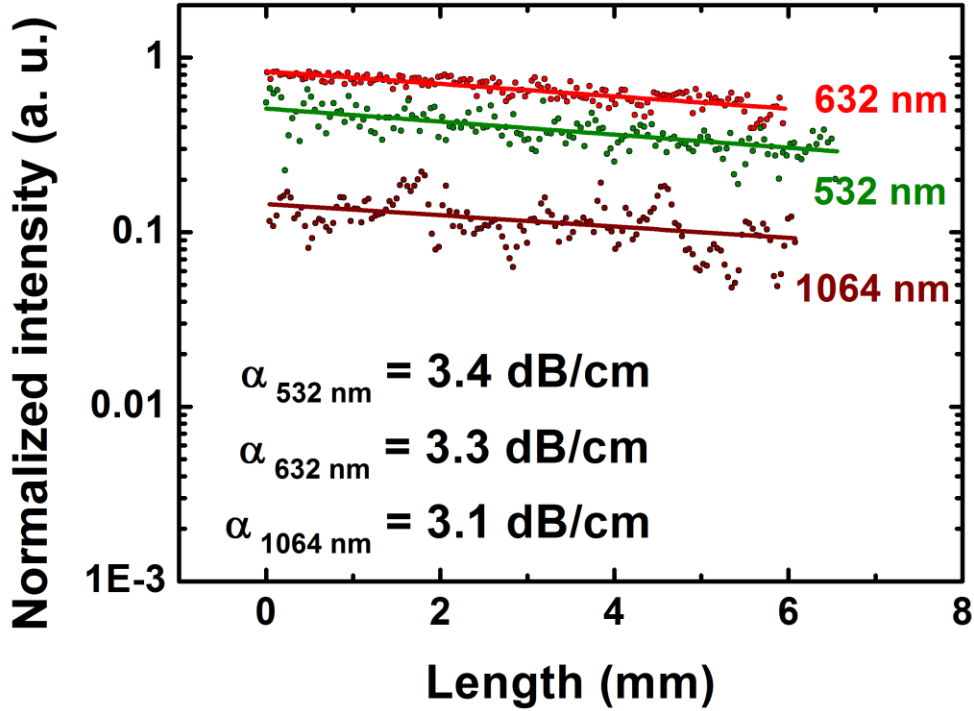


Figure 3.7: Overall optical losses obtained from the middle pixel line of the images in Fig. 3.6 at 532 nm (green dots) 632 nm (red dots) and 1064 nm (brown dots) along the He+ implanted 2D PPLN waveguides (PPLN 1).

Another technique is based on top-view image only. In that case, we have to take care of the Gaussian decreasing measurement with a distance x in the waveguide. The intensity profile is expressed:

$$I(r, z) = I(z) e^{-\frac{2r^2}{w^2(z)}} \quad (3.3.a)$$

with $r^2 = x^2 + y^2$ and $w(x)$ the beam waist size is written as:

$$w(z) = w_0 \sqrt{1 + \left(\frac{\lambda z}{\pi w_0^2}\right)^2} \quad (3.3.b)$$

Figure 3.8 shows few results from this technique. The image in Fig. 3.8(a) is captured by Camera 1. The light intensity of each pixel column of the image is averaged along the light trace of 3.7 mm and linearly fitted in Fig. 3.8(b). From the fitting, the loss is obtained as 0.143 /mm which corresponds to 6.2 dB/cm from Eq. (3.3.a).

However, the beam in the planar waveguide spreads out during the propagation as seen in Fig. 3.6. With the optical confinement in y direction, we can write that $r^2 \rightarrow x^2$. If we now consider the intensity average in x direction, we get from equation (3.3.a):

$$\overline{I(z)} = \frac{I_0 \cdot e^{-\alpha z} \int_{-x}^x e^{-\frac{2x^2}{w^2(z)}} dx}{\Delta x} \quad (3.3.c)$$

with Δx the number of pixels in the image in x direction. If we consider that $x \rightarrow +\infty$, the integration can be simplified as:

$$\overline{I(z)} = \frac{I_0 \cdot e^{-\alpha z} \sqrt{\frac{\pi}{2}} w_0 \sqrt{1 + \left(\frac{\lambda z}{\pi w_0^2}\right)^2}}{\Delta x} \quad (3.3.d)$$

Taking into account the beam waist increase, the averaged intensity is refitted from Eq. (3.3.d) in Fig. 3.8(c).

The fit curve matches to the averaged intensity very well. The loss is obtained as 0.069 mm^{-1} which corresponds to 3 dB.cm^{-1} . This loss is considered as the loss of our sample hereafter.

These both methods give the similar attenuation coefficient. All depends on the image area included in the calculation.

Different ways allow the attenuation improvement along the waveguide:

- By broadening the optical barrier through multiple-implantation energies ion implantation, it is possible to reduce the tunnelling effects.
- The attenuation can be improved by increasing the annealing time after implantation. However, it may destroy the optical barrier if the annealing time is too long. Vincent et al.

demonstrated that 2-hour annealing at 200°C allows reducing the optical loss without destroying the guiding layer [1].

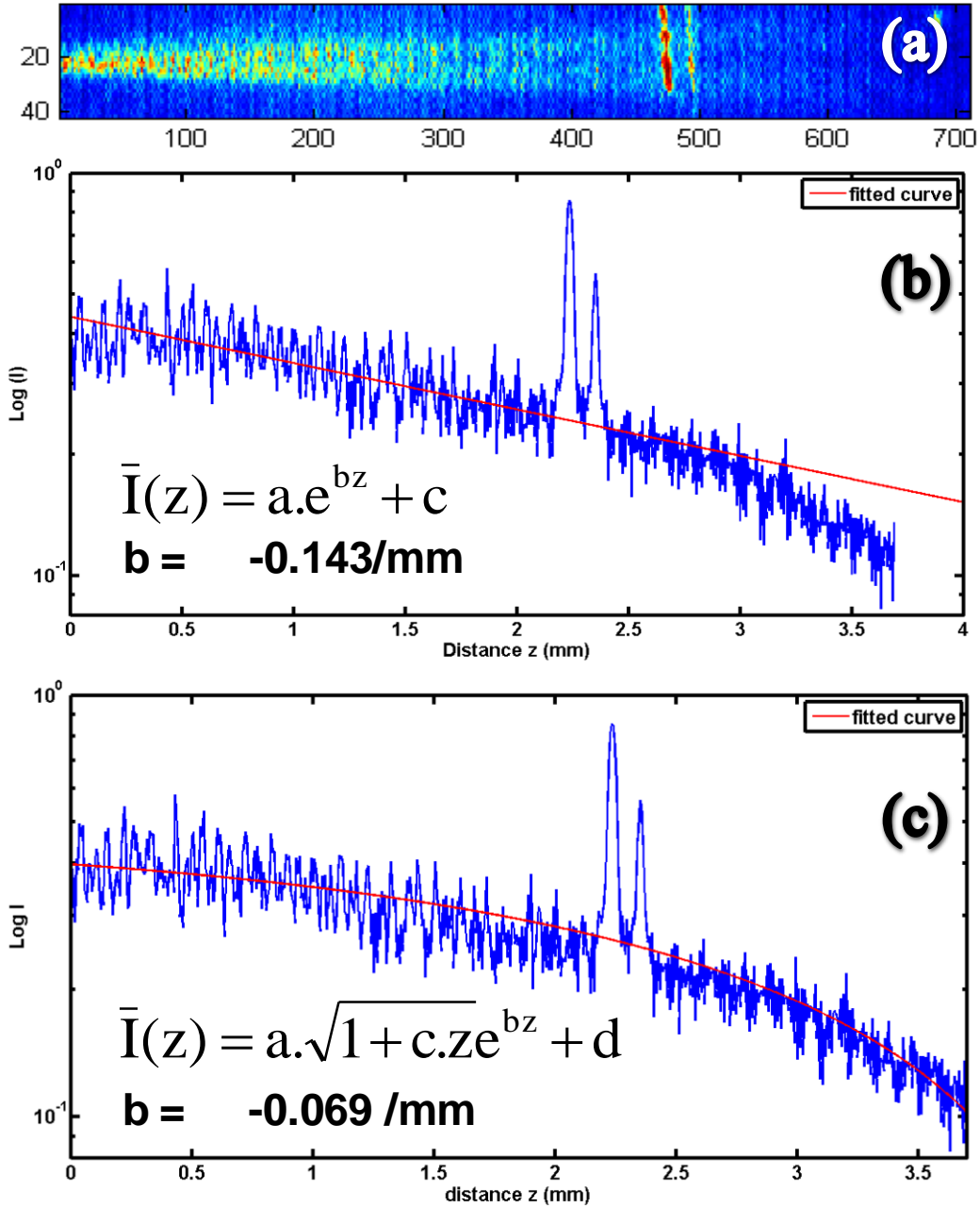


Figure 3.8: (a) Top view image of the light collected on the planar waveguide surface. (b) Averaged intensity of each pixel column along the light trace in log-scale with a linear fit curve in red line (c) with a modified fit curve taking into account the beam spread in red.

3.2.2. Nonlinear characterisation

The waveguide fabricated by He⁺- implantation is characterised by the refractive index and optical loss. As it has nonlinear properties, it is now essential to undertake its nonlinear characterisation. The experimental results for nonlinear characterisation include exclusively second harmonic generation (SHG) measurements from 2D-PPLN: The SHG intensity for different reciprocal lattice vectors (RLV) is measured according to the temperature, the angle dispersion and finally the SHG conversion efficiency is measured in cw-regime and in pulsed regime. The efficiencies in bulk and waveguides are compared.

3.2.2.1. Optical setup

The nonlinear characterisation of our sample is undertaken with different pump sources at 1064 nm. In fact we have decided to study the influence of the optical power density on SHG conversion efficiency in CW (Continuous Wave) and pulse regimes.

In cw-regime, we have used a laser diode Axcel Photonics (M9 A64-0350-S50) emitting cw at 1064 nm \pm 5 nm with a maximum optical power of 300 mW. The emission spectra of our laser diode are measured according to the driving current and temperature. This measurement allows finding the optimal conditions for our experiment and to check the stability of our source. We have measured the emission spectra using an OSA (Optical Spectrum Analyser Yokogawa Q8341) via an optical fibre while scanning the driving current. The measurement has been repeated for different temperature, in order to find a single-mode operating condition at 1064 nm. Figure 3.9(a) presents the spectra measurements as a function of the laser current at 38°C. The current is varied from 0 to 450 mA by a step of 1 mA (500mW corresponds to the kink current).

From the figure the current threshold is measured as 28 mA and the laser diode emits a single-mode emission at 1064 nm between 400 mA and 450 mA. The working conditions have been determined at 38°C and 430 mA. The corresponding spectrum is presented in Fig. 3.9(b), with a FWHM (Full-Width Half Maximum) of $\Delta\lambda = 0.11$ nm at 1064.09 nm. We have also checked the drift of the optical power with the temperature. The laser source delivers a relative constant power with a drift of 0.3 mW/°C.

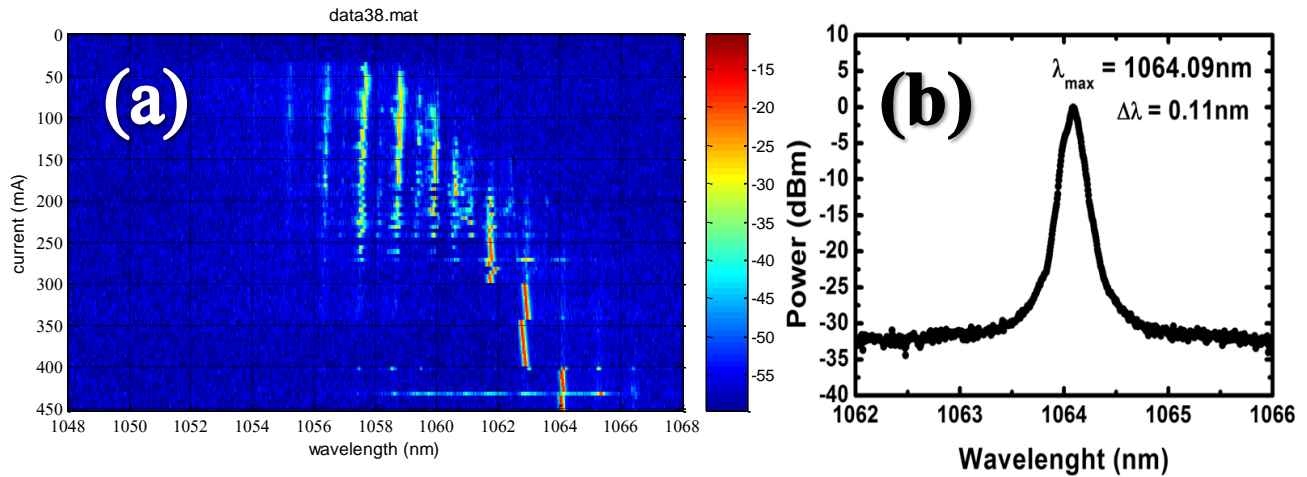


Figure 3.9(a): Emission spectra of laser diode emitting cw at 1064 nm at 38°C with respect to the driving current. The colour scale indicates the optical power of the spectra in dBm. (b) Wavelength spectrum of the laser diode at 38°C and 430 mA.

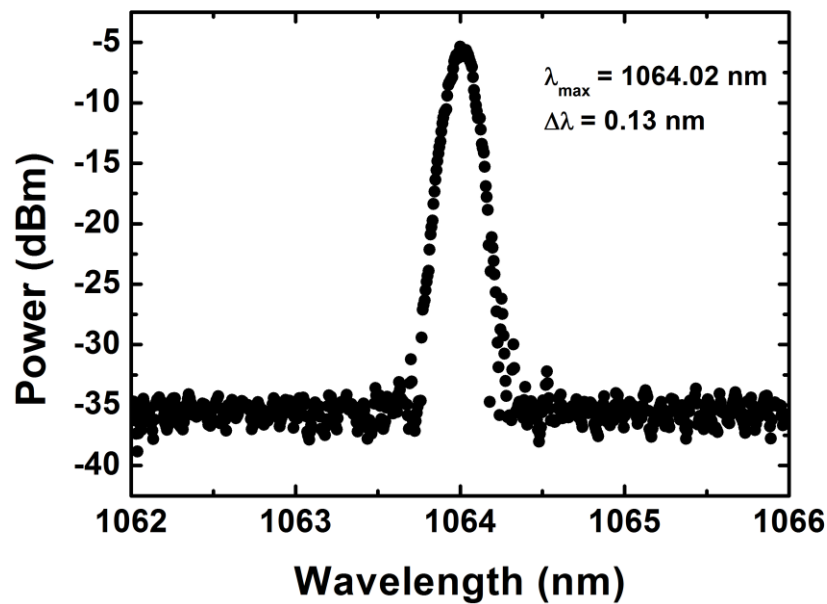


Figure 3.10: Spectrum of the Nd:YAG Q-switched-Laser.

For the pulsed regime, we have used an Nd:YAG Q-switched-Laser with a repetition rate of 10 Hz and a pulse width (FWHM) of 6 ns at 1064 nm. The laser spectrum is shown in Fig. 3.10.

The experimental setup is illustrated schematically in Fig. 3.11. In the first place, the laser diode or the Q-switched laser is used as the pump laser. For the laser diode, the beam is collimated with an aspherical lens with a focal length of 4.51 mm. In this way, the beam-size is fixed to a diameter of 4 mm.

For the Q-switched laser, we have used a 50 cm focal length lens to reduce the beam waist from 3.5 mm to 450 μm in front of the microscope objective. The laser beam waist measured by a SPIRICON CCD camera in combination with a graticule grid at the beam waist location. Most of nonlinear measurements are undertaken with the Q-switched laser and the laser diode is used only for the conversion efficiency measures in the cw-regime.

Between the lens and the objective, two polarising beam splitter cubes and a half-wave plate ensure the laser polarisation and attenuation. TE- or TM-polarisation can be selected by these components and the pump power is adjusted by turning the half-wave plate.

A microscope objective (MO x20) is placed at the beam waist position of the pump and AR coated at 1064 nm. Finally, the laser beam is coupled to the waveguide. However, this coupling configuration is not adapted for bulk case. This will be discussed later.

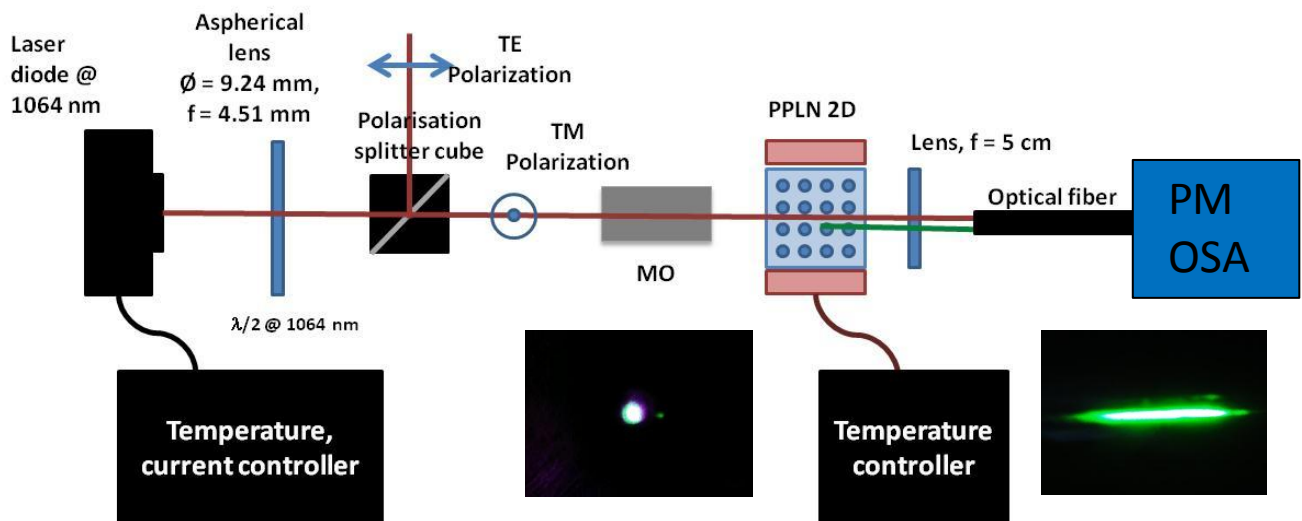


Figure 3.11: SHG experimental setup.

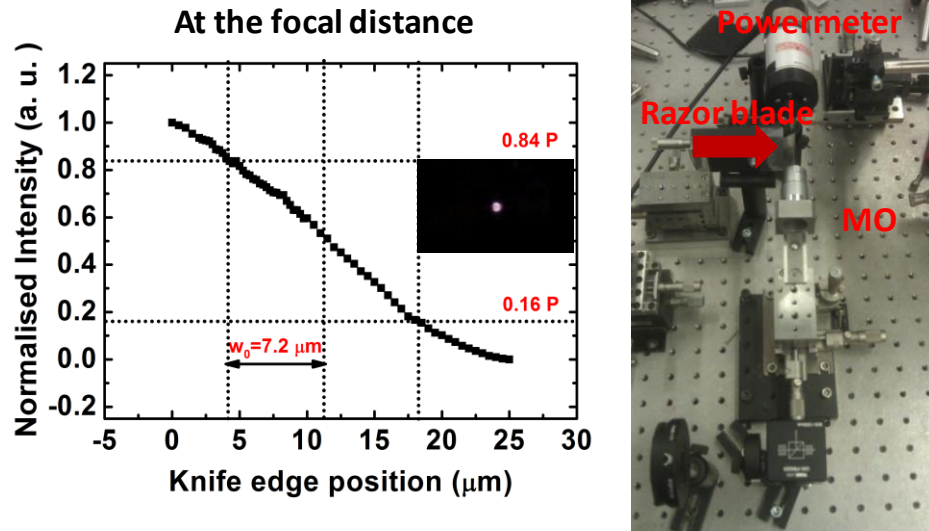


Figure 3.12: Knife edge method used to measure the coupling beam waist. From the intensity obtained along the straight cut-section of a Gaussian profile, the beam waist at $I(z)/e^2$ is measured as $7.2 \mu\text{m}$.

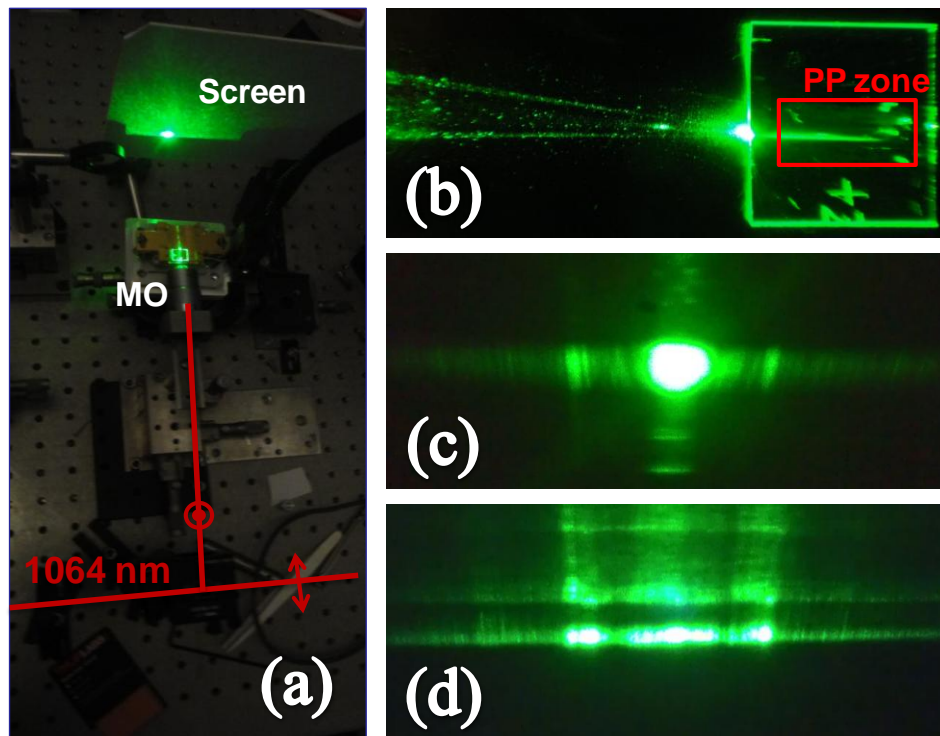


Figure 3.13: (a) SHG from the PPLN 1 waveguide. (b) Top-view of PPLN 1 pumped at 1064 nm. The output SHG far-field image(c) from the PPLN 1 bulk and (d) from the PPLN 1 planar waveguide.

The beam waist focused on the facet of waveguides has been measured by knife-edge method with a razor blade. The laser light is collected as moving the blade in a microscale at the focus position as shown in the photo of Fig. 3.12. The graph of Fig. 3.12 shows the normalised light intensity measured as a function the razor blade position. From the measure, beam size is obtained as 14.4 μm . We will consider this measure as the beam waist at the front facet of the waveguide.

With this configuration, the light is injected into waveguide at the normal incident angle and generates SHG signal as shown in Fig. 3.13. The NLPC samples are on a hotplate and temperature-controlled in order to achieve phase matching at the pump laser wavelength. The output SHG signal is then collected by an optical fibre through a lens and sent to an Optical Spectrum Analyser (Yokogawa AQ6373). For SHG power measurements, instead of the lens and the fibre a dichroic mirror HR tilted at 45° for removing 1064 nm and a powermeter are placed at the crystal output.

3.2.2.2. SHG temperature tuning

A first step is to measure the optimal crystal temperature conditions for SHG in PPLN 1. The hotplate is driven with a precision of 0.1°C and we heat the crystal from room temperature to 140°C . A first measure is made with the OSA in order to observe the evolution of the SHG spectrum with temperature. Figure 3.14 shows the spectrum of the SHG emitted in normal direction from the sample. The maximum-peak wavelength is not shifted during the acquisition and remains at 532 nm. As we have seen in section 1.5.6, the temperature dependence of the SHG power can be fitted with a *sinc* function with a maximum measured at 53°C .

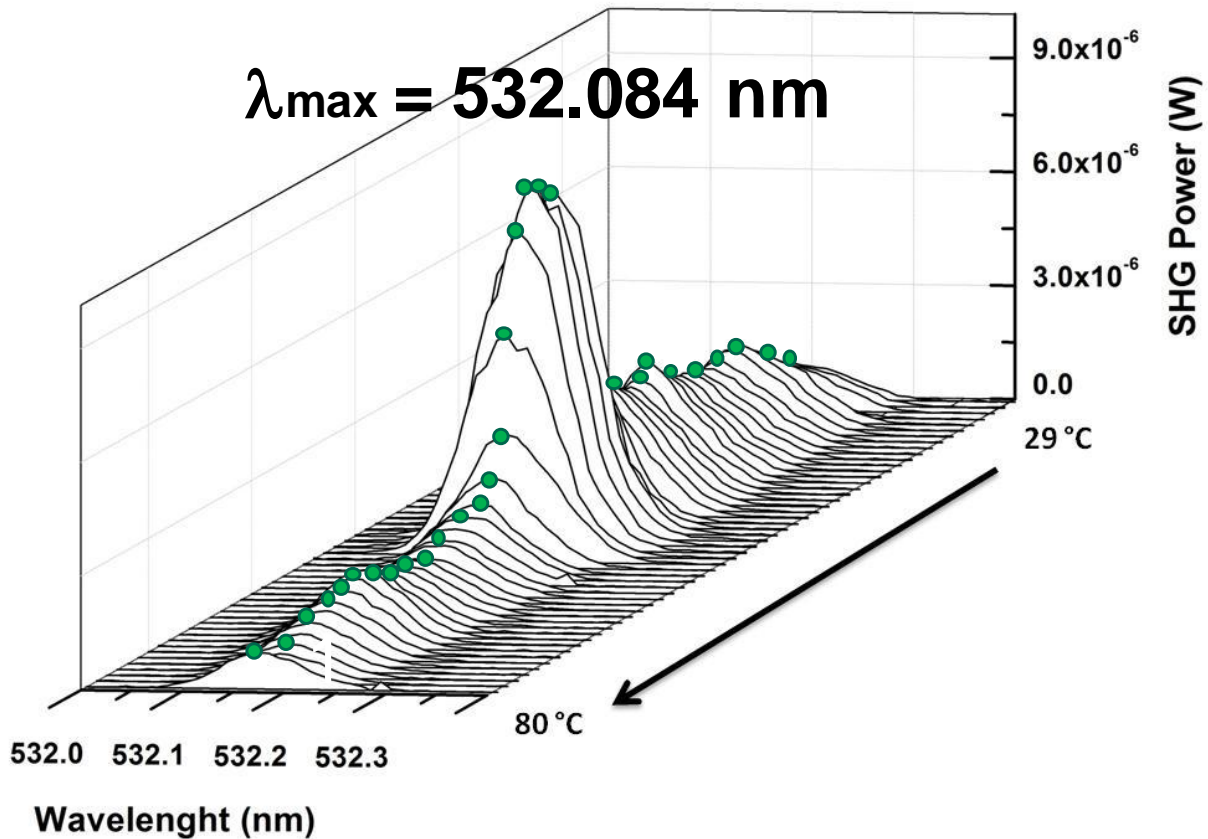


Figure 3.14: SHG spectrum of PPLN 1 taken at different temperatures.

Then, the SHG power dependence with temperature (Figs. 3.15) is measured with a powermeter. Concerning the PPLN 1 bulk, the SHG from the RLV \mathbf{K}_{10} is observed with a maximum power obtained at 53°C in Fig. 3.15(a). So, a QPM is achieved at this temperature. However, in 2D PPLN QPM is also possible from the reciprocal lattice vectors (RLV). At higher temperatures, the RLVs $\mathbf{K}_{1\pm 1}$ involve in producing a new QPM condition. The new QPM condition due to these RLVs is observed at 102°C. In the inset of Fig. 3.15(a), the image taken from the CCD camera clearly shows three SHG spots for the RLV \mathbf{K}_{10} in the middle and $\mathbf{K}_{1\pm 1}$ at the outer side.

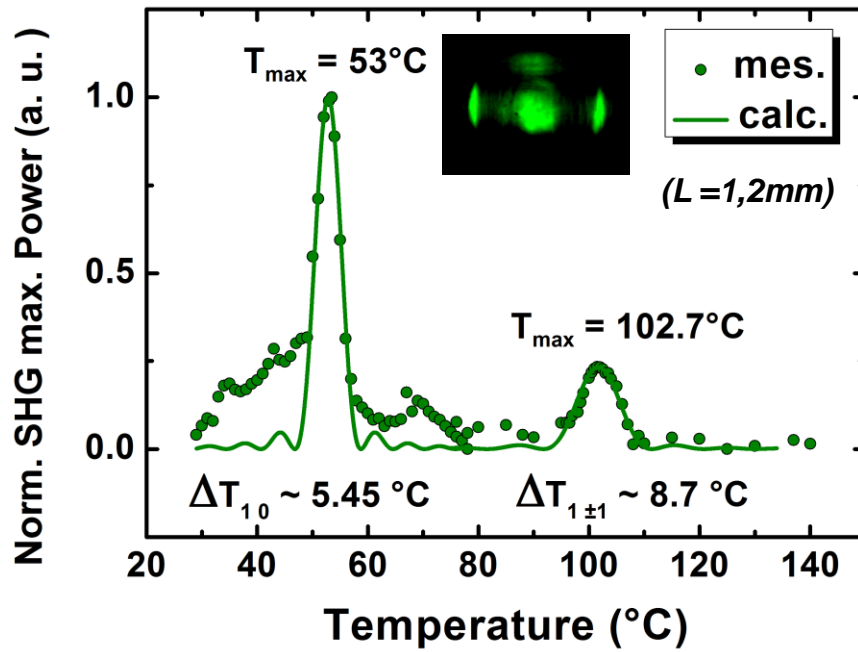


Figure 3.15(a): Normalised optical SHG powers vs. temperature from PPLN 1 bulk

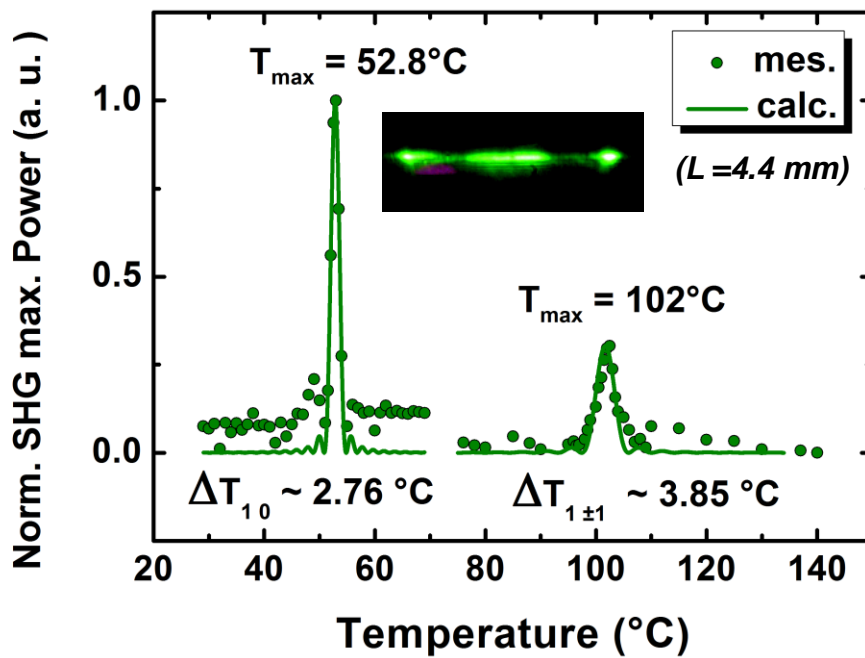


Figure 3.15(b): Normalised optical SHG powers vs. temperature from PPLN 1 waveguide.

Figure 3.15(b) shows the results for the waveguide case. The temperatures for the RLVs agree to those for the bulk case.

- We observe a slight shift of the maximum peaks temperature in the waveguide configuration ($\approx +0.2$ °C). This shift is due to the slight modification of the extraordinary index in the waveguide and determined in section 3.2.2. From the model plotted in Fig. 3.15, the maximum SHG power is calculated at 56°C, one supposition could be a modification of the poling period by thermal expansion of the crystal
- However, the temperature bandwidths are different in waveguide or bulk configurations. For both QPM orders, the temperature bandwidth is lower in the waveguide than in the bulk. From the fitted curves, the interaction length L is obtained as 1.2 mm in the bulk ($\Delta T_{10} = 5.45$ °C) and 4.4 mm in the waveguide ($\Delta T_{10} = 2.76$ °C) for PPLN 1. So the nonlinear interaction has not occurred over 6 mm which is the total length of the poled region. As we work with a planar waveguide, the light confinement happens in only one direction. We suppose that the underestimated interaction length is due to the fundamental beam divergence in the non-confined direction.

3.2.2.3. SHG angular dependence

As shown in the previous section, we observe SHG at different QPM orders: at least (1, 0) and (1, ± 1) when the temperature changes. Figure 3.16 shows the far-field SHG images in the PPLN 1 bulk and waveguide configurations. It indicates that the TM-modes can contribute to the SHG for the RLVs of \mathbf{K}_{10} , and $\mathbf{K}_{1\pm 1}$. By using the nonlinear Bragg law (Eq. 1.63), we can predict the walk-off angles ψ_{mn} of each RLV.

From Eq. 2.20, the calculated angles ψ_{mn} at 53°C are 0° for \mathbf{K}_{10} , ± 4.6 ° for $\mathbf{K}_{1\pm 1}$ and ± 8.9 ° for $\mathbf{K}_{1\pm 2}$. In Fig. 3.17(b), at 53°C the SHG signal is observed for \mathbf{K}_{10} only. In Fig. 3.17(c), at 102°C the SHGs are also observed around ± 5 ° in both the bulk and the waveguide, which are close to the calculated ones.

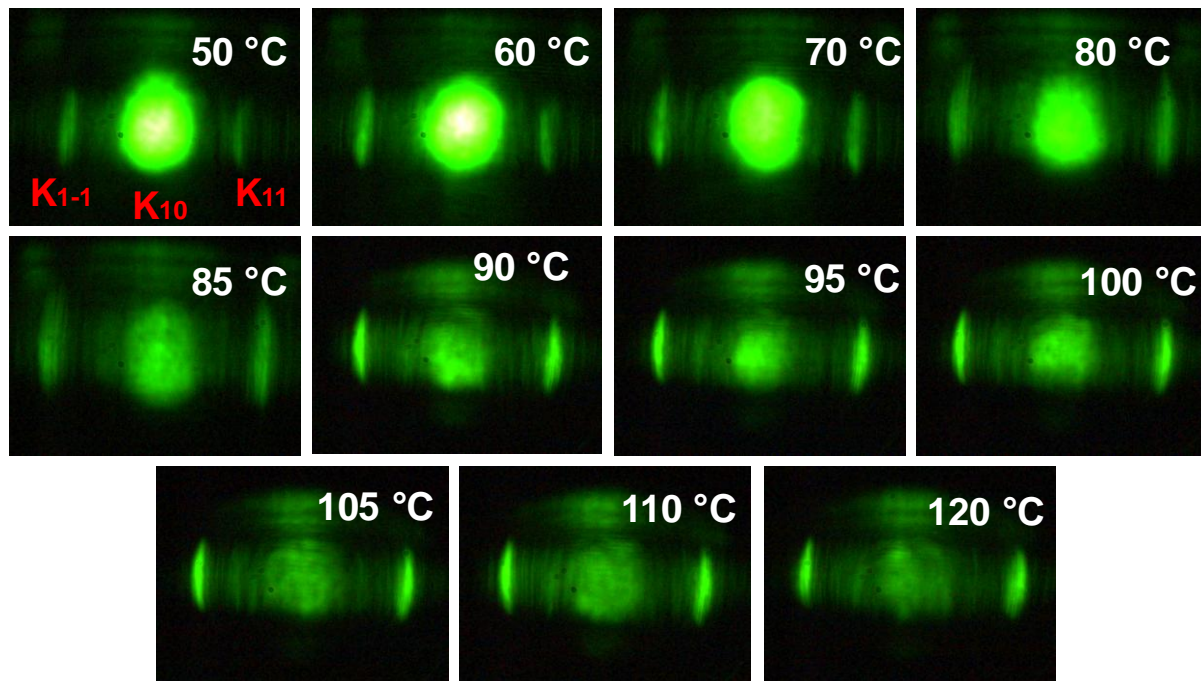


Figure 3.16(a): Far-field SHG images observed by a CCD camera in PPLN 1 for the bulk configuration

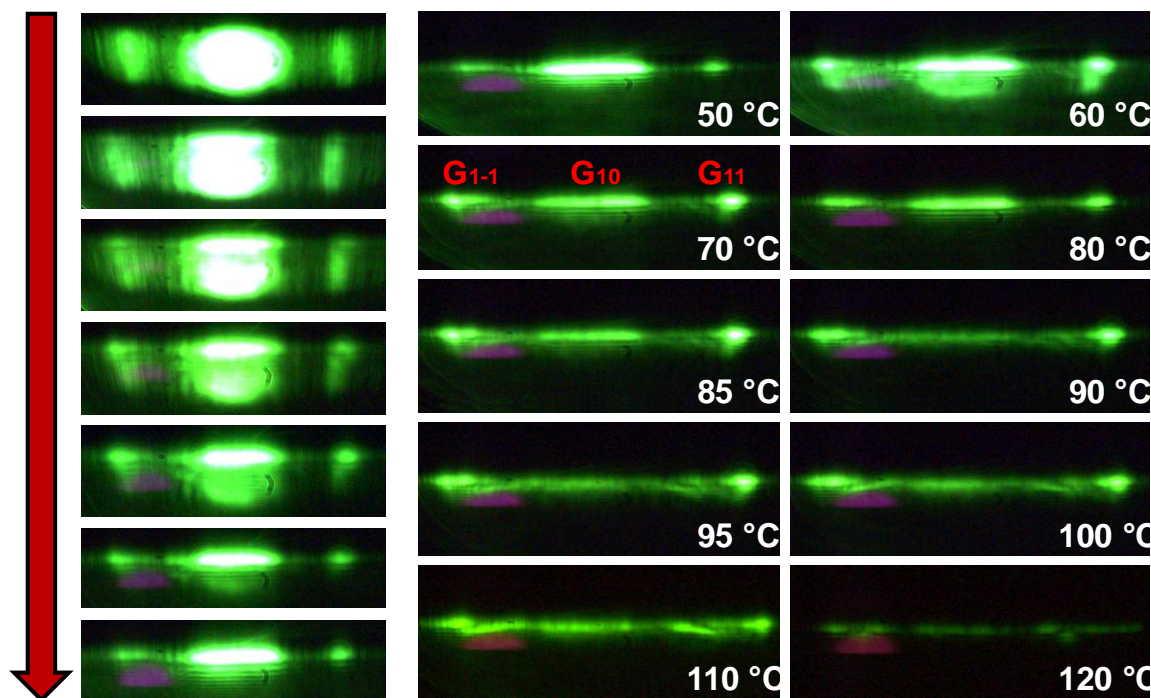


Figure 3.16(b): Far-field SHG images observed by a CCD camera in PPLN 1 for the waveguide configuration. The first column shows SHG signal when the pump source is coupled into the planar waveguide.

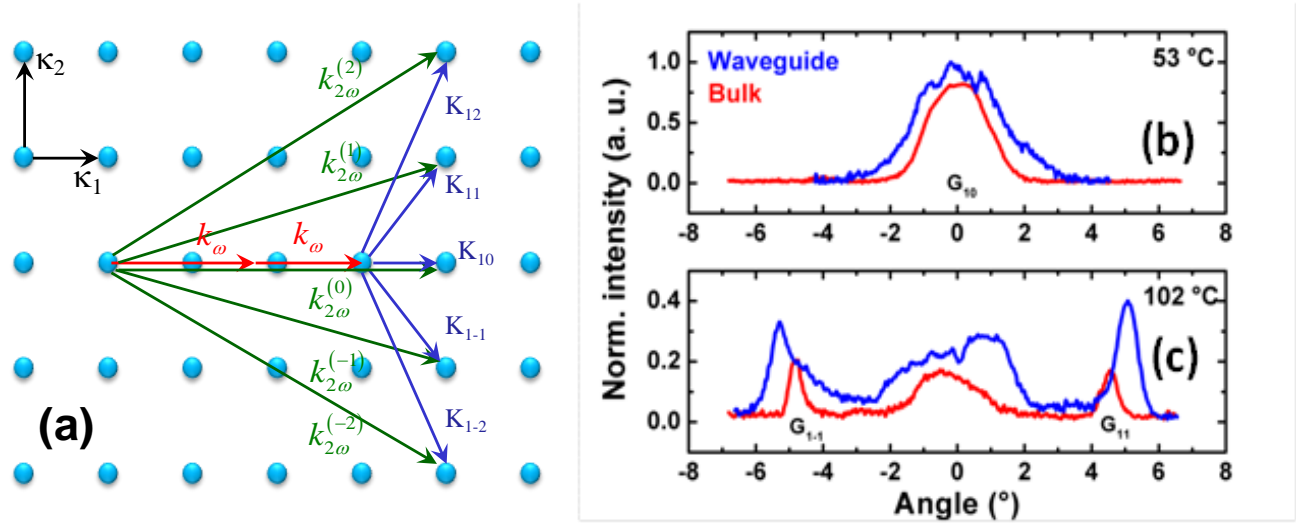


Figure 3.17: (a) Schematic geometrical reciprocal lattice for SHG interaction. (b) Normalised far-field SHG intensity distribution from PPLN 1 obtained at crystal temperatures of 53°C and (c) 102°C, in bulk (red trace) and waveguide (blue trace). The QPM orders (1, 0) and (1, ± 1) are visible.

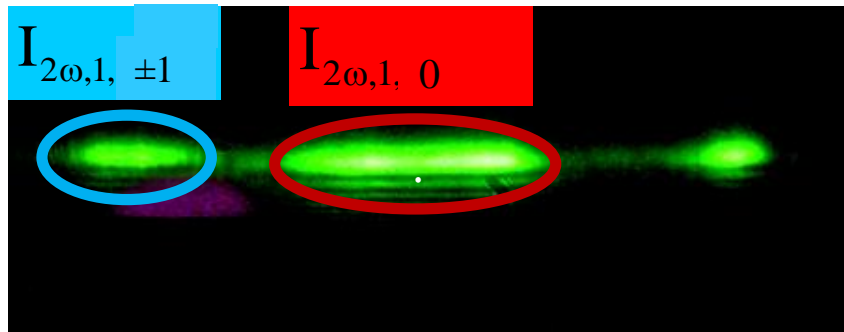


Figure 3.18: Measure of the maximum SHG intensity ratio between the QPM orders (1,0) and (1, ± 1).

This is a clear evidence of the RLV contribution to SHG, which is not observed in 1D-PPLN. Moreover, the SHG intensity for $K_{1\pm 1}$ in the waveguide is higher than that in the bulk with a slight drift angle due to the refractive index change in the waveguide. It is clearly seen from the figure that the SHG efficiency is improved in the waveguide.

Concerning the SHG intensity ratio between the QPM orders (1, 0) and (1, ± 1) and defined by $r_{\pm 1/0} = I_{2\omega,1,\pm 1} / I_{2\omega,1,0}$, we observe that it never exceed experimentally 0.55 in the waveguide.

In theory, it has been demonstrated in section 1.6.2 that the effective nonlinear coefficient depends on the Fourier coefficients G_{mn} obtained from the Fourier transform of the reversed poled distribution. Thus, in the case of phase matching with $\Delta k = 0$, the SHG intensity is written:

$$I_{2\omega,m,n} = \frac{2\omega^2 d_{33} |G_{mn}|^2}{n_{2\omega} n_{\omega}^2 c^3 \epsilon_0} I_{\omega}^2 L^2 \quad (3.4)$$

with ω the fundamental frequency, d_{33} the nonlinear coefficient, $n_{2\omega}$ and n_{ω} the refractive index of the crystal at the SHG and fundamental wavelengths, I_{ω} the pump intensity and L the interaction length in the crystal. These parameters remain unchanged between two QPM orders in bulk or waveguide configuration.

From Eq. (1.56), if we consider a square lattice with circular motif, we get:

$$|G_{mn}|^2 = \left| \frac{D}{\sqrt{m^2+n^2}} \cdot J_1(\pi D \sqrt{m^2+n^2}) \right|^2 \quad (3.5)$$

with (m, n) the QPM order, D the duty cycle (fixed at 50%) and J_1 the first-order Bessel function.

Finally, we assume that the limiting factor for $r_{\pm 1/0}$ is only the rate between the absolute square of the relevant Fourier coefficients, such as:

$$r_{\pm 1/0} = \left| \sqrt{2} \frac{J_1(\pi/2)}{J_1(\sqrt{2}\pi/2)} \right|^2 \approx 0.47$$

We observe that this limiting factor is reached in the optimal waveguide configuration.

3.2.2.4. Conversion efficiency measurement in cw- and pulsed regime

We report the SHG power at 532 nm versus the pump power at 1064 nm. For this work, we will study SHG in pulsed regime with the Q-switched laser as well as in cw regime at much lower pump power density with the diode laser. In both the cases, the Fresnel reflection is considered at the air/PPLN interface to estimated coupled power. These reflections occur when the optical connection presents a discontinuity, particularly during the coupling of light in the waveguide. The light which propagates in air undergoes partial reflection due to the abrupt change of refractive index of the propagation medium at the input waveguide face. This reflection can be evaluated from the Fresnel coefficient R , which represents the ratio between the reflected power

by the discontinuity P_R and the incident power P_I . If we consider that the input and output faces are polished, with non anti-reflection coating or index matching materials and if the incident wave propagation is perpendicular to these faces, we have:

$$R = \frac{P_R}{P_I} = \left(\frac{n_w - n_a}{n_w + n_a} \right)^2 \quad (3.6)$$

with n_a the refractive index of the external medium (air) and n_w the refractive index of the waveguide. Concerning the nonlinear characterisation of our samples, the input power at 1064 nm has been measured and weighted by the Fresnel coefficient such as $n_a = 1$, $n_w = 2.1555$ and finally $R = 13.4 \%$. Thus, 86.6 % of the measured fundamental power is considered as the pump power. It represents a loss due to the Fresnel reflection:

$$L = 10 \log(1 - R) = -0.62 \text{ dB} \quad (3.7)$$

between the injecting input power and the real power injected into the waveguide. This means that the reflected power is not negligible compared to the incident power. We have also estimated the coupling coefficient in waveguide which corresponds to 18% of the measured pump power. This value corresponds to the coupled energy of the pump beam with a waist of 7.2 μm in a waveguide with a thickness of 3.6 μm .

The SHG intensity is measured at the output of the waveguide and the pump source is filtered out. As SHG from different QPM orders (1, 0) at 53°C and (1, ± 1) at 102°C are visible in pulsed regime for PPLN 1, we have measured the SHG power at these temperatures and by varying the pump power. The SHG power results in pulsed regime are shown in Figure 3.19 (a) from waveguides (b) and bulk and are expressed in peak power (the repetition rate is 10 Hz and the pulse width is 6 ns). Furthermore, Fig. 3.19 (c) shows that SHG curve tends to a saturation regime. The SHG saturation of the crystal results in the same saturating power at high pump power. Nevertheless, we observe a SHG improvement of $\approx 65 \%$ in the waveguide configuration compared to the bulk configuration. However, the improvement lowers at 102°C from the QPM order (1, ± 1).

At high power density, we clearly see that the saturation regime is reached at lower pump intensity in the waveguide: around 200 MW/cm² with a conversion efficiency of 56% in the waveguide and around 250 MW/cm² with a conversion efficiency of 8.5% in the bulk.

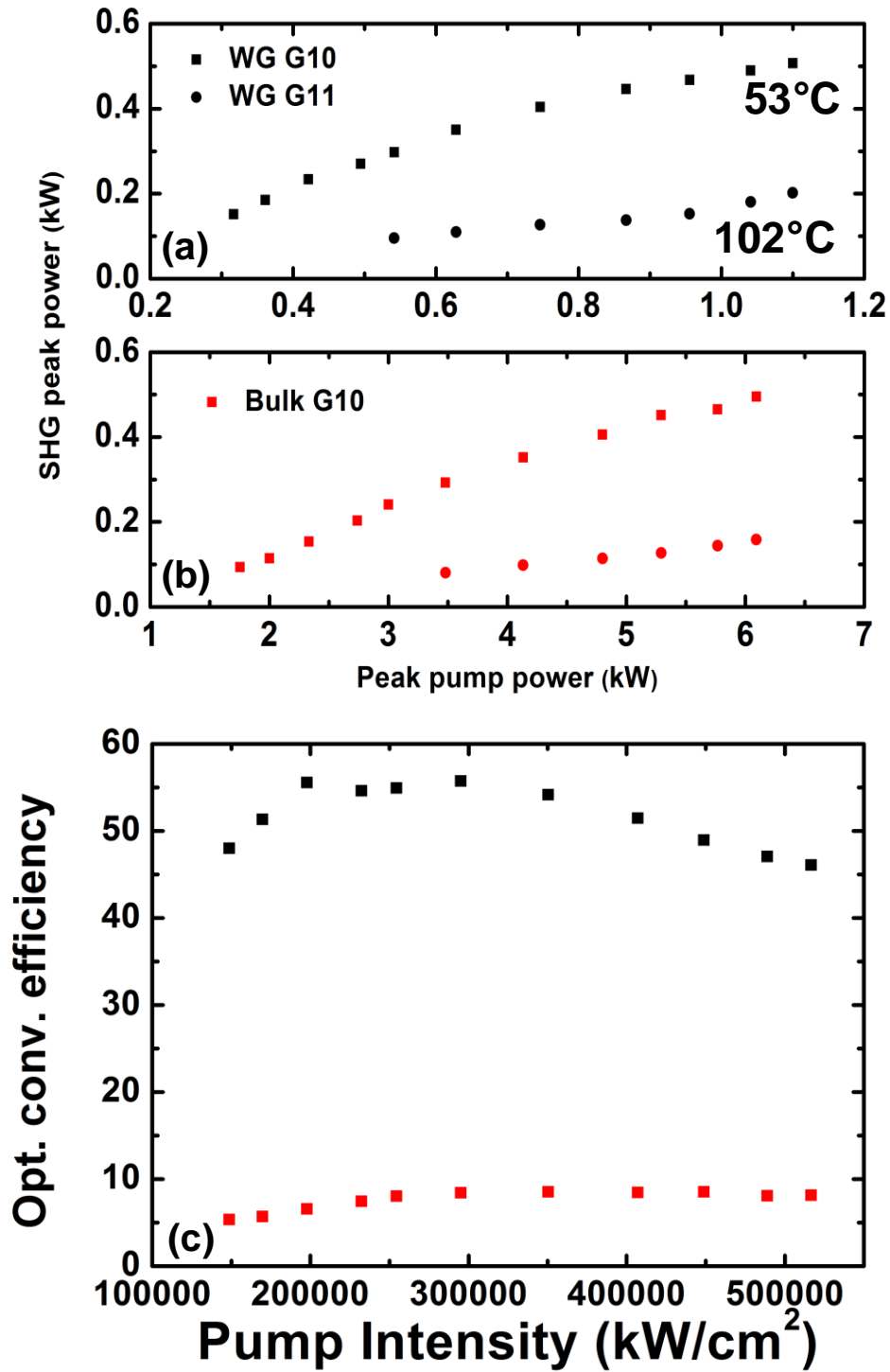


Figure 3.19(a) SHG output power vs. pump power in the pulsed regimes in PPLN 1. (b) Conversion efficiency resulting from the PPLN 1 waveguide (black points) and the bulk (red points) in pulsed regime.

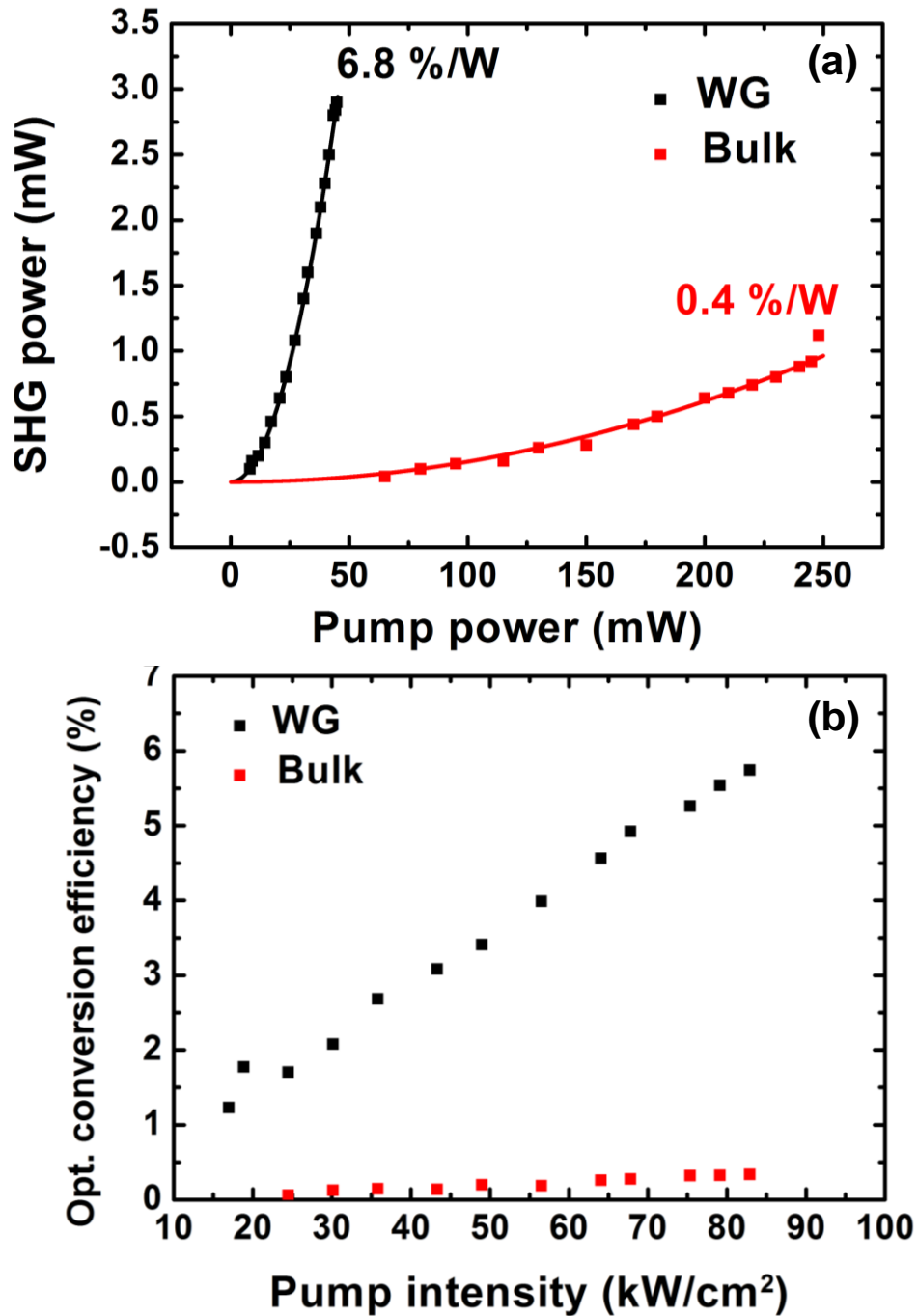


Figure 3.20(a) SHG output power vs. pump power in the CW regimes in PPLN 1. the numerical fit results in a nonlinear conversion efficiency of 6.8%/W for the waveguide configuration and 0.4%/W in the bulk case. (b) Conversion efficiency resulting from the PPLN 1 waveguide (black points) and the bulk (red points) in CW regime.

The same measure is also realised in cw-regime. The results are presented in Fig. 3.20. The pump power is sufficiently low to measure the SHG quadratic behaviour. At the maximum power of the laser diode, the SHG power from the waveguide reaches 2.9 mW whereas 1.1 mW is measured from the bulk. Thus, the SHG power from the waveguide is three times stronger than that from the bulk. Taking into account the coupling loss, Figure 3.20 (a) shows the experimental results, fitted to the theoretical curve for second harmonic generation with a polynomial function. The fitting gives a nonlinear conversion efficiency of 6.8 %/W for the waveguide and 0.4 %/W for the bulk case.

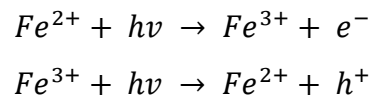
From these measures, Figure 3.20 (b) shows the SHG conversion efficiency (see Eq. (1.32)) dependence with the pump power density (normalised by the beam area). In cw-regime, a maximum conversion efficiency of 5.8 % is reached. The bulk and waveguide cases have linear behaviour with pump intensity, and their slope difference is firstly attributed to the interaction length difference, having a factor 16 between conversion efficiencies.

At high power density, we clearly see that the saturation regime is reached at lower pump intensity in the waveguide: around 200 MW/cm² with a conversion efficiency of 10% in the waveguide and around 250 MW/cm² with a conversion efficiency of 8.5% in the bulk.

3.2.2.5. Photorefractive effects

At a high power density, the light in NLPC waveguide undergoes photorefractive effect. This nonlinear phenomenon is due to the onset of an electrical current proportional to the light intensity. This causes local damage of the crystal and leads to lowering conversion efficiency with the deformation of the optical beam. This section describes the causes of photorefractive effect in lithium niobate. One of solutions to overcome this disadvantage is doping crystals. In this thesis, MgO is proposed for a doping material. For this purpose a study on MgO-doped PPLN is undertaken.

When the light propagates in a medium such as lithium niobate, ionic impurities and dopants (Fe^{2+}/Fe^{3+}) can be photo-excited and produce carrier charges, following the mechanism [6]:



The created carrier charge may have different displacement in the crystal, following different physical phenomena. Generally the photo-excited electrons and holes have a higher density at the maxima of the light intensity. If the optical beam has non-uniform distribution intensity, the free-carriers move towards the minima of the light intensity until they are trapped. The resulting charge distribution causes diffusion current:

$$j_D = D \nabla n \quad (3.8)$$

with D the diffusion coefficient and n the carrier density. As their distributions are identical with opposite charge, the generated electrons and holes currents have opposite directions.

The photovoltaic contribution is also considered. Noting that the free carrier density is proportional to the light intensity and knowing that these carriers are under an asymmetric potential in ferroelectric crystals (according to the c -axis for lithium niobate), they migrate in opposite directions, creating a photovoltaic current following the c -axis such as:

$$j_{PV} = \alpha G I \quad (3.9)$$

with α the linear absorption coefficient, G the Glass constant [6] and I the light intensity.

The generated currents create a charge density ρ as:

$$\vec{\nabla}(\vec{j}_D + \vec{j}_{PV}) + \partial_t \rho = 0 \quad (3.10)$$

The charge density is associated with a macroscopic electric field E_{PR} :

$$\nabla(\epsilon \cdot E_{PR}) = \frac{\rho}{\epsilon_0} \quad (3.11)$$

The generated electrical field is generally written as the current j_Ω considering Ohm's law with σ the total conductivity of the material:

$$j_\Omega = \sigma E_{PR} \quad (3.12)$$

where j_Ω compensates the free-carriers displacement: $\vec{j}_D + \vec{j}_{PV} + \vec{j}_\Omega = \vec{0}$. The total conductivity σ takes into account the intrinsic conductivity of the material (without illumination) and the photoconductivity (depending on the carrier density and thus the light intensity).

Generally it is considered that the local diffusion of carriers is made on a small surface compared to the beam size. The effect can be neglected but increases if the thickness of the waveguide decreases. The photovoltaic effect is rapidly saturated with the light intensity. Its contribution to photorefractive effect does not change even if the beam size changes. Moreover, the photo-excitation of impurities is sensitive to wavelength. This phenomenon is more important for SHG than OPO applications.

The charge distribution causes an electro-optic effect causing a modification of the refractive index:

$$\Delta n_{PR} = -n^3 r \frac{E_{PR}}{2} \quad (3.13)$$

In our case, this modification is higher in z-direction compared to y-direction as the electro-optic coefficient $r_{33} > r_{13}$. The typical modification of the refractive index is around 10^{-4} to 10^{-3} . If the photorefractive effect is sufficient to modify the refractive index, we can observe a beam deformation along the c-direction.

Different solutions are possible to increase the conductivity of the material (increasing the Ohm's current and decreasing the photovoltaic current). By increasing the temperature or by doping the material with Mg, Zn, In, Sc, etc... (called extrinsic defects), it is possible to reduce the photorefractive sensitivity of crystal. It was reported the first time by Sweeney *et al.* [7]. The defect structure of MgO-doped LiNbO₃ was characterised by Iyi *et al.* [8]. They concluded that optical damage threshold in doped crystal improves due to increase in Li vacancies. In general, it has been reported that Li/Nb ratio improves up to the doping concentration of 4.5 mol.% of MgO. At 7 mol.% doping, this ratio goes down even below congruent LiNbO₃. In our works, we are interested in 5 mol.% MgO-doped LiNbO₃ and we compared our SHG results with congruent crystal. In stoichiometric LiNbO₃, a threshold doping at 1.8 mol.% is necessary to increase the optical damage threshold [9].

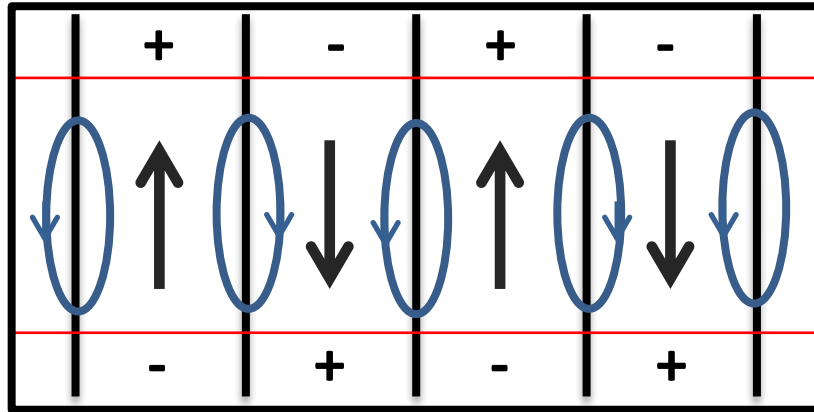


Figure 3.21: Simplified scheme of the created photovoltaic current (blue arrows) in PPLN under light radiations. A loop is created, where carriers go through the inverted domains and return to their positions.

It is also interesting to note, that photorefractive effects is weaker in PPLN crystal than mono-domain crystals. In fact the created photovoltaic current changes its direction along the c-axis and periodically (Fig. 3.21). There can be charge compensation between two domains decreasing the electro-optic effect. Peng *et al.* [10] showed that it was possible to decrease the coercive field and control the propagation domains at the same time, in doped ZnO:LiNbO₃.

3.2.2.6. Photorefractive effect in the waveguide

We have seen in the previous section that the nonlinear crystals are largely subject to photorefractive effects. The evolution of this nonlinear effect is measured over time in the 2D PPLN waveguides. A similar study was carried out by Vincent *et al.* with Zn-doped PPLN planar waveguide fabricated by He⁺ implantation. Firstly, we measure the SHG power from the PPLN 1 waveguide at 58°C at different pump power using the Q-switched laser during 200 min. Three powers of 150 MW/cm², 170 MW/cm² and 200 MW/cm² are chosen to investigate how the performance of sample deteriorates over 200 min. The results are shown in Fig. 3.22. The SHG intensity is normalised by the initial SHG intensity at $t = 0$. As expected, when the pump intensity increases, the photorefractive effect influences on the deterioration of SHG emission.

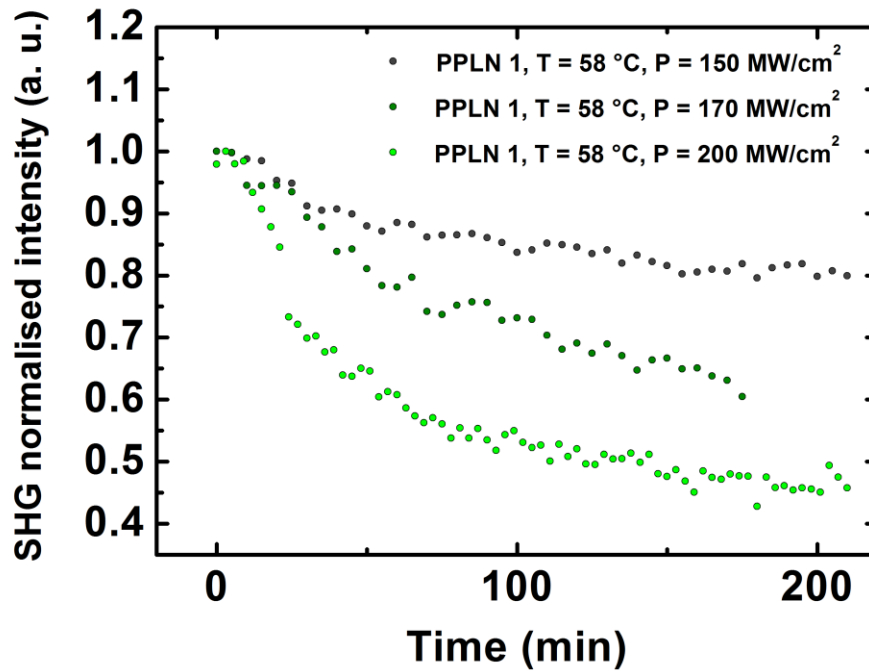


Figure 3.22: Normalised SHG intensity vs. time at different pump power intensity in the PPLN 1 waveguide at 58°C.

In literature, the optical damage threshold of raw lithium niobate is estimated to an intensity of 1 kW/cm² at 532 nm [6]. At a pump intensity of 150 MW/cm², we still observe 80% of the SHG intensity after 200 min. At 200 MW/cm², only 45% of the measured SHG intensity is collected after 200 min. Furthermore, we note that the SHG intensity behaviour decreases exponentially with time. This behaviour can be explained by the fact that the photorefractive effect creates accumulated defects in crystal during time. At the end of the experimentation, we clearly see these created damages in the crystal.

We have also measured the crystal temperature influence on photorefractive damages. The crystal temperature is set to 58°C for QPM orders (1,0) and 102°C for (1,±1). The SHG from both QPM orders is collected by a lens to the power meter. As it was made before, the SHG intensity is normalised with the SHG intensity measured at $t = 0$. The normalised SHG intensities at these two temperatures are shown in Fig. 3.23.

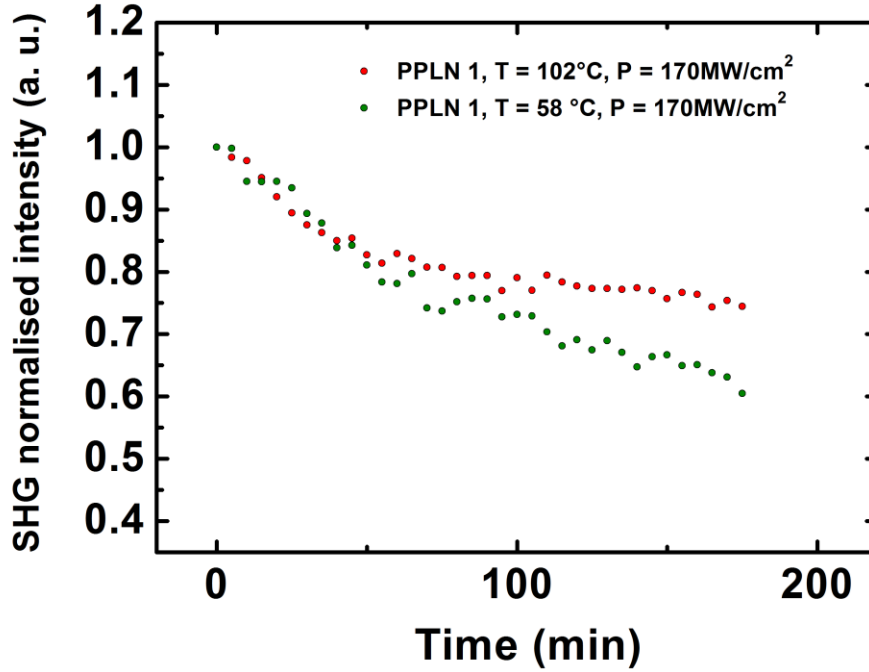


Figure 3.23: Normalised SHG intensity vs. Time at different crystal temperature in PPLN 1 waveguide configuration and at a fixed pump intensity of 170 MW/cm².

As expected, by increasing the crystal conductivity with temperature, it is possible to reduce optical damages due to photorefractive effect in the crystal. This is clear evidence that the photorefractive effect involves in lowering the SHG performance of sample.

In order to carry out a quantitative comparison with the theory, we have fitted the SHG intensity by Eq. (3.18):

$$I_{SH}(t) = I_1 e^{-t/\tau} + I_2 \quad (3.14)$$

with τ the estimated life time, I_2 the value of I_{SH} when $t \rightarrow +\infty$ and I_1 a constant like $I_{SH}(0) = I_1 + I_2$. In fact, the results show that the SHG intensities tend to a certain level which corresponds to I_2 . As the time increases, it is expected that a further deterioration does not occur below this level.

Considering all configurations, the values of τ and I_2 are given in Table 3.2 for the above result:

PPLN 1	τ	I_2
T = 58°C, P = 150 MW/cm ²	65.9	0.80
T = 58°C, P = 170 MW/cm ²	42.8	0.56
T = 58°C, P = 200 MW/cm ²	40.5	0.47
T = 102°C, P = 170 MW/cm ²	44.2	0.75

Table 3.2: Values of τ and I_2 from the fitting expression 3.14 of SHG intensity vs. Time.

We observe two different things from this fitting:

- Near the SHG saturation regime, the life-time of congruent PPLN is very short, between 40 min and 1h.
- From I_2 , we notice that SHG photorefractive damages in crystal reach a limited damage (when $t \rightarrow +\infty$) which is different from one configuration to another, thus the effect of photorefractive saturation is linked to the pump intensity and the crystal temperature.

3.3. Characterisation of implanted waveguide in doped MgO:2D-PPLN

3.3.1. Linear characterisation

The same experimental process is followed for He⁺-implanted 2D-PPLN doped at 5% mol. with magnesium oxide (MgO) and noted PPLN 2. The implantation dose and energy are the same than PPLN 1: successively 1.5×10^{16} ions/cm² and 1.5 MeV. This time, the poling period is set at 6.96 μm . We will see that this period modification has a direct influence by decreasing the SHG peak temperature for the different QPM orders. For now we follow the same experimentation process for linear characterisation.

3.3.1.1. Refractive index profile

We use the same experimental dark *m*-line setup described in section 3.2.1.1. Figure 3.24 shows the measured effective indices $N_{eff,m}$ and calculated by Eq. (3.1.b).

The refractive index profile is also calculated by i-WKB method. This time, the index changes (Δn) are obtained by subtracting the effective indices from the refractive indices of 5% mol. LiNbO₃ at 632 nm ($n_o = 2.2827, n_e = 2.1930$). As we expected, Figures 3. 25 show that a quasi-step index optical waveguide is formed in PPLN 2 with a similar behaviour of the refractive index profile than PPLN 1. We conclude that MgO doping has no significant influence on the guiding properties.

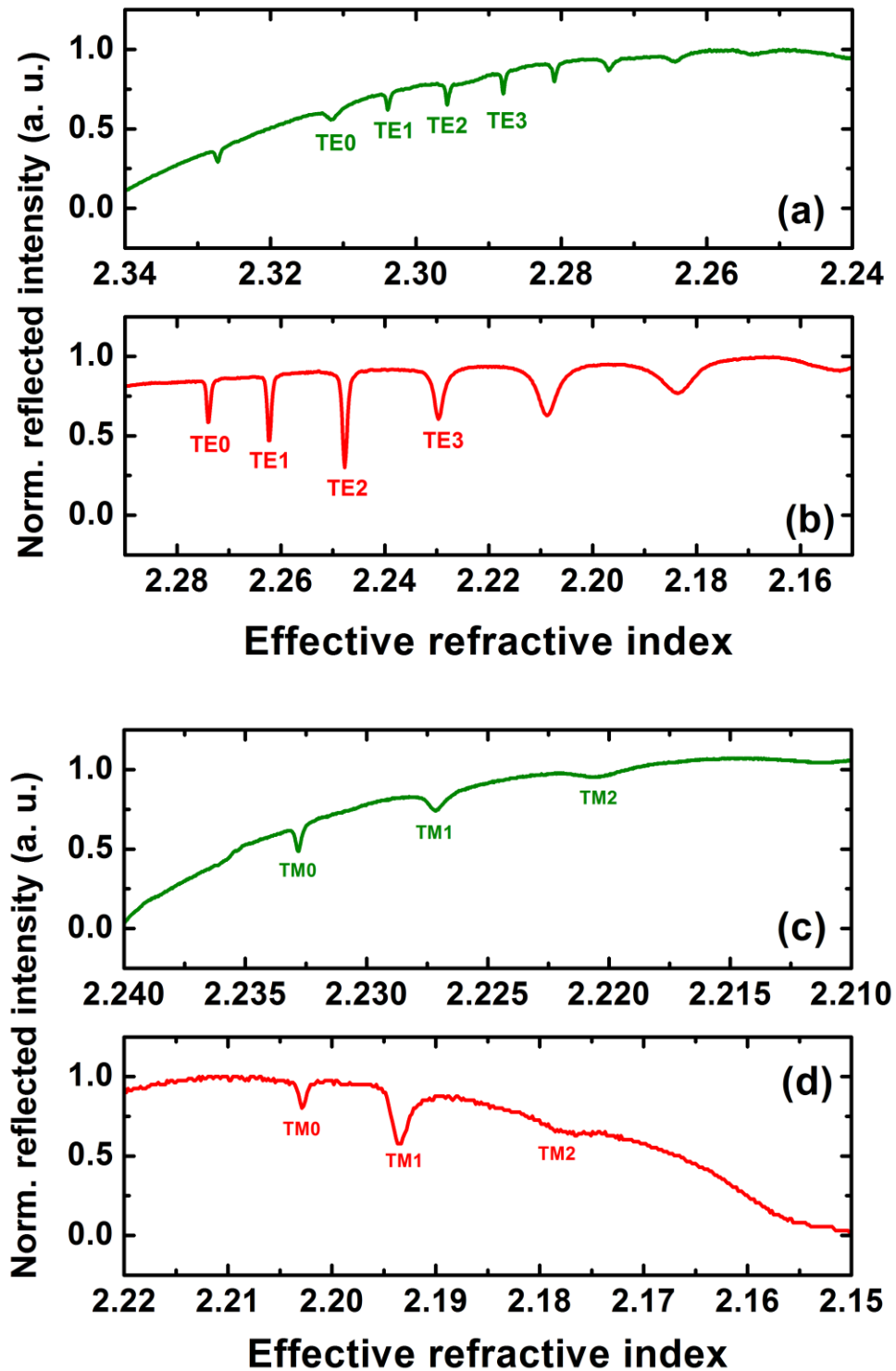


Figure 3.24: M-line measurements in PPLN 2 for TE-modes (a) at 532 nm and (b) 633 nm (red line), and TM-modes (c) at 532 nm and (d) 633 nm (red line).

At 532 nm	Pol.	n_{wg}	Depth (μm)	Mode order	Eff. index
PPLN 2	TE	2.3195	3.61	0	2.3116
				1	2.3039
				2	2.2957
				3	2.2879
				4	2.2810
	TM	2.2406	3.59	0	2.2328
				1	2.2272
2				2.2205	
At 632 nm	Pol.	n_{wg}	Depth (μm)	Mode order	Eff. index
PPLN 2	TE	2.2830	3.54	0	2.2743
				1	2.2643
				2	2.2513
				3	2.2358
				4	2.2177
	TM	2.2126	3.47	0	2.2028
				1	2.1935
				2	2.1815

Table 3.3: Effective index measured at 532 nm and 632 nm for PPLN 2

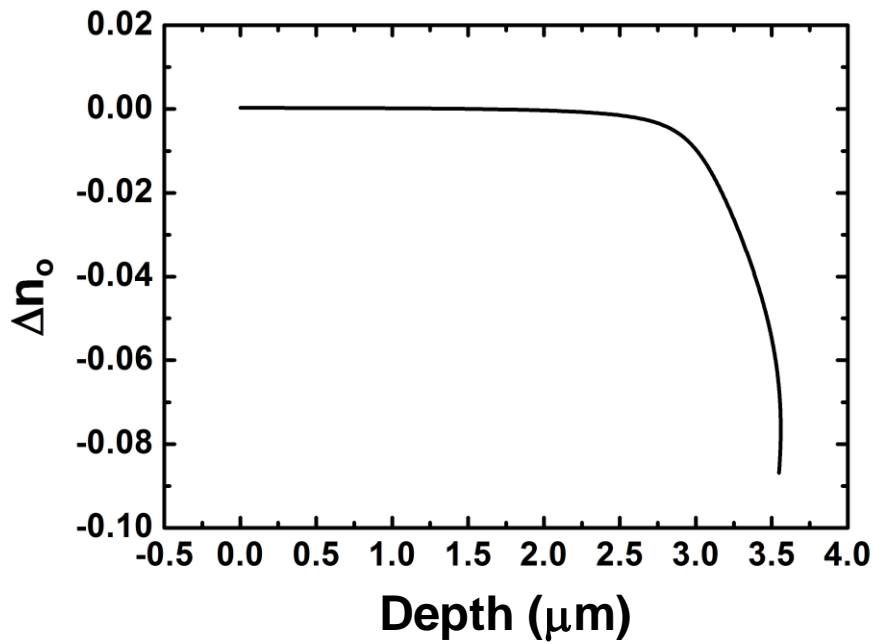


Figure 3.25 (a): Ordinary refractive index profile of PPLN 2 obtained by i-WKB resolution.

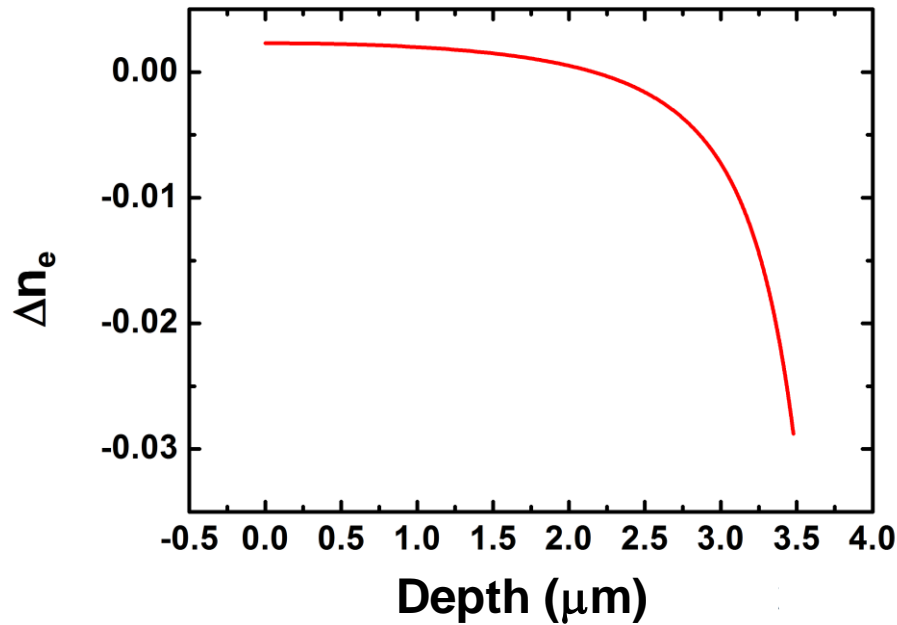


Figure 3.25 (b): Extraordinary refractive index profile of PPLN 2 obtained by i-WKB resolution.

3.3.1.2. Attenuation loss

As it has been done before, the attenuation has been measured with CCD camera at three different wavelengths: 532 nm, 632 nm and 1064 nm. From Fig. 3.26, we remark two points:

- The optical loss decreases as the wavelength increases for both samples.
- The measured loss is 11% lower in PPLN 2 than in PPLN 1. This difference can be considered as negligible, knowing that this method has low accuracy.

A loss lower in MgO-doped PPLN 2 than in non-doped PPLN has never been observed before. It will need further investigations to confirm this claim. As both the samples undergo through the same treatment (implantation and annealing), it is expected that they manifest the same loss.

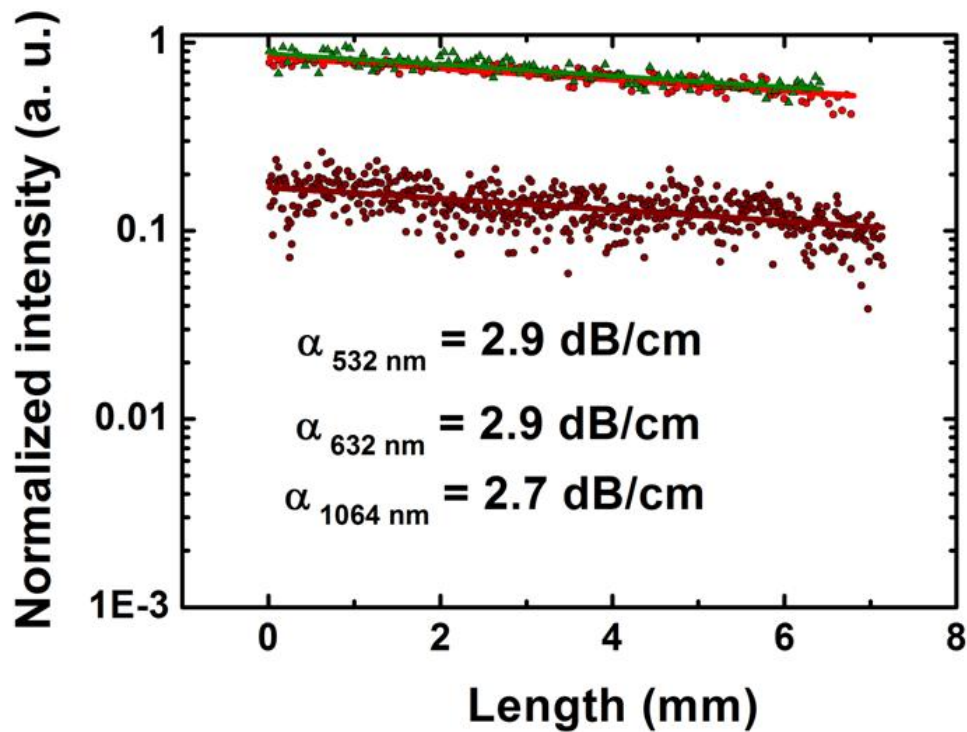


Figure 3.26: Overall optical losses obtained from MgO doped PPLN (PPLN 2) at 532 nm (green dots) 632 nm (red dots) and 1064 nm (brown dots).

3.3.2. Nonlinear characterisation

In the following sections, the interest is to study the influence of doping on SHG. Except the refractive index difference between undoped and doped LiNbO_3 , we have seen, minor differences between waveguides in PPLN 1 and PPLN 2. The difference will certainly when we measure the photorefractive damages. It is first important to show that SHG is possible in PPLN2.

3.3.2.1. SHG temperature tuning

The optimal crystal temperature conditions for SHG in PPLN 2 are measured following the same process described in section 3.2.2.2.

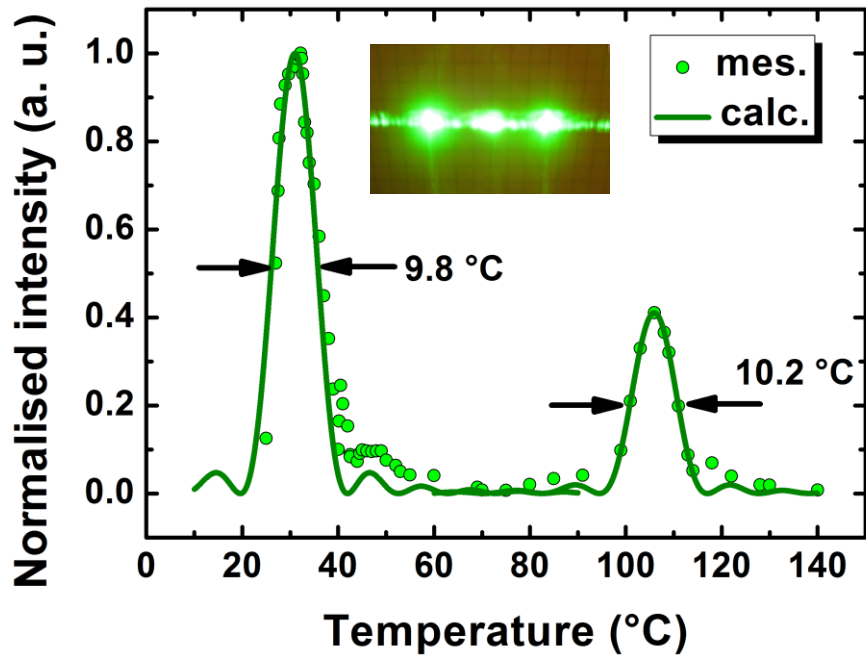


Figure 3.27(a): Normalised optical SHG powers vs. temperature from PPLN 2 bulk.

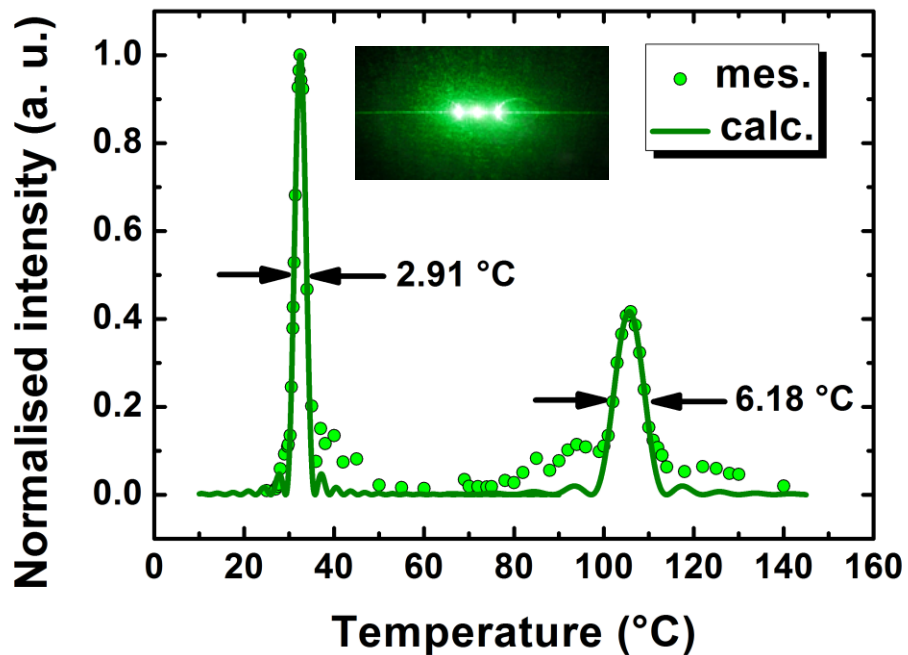


Figure 3.27(b): Normalised optical SHG powers vs. temperature from PPLN 2 waveguide.

If we compare the results between PPLN 1 (Fig. 3.15) and PPLN 2 (Fig. 3.27), we can observe two points:

- In PPLN 2, the SHG peaks are measured at 34°C for the QPM order (1, 0) and 91°C for the QPM order (1, ± 1), which are different to those in PPLN 1. These temperature shifts are due to the poling period difference between PPLN 1 ($\Lambda = 6.92 \mu\text{m}$) and PPLN 2 ($\Lambda = 6.96 \mu\text{m}$)
- In PPLN 2, the broadband temperature is wider in bulk and waveguide configuration. We only deduce that the coupling conditions are not exactly the same between PPLN 1 and PPLN 2. In fact, from Fig. 3.25, it is known that the optical confinement quality is identical in PPLN 1 and PPLN 2. Furthermore, the fundamental beam divergence was more important when we measured the SHG temperature dependence in PPLN 2. This illustrates the difficulty to have similar coupling conditions at each measure. With a higher divergence, the beam-waist is smaller, improving the coupling in the waveguide. In the PPLN 2 waveguide configuration, we obtain an unchanged interaction length of 4.2 mm ($\Delta T_{10} = 2.91^\circ\text{C}$), whereas the beam divergence remains unchanged with PPLN 2 bulk configuration.

3.3.2.2. SHG angular dependence

The far-field SHG intensity profile from PPLN 2 is observed in bulk and waveguide configurations. We remark that SHG from (1, 0), (1, ± 1) and (1, ± 2) QPM orders are visible as shown in Fig. 3.28. Furthermore, we note from the figure that the SHG intensity for the $\mathbf{K}_{1\pm 2}$ RLVs is also observed in PPLN 2 at temperature above 140°C unlike PPLN 1. The lattice period of PPLN 2 (6.96 mm) is adapted to study SHG at lower temperature.

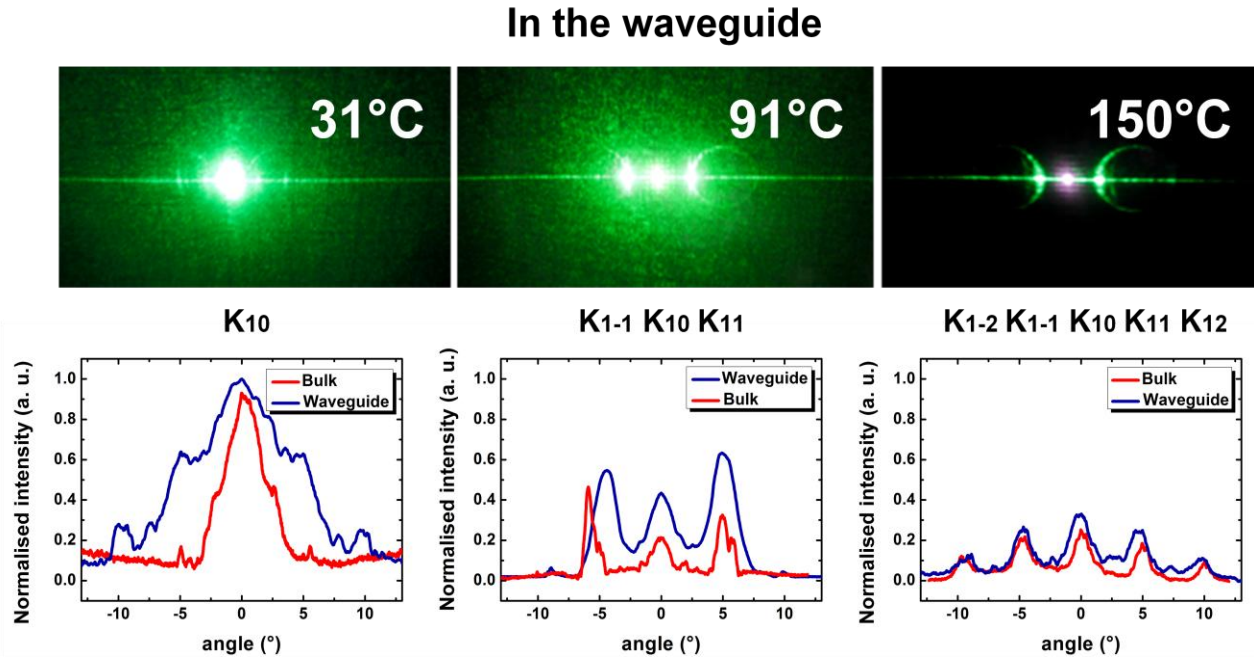


Figure 3.28: Normalised far-field SHG intensity distribution from PPLN 2 obtained at crystal temperatures of 34°C, 91°C and 150°C, in bulk (red trace) and waveguide (blue trace). The QPM orders $(1, 0)$, $(1, \pm 1)$ and $(1, \pm 2)$ are visible.

3.3.2.3. Conversion efficiency measurements

The same process is followed for PPLN 2. The results cw-regimes are presented in Fig. 3.29. At the maximum pump power in cw-regime (Fig. 3.28(a)), the SHG power attains 1.35 mW in the waveguide and 0.58 mW in the bulk configuration. From the polynomial fit, the conversion efficiency is obtained as 4.33 %/W for the waveguide configuration and 0.41 %/W for the bulk configuration. Thus, compare to the waveguide in PPLN 1, the conversion efficiency is almost half of that one. The nonlinear susceptibility of congruent PPLN is 25.2 pm/V and that of 5%-mol. MgO PPLN is 25 pm/V, so the lower efficiencies may come from measurement error. However the SHG emission from the waveguide is 10 times higher than that from the bulk. From Fig. 3.30 in pulsed regime, we observe that the saturation behaviour in PPLN 2 is similar to that in PPLN 1. The SHG is saturated at around 200 MW/cm^2 with a maximum conversion efficiency of 50.3 % in the waveguide.

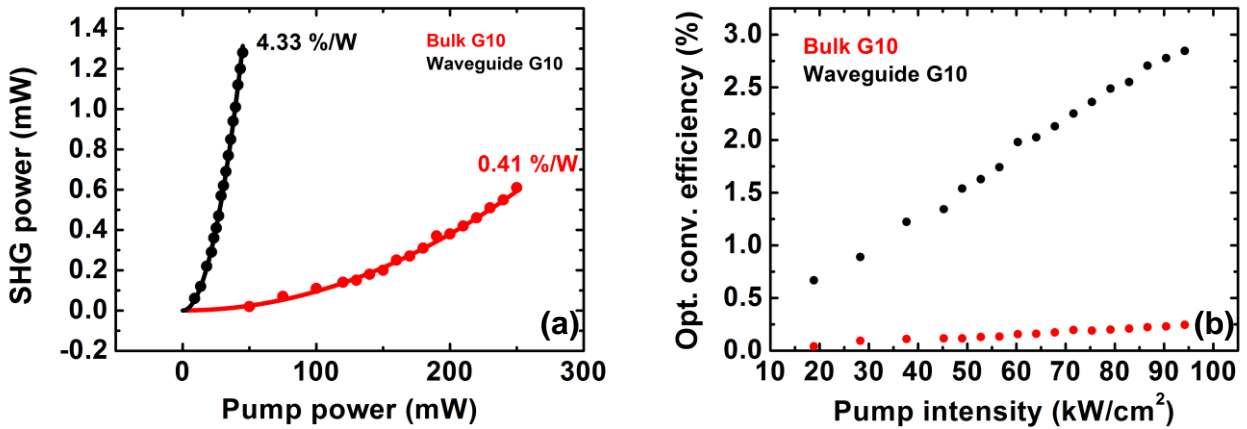


Figure 3.29(a): SHG output power vs. input power in CW regime for the PPLN 2 waveguide (black dots) and bulk (red dots). (b) Conversion efficiencies in CW regime.

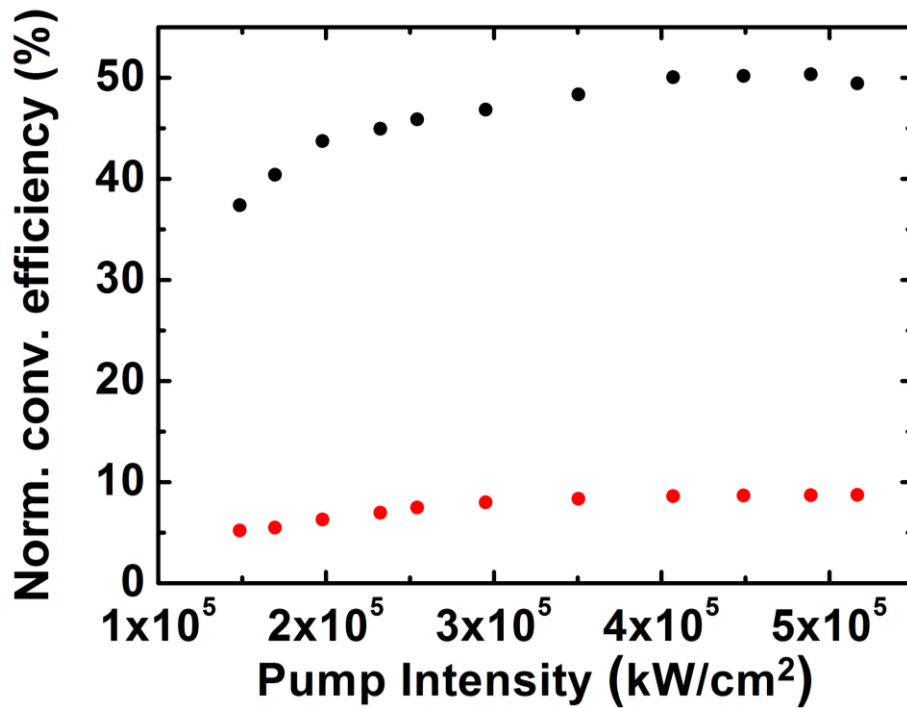


Figure 3.30: SHG conversion efficiency resulting from the PPLN 2 waveguide (black points) and the bulk (red points) in pulsed regime.

3.3.2.4. Photorefractive effect

Likewise, the photorefractive effect is studied in the PPLN 2 waveguide with the same experimental process as the PPLN 1 one, but the temperatures are set to 34°C for QPM order (1,0) and 91°C for (1,±1), which correspond to the optimum QPM conditions. In this case, we know that the photorefractive damage threshold of LiNbO₃ doped with 5% mol. MgO is estimated to 300 MW/cm² at 532 nm. Thus the pump intensities used in this work should not produce photorefractive effects.

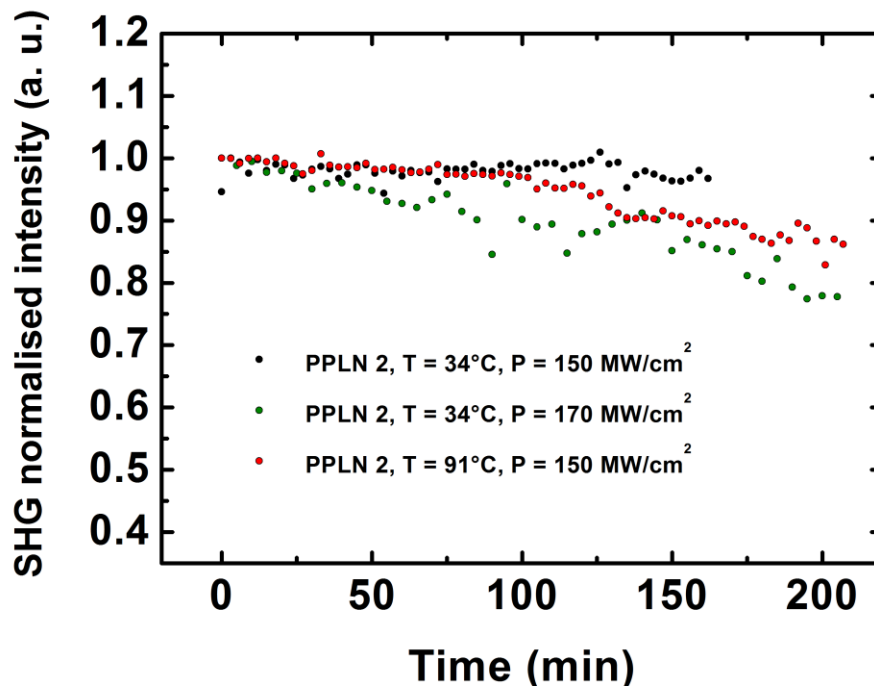


Figure 3.34: Normalised SHG intensity vs. Time at different crystal temperature (34°C and 91°C) and pump intensity (150 MW/cm² and 170 MW/cm²) in PPLN 2 waveguide configuration.

This time, it is interesting to note that the SHG intensity decay has not an exponential behaviour. We can even observe that at the lower pump intensity, the SHG signal remain stable. However, at 170 MW/cm² we observe a SHG intensity decreasing. The photorefractive defects created in the crystal is much less dependent on pump intensity or crystal temperature. This phenomenon becomes minor and seems to follow a random statistical.

It is clearly seen from Fig. 3.34 that the SHG intensity decay does not show an exponential behaviour. We can even observe that at the lower pump intensity, the SHG signal remain almost constant. However, at 170 MW/cm^2 we observe a SHG intensity decreasing. The photorefractive effect in the crystal is much less dependent on pump intensity or crystal temperature. This phenomenon becomes minor.

Summary

This chapter experimentally complete the linear and non-linear studies of the NLPC waveguides fabricated by He^+ implantation. All along our study, we have compared congruent PPLN and PPLN waveguide. This investigation demonstrates the feasibility of waveguide structure in 2D PPLN with an important conservation of the nonlinear properties of the crystal and the PP lattice. We have experimentally described the influence of the waveguide on SHG emission in NLPC, especially its influence on QPM according to the temperature, the QPM order and the SHG conversion efficiency. Moreover we have demonstrated that the MgO-doped PPLN waveguide resists better at high-pump power than the non-doped PPLN one.

Reference:

- [1] J. P. Biersack, J. F. Ziegler, U. Littmarck, vol.1, Pergammon Press, New-York (1985).
- [2] B. Vincent, A. Boudrioua, R. Kremer, P. Moretti, *Second harmonic generation in helium implanted periodically poled lithium niobate planar waveguides*, Opt. Comm. **247**, 461 – 469 (2005).
- [3] V. V. Atuchin, *Causes of refractive indices changes in He-implanted LiNbO₃ and LiTaO₃*, Nucl. Instr. and Meth. In Phys. Res. **B 168**, 488 – 502 (2000).
- [4] F. Chen, *Photonic guiding structures in lithium niobate crystals produced by energetic ion beam*, J. Appl. Phys. **106**, 081101 (2009).
- [5] L. Zhang, P. J. Chandler, P. D. Townsend, *Extra “strange” modes in ion implanted lithium niobate waveguides*, J. Appl. Phys. **70**(3), 1185 - 1190 (1991).
- [6] A. M. Glass, D. Von der Linde, T. J. Negrain, *High-Voltage bulk photovoltaic effect and the photorefractive process in LiNbO₃*, Appl. Phys. Lett. **25**(4), 233 – 235 (1974).
- [7] K. C. Sweeney, L. E. Hulliburton, D. A. Bryan, R. R. Rice, R. Gerson, H. E. Tomaschbe, *Point defects in MgO-doped lithium niobate*, J. Appl. Phys. **57**, 1036 – 1044 (1985).
- [8] N. Iyi, K. Kitamura, Y. Yajima, S. Kimura, Y. Furukawa, M. Sato, *Defectstructure model of MgO-doped LiNbO₃*, J. Solid State Chem. **118**(1), 148 – 152 (1995).
- [9] N. Iyi, K. Kitamura, Y. Yajima, S. Kimura, Y. Furukawa, M. Sato, *Defectstructure model of MgO-doped LiNbO₃*, J. Solid State Chem. **118**(1), 148 – 152 (1995).
- [10] L.H. Peng, Y.-C. Zhang, and Y.-C. Lin, *Zinc oxide doping effect in polarization switching of lithium niobate*, Appl.Phys. Lett. **78**(1), 4-6 (2001).

Conclusions

This thesis work has been performed in collaboration with the Laboratoire de Physique des Lasers (LPL) at the University of Paris 13 and the Graduated Institute of Photonics and Optoelectronics (GIPO) at the National Taiwan University. The main objective of the thesis consists of the study of SHG in 2D-PPLN implanted waveguides..

In order to demonstrate these objectives, the works have been undertaken mainly by characterising the waveguides:

- linear characterisation: refractive index profile and optical loss
- nonlinear characterisation: second-harmonic generation, observation of 2D reciprocal lattice vector, conversion efficiency, photorefractive damage over time

In this context, we have demonstrated for the first time planar optical waveguides in 2D-PPLN by helium implantation technique. Second harmonic waves have successfully been generated from our waveguides using quasi-phase matching.

A 2D structure period of 6.92 μm and a duty cycle of 50 % have been chosen to obtain quasi-phase matching at a pump wavelength of 1064 nm. This structure has been realised by micro-electrodes and high electric fields applied on LiNbO_3 according to Miller's method. This study has been done in the group of Professor L. -H. Peng at the GIPO.

The optical waveguides have been fabricated in 2D-PPLN samples by helium implantation in the CEMHTI laboratory at the University of Orleans in collaboration with Professor E. Ntsoenzok. The implantation dose has been set to 1.5×10^{16} ions/ cm^2 for all samples in order to ensure a maximum refractive index variation at the optical barrier. The implantation energy has been set to 1.5 MeV with TRIM in order to create an optical barrier at 3.5 μm below the z^+ face.

The refractive index profiles of the waveguides fabricated by He^+ implantation have been measured by dark m -line spectroscopy at 532 nm and 632 nm. By observing several TM and TE modes in the samples, the guiding properties have been confirmed with a thickness of 3.9 μm which corresponds to the position of the optical barrier. With the implantation parameters, we have calculated by i-WKB resolution refractive index contrasts $\Delta n_e = 0.034$ and $\Delta n_o = 0.075$ which ensure the guiding properties for TE and TM modes. We have measured a global optical

loss of 3 dB/cm at different wavelengths by a surface analysis of the light scattered from our optical waveguides.

For SHG, the laser beam is injected into the waveguides and the optimal quasi-phase matching conditions are obtained at 53 °C for the reciprocal lattice vector \mathbf{K}_{10} and 102 °C for $\mathbf{K}_{1\pm 1}$, confirming the 2D structure. From this measurement, the SHG interaction length in the waveguide is obtained as 4.4 mm which is 3 times longer than that in the bulk. Due to this long interaction the conversion efficiency in the waveguides is obtained 3 times higher than that in the bulk. It is clearly shown from the experimental results that the pump power is well confined in the waveguides and the nonlinear properties of 2D-PPLN lattice are well preserved.

We have also investigated a He-implanted 2D-PPLN waveguide doped with MgO in order to reduce the optical damage effects. A raw LiNbO_3 is doped by MgO with 5% mol. before 2D structuring of the crystal. The same fabrication process of waveguide is applied to the doped sample. From the linear characterisation, the MgO-doped waveguide manifests the guiding properties similar to those of the non-doped waveguides. The SHG measurements have also been carried out in the MgO-doped bulk PPLN and waveguide. The experimental results show that the conversion efficiency in the waveguide is 2.3 higher than that in the bulk.

The real interest of doping MgO lays down on improving the optical damage of waveguide due to optical high power density. For this purpose we have studied the photorefractive effect over 200 minutes at near the SHG saturation regime. The MgO-doped waveguides have shown the resist to the high density power stronger than that of the non-doped waveguides. Particularly, the waveguide performance remains almost unchanged at a pump-power density of 150 MW/cm².

This study may provide the potential feasibility of tuneable micro-source lasers by using implanted optical waveguide. Some characteristics such as optical loss can be optimised. The study demonstrates that helium implantation is an excellent technique for fabricating optical waveguides. This technique potentially allows the fabrication of PPLN thin films or step-index waveguides by Crystal Ion-Slicing (CIS). In this case, it will be necessary to perform implantation at a dose over 5.10^{16} He⁺/cm². However, a prior study would be necessary on the optical quality of the thin films particularly on the nonlinear conservation properties of PPLN at high implantation dose and the high modification of anisotropy in crystal. A study on the index

profile of PPLN at a high implantation dose has been realised with a high modification of the refractive index in the implanted region. We have especially observed a large decrease of the ordinary refractive index. However, this observation remains to be confirmed by other technical means like Raman spectrography. These studies will be the subject of future works.

It will also be interesting to study channel optical waveguides in 1D-PPLN in order to increase the optical confinement and couple optical fibre system.

Annexe:

Implantation in nonlinear crystals

The non-linear crystals usually have high non-linear optical coefficients, which can be used for SHG, OPO and OPA. In this section, implanted waveguides in several important non-linear crystals will be discussed (except LN and PPLN).

- **Potassium Niobate**

Potassium Niobate has a large birefringence combined with a high nonlinearity and photorefractive sensitivity. Its densely-packed lattice and low Curie temperature make ion implantation the unique method for waveguide fabrication. The first successful waveguide in KNbO_3 was reported by Bremer *et al.* [1], and more detailed investigation of waveguides formation and non linear property characterisation was performed by the group of Gunter [2]. One should point that the extraordinary refractive index has a positive change in the guide region, due to electronic energy deposition [2]. Moreover ridge waveguides were performed by combining He^+ ion implantation and Ar^+ ion sputter etching [3]. The highest conversion efficiency for SH blue light generation is 12.1 %/W for a ridge waveguide [4].

- **Potassium titanium oxide phosphate (KTiOPO_4)**

KTP is an efficient non-linear optical crystal in the visible and infrared spectra. Waveguides in KTP have been fabricated by the implantation of H, He, Li, B, F, or P ions. Binder *et al.* [5] reported KTP waveguide formed by 2 MeV H^+ implantations with a dose of 10^{16} ions/cm². In their work the index increases (< 0.5%) very high at the surface region and decreases (< 9%) at the end of the ion range which builds up an optical confinement barrier. The technique progressed these last years with propagation loss in the channel waveguides determined at 2.9 dB/cm [6]. Recently, Wang *et al.* [7] reported buried channel waveguide in KTP by multiple He ion implantations with the combination of masking technique and ion exchange. Up to 500°C. The SHG was reported in He^+ implanted KTP waveguides with conversion efficiency of 25 % or incident pulses of 1 μJ (pulse width of 20 ns) [8].

- **Lithium triborate (LiB₃O₅)**

LBO has a wide transparency range (particularly in UV range), moderately high non-linear coupling and high damage threshold [9]. Conventional methods such as metal-diffusion and ion exchange cannot be applied to LBO, and only He⁺ ion-implantation allows LBO waveguides [10]. Davis *et al.* reported the channel waveguides in LBO, which were formed by multiple He⁺ ion implantations with a gold mask to form sidewalls of channel waveguides [10]. The SHG conversion efficiency of 7.10⁻⁵% was achieved at a pump wavelength of 937 nm and a power of 9.6 mW. The reason for this low value was attributed to the very low pumping power density and the multimode structures of the waveguide. Moreover, Bakhouya *et al.* [11] investigated the SHG in a LBO planar waveguide formed by double energy He⁺ ion implantation at a total dose of 3.9.10¹⁶ ions/cm² and obtains 10⁻⁴%/W/cm² at 923 nm with a pump power of 250 mW.

- **Gadolinium calcium oxoborate (Ca₄GdO(BO₃)₃)**

GdCOB is one of the most interesting crystals for frequency doubling infrared laser diode light to achieve visible lasers. It is an ideal medium to realise possible self-frequency conversion [12]. As yet it seems that the ion implantation is the only method for the waveguide formation in the crystal [12]. Boudrioua *et al.* reported the formation of both planar and channel waveguides in GdCOB by MeV He⁺ implantation [13, 14]. It was proved that multiple-energy implantation is usually helpful to reduce the losses (2dB/cm) by widening the barrier and hence minimizing the tunnelling effect [14]. The SHG was achieved at the pumping laser excitation of 823 and 960 nm for an arrangement of type I phase matching [15]. A conversion efficiency of 10⁻² % was obtained for the As-implanted planar waveguide in fundamental TM mode to harmonic TE mode and at pumping power of 250 mW.

- **β-Barium borate (β-BBO)**

It has a wide transparency range, large non-linear coefficients, wide thermal acceptance bandwidth and high damage threshold [16]. Up to now, planar waveguides in β-BBO have been fabricated by using MeV He⁺, O⁺ or Si⁺ ion implantation [17 - 18]. In the He⁺ implanted cases, both n_o and n_e have an index-decreased barrier; however, in the guide region, n_o decreases slightly while n_e has a small positive change even for high dose of 2.10¹⁶ ions/cm² [18].

- [1] T. Bremer, W. Heiland, B. Hellermann, P. Hertel, E. Kratzig, D.Kollewe, *Waveguides in KNbO₃ by He⁺ implantation*, *Ferroelectric Lett.* **9**, 11- 13 (1988).
- [2] D. Fluck, P. P. Gunter, *Second-harmonic generation in potassium niobate waveguides*, *IEEE J. Sel. Top. Quant. Electron.* **6**(1), 122 - 131 (2000).
- [3] D. Fluck, P. P. Gunter, R. Irmsher, C. Buchal, *Optical strip waveguides in KNbO₃ formed by He ion implantation*, *Appl. Phys. Lett.* **59**(25), 3213 - 3216 (1991).
- [4] T. Pliska, D. Fluck, P. P. Gunter, E. Gini, H. Melchior, L. Beckers, C. Buchal, *Birefringence phase-matched blue light second-harmonic generation in a KNbO₃ ridge waveguide*, *Appl. Phys. Lett.* **72**, 2364 - 2367 (1998).
- [5] P. Binder, A. Boudrioua, J. C. Loulergue, P. Moretti, *Formation of optical waveguides in potassium titanyl phosphate by double implantation of protons*, *Appl. Phys. Lett.* **79**(16), 2558 - 2560 (2001).
- [6] Y. Tan, F. Chen, L. Wang, W. Xue-Lin, *Optical waveguides in KTiOPO₄ crystal produced by proton implantation*, *IEEE Light. Techn. J.* **26**(10), 1304 – 1308 (2008).
- [7] L. L. Wang, K. M. Wang, F. Lu, B. R. Shi, X. L. Wang, L. Wang, Q. M. Lu, *Monomode low loss optical waveguide in KTiOPO₄ formed by combining ion implantation with ion exchange*, *J. Appl. Phys.* **104**(6), 063115 (2008).
- [8] L. Zhang, P. J. Chandler, P. D. Townsend, Z. T. Alwahabi, S.L. Pityana, A. J. McCaffery, *Frequency doubling in ion-implanted KTiOPO₄ planar waveguides with 25% conversion efficiency*, *J. Appl. Phys.* **73**(6), 2695 – 2700 (1993).
- [9] S. Zhao, C. Huang, H. Zhang, *Crystal growth and properties of lithium triborate*, *J. Cryst. Growth* **99**(1 - 4), 805 – 510 (1990).
- [10] G.M. Davis, L. Zhang, P.J. Chandler, P.D. Townsend, *Planar and channel waveguide fabrication in LiB₃O₅ using MeV He⁺ ion implantation*, *J. Appl. Phys.* **79**(6), 2863 - 2868 (1996).

- [11] C. Bakhouya, A. Boudrioua, R. Kremer, P. Moretti, J.C. Loulergue, K. Polgar, *Implanted waveguides in borate crystals (LTB, β -BBO and LBO) for frequency conversion*, Opt. Mater. **18**, 73 - 76 (2001).
- [12] G. Aka, A. Kahn-Harari, D. Vivien, J.M. Benitez, F. Salin, J. Godard, *A new nonlinear and neodymiumlaser self-frequency doubling crystal with congruent melting $Ca_4GdO(BO_3)_3(GdCOB)$* , Eur. J. Solid State Inorg. Chem. **33**, 727 - 730(1996).
- [13] A. Boudrioua, J.C. Loulergue, P. Moretti, B. Jacquier, G. Aka, D. Vivien, *Second-harmonic generation in He^+ implanted gadolinium calcium oxoborate planar waveguides*, Opt. Lett. **24**(18), 1299 - 1301 (1999).
- [14] B. Vincent, A. Boudrioua, J.C. Loulergue, P. Moretti, S. Tascu, B. Jacquier, G. Aka, D. Vivien, *Channel waveguides in $Ca_4GdO(BO_3)_3$ fabricated by He^+ implantation for blue light generation*, Opt. Lett. **28**(12), 1025 - 1027 (2003).
- [15] R. F. Xiao, L. C. Ng, P. Yu, G. K. L. Wong, *Preparation of crystalline beta barium borate thin films by pulsed laser deposition*, App. Phys. Lett. **67**(3), 305 – 308 (1995).
- [16] X. L. Wang, F. Chen, K. M. Wang, Q. M. Lu, D. Y. Shen, R. Nie, *Planar optical waveguides in β -BaB₂O₄ produced by oxygen ion implantation at low doses*, Appl. Phys. Lett. **85**(9), 1457 - 1460 (2004).
- [17] X.L. Wang, F. Chen, F. Lu, G. Fu, S.L. Li, K.M. Wang, Q.M. Lu, D.Y. Shen, H.J. Ma, R. Nie, *Refractive index profiles of planar optical waveguides in β -BBO produced by silicon ion implantation*, Opt. Mater. **27**, 459 - 463 (2004).
- [18] R. Degl'Innocenti, A. Guarino, G. Poberaj, P. Gunter, *Second harmonic generation of continuous wave ultraviolet light and production of β -BaB₂O₄ optical waveguide*, Appl. Phys. Lett. **89**(4), 041103 (2006).

Scientific articles

Articles:

[1] Q. Ripault, M. W. Lee, F. Mérique, T. Touam, B. Courtois, E. Ntsoenzok, L. -H. Peng, A. Fischer and A. Boudrioua, *Investigation of a planar optical waveguide in 2D PPLN using Helium implantation technique*, Opt. Exp. **21**(6), 7202 – 7208 (2013).

[2] Q. Ripault, M. W. Lee, E. Ntsoenzok, L. -H. Peng and A. Boudrioua, *Second-harmonic generation in Helium implanted nonlinear photonic crystal (doped MgO 2D-PPLN) waveguide: optical damage effects* (to be submitted).

Conferences:

[1] Q. Ripault, M. W. Lee, T. Touam, B. Courtois, E. Ntsoenzok, L. -H. Peng, A. Boudrioua, *Démonstration de guide d'ondes sur PPLN 2D dopé MgO*, JNOG 8 – 11 Juillet 2013, Villetaneuse (Poster).

[2] M. Lazoul, Q. Ripault, A. Boudrioua, L. M. Simohamed, A. Fisher, L. H. Peng, *Génération paramétrique multilongueur d'onde dans le PPLT-2D*, JNOG 8 – 11 Juillet 2013, Villetaneuse (Oral).

[3] Q. Ripault, A. Boudrioua, L. -H. Peng, P. Moreti, T. Touam, Faiza, Mérique, E. Ntsoenzok, *Guides d'ondes par implantation ionique d'hélium (He^+) dans le PPLN 2D*, JNOG 10 – 12 Juillet 2012 Lyon (Oral).

[4] Q. Ripault, A. Boudrioua, L. -H. Peng, P. Moreti, T. Touam, Faiza, Mérique, E. Ntsoenzok, *Cristaux photoniques non-linéaires sur niobate de lithium : application aux sources lasers multi-longueur d'ondes*, JNOG 4 – 7 Juillet 2011, Marseille (Poster).

[5] Q. Ripault, M. Lazoul, A. Boudrioua, L. -H. Peng, P. Moreti, T. Touam, E. Ntsoenzok, *Cristaux photoniques non-linéaires sur niobate de lithium*, C'Nano IdF, 24 – 25 Mars 2011, Paris (Poster).

Second-Harmonic Generation in Helium-implanted 2D-PPLN waveguides

The optical confinement for second-harmonic generation (SHG) by Quasi-Phase Matching (QPM) has the interest to highly improve the conversion performances from the periodically poled structures (PP). It allows the use of low pump-power. The originality of our works is that we have performed optical waveguides by helium implantation at MeV energies in congruent and MgO doped 2D-PPLN, having a square PP lattice and a periodicity of 6.92 μm .

Firstly, we have measured the linear properties of our samples by nondestructive methods. The refractive index profiles reconstruction by i-WKB method of the waveguides (n_o et n_e) have been estimated from the effective indices measured at 532 nm, 633 nm and 1064 nm by prism-coupling method (m -line by reflection). We have also measured the overall losses of the samples in implanted PP zone with CCD-camera at these wavelengths.

A SHG experimental setup has been built in order to characterise and compare the nonlinear properties of our 2D-PPLN in bulk and waveguide configurations (SHG at different QPM orders according to temperature, SHG emission angle, conversion efficiency). The nonlinear optical setup uses a microscope objective -coupling system - optical fibre-decoupling system and the pump is a cw-laser diode at 1064 nm, allowing a maximum optical power of 300 mW. We find a conversion efficiency of 6.8 %/W in waveguide configuration and 0.4 %/W in bulk configuration.

Guide d'onde optique dans le PPLN-2D par implantation Hélium pour la génération de second-harmonique

Le confinement optique dans le cadre de la génération second-harmonique (GSH) par Quasi-Accord de Phase (QAP) a l'intérêt d'améliorer grandement les performances de conversion de la structure Périodiquement Polarisée (PP), autorisant l'utilisation de sources lasers à faible puissance de pompe. L'originalité de notre travail est d'avoir réalisé ces guides d'ondes par implantation d'ions He^+ à des énergies de l'ordre du MeV dans des PPLN 2D congruent non dopés et dopés MgO à 5%, de maille PP carrée et de période 6,92 μm .

Dans un premier temps nous avons cherché à mesurer les propriétés linéaires de nos échantillons par des méthodes non-destructives. La reconstruction des profils d'indice de réfraction i-WKB de nos guides d'ondes (n_o et n_e) ont été extrapolé à partir de la mesure des indices effectifs a 532 nm, 633 nm et 1064 nm, et en utilisant la méthode du couplage par prisme (m -line en réflexion). Nous avons également mesuré les pertes optiques globales des échantillons dans la zone PP implantée avec une camera CCD à ces longueurs d'ondes.

Un dispositif expérimental de GSH a également été monté afin de caractériser et comparer les propriétés non-linéaires de nos PPLN-2D massifs et guides (GSH pour différents ordres du QAP et suivant la température, angle d'émission de la GSH, efficacité de conversion). Le banc de caractérisation d'optique non-linéaire utilise un système de couplage par objectif de microscope - découplage par fibre et utilisant comme source une diode laser à 1064 nm en continue, pouvant monter à une puissance optique de 300 mW. Nous avons trouvé une efficacité de conversion de 6.8 %/W pour le guide et de 0,4 %/W dans le substrat.